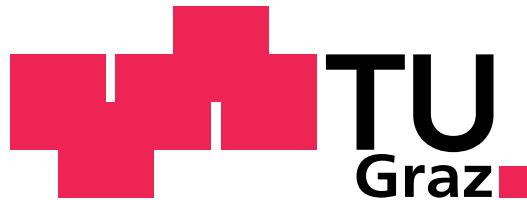Dissertation submitted to the Graz University of Technology,
Institute of Hydraulic Engineering and Water Resources Management, for the attainment of the
degree of Doctor of Engineering Sciences (Dr. techn.)

Hydraulic Investigations of a
Y-bifurcator

Wolfgang Dobler
23.01.2012

Reviewed and Examined by:

Prof. Dr. Gerald Zenz
Institute of Hydraulic Engineering
and Water Resources Management
Graz University of Technology

Prof. Dr. Robert Michael Boes
Laboratory of Hydraulics
Hydrology and Glaciology
ETH Zurich

Abstract

The demand for electrical energy has been increasing constantly during the past decades but contrary to the demand the resources of fossil energy are finite. It is essential therefore, that humanity is provided with renewable energy in order to be able to maintain prosperity. Water Hydro power is the spine of renewable energy, hence it is essential to design new and efficient high-head power plants in alpine areas. The plant components consist mostly of an intake at a reservoir which conveys the water into a pressure tunnel. The pressure tunnel and the subsequent penstock are divided by a surge chamber with a valve chamber to be able to close the penstock, if necessary. The main purpose for the surge chamber is the protection of the pressure tunnel from a water hammer initiated by a discharge change in the penstock. After the surge chamber follows the high-pressure penstock which conveys the water to the power house. Shortly before the power house the water will be distributed with a bifurcator to several turbines.

In this thesis the model test of a Y-bifurcator of a high-head power plant will be presented. The model test consisted of $42°$ bend, a straight pipe (18 diameters long) from the bend to the Y-branch and two branching pipes with a branching angle of $40°$. The secondary flow caused by the bend has been made visible by a Particle Image Velocimetry (PIV). The results of the secondary flow have been quantified with the velocity correction factor α. The PIV-Measurements have been carried out with natural seeding; the accuracy of this procedure is presented and proves reliable results. The upscaling of the hydraulic model test has been based on the Reynolds law. This caused too high discharge rates in the model test, thus, an extrapolation with a quadratic polynomial, based on the least square method, has been conducted to get the discharge rate in respect to the head loss. The results of the secondary flow and the head losses have been verified with a numerical simulation. Also, the results of the PIV-measurement (turbulent kinetic energy, Reynolds-stress, production etc.) have been compared with the numerical simulation. The CFD calculations have been double-checked with the free and open software OpenFoam. In order to achieve a reduction of the hydraulic head losses a guide vane device has been applied. A water-hammer calculation, based on the method of characteristics, has been carried out to determine the highest pressure in the Y-Bifurcator. The code for the water-hammer calculation has been written with TCL/TK and Matlab/Octave.

Kurzfassung

Der Bedarf an elektrischer Energie ist seit den letzten Jahrzehnten stark am Steigen und im Gegensatz dazu, sind die Vorkommen von fossilen Energien begrenzt. Es ist daher notwendig, dass die Menschheit mit erneuerbarer Energie versorgt wird, um damit unseren Wohlstand halten zu können. Wasserkraftanlagen - im Besonderen Hochdruckanlagen, stellen einen wesentlichen Teil der erneuerbaren Energien dar und eine effiziente Auslegung der Anlage ist daher wünschenswert. Eine Hochdruckanlage besteht generell aus einer Rohrleitung, die einen alpinen Speicher mit den Turbinen im Tal verbindet. Kurz vor den Turbinen wird der Wasserstrom mit Bifurkatoren auf einzelne Rohre aufgeteilt.

Ein typischer Bifurkator wurde in dieser Arbeit an Hand eines Modellversuchs und mit numerischen Berechnungen näher untersucht. Der Modellversuch besteht aus einem 42° Bogen, einem geraden Rohrstück und dem anschließenden Y-Bifurkator mit einem Verzweigungswinkel von 40°. Die Sekundärströmung, verursacht durch den Bogen, wurde mit Particle Image Velocimetry (PIV) sichtbar gemacht. Die PIV-Messungen wurden mit natürlichen Schwebstoffpartikeln (Seeding) durchgeführt; die Genauigkeit dieser Methode ist dargestellt und zeigt verlässliche Ergebnisse. Der Modellversuch ist nach dem Reynold'schen Gesetz betrieben. Die dadurch bedingten Durchflussraten im Modell sind zu hoch und daher wurde eine Extrapolation mit einem quadratischen Polynom durchgeführt, um die hydraulischen Verluste in Abhängigkeit des Durchflusses zu erhalten. Die Ergebnisse der Sekundärströmungen und der hydraulischen Verluste sind mit einer numerischen Simulation (Fluent und OpenFoam) nachgerechnet und miteinander verglichen worden (Turbulente kinetische Energie und deren Produktion, Reynolds Spannung etc.). Um eine Verringerung der hydraulischen Verluste zu erreichen, wurde der Bifurkator mit einer Drallströmung beaufschlagt; für eine Durchflussaufteilung konnten dabei geringere Verluste festgestellt werden, als ohne Drallströmung. Eine Druckstoßberechnung der gesamten Anlage wurde nach dem Charakteristikenverfahren in der Skriptsprache Matlab/Oktave und TCL/TK verfasst, um damit den größten Druck im Bifurkator zu bestimmen. Mit dem berechneten größten Druck ist eine Dimensionierung des Bifurkators möglich. Die Druckstoßberechnung wurde auch mit dem kommerziellen Programm Wanda verglichen und zeigte übereinstimmende Ergebnisse.

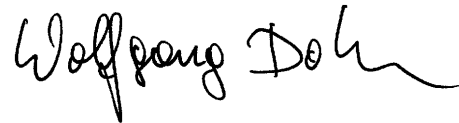# Acknowledgements

Statutory declaration

I declare that I have authored this thesis independently, that I have not used other than the declared sources / resources, and that I have explicitly marked all material which has been quoted either literally or by content from the used sources.

January 24, 2012
. . . .
Date

. . . .
Signature

Contents

Nomenclature

Constants

g Gravity , page 5 $\frac{m}{s^2}$

Greek

α Velocity correction factor , page 90   —

$\alpha_{conf,limit}$ Confidence limit , page 68   —

β Angle , page xxi $^\circ$

$\chi^2(n)$ χ^2-distribution , page 68   —

Δh Piezometer head differential , page 82 m

Δh_f Head level loss due to pipe friction , page 5 m

Δh_{local} Local head loss (excluding pipe friction) , page 5 m

Δh_{tot} Total head level loss (including pipe friction) , page 5 m

ϵ Dissipation , page 110 $\frac{m^2}{s^3}$

Γ Diffusion coefficient , page 107 $\frac{m^2}{s}$

λ Friction coefficient, page 5   —

λ_{wave} Wavelength , page 66 m

μ Dynamic viscosity , page 63 $\frac{Ns}{m^2}$

ν Kinematic viscosity , page 63 $\frac{m^2}{s}$

ν_t Eddy viscosity , page 110 $\frac{m^2}{s}$

Φ Transport quantity , page 106   —

ψ Relative power loss , page 33   -

ρ Density , page 63 $\frac{kg}{m^3}$

τ_{ij} Stress tensor , page 109 $\frac{N}{m^2}$

τ_s Relaxation time , page 63 s

τ_w Wall shear stress , page 79 $\frac{N}{m^2}$

K	Kinetic energy of the mean flow , page 75	$\frac{Joule}{kg}$
k	Turbulent kinetic energy , page 110	$\frac{Joule}{kg}$
k_s	Equivalent sand roughness , page 79	$-$
K_{tot}	Kinetic energy of the flow , page 75	$\frac{Joule}{kg}$
L	Length , page 5	m
L_{mo}	Length - Model , page 38	m
L_{pr}	Length - Prototype , page 38	m
M	Magnification factor , page 66	$-$
m	Mass , page 90	kg
N	f-number (f/D_a) , page 66	$-$
n	Sample size , page 68	$-$
n_w	Distance normal to the wall , page 117	m
P	Pressure , page 109	$\frac{N}{m^2}$
P_{kin}	Kinetic power , page 33	W
P_{loss}	Power loss , page 33	W
q	Dynamic velocity head , page 28	m
Q_3	Discharge at time step j-1, page 139	$\frac{m^3}{s}$
Q_P	Discharge at time step j , page 139	$\frac{m^3}{s}$
$Q_{throttle}$	Discharge of the throttle , page 140	$\frac{m^3}{s}$
R	Abbreviations for char. Method , page 136	$\frac{s^2}{m^5}$
r	Radius , page 15	mm
Re	Reynolds number , page 63	$-$
S	Source or sink , page 106	$-$
s	wall thickness , page xxiii	m
S_{ij}	Deformation Tensor , page 110	$\frac{1}{s}$
t	Time , page 63	s
$t(n)$	t-distribution , page 68	$-$
TU	Turbulence Intensity , page 68	$-$
U	Voltage , page 49	$Volt$
$u,\ v\ and\ w$	Velocity components , page 63	$\frac{m}{s}$

u^+	Dimensionless u ($u^+ = \frac{\bar{u}}{u_\tau}$) , page 87	$-$
u_τ	Shear velocity , page 87	$\frac{m}{s}$
V	Velocity , page 5	$\frac{m}{s}$
Vz	Sign: + or - , page 138	
x	Integration variable , page 63	$-$
y^+	Dimensionless y ($y^+ = \frac{u_\tau \cdot y}{\nu}$) , page 87	$-$
Z_0	distance: lens - object , page 66	m
z_0	distance: lens - image , page 66	m
z_3	Height at time step j-1, page 139	m
z_P	Height at time step j , page 139	m

Chapter 1

Introduction and objectives

The demand for electrical energy has been increasing constantly during the past decades but contrary to the demand the resources of fossil energy are finite. It is essential therefore, that humanity is provided with renewable energy in order to be able to maintain prosperity. Hydro power plants - especially high-head power plants represent a substantial part of renewably energies, an efficient design of such plants is, therefore, desirable.

The plant components (see Figure 1.1) consist mostly of an intake at a reservoir which conveys the water into a pressure tunnel. The pressure tunnel and the following penstock are divided by a surge chamber with a valve chamber to close the penstock if necessary. The main purpose for the surge chamber is the protection of the pressure tunnel from a water hammer, initiated by a discharge change in the penstock. After the surge chamber follows the high-pressure penstock which conveys the water to the power house. Shortly before the power house the water will be distributed with a bifurcator to several turbines.
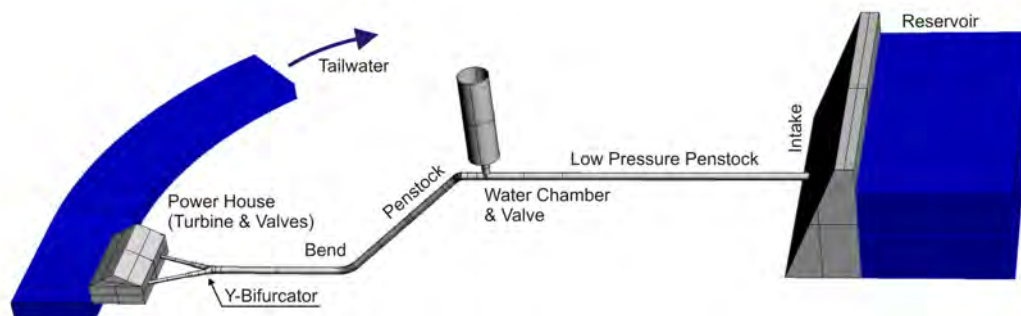
Figure 1.1: *Sketch of a general layout of a high-head plant*

The aforementioned Y-bifurcator is the subject of this thesis. In the Hydraulic Engineering Laboratory of Graz University of Technology a hydraulic model of the Y-bifurcator has been set up to investigate the hydraulic behavior of a dividing flow. As a further challenge a bend has been located 18 times the diameter upstream of the Y-bifurcator which causes a slight secondary flow in the pipe installation. This makes it necessary to get more information on the velocity and pressure distribution along the pipe installation of the hydraulic model test. This has been conducted with Particle Image Velocimetry (PIV), differential pressure measurements and numerical simulations. The general purpose of this thesis is to demonstrate the head losses of the Y-bifurcator with an extrapolation method, including the secondary flow. The free software package OpenFoam (CFD) and Wanda (water hammer) have been double-checked with a commercial and a self-written software

package. A short summary of the individual chapters of this thesis are as follows:

Literature review

A literature review of hydraulic model tests on bifurcators will be presented. It gives general considerations of local losses in bifurcations, like in a T-bifurcator, model set up and so on. The second part of the review deals with Y-bifurcators itself. Again, the model set up and the calculation of the loss coefficient ζ will be presented and a short summary of the Y-bifurcators will finish the review. (see Chapter 2, beginning at Page 5).

Particle Image Velocimetry

As aforementioned, it is necessary to quantify the secondary flow in the pipe. This is done by means of a Particle Image Velocimetry (PIV) which is an optical method to obtain instantaneous velocity vector fields of 2D-planes within a fluid. The whole measuring campaign has been carried out by using the natural seeding of the flow. The velocity lag and the minimum detectable velocity of the seeding have been calculated. The results of the PIV-data, after having validated the velocity vectors, have been statistically analyzed with the confidence interval of the mean velocity and the standard deviation of the velocity. With the PIV-results the secondary flow (via the velocity correction factor α) and the equivalent pipe roughness k_s could be determined. Finally, based on the statistical data retrieved from the PIV, several parameters of the flow have been calculated like turbulent intensity, kinetic energy, production of kinetic energy, Reynolds-stress and vorticity (see Chapter 4, beginning at Page 51).

Hydraulic losses - Loss coefficient ζ

The loss coefficient ζ of the Y-bifurcator has been calculated as the head loss Δh divided by the kinetic velocity height, excluding any pipe friction. The equivalent sand roughness k_s, which is needed for the Colebrook equation in order to determine the pipe friction coefficient λ, has been measured with two different methods. The first method used the differential pressure loss between several control sections where a linear friction gradient exists (Darcy-Weisbach). The other method for the k_s-calculation has been conducted with Particle Image Velocimetry (PIV) where the logarithmic law of the wall is evaluated.

Due to the bend upstream of the Y-bifurcator a secondary flow occurs in the pipe installation. Because of the 1D-consideration for the local loss calculation ζ the influence of the secondary flow needs to be taken into account by the means of a velocity correction factor α.

The hydraulic model test has been scaled after the Reynolds law which implies that the velocity in the model test is the product of the scaler and the velocity of the prototype. This yields a velocity (max. 43 m/s!) in the model test which is far too high for the pumps in the laboratory. Therefore, the results have been extrapolated with the least square method. This is also checked with a numerical calculation where the desired discharge rate due to the Reynolds model can be set and the resulting head losses are compared with the extrapolated head losses of the model test.

Another way to reduce the loss coefficient ζ was the use of a guide vane apparatus. The guide vane induces a swirling flow upstream of the Y-bifurcator. As a result, the loss coefficient could be reduced for one flow distribution (see Chapter 5, beginning at Page 77).

Computational Fluid Dynamics

For the complete model test a numerical CFD calculation has been conducted. The CFD calculation was carried out with the commercial program Fluent. The setting for the simulations was the unsteady second order implicit method together with the k-ϵ model. (see Chapter 6, beginning at Page 105). The CFD-package of Fluent has been compared also with the open source software OpenFoam.

Programming of water-hammer with the method of characteristics

The final chapter demonstrates a water hammer calculation of the power plant Pirris. The entire pipe installation has been discretized and numerically solved with the method of characteristics. The numerical simulation has been written as a Matlab/Octave script. The objective of the numerical simulation has been the calculation of the highest and lowest pressure height in the Y-bifurcator. With the known pressure, a design of the Y-bifurcator is possible. The simulation has been double-checked with the commercial software Wanda (Version: 3.72.851).

Chapter 2

Literature Review

Due to the complex flow structures in pipe flows hydraulic model tests are often necessary. Various model tests have been carried out in the past and abundant data are available (see Idelchik [1994] and Miller [1990]).

A notable amount of literature studies for trifurcations, which are similar to Y-bifurcations, are published where energy losses or the general hydraulic behavior for dividing and combining flow are investigated (see John and Gladwell [1965], Berner [1970], Richter [1988], Ruprecht et al. [1998], Ruus et al. [1966] and Klasinc et al. [1999]).

Of particular interest are the papers of Mayr [2009], Jahrbacher [2001] and Imitzer [2000] where a swirling induced flow on a trifurcation is investigated. Mayr [2009] reported for some flow distributions lower hydraulic losses than without a swirling flow.

The following literature review gives a short overview of the history of hydraulic model tests with emphasis on Y-bifurcators of dividing flows. Every loss coefficient ζ - if not other stated - is the coefficient for the local losses without any pipe friction. The loss coefficient ζ (see Figure 2.1) is made dimensionless with the dynamic velocity head of the pipe carrying the total flow, that is

$$\zeta = \frac{\Delta h_{local}}{V_{mean}^2/2g} \tag{2.1}$$

whereas $\Delta h_{local} = \Delta h_{tot} - \Delta h_f$ is the total loss subtracting the pipe friction Δh_f. The total loss Δh_{tot} is defined with the Bernoulli Equation as

$$z_1 + \frac{P_1}{\rho g} + \frac{V_1^2}{2g} = z_2 + \frac{P_2}{\rho g} + \frac{V_2^2}{2g} + \Delta h_{tot} \tag{2.2}$$

and the pipe friction is calculated, according to Darcy and Weisbach equation, as

$$\Delta h_f = \lambda \cdot \frac{L}{D} \cdot \frac{V^2}{2 \cdot g} \tag{2.3}$$

With the set of equations from Eq. 2.1 to Eq. 2.3 the loss coefficient ζ can be determined.
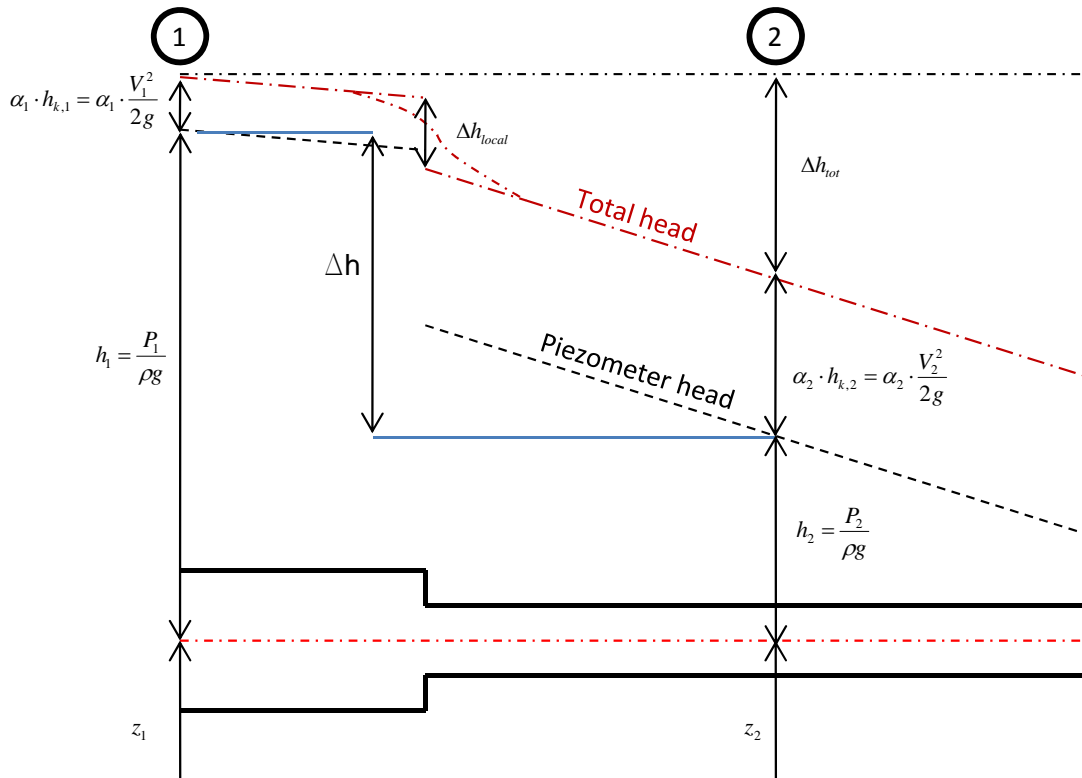
Figure 2.1: *Example of energy losses of a pipe with an installed component*

The review can be split into two parts whereas the first part deals with general considerations of local losses in bifurcations. This includes the model set up for the pressure loss measurement as well as the calculation of the loss coefficient ζ.

The second part of the review deals with Y-bifurcators. Again the model set up and the calculation of the loss coefficient ζ will be presented and a short summary of the Y-bifurcators will finish the review.

2.1 Hydraulic model test of T-bifurcators

2.1.1 *Munich experiments*: T-bifurcator or 90°-bifurcator

One of the earliest hydraulic model test to calculate the loss coefficient ζ was done in the work of Brabbée [1913]. In this paper the loss coefficients for fittings in a heating system were determined but unfortunately the geometrical quantities like the radii of the intersection shape of the fittings were not given. Therefore, the first remarkable hydraulic model test for a right-angled T-bifurcator, including the features of the intersection shape, was done by Vogel [1926]. This was the beginning for several test series at the Technical University of Munich and those investigations are also known under the name of *Munich experiments* (see 90°-bifurcator by Vogel [1926], 45°-bifurcator by Petermann [1929] and 60°-bifurcator by Kinne [1931]).

The set-up of the hydraulic model test of Vogel [1926] consists of a main-pipe with Ø43 mm and two branching pipes with Ø15 mm and Ø25 mm, respectively. This yields

diameter ratios of 15/43=0.349 and 25/43=0.581. Note, that Vogel [1926] conducted also a test series with a branching diameter of Ø43 mm which is not presented here.
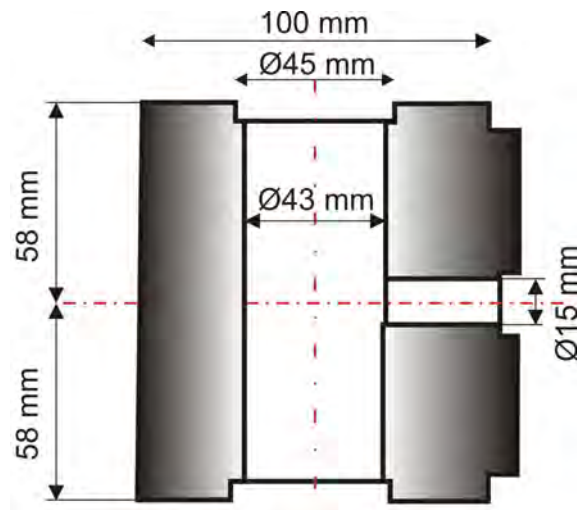
Figure 2.2: *Detail of the T-bifurcator of Vogel [1926]. Main pipe with a diameter of Ø43 mm, branching pipes either Ø15 mm or Ø25 mm, respectively*

The branching angle was always 90°. The water supply was supplied by a reservoir situated above the model test and the water discharge rate was regulated by two valves placed at the end of the main and branching pipe. At several control sections the local static pressure was measured by four bore holes with a diameter of 2 mm, arranged radially around the pipe. The static pressure was measured with a water column gauge glass. The material of the pipe was steel and treated with a anti-rust priming coat. During the whole measurement campaign, Vogel [1926] reported no changes in the roughness of the pipe surface.

The first pretest included the determination of the pipe friction loss without the T-bifurcator. For that purpose, the static head level at several control sections for the main pipe with a length of 2000 mm was measured. The distance between the entrance of the water in the hydraulic model test and the first control section was at least 8 times the diameter and served as a flow calming section. With the Darcy and Weisbach equation the friction coefficient λ can be calculated with the measured head level loss δh_f. The temperature was assumed to be constant during the measurement campaign due to the large reservoir with 800 m^3.

The main tests were carried out either for combining or dividing flow (see Figure 2.3). Also, four different intersection shapes (see Figure 2.4, No.1 to No.4) are chosen for the head loss measurements which have the shapes

- Sharp-edged

- Rounded (Radius R = 1.5 mm)

- Rounded with a conical transition of $\alpha = 6.33°$

- Rounded with a conical transition of $\alpha = 8.18°$
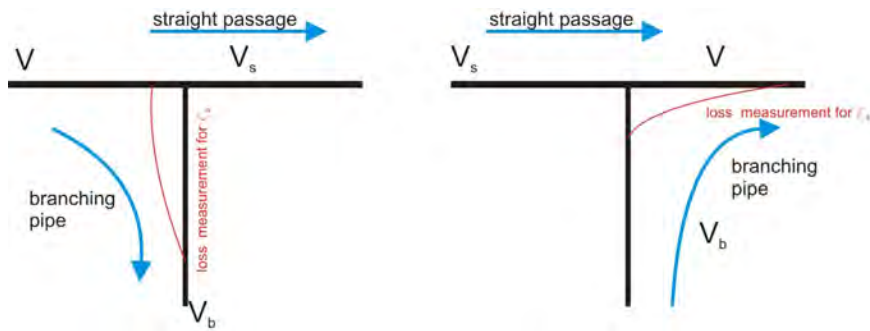
Figure 2.3: *Sketch of the T-bifurcator and its nomenclature: V is the velocity of the pipe with the total flow, V_s the velocity of the straight pipe and V_b the velocity of the branching pipe. The red line indicates the differential pressure loss measurement for the branching pipe.*
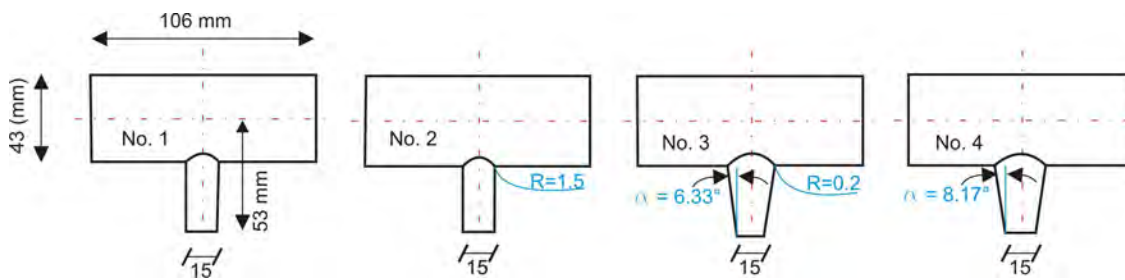
Figure 2.4: *Four different intersection shapes are presented in the paper of Vogel [1926] for branching pipe diameter of 15 mm (R = radius [mm] and α = angle [°]).*

Figure 2.5 shows the results for the T-bifurcator with a branching pipe diameter of 15 mm for dividing and combining flow. The loss coefficient ζ_b (index b indicates branching pipe) is made dimensionless with the velocity V (pipe with the total flow), see Figure 2.3. This is also the reason why the loss coefficient ζ_b is either -1 or +1 for the two identical flow distributions with $\frac{Q_b}{Q}$=0 for combining or dividing flow in Figure 2.7. Note, that for ζ_s (index s stands for straight passage) no values are plotted due to the too small quantities of the static pressure.

An important feature in the paper of Vogel [1926] is the nearly linear relationship between the **loss coefficient ζ_b in respect to the quadratic discharge rate at a constant distribution of $\frac{Q_b}{Q}$**. The loss coefficient ζ does not depend on the absolute velocity and therefore ζ_s and ζ_b need to be plotted only against the flow distribution $\frac{Q_b}{Q}$. The influence of the intersection shapes can also be seen clearly from Figure 2.5: The loss coefficient ζ decreases with a rounded intersection edge and a conical transition geometry for the branching pipe.

Similar to the previous geometry another 5 intersection shapes are defined for the T-bifurcator with a branching pipe diameter of 25 mm. These shapes for the branching pipe are

- Sharp-edged

- Rounded (R = 2.5 mm)

- Rounded with a conical transition of $\alpha = 8.60°$
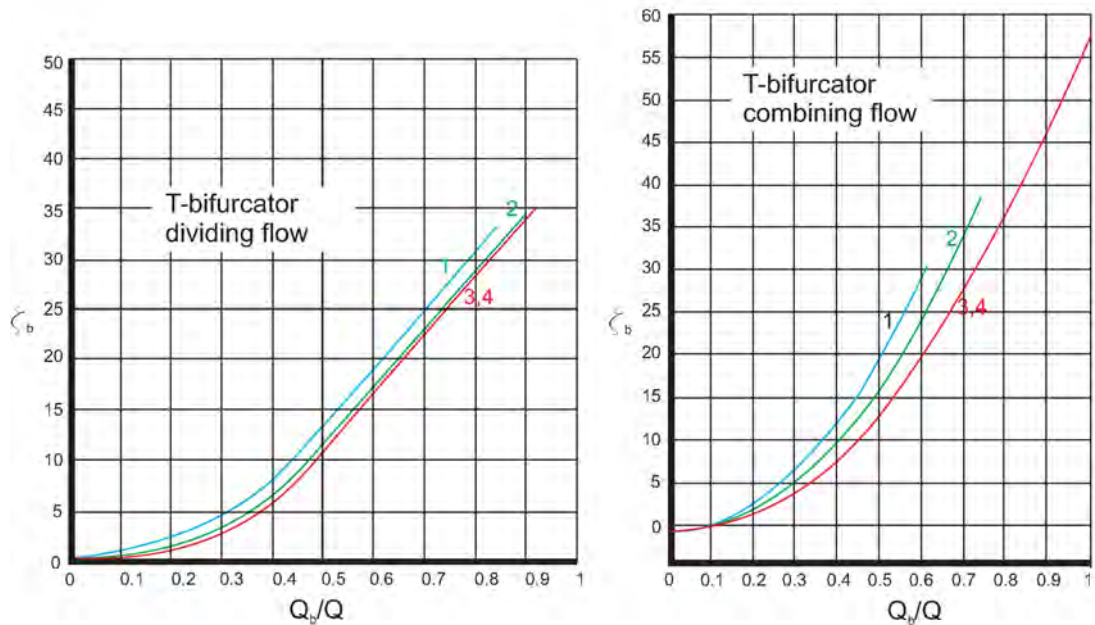
Figure 2.5: *Results of the loss coefficient ζ_b according to Vogel [1926] for the four inter-section shapes with branching pipe diameter of 15 mm. The left figure shows the case for dividing and the right figure for combining flow, respectively. The loss coefficient is always made dimensionless with the pipe carrying the total flow. Index b stands for the branching pipe.*

- Rounded with a conical transition of $\alpha = 12.40°$

- Rounded with a conical transition of $\alpha = 16.34°$
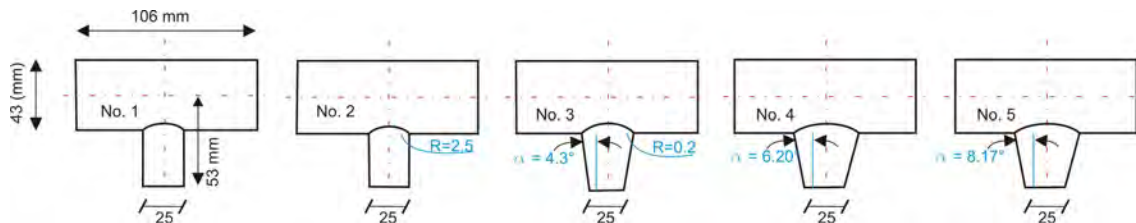
Figure 2.6: *Five different intersection shapes are presented in the paper of Vogel [1926] for branching pipe diameter of 25 mm (R = radius [mm] and α = angle [°]).*

Again, the loss coefficient is independent of the absolute velocity in Figure 2.7 but not of the ratio Q_b/Q. The rounded intersection edge and the conical transition improve the loss coefficient ζ. The loss coefficients for a conical transition (cone angle $2 \cdot \alpha = 16.34°$) in the branching pipe (curve 5 in Figure 2.7) show worse values than the other two conical transitions. This behavior can be ascribed to the flow separation due to the strong confuser angle.
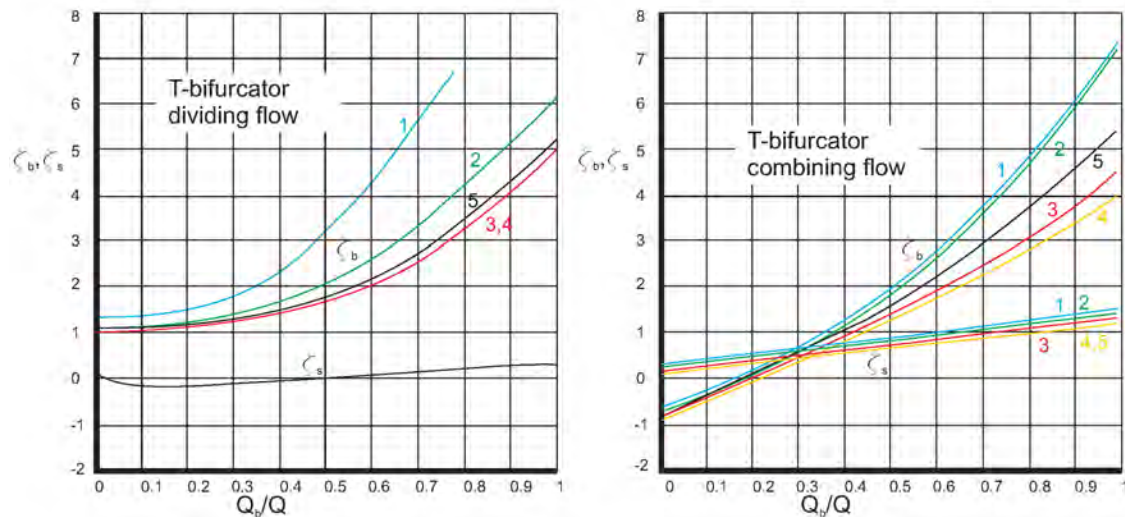
Figure 2.7: *Results of the loss coefficient ζ according to Vogel [1926] for the four inter-section shapes and branching pipe diameter of 25 mm. The left figure shows the case for a dividing and the right figure for combining flow, respectively. The loss coefficient is always made dimensionless with the pipe carrying the total flow. Index s stands for the straight pipe and Index b for the branching pipe.*

2.1.2 *Munich experiments*: 45°-bifurcator

Based on the hydraulic model test of a T-bifurcator with 90° branching angle, Petermann [1929] conducted another test series for a 45°-bifurcator with a branching angle of 45° (see Figure 2.8). Basically, the set-up for the hydraulic model test was almost the same as for the test series of Vogel [1926]. Instead of the steel pipe and the risk of rust stains, Petermann [1929] used brass pipes. This pipe-material produced lower head losses due to pipe friction which makes the calculation of ζ more accurate.

The developing length from the beginning of the pipe brass to the 45°-bifurcator was at least 46 D. The transition between the 45°-bifurcator and the brass-pipes is much better manufactured as in the model test of Vogel [1926]. This could be achieved by a flange between 45°-bifurcator and the pipes and thus no shock losses occurred because of mis-aligned components. Three intersection forms, similar to Vogel [1926], are used and shown in Figure 2.10. In the hydraulic model test of Petermann [1929] the discharge rate was measured by three different methods, these are:

- Weighing a water volume in a basin and recording the elapsing time,

- Using a rotameter and

- Using an orifice plate.

The first two methods obtained good measuring accuracy; the measurement error was between 0,1 ‰ and 0,8 ‰, whereas the last method, the orifice plate, showed lower measuring accuracy (3 ‰).

The pressure was measured with two independent systems. The first method, similar to Vogel [1926], was a column gauge glass and the second method was an upside down
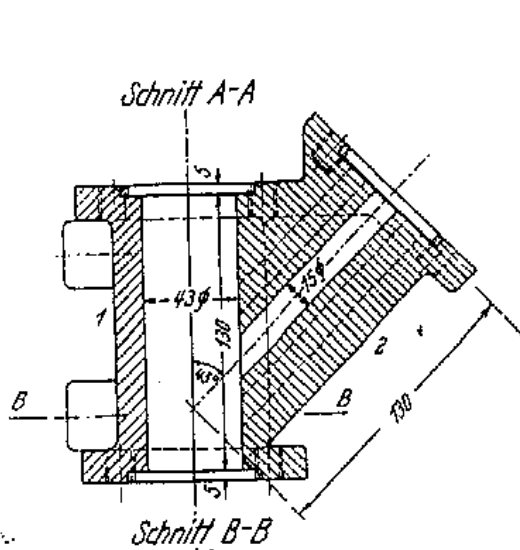
Figure 2.8: *Detail of the 45°-bifurcator of Petermann [1929]. Main pipe has a diameter of Ø43 mm, branching pipes either Ø15 mm or Ø25 mm respectively*
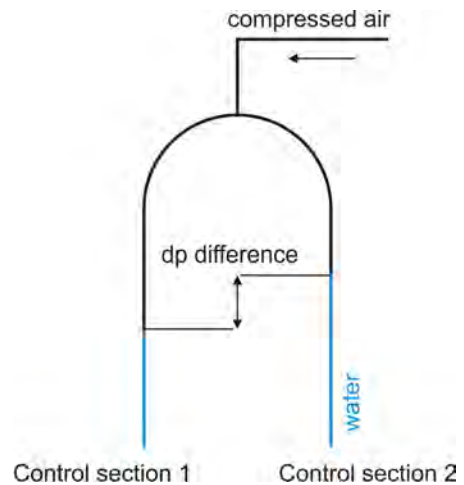
Figure 2.9: *Differential measurement: The upside down U is filed with air at the top. This allows to measure more easily higher pressures than with a column gauge glass.*

U with an air cushion at the top (see Figure 2.9). The column gauge glass has a reading accuracy of ± 0.25 mm and a deviation due to the turbulent fluctuation in the pipe of 1 mm. For the differential measurement a reading accuracy of ± 0.25 mm is also achieved.

Before the actual measurement campaign started some pretests had been carried out. The first test was the same as in Vogel [1926], that is, the 45°-bifurcator *without* the 45° bore hole was placed in the pipe installation and the pipe friction loss was measured. The pipe length before the 45°-bifurcator was 2000 and behind the 45°-bifurcator 3000 mm. The result for λ matched the friction coefficient for brass.

The main test for ζ_s and ζ_b coefficients are shown from Figure 2.11 to Figure 2.18. Note, that the loss coefficient is made dimensionless with the kinetic head of the pipe with the total flow.

45°-bifurcator 1 (cf. Figure 2.10 - top):

An interesting result can be seen in Figure 2.11 and Figure 2.15 where negative loss coefficients ζ_s for the straight passage exists at a distribution of $Q_b/Q \leq 0.5$. This happens because the slower boundary layer (in terms of velocity) of the straight pipe flow is diverted to the branching pipe and therefore only the higher energetic fluid particles flow straight ahead. In Figure 2.11 it can also clearly be seen that the rounded intersection form yields smaller loss coefficients for dividing flow in the 45°-bifurcator. Negative loss coefficients ζ_s are also shown in Figure 2.13 for a combining flow due to the suction effect at higher flow distribution ($Q_b/Q \geq 0.18$). For dividing flow, as shown in Figure 2.12, the quadratic polynomial behavior, similar as in the experiment of Vogel [1926] (compare with Figure 2.5), can be seen, although the loss coefficient of the T-bifurcator is naturally higher than of the 45°-bifurcator.

45°-bifurcator 2 (cf. Figure 2.10 - bottom):

As expected, the 45°-bifurcator with the bigger branching diameter of 25 mm yields much lower ζ_s and ζ_b coefficients due to the smaller velocity. If one compares Figure 2.12 with Figure 2.16 the loss coefficient decreases to $\approx 90\%$ for curve No. 1. Similar results,
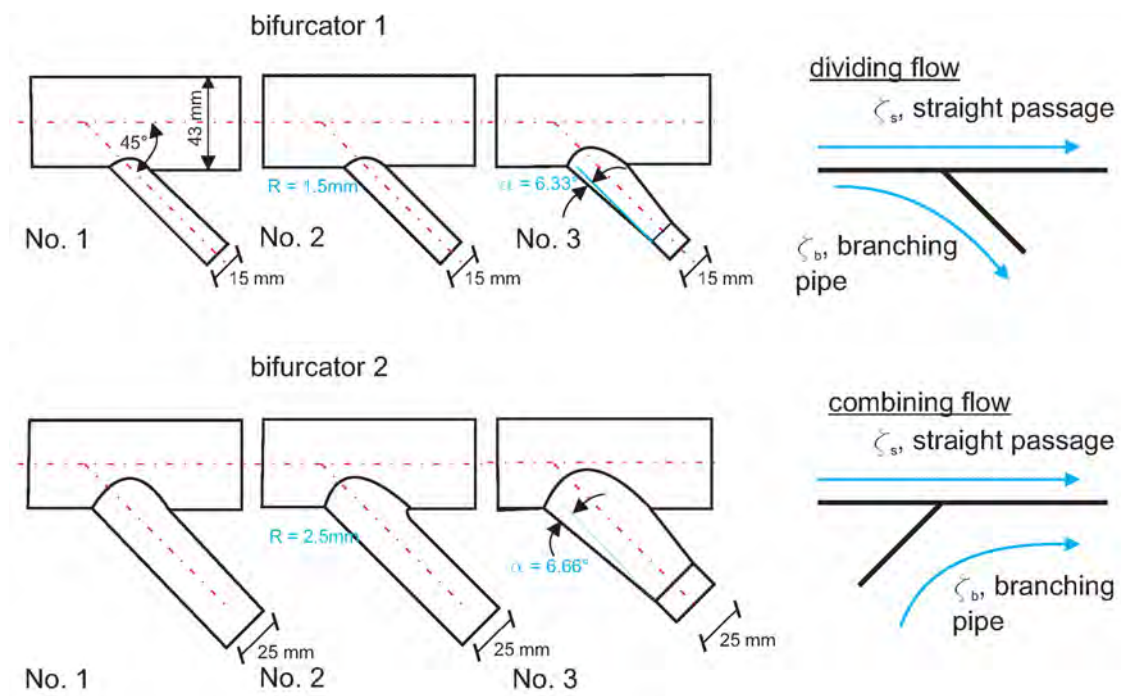
Figure 2.10: *On the left: Detail for the three intersection forms of the 45°-bifurcator of Petermann [1929] for branching diameters of 15 and 25 mm, respectively. On the right: sketch of dividing and combining flows. Index s stands for the straight and Index b for the branching pipe.*

and therefore much lower loss coefficient for 45°-bifurcator 2 can be seen if one compares Figure 2.14 with Figure 2.18, Figure 2.13 with Figure 2.17 and Figure 2.11 with Figure 2.15.

Figure 2.11: ζ_s *for 45°-bifurcator 1, dividing flow, straight pipe. Main pipe has a diameter of Ø43 mm and the branching pipe Ø15 mm, respectively*

Figure 2.12: ζ_b *for 45°-bifurcator 1, dividing flow, branching pipe. Main pipe has a diameter of Ø43 mm and the branching pipe Ø15 mm, respectively*

Figure 2.13: ζ_s *for 45°-bifurcator 1, combining flow, straight pipe. Main pipe has a diameter of Ø43 mm and the branching pipe Ø15 mm, respectively*

Figure 2.14: ζ_b *for 45°-bifurcator 1, combining flow, branching pipe. Main pipe has a diameter of Ø43 mm and the branching pipe Ø15 mm, respectively*

Figure 2.15: ζ_s *for 45°-bifurcator 2, dividing flow, straight pipe. Main pipe has a diameter of Ø43 mm and the branching pipe Ø25 mm, respectively*

Figure 2.16: ζ_b *for 45°-bifurcator 2, dividing flow, branching pipe. Main pipe has a diameter of Ø43 mm and the branching pipe Ø25 mm, respectively*

Figure 2.17: ζ_s *for 45°-bifurcator 2, combining flow, straight pipe. Main pipe has a diameter of Ø43 mm and the branching pipe Ø25 mm, respectively*

Figure 2.18: ζ_b *for 45°-bifurcator 2, combining flow, branching pipe. Main pipe has a diameter of Ø43 mm and the branching pipe Ø25 mm, respectively*

2.1.3 *Munich experiments*: 60°-bifurcator

Kinne [1931] continued the work of Vogel [1926] and Petermann [1929]. The test campaign of Kinne [1931] included a 60°-bifurcator with a branching angle of 60°. The set-up was the same as in Petermann [1929] and also the intersection forms had the same appearance.
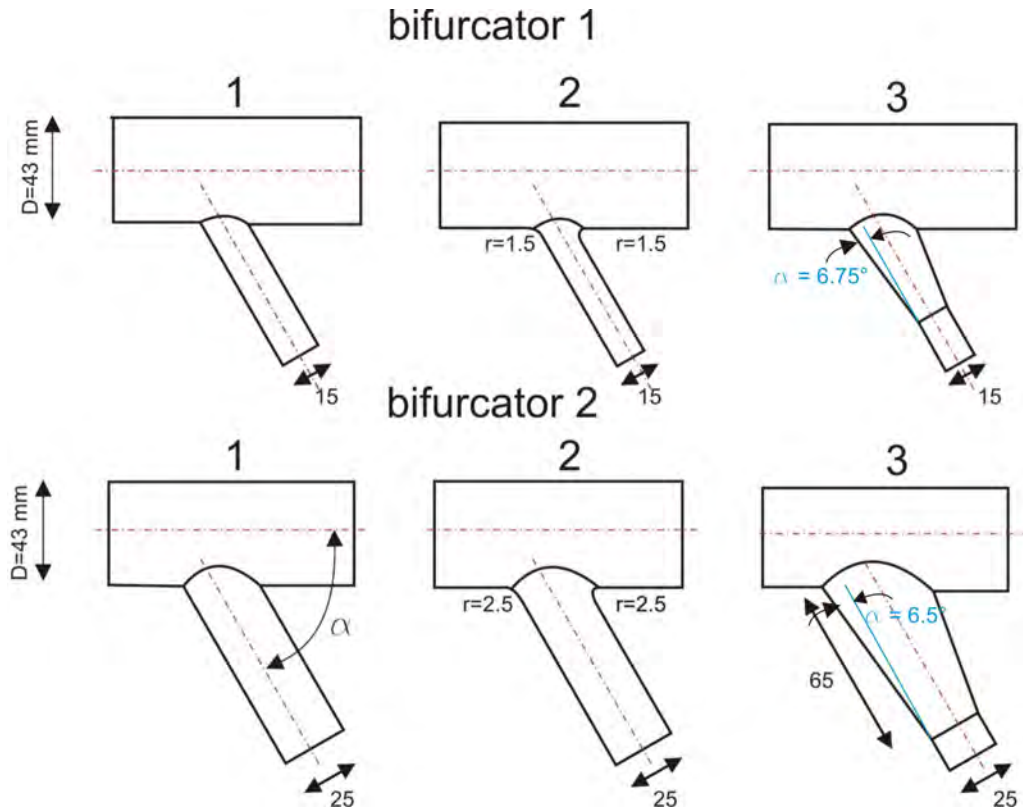
Figure 2.19: *Detail for the three intersection forms of the 60°-bifurcator of Kinne [1931] for branching diameter of 15 or 25 mm, respectively. All units in millimeter.*

In the hydraulic model test Kinne [1931] also observed that the loss coefficient ζ does not depend on the absolute velocity just like Vogel [1926] and Petermann [1929] had reported in their earlier works. The results ζ_b for the bifurcator 1 (see Figure 2.19) for dividing flow shows an improvement with a rounded intersection form in comparison to the sharp-edged intersection form (compare curve 1 and curve 2 in Figure 2.21). The loss coefficient can be even more improved by using a conical transition in the branching pipe. For ζ_s (bifurcator 1) negative values exist for curve 3 in Figure 2.20 up to a flow distribution of $Q_b/Q \approx 0.3$ for dividing flow. The reason for this behavior was also shown in the work of Petermann [1929] where the low energetic boundary layer of the straight passage was diverted to the branching pipe. For combining flow (bifurcator 1) in Figure 2.23 hardly no improvement for a rounded intersection form can be seen (compare curve 1 with curve 2) but if a conical transition is used in the branching pipe the loss coefficient decreases considerably. For combining flow (bifurcator 1) and a flow distribution of $Q_b/Q \geq 0.3$ high negative ζ_s exist due to the suction effects of the branching flow in the straight passage (see Figure 2.22).

For bifurcator 2 in Figure 2.19 the results are similar to the bifurcator 1 although the level for ζ_b is much smaller (compare Figure 2.21 with Figure 2.25 or Figure 2.23 with Figure 2.27).

Figure 2.20: ζ_s *for 60°-bifurcator 1, dividing flow, straight pipe. Main pipe has a diameter of Ø43 mm and the branching pipe Ø15 mm, respectively*

Figure 2.21: ζ_b *for 60°-bifurcator 1, dividing flow, branching pipe. Main pipe has a diameter of Ø43 mm and the branching pipe Ø15 mm, respectively*

Figure 2.22: ζ_s *for 60°-bifurcator 1, combining flow, straight pipe. Main pipe has a diameter of Ø43 mm and the branching pipe Ø15 mm, respectively*

Figure 2.23: ζ_b *for 60°-bifurcator 1, combining flow, branching pipe. Main pipe has a diameter of Ø43 mm and the branching pipe Ø15 mm, respectively*

Figure 2.24: ζ_s *for 60°-bifurcator 2, dividing flow, straight pipe. Main pipe has a diameter of Ø43 mm and the branching pipe Ø25 mm, respectively*

Figure 2.25: ζ_b *for 60°-bifurcator 2, dividing flow, branching pipe. Main pipe has a diameter of Ø43 mm and the branching pipe Ø25 mm, respectively*

Figure 2.26: ζ_s *for 60°-bifurcator 2, combining flow, straight pipe. Main pipe has a diameter of Ø43 mm and the branching pipe Ø25 mm, respectively*

Figure 2.27: ζ_b *for 60°-bifurcator 2, combining flow, branching pipe. Main pipe has a diameter of Ø43 mm and the branching pipe Ø25 mm, respectively*

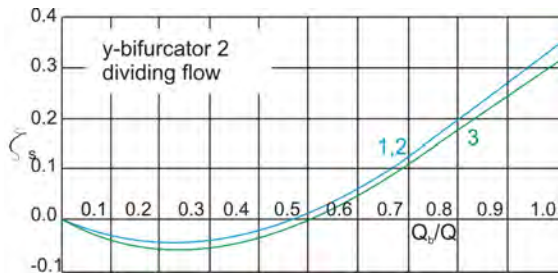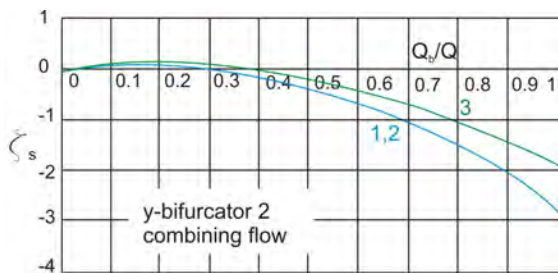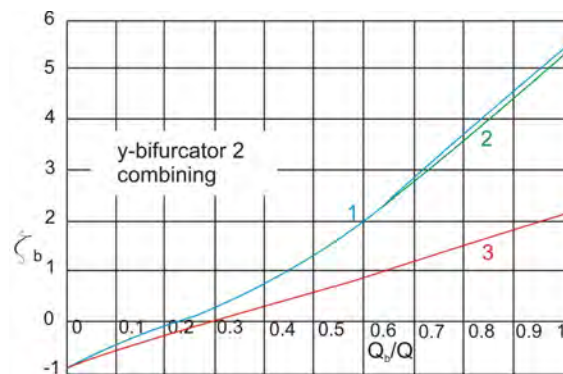### 2.1.4 Discussion of the *Munich experiments*

The so-called experiments of *Munich* were the first comprehensive model tests for dividing and combining flows. In the work of Williamson and Rhone [1973], the *Munich Experiments* were compared with the work of Gardel [1970], McNown [1954] and others. A short summary of the *Munich experiments* and the comparison of Williamson and Rhone [1973] will be shown below.

In Section 2.1.1, Section 2.1.2 and Section 2.1.3 a T-bifurcator, a 45°-bifurcator and a 60°-bifurcator were presented, respectively. The diameter ratios D_b/D_s was either 0.349 or 0.581 (s stands for straight passage and b for branching pipe. The *Munich experiments* were also conducted with a diameter ratio of 1, not shown in this work). For the straight passage the diameter was 43 mm and for the branching pipe 15 or 25 mm, respectively. The intersection forms of the *Munich experiments* were either sharp-edge or rounded with R = 0.1 · D_b and for the branching pipe a conical transition is also tested with a cone angle between (2 · α) 12.66 - 16.34°. The Reynolds number was between $4 \cdot 10^3$ - $9 \cdot 10^4$. The most significant conclusion of the *Munich experiments* is that the loss coefficient is independent of the absolute discharge rate and is only a function of the flow ratio in the branching and main pipe. In the first test series of Vogel [1926] iron pipes were used and for the later experiments of Petermann [1929] and Kinne [1931] brass pipes were used to avoid rust stain on the pipe surface.

The test series of the *Munich experiments* showed a reduction of the branching angle from 90 to 60 or 45° leads to an improvement of the loss coefficient (compare for example dividing flow for Figure 2.5, Figure 2.12 and Figure 2.21). For the conical transition, the cone angle of 2 · $\alpha \approx 13°$ showed the lowest loss coefficient (cf. Figure 2.7: the curve 4 with 2 · $\alpha \approx 13°$ has the lowest loss coefficient).

Gardel [1970] made similar experiments at the University of Lausanne as shown in the *Munich experiments*. The diameter ratios D_b/D_s were 1.00, 0.83, 0.66, 0.53 and 0.40 for a T-bifurcator, and for $D_b/D_s = 1$ for a 60- and 45°-bifurcator. The studies included dividing and combining flows. The model set up of Gardel [1970] consists of a straight passage with a diameter of 150 mm and branching diameters between 150 and 60 mm. The pipe material was asbestos-cement and thus much rougher than the brass pipe of the *Munich experiments*. The maximum Reynolds number was $4 \cdot 10^5$.

McNown [1954] conducted another test series for a T-bifurcator which is also known as the *Iowa experiments*. The intersection form was sharp edged with diameter ratios D_b/D_s of 0.25, 0.5 and 1. The main pipe diameter was 51 mm and the branches diameter were 51, 25 and 13 mm. The pipe material was brass.

In Figure 2.28 the comparison of the *Munich experiments*, *Iowa experiments* and Gardel [1970] are shown for T-bifurcators. Note, that the loss coefficient is plotted against the velocity ration v_b/v_s instead of a discharge distribution. This makes it simpler to compare similar bifurcators where only the ratios of the cross-sectional area of the branch to the main pipe are slightly different. This automatically takes into account the different cross-sectional areas.

The loss coefficients ζ_b of the *Munich experiments* for cylindrical branches with sharp edges and $D_b/D_s = 0.58$ are compared with the *Iowa experiments* with $D_b/D_s = 0.50$. It can be seen in Figure 2.28 that considerable larger loss coefficients are determined by *Munich experiments*. For the loss coefficient measured by Gardel [1970] the coefficients are the lowest in Figure 2.28 for a diameter ratio of $D_b/D_s = 0.53$, although the results of

Iowa experiments and Gardel [1970] lie closer together. The difference between the loss coefficient increases with higher velocity distribution. Only for a area ratio of $D_b/D_s = 1$ (not shown here) the results lie closer together.
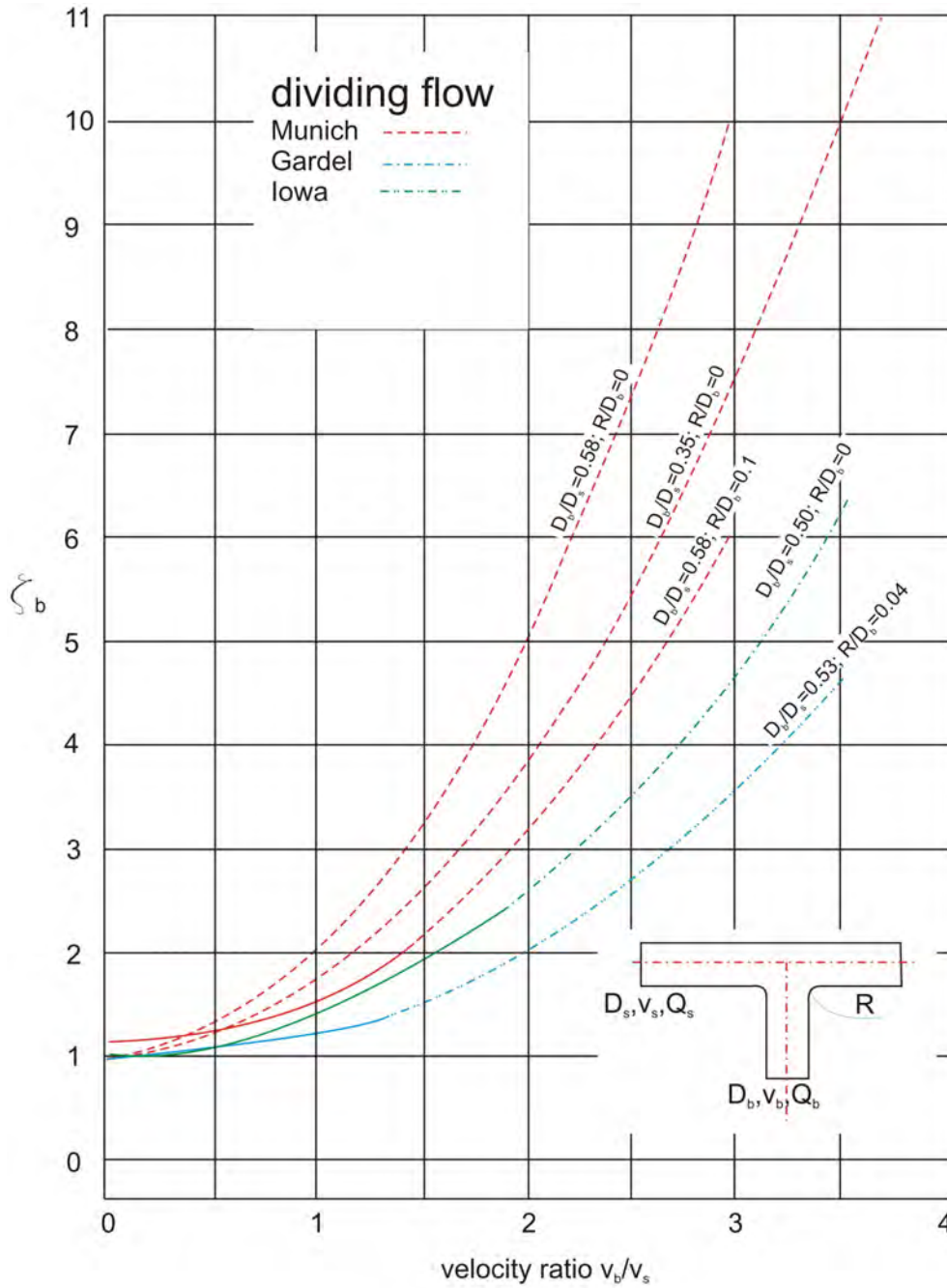
Figure 2.28: *Comparison of the* Munich experiments *with Gardel [1970] and McNown [1954]. (taken from Williamson and Rhone [1973])*

2.2 Hydraulic model test of Y-bifurcators

2.2.1 Causey Dam at the Ogden River

The hydraulic model test of King [1963] consists of a channel spillway located in the right abutment of the Causey Dam and a slide gate. The gate flow is divided by a symmetrical Y-bifurcator. The scale factor was 1 to 11. Piezometers were placed in the Y-bifurcator to investigate adverse subatmospheric or unusually high dynamic pressures. The discharge rates through the model were measured by volumetrically calibrated Venturi meters. In Figure 2.29 the geometry of the Y-bifurcator is shown. The piezometers for the pressure difference measurement (marked as blue dots in Figure 2.29) are placed $1 \cdot D$ upstream of the Y-bifurcator and downstream in the circular-to-square-transition.
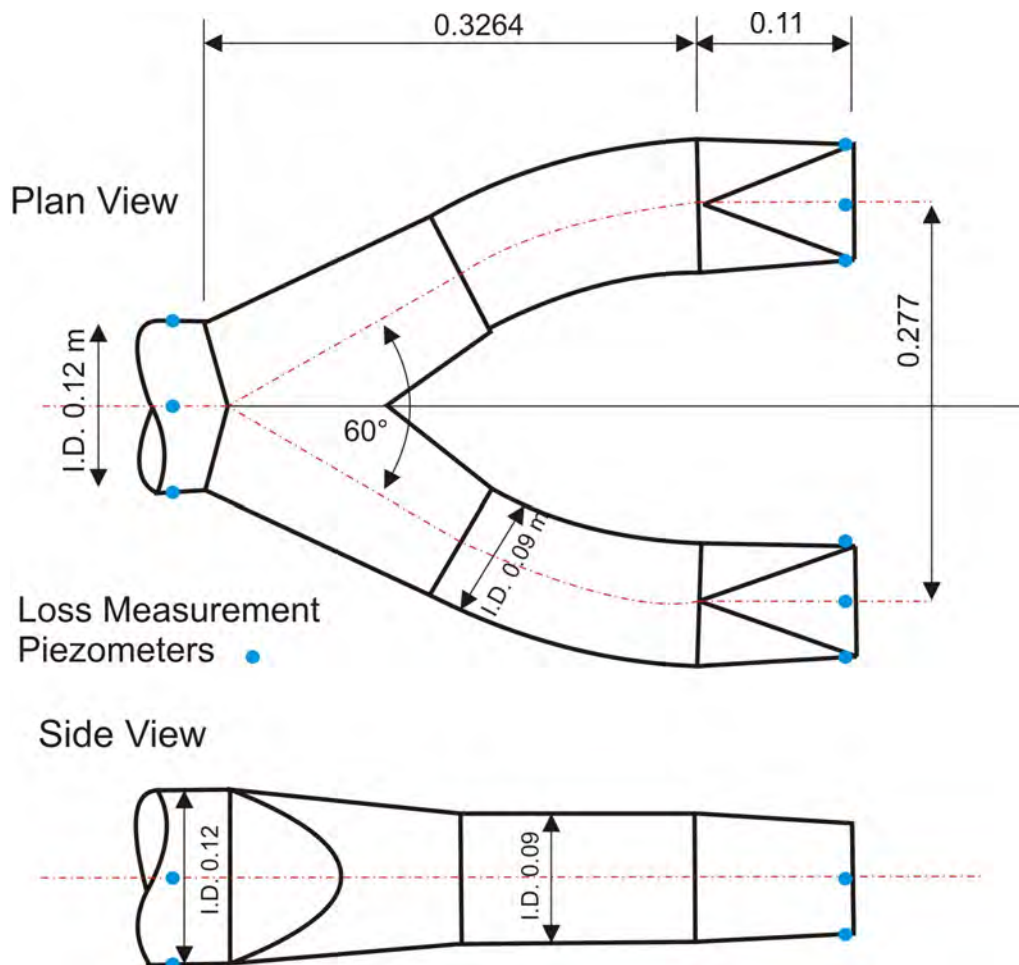
Figure 2.29: *Plan and side view of the hydraulic model test of King [1963]. Downscaled model (1 to 11) with units in meter.*

In Figure 2.30 the total loss coefficient $\zeta_{tot,L}$ and $\zeta_{tot,R}$ are presented. Note, that it is not reported if the pipe friction is subtracted. The loss factors in Figure 2.30 are made dimensionless with the upstream dynamic velocity head. As expected, the lowest loss coefficient is quantified with 0.29 at a distribution of $Q_L/Q_M = Q_R/Q_M \approx 0.5$. The highest value for ζ_{tot} occurs for an asymmetric flow distribution, that is, Q_L/Q_M or $Q_R/Q_M = 1$. The loss coefficient includes also the horizontal bend and the circular-to-square transition.
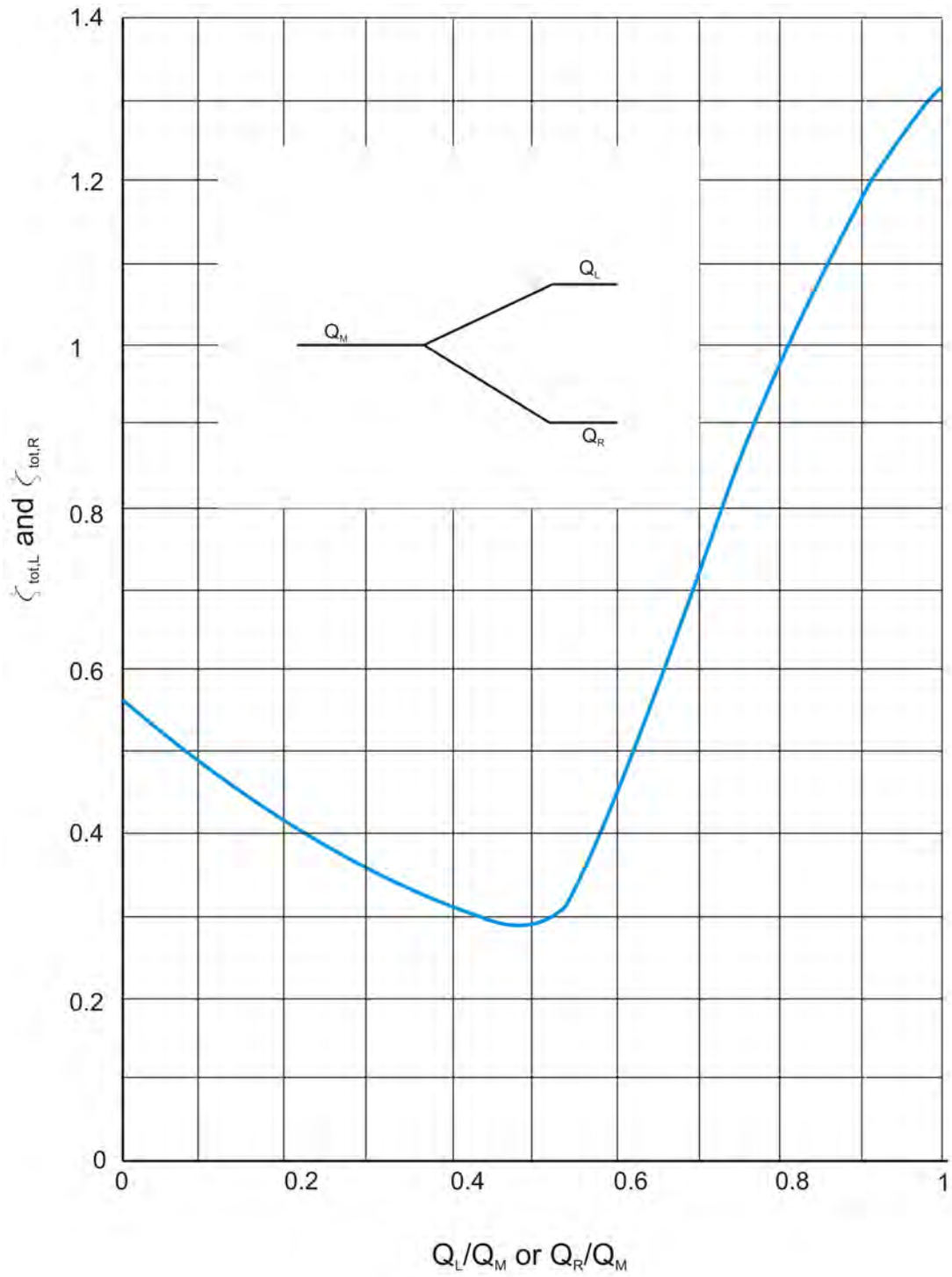
Figure 2.30: *Result of ζ according to King [1963]. Index M, L and R stands for Main, Left and Right pipe*

2.2.2 Pumped storage plant *Erzhausen*

In the work of Ure [1968] the loss coefficient for a symmetrical Y-bifurcator are given for the pumped storage plant *Erzhausen*. The power plant consists of 4 turbines and 4 pumps as can be seen in Figure 2.31. The water distribution is done by two Y-bifurcators and four 60°-bifurcators. The branching angle for the Y-bifurcator was also 60°.
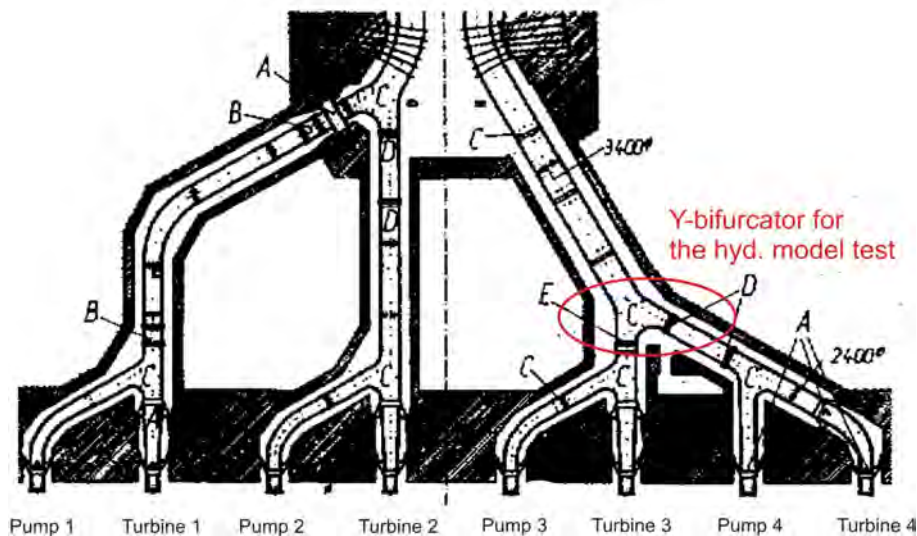
Figure 2.31: *Manifold of the pumped storage plant **Erzhausen** with four pumps and turbines.*

The Y-bifurcator for the hydraulic model test consists only of shell elements without any stiffener inside the Y-bifurcator. The intersection form was sharp-edged. For statical reasons, the form of the Y-bifurcator has a spherical shape which can be seen in Figure 2.32

Figure 2.32: *View of the Y-bifurcator for the hydraulic model test.*

The spherical form of the Y-bifurcator causes separation flows. Therefore Ure [1968] defines another two Y-bifurcators to investigate the performance of the Y-bifurcator either with guiding plates or with a hydraulic favorable form. The three forms of the hydraulic model test are therefore:

No. 1: Without any built-in components.

No. 2: With built-in components of cylindrical form.

No. 3: Hydraulically favorable form (Nearly constant velocity along the Y-bifurcator).

In Figure 2.33 the three intersection forms of the Y-bifurcator are shown. The piezometers for the head loss measurement are located shortly before and after the Y-bifurcator. No information are available about the behavior of the secondary flow in the Y-bifurcator.
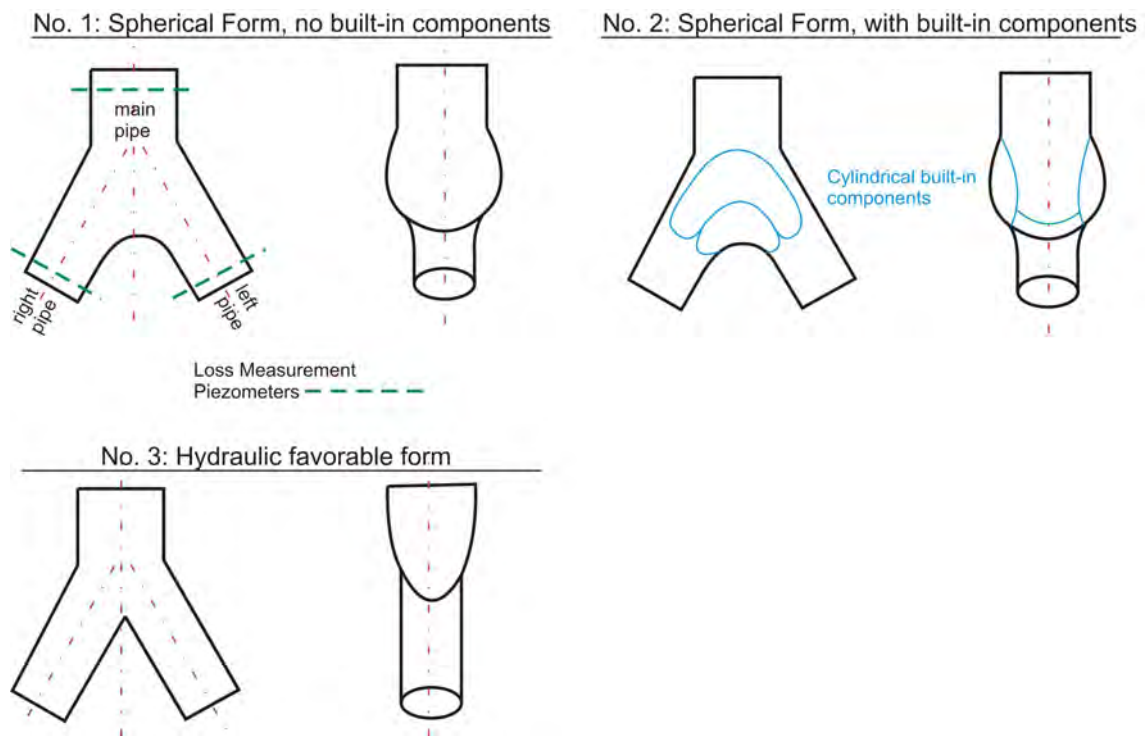
Figure 2.33: *Three different Y-bifurcator forms (No.1 to No.3) for the hydraulic model test. No.1 has a spherical form, No.2 has two built-in cylinders to avoid flow separations and No.3 consist of a hydraulically favorable form*

In Table 2.1 the results of the loss coefficient ζ_{tot} are given. As expected, the form No.3 with a loss coefficient $\zeta_{tot} = 0.22$ is the smallest value for the symmetrical distribution. For the asymmetrical distribution the form No.1 and No.2 show the smallest values with 0.27. Be aware that even though the flow distribution is symmetrical the result of the loss coefficient is not. The reason for that is the non-symmetrical pipe installation of the Y-bifurcator for turbine/pump 3 and 4.

Table 2.1: *Results of the loss coefficient ζ_{tot} for the Y-Bifurcator for turbine 3 and 4 in Figure 2.31. Symmetrical stands for $Q_{left}/Q_{main} = 0.5$ or $Q_{right}/Q_{main} = 0.5$ and asymmetrical for $Q_{left}/Q_{main} = 1$ or $Q_{right}/Q_{main} = 1$.*

	Asymmetrical		**Symmetrical**	
	Left	*Right*	*Left*	*Right*
Without built-in components	0.27	0.27	0.23	0.36
With built-in components	0.27	0.27	≈ 0	0.07
Hydraulically favorable form	0.44	0.44	≈ 0	0.06

2.2.3 Loss coefficient for a branch angle of 60° and 45°

Ruus [1970] carried out a large test series for different branching angles and geometrical forms of Y-bifurcators. Three Y-bifurcators with branching angles 60° and 45° are shown.
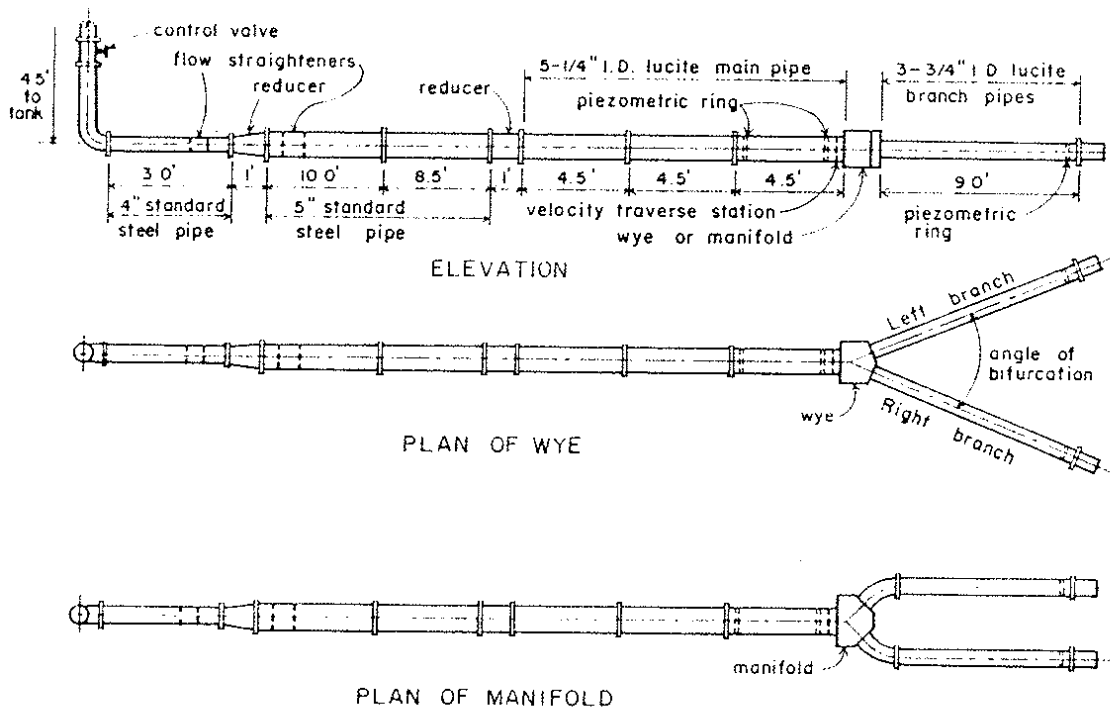
Figure 2.34: *Installation of the model test of Ruus [1970].*

The Y-bifurcators of the hydraulic model test in Figure 2.34 and Figure 2.35 were turned on a lathe or machined on a milling machine to a tolerance of 0.0254 mm. Afterwards, the pieces of the Y-bifurcators (cylindrical and conical) were polished by hand. In the main and/or branching pipes conical confusers with an angle of 8° or 10° are located.

The length upstream and downstream of the Y-bifurcator was 75 times and 30 times the diameter of the Y-bifurcator, respectively. Ruus [1970] considered this length as adequate to obtain a reasonable fully turbulent velocity profile.

The discharge rate at the inlet was controlled by a control valve and at the branching outlets by a series of orifices of various diameters. During all tests for symmetrical flow

conditions a maximum deviation between the branches was less than 1%. Discharge was measured by a weighing tank with a maximum capacity of 9072 kg and a stopwatch with an accuracy of 0.1 second. Three readings with a minimum duration of 180 seconds were taken for any flow conditions.

Per control section four pressure taps were symmetrically distributed around the pipe cross-section. The bore holes were burr-free and sharp-edged. Each pressure tap is connected to a U-manometer tube. Additionally, each of the four pressure taps are connected to a gage well with a diameter of 140 mm. With this arrangement the piezometric pressure measurement is double-checked. Also, the high pressure fluctuations can be damped by the gage well.

Figure 2.35: *Three Y-bifurcators with branching angles of 60° and 45°.*

Before the actual main tests were carried out, some preliminary investigations had been done to verify the symmetry of the model test and to establish suitable lengths for head losses of the main and the branching pipe. To avoid any asymmetric velocity profile shortly before the flow enters the Y-bifurcator a flow conditioner is located at the beginning of the model test. To determine the extent of the uneven velocity profile downstream of the Y-bifurcator the pipe friction loss, beginning at 30-D downstream of the Y-Bifurcator and having a length of $30 \cdot D$, is measured. If the pipe friction loss is compared to the head loss of an undisturbed pipe the difference was less than 2%. The head loss of the main and branching pipe was plotted on a Moody diagram and the difference between the Blasius curve for a smooth pipe and the measured head loss was less than 5%.

For the loss coefficient ζ the pipe friction was subtracted from the total head loss to get the local head loss. For the total head loss, which was measured between two control sections, it was assumed that the velocity profile was steady and irrotational. Thus, the loss calculation can be based on Bernoulli's energy equation for one-dimensional flow condition. The velocity head of the main pipe is chosen to define the ζ coefficient.

The main test with individual Y-bifurcators were carried out for discharge rates between 9 and 42.5 l/s. The corresponding maximum and minimum Reynolds numbers for the flow in the main pipe were between $0.8 \cdot 10^5$ and $4 \cdot 10^5$.

The results of the loss coefficient ζ for the three types of Y-bifurcators are shown in Figure 2.36. Ruus [1970] reported that even though a symmetrical discharge distribution was chosen the head loss in the left and right branch were not equal. The maximum deviation between the two legs was less than 12%. Ruus [1970] described this effect as similar to the Coanda-Effect (tendency of a fluid jet to be attracted to a surface), where the fluid would prefer one side of a symmetrical branching.
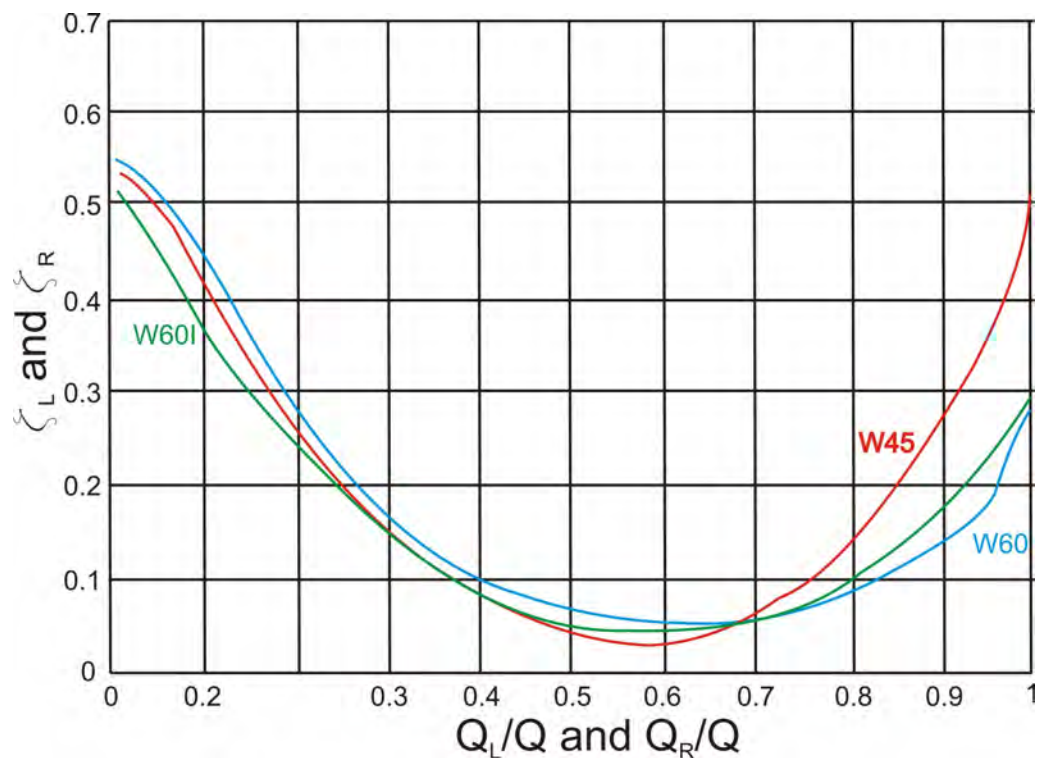
Figure 2.36: *Results of the loss coefficient ζ for Y-bifurcators with branching angles 60° and 45°.*

The difference in head loss measurements between two identical test series with symmetrical flow distribution was less than 6%. For any asymmetrical flow distribution the difference between repeated head loss measurements was less than 15%.

As can be seen in Figure 2.36 the head loss for symmetrical flow distribution is below $\zeta_b = 0.1$. With smaller branching angle (60 to 45°) the loss coefficient gets even smaller. With asymmetric flow, that is, one branch closed, the loss coefficient increases to a value of $\zeta_b \approx 0.5$ for branching angle of 45°. For the other two Y-bifurcators with branching angle of 60° the loss coefficient decreases to a value of $\zeta_b \approx 0.3$. The conical form in the main pipe for the Y-bifurcator **W60I** shows almost the same loss coefficient than does the Y-bifurcator **W60**.

2.2.4 Pumped storage plant *Muju*

Lee et al. [1993] conducted a hydraulic model test for Y-bifurcators (with stiffener) with a 48° bend. The Y-bifurcator is part of the Pumped storage plant in *Muju* with a capacity of 600 MW. The Y-bifurcator splits the main pipe with a diameter of 4 m into two branching pipes with a diameter of 2.8 m (see Figure 2.37). This gives a diameter ratio of 0.7. The scale factor was 1 to 13.7. The length upstream of the Y-bifurcator was ≈ 15 and downstream $10 \cdot D$. A flow conditioner at the beginning of the main pipe is located to reduce any secondary flow.

The loss coefficient ζ is based on the velocity head of the main pipe. The pipe friction loss is not included in the loss coefficient ζ. The results for the loss coefficients are shown in Table 2.2.
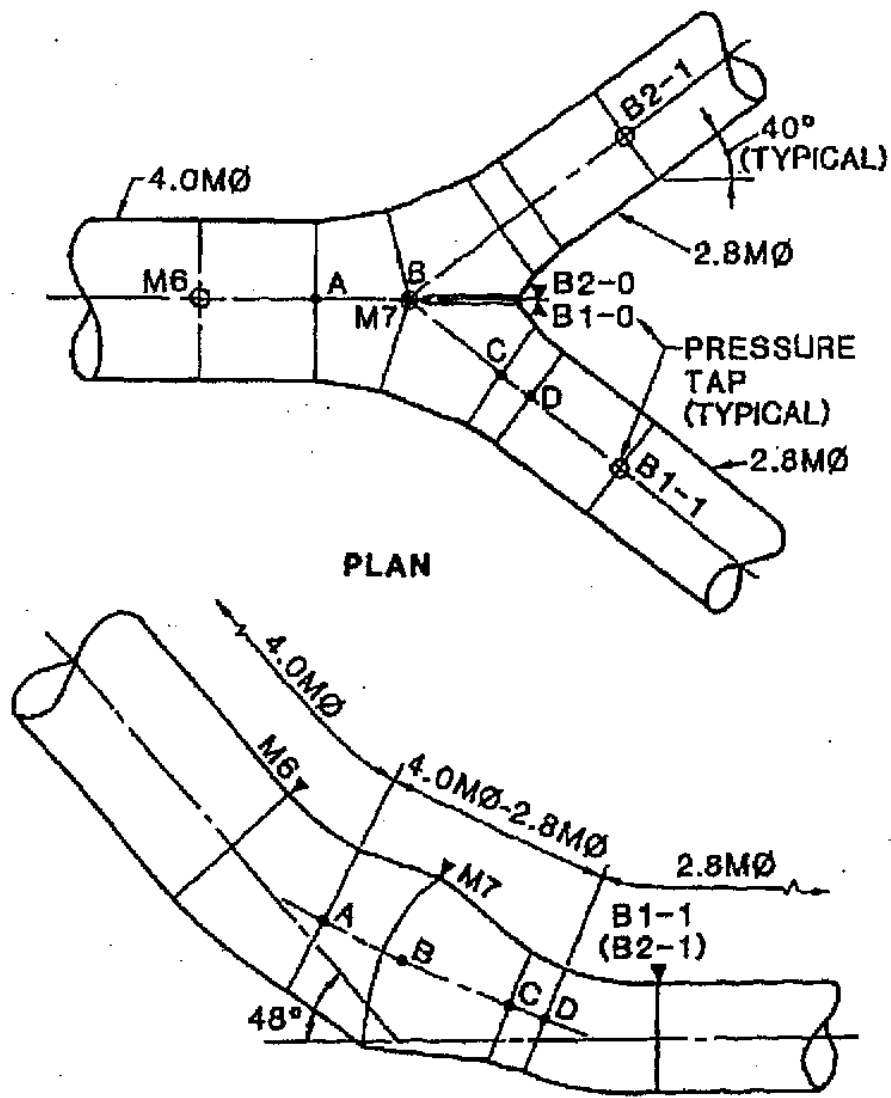
Figure 2.37: *View of the Y-bifurcator of the pumped storage plant Muju (Lee et al. [1993])*

Table 2.2: *Results of the loss coefficient ζ for the Y-Bifurcator. Symmetrical stands for $Q_{left}/Q_{main} = 0.5$ and Asymmetrical for $Q_{left}/Q_{main} = 1$ and $Q_{right}/Q_{main} = 1$.*

	Asymmetrical		**Symmetrical**	
	lower range	*upper range*	*lower range*	*upper range*
ζ	1.25	1.67	0.21	0.38

2.2.5 Sulzer

Müller and Stratmann [1971] carried out a hydraulic model test to calculate the loss coefficient ζ for dividing flows. Based on the *Munich experiments* (Vogel [1926], Petermann [1929]and Kinne [1931]) they derived ζ-values for several flow aspects like

- different discharge rates,

- different branching angles.

Müller and Stratmann [1971] summarized the total head losses as friction head losses and head losses due to the secondary flows. The friction head losses have their seeds in the viscosity and the roughness of the wall whereas the secondary flow are caused by components in the pipe which turns the flow into another direction or destroy the boundary layer at the wall. A quantitative separation of friction and secondary head losses is not possible in the hydraulic model test. Therefore, to take the friction head losses into account equivalent pipes with a fully developed turbulent flow are chosen to calculate the friction head losses. These pipes are also called substitution cylinders with length L, diameter D and sand roughness k; the friction head loss Δh_f can be calculated (see also Eq. 2.3). With the known friction head loss of the substitution cylinders the losses due to the secondary flow can be calculated by subtracting the total loss and the friction loss of the cylinders.

The previously mentioned test at the TU Munich shows, based on numerous hydraulic model tests, that a relationship of

$$\Delta h_f = \zeta \cdot q \tag{2.4}$$

exists for Reynolds numbers above 10^5. The variable q represents the dynamic velocity head which can be written as

$$q = \frac{V^2}{2 \cdot g} \tag{2.5}$$

The set up of the model test is similar to the previously introduced model tests: At the entrance of the pipe installation a flow conditioner is installed to smooth out any secondary flow. The pipe material is metal with a special coat of lacquer. The Y-bifurcator itself consists of wood. The fluid for the hydraulic model test is air; therefore Reynolds numbers up to $3.6 \cdot 10^5$ are possible. The discharge rate is controlled by two butterfly valves, whereas Müller and Stratmann [1971] mentioned to have some difficulties to achieve a steady state condition. Upstream of the Y-bifurcator the flow is measured by an orifice plate and downstream by a Venturi-Tube. The inaccuracy of the discharge is less than 1%. The temperature is also recorded at the beginning and at the end of the pipe installation. Each control section has 4 bore holes and is connected with a ring line. The details of the Y-bifurcator are shown in Figure 2.38.
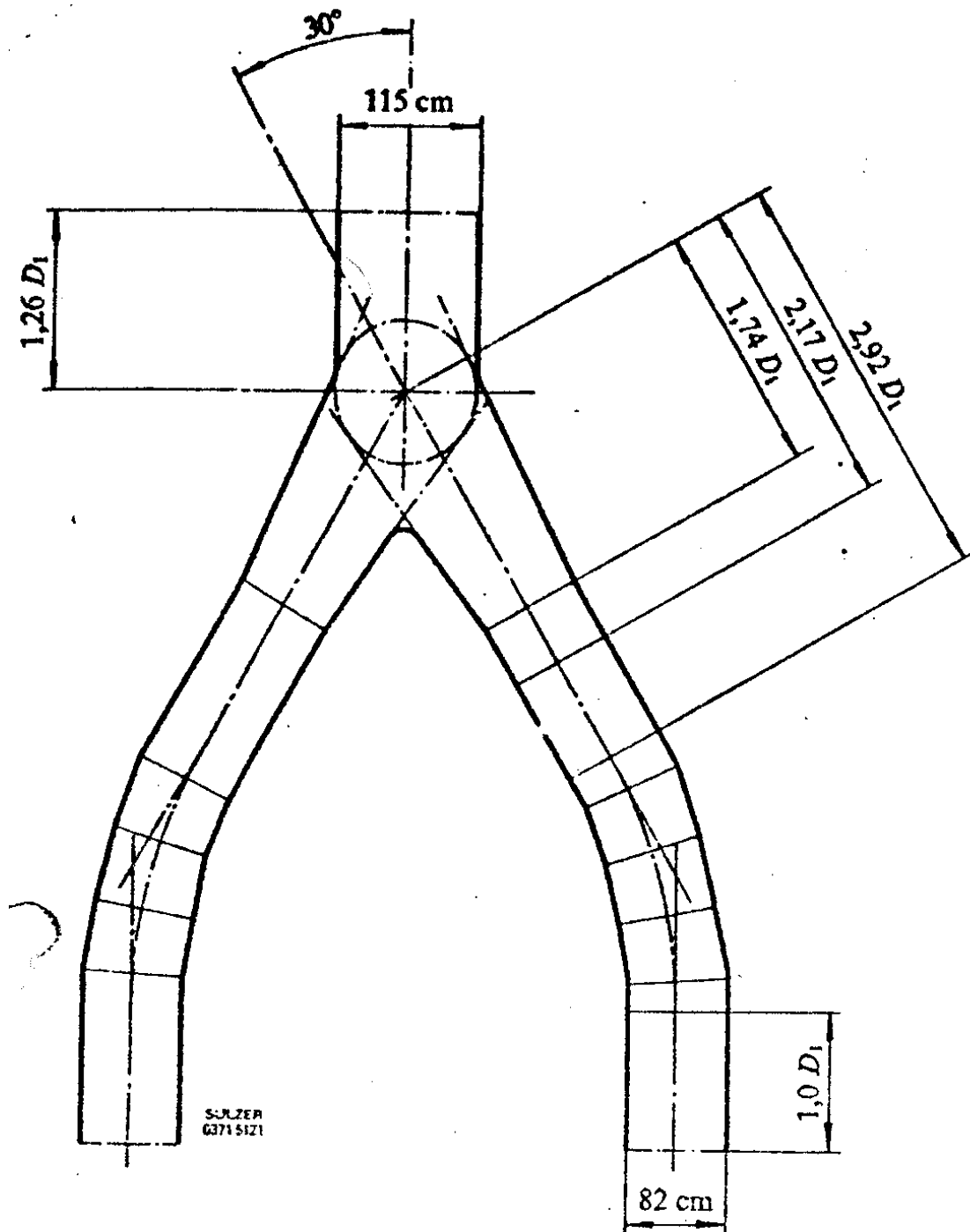
Figure 2.38: *View of the Y-bifurcator (Müller and Stratmann [1971]) with branching angle of 60° and diameter ratio of 1.41.*
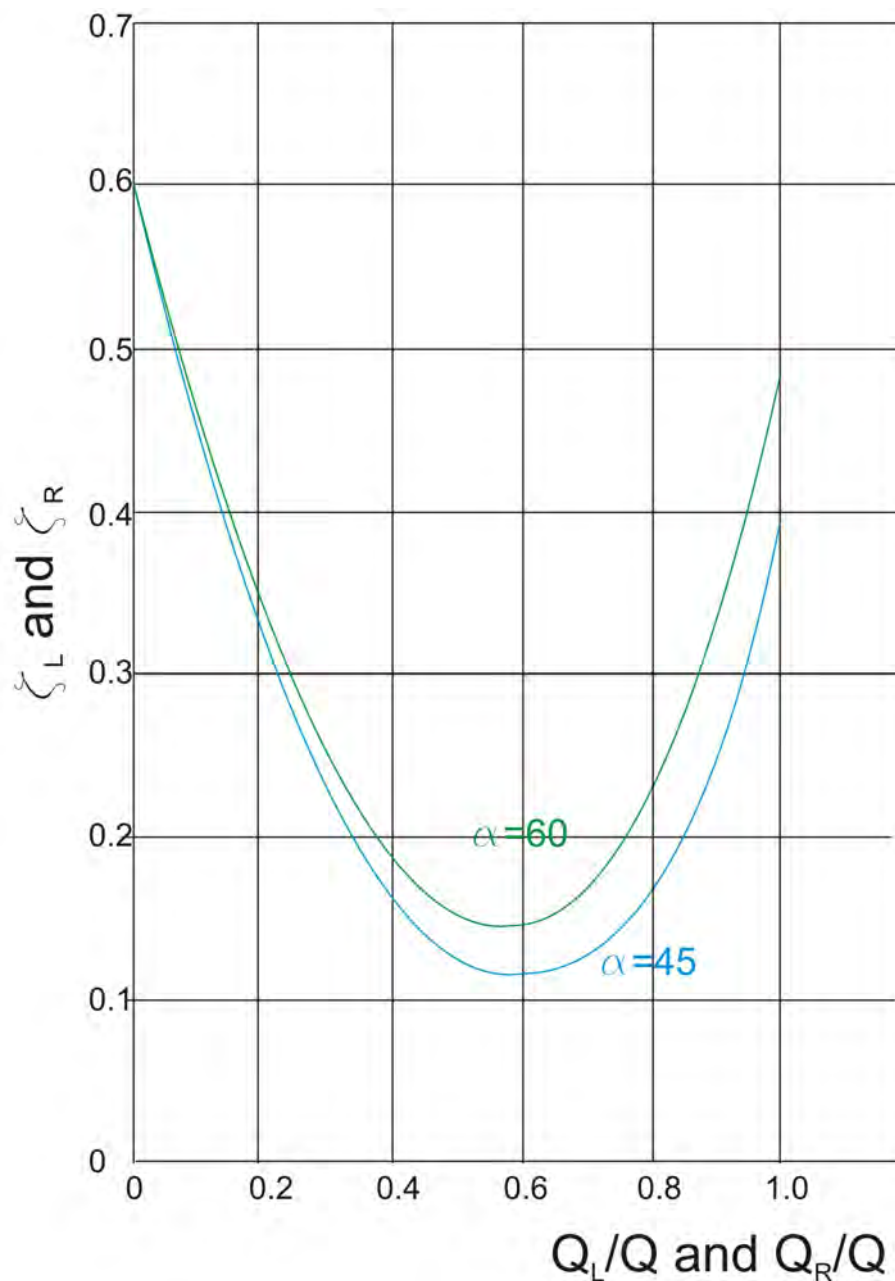
Figure 2.39: *Results of the Y-bifurcator (Müller and Stratmann [1971]) with branching angle of 60° and 45°.*

The results for branching angles of 30° and 45° are shown in Figure 2.39. The minimum loss coefficient ζ in Figure 2.39 does not occur at a flow distribution of $Q_A/Q = 0.5$ but for ≈ 0.6. This means that a slightly accelerating flow in the branch pipe causes the lowest head losses (Note, that the velocity in the main and branching pipe is equal for flow distribution of $Q_A/Q = 0.5$). The loss coefficient ζ also decreases with decreasing branching angle, similar to the T-bifurcator.

2.2.6 Alberschwende

Klasinc et al. [1992] performed an investigation on a symmetrical Y-bifurcator with a slight bend located $3 \cdot D$ upstream of the bifurcator. The applied law of similitude is

according to Reynolds and the scaling factor is 1 : 12.85. The pipe installation is made of plexiglass. The water was supplied to the model from an overhead tank with a piping system and a stilling element to keep the inflow as constant as possible. Downstream of the Y-bifurcator there are two flow meters and two electrically controlled Howell-Bunger valves.

The pressure differences are measured at 6 control sections before and 4 control sections after the Y-bifurcator. A single control section consists of four bore holes which are burr-free and sharp-edged. For each control section all four bore holes are connected together by a single ring line. (see Figure 2.40). The pressure difference is measured at least $2 \cdot D$ upstream and $10 \cdot D$ downstream of the Y-bifurcator. To include also the local loss of the slight bend before the bifurcator the pressure differences are measured between control section O4 and R3, L3 respectively.
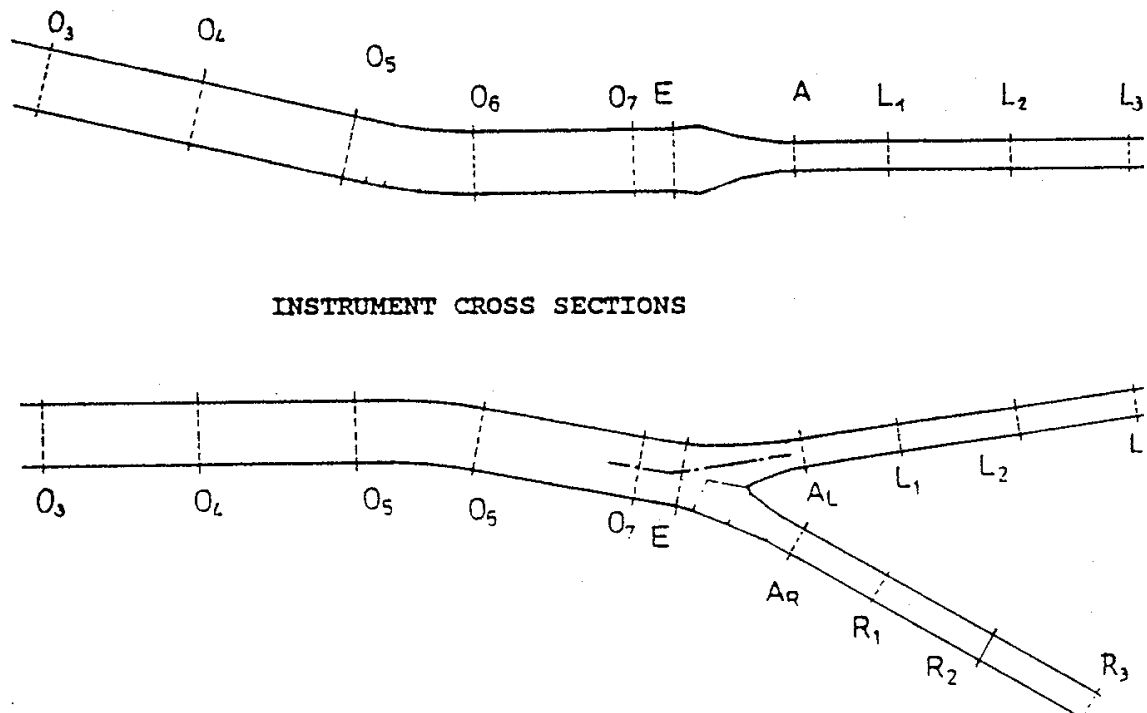
Figure 2.40: *View of the hydraulic model test of Klasinc et al. [1992]; longitudinal profile (top) and plan view (bottom). Label O, E, L, R and A are the position of the control sections*

To get the local head loss the pipe friction loss must be extracted from the total loss. This is achieved by a set of substitution cylinders similar to the work of Müller and Stratmann [1971].

To fulfill the Reynolds law of similarity the velocity in the pipe installation must be 12.85 (scaler) times higher than the velocity in the prototype. This is not achievable and Klasinc et al. [1992] performed a polynomial regression using the method of least squares. As can be seen in Figure 2.41 the regression with a polynomial of second order shows the expected quadratic behavior of a fully turbulent flow and is therefore chosen for further loss coefficient calculations. The results for symmetrical and asymmetrical distribution are shown in Table 2.3.
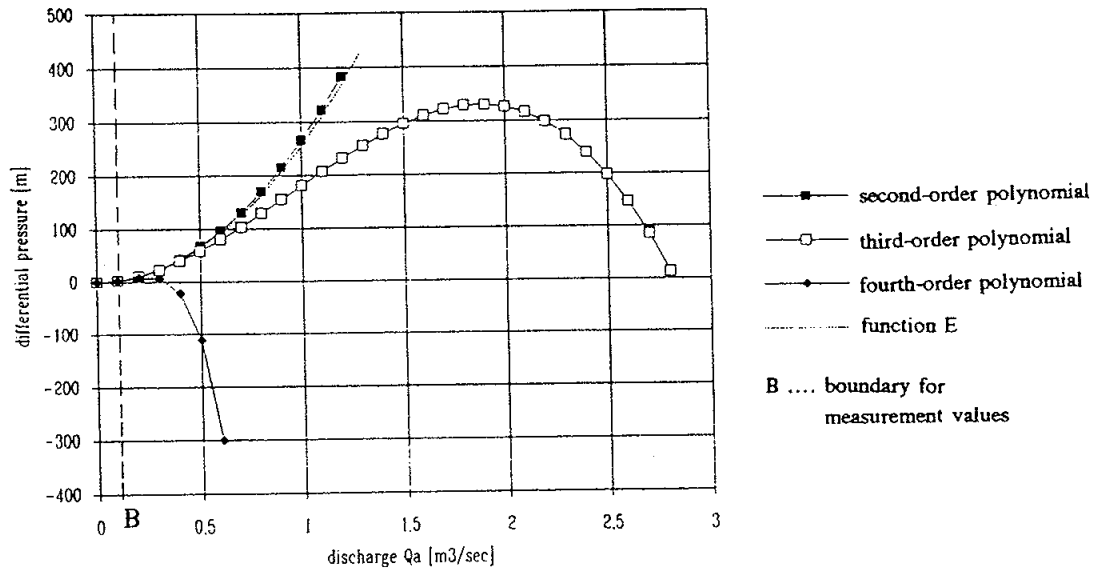
Figure 2.41: *Example of polynomial regressions of a head loss measurement. The E-function represents the dynamic velocity head ($V^2_{main\ pipe}/2g - V^2_{branch\ pipe}/2g$). The second order polynomial shows reasonable results if compared with the E-function. All other polynomials are far away from the E-function.*

Table 2.3: *Results of the loss coefficient ζ for the Y-Bifurcator. Symmetrical stands for $Q_{left}/Q_{main} = 0.5$ and Asymmetrical for $Q_{left}/Q_{main} = 1$ or $Q_{right}/Q_{main} = 1$.*

	Symmetrical	Asymmetrical
ζ	0.13	0.36

2.3   Summary of the Results for Y-bifurcators

In Table 2.4 a short summary of the characteristic of Y-bifurcators presented in Section 2.2.1 to Section 2.2.6 is given. Several properties of the Y-bifurcators labeled as D (diameter of the main D_{in} and branching pipe D_{out}), A (cross-sectional area), V (velocity), α (branch angle) and ψ (relative power loss) are shown in Table 2.4. If one checks the velocity ratio $sym : V_{out}/V_{in}$ a value close to 1.00 is stated. This means that almost no "velocity jump" occurs when the water flows from the main to the branching pipe and therefore the velocity ratio $sym : V_{out}/V_{in} \approx 1$ is one of the design criteria. Only the model test by Klasinc et al. [1992] and of Causey dam do not satisfy the velocity ratio $sym : V_{out}/V_{in} \approx 1$.

The relative power loss coefficient is defined as:

$$\psi = \frac{P_{loss}}{P_{kin}} = \zeta_{left} \cdot \frac{Q_{left}}{Q_{main}} + \zeta_{right} \cdot \frac{Q_{right}}{Q_{main}} \qquad (2.6)$$

$$P_{loss} = \sum_{i=1}^{2} \cdot \Delta h_{local,i} \cdot \rho \cdot g \cdot Q_i \qquad (2.7)$$

$$P_{kin} = \frac{V_{main}^2}{2} \cdot \rho \cdot Q_{main} \qquad (2.8)$$

whereas P_{loss} is the power loss, P_{kin} is the kinetic power and Δh_{local} stands for the head loss. For the results in Table 2.4 the discharge distributions are either $\frac{Q_{left}}{Q_{main}} = 0.5$, $\frac{Q_{right}}{Q_{main}} = 0.5$, $\frac{Q_{left}}{Q_{main}} = 1$ and $\frac{Q_{right}}{Q_{main}} = 0$.

If the power loss coefficient ψ is compared with each other care has to be taken. As mentioned in the paper of Williamson and Rhone [1973] a tentative comparison of the individual loss coefficient (or power loss coefficient) can be done when the ratio of the cross section areas are nearly the same. Therefore, the model test of the Causey Dam and the model test of Klasinc will not be plotted in the comparison of the relative power loss coefficient in Figure 2.42 and Figure 2.43.

The comparison of the ψ coefficient in Figure 2.42 and Figure 2.43 are approximately in the range of 0.03 to 0.3 for symmetrical and 0.3 to 0.6 for asymmetrical flow distribution. If one takes the mean of the symmetrical and asymmetrical ψ coefficient a value of 0.1 and 0.37 are gained, respectively. These values are in good agreement with the model test Pirris in the next chapters.

Table 2.4: *Summary of the characteristics of the Y-bifurcators. The dimension of the Y-bifurcator is downscaled based on the individual scale factors. Only Erzhausen has prototype size. In the model tests of Causey dam and Erzhausen it has not been reported if the pipe friction has been subtracted.*

Typ	D_{in}	D_{out}	$\frac{D_{in}}{D_{out}}$	$\frac{A_{in}}{A_{out}}$	$sym : \frac{V_{out}}{V_{in}}$	$asym : \frac{V_{out}}{V_{in}}$	α	ψ_{sym}	ψ_{asym}
[-]	[m]	[m]	[-]	[-]	[-]	[-]	°	[-]	[-]
Causey dam at Ogden river	0.12	0.09	1.33	1.78	0.89	1.78	60.00	0.29	1.32
Erzhausen, no built-in components	3.40	2.40	1.42	2.01	1.00	2.01	60.00	0.29	0.27
Erzhausen, built-in components	3.40	2.40	1.42	2.01	1.00	2.01	60.00	0.04	0.27
Erzhausen, hyd. favorable form	3.40	2.40	1.42	2.01	1.00	2.01	60.00	0.06	0.44
Ruus - W45	0.13	0.10	1.38	1.90	0.95	1.90	45.00	0.03	0.52
Ruus - W60	0.13	0.10	1.38	1.90	0.95	1.90	60.00	0.07	0.28
Ruus - W60I	0.13	0.10	1.38	1.90	0.95	1.90	60.00	0.05	0.29
Hyd. model test of Lee	0.29	0.20	1.43	2.04	1.02	2.04	80.00	0.30	1.46
Sulzer - 60 degree branching angle	0.11	0.08	1.40	1.97	0.98	1.97	60.00	0.15	0.48
Sulzer - 45 degree branching angle	0.11	0.08	1.40	1.97	0.98	1.97	60.00	0.10	0.39
Hyd. model test of Klasinc	0.29	0.13	2.24	5.03	2.51	5.03	38.00	0.22	1.77
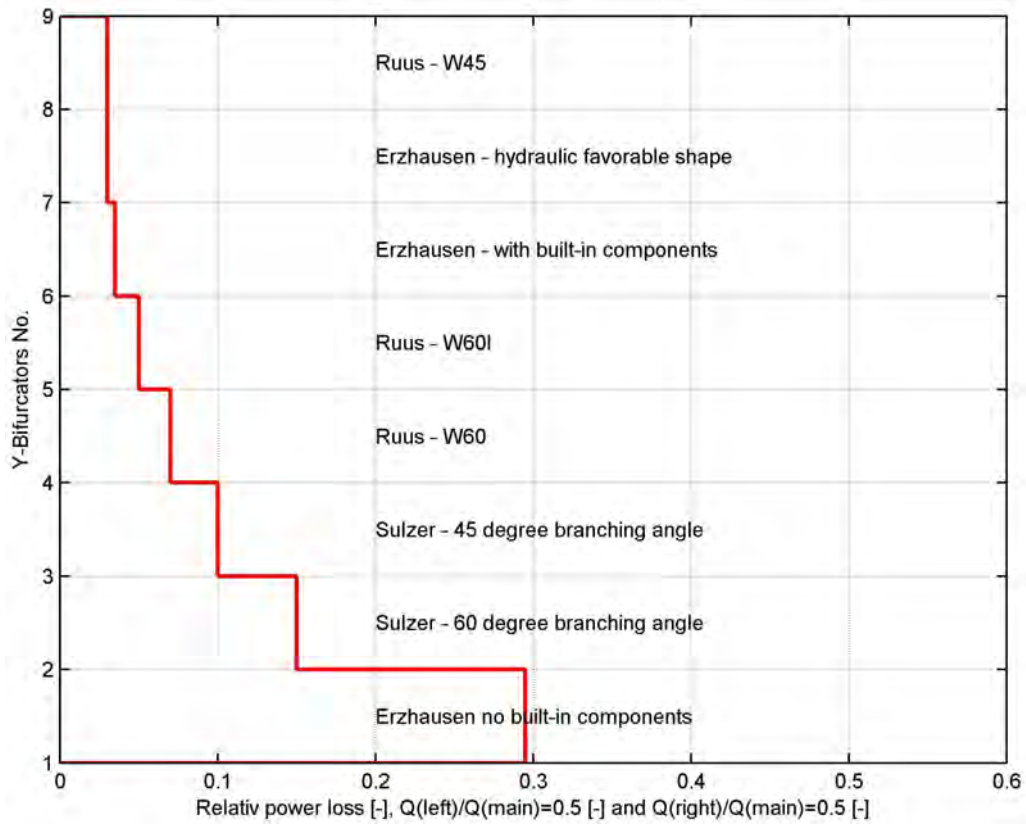
Figure 2.42: *Relative power loss ψ for all Y-bifurcator, symmetrical discharge rate*
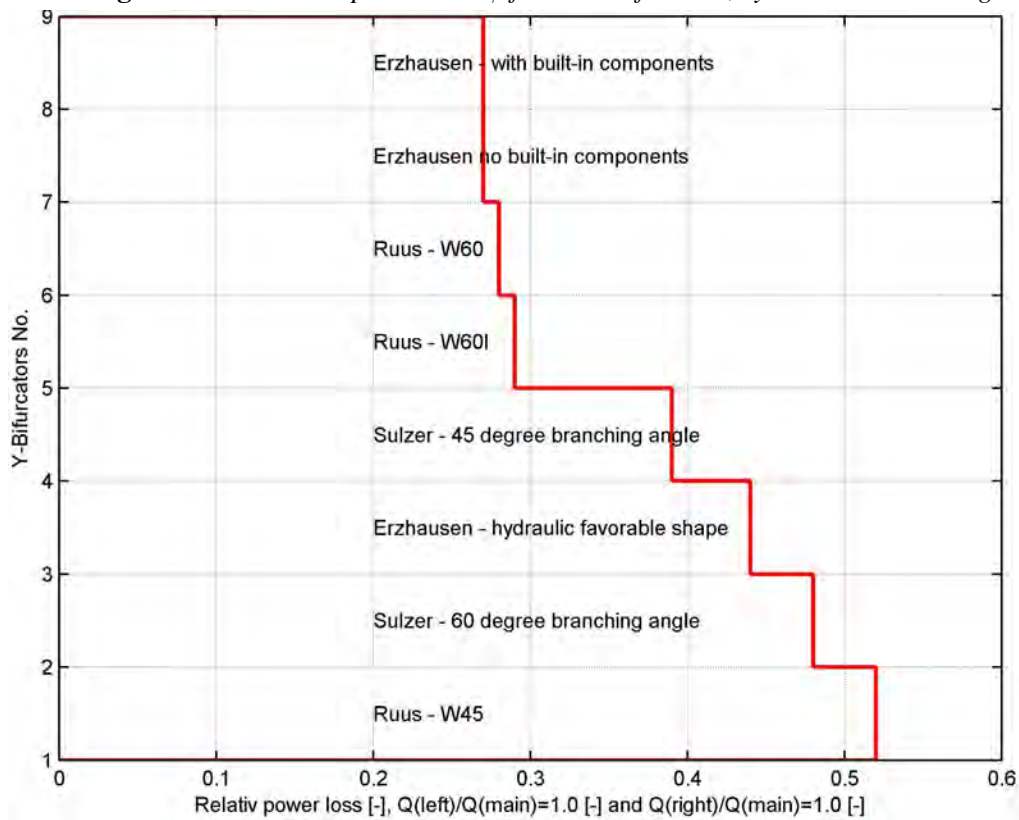
Figure 2.43: *Relative power loss ψ for all Y-bifurcator, asymmetrical discharge rate*

2.4 Numerical investigations of bifurcators

A notable amount of literature studies of numerical investigations on trifurcations are available. A detailed study of the influence of the boundary layer in a numerical calculation of a Y-bifurcator can be found in Lasminto and Klasinc [2011]. The applied turbulence model in Lasminto and Klasinc [2011] was the realizable k-ϵ model. The comparison for the velocity and pressure distribution in the Y-bifurcator is in good agreement with the corresponding model test.

Further papers were published by Basara et al. [1999], Klasinc and Knoblauch [1994], Dobler et al. [2010c] and Dobler et al. [2010b] where the hydraulic behavior in a trifurcation and y-bifurcation is investigated. A direct numerical simulation (DNS) was done by Tadjfar and Smith [2004], where the pressure losses of different branching angles of the Y-bifurcator have been investigated. A CFD calculation of a T-bifurcator was conducted by Moujaes and Deshmukh [2007], where the pressure loss of the fittings was of interest. Ramamurthy et al. [2006] also investigated a T-bifurcator with the k-ω turbulence model to determine several loss coefficients for different flow distributions.

The main task of these numerical investigations is to check the accuracy of the results (mostly with a model test). It could be possible that CFD simulations will replace the hydraulic model test in the near future. Additionally, which is also shown in this thesis, non-commercial software packages are gaining in importance.

Chapter 3

Y-Bifurcator Pirris - Hydraulic Model Set-Up

In Central America a new hydro power plant is constructed and located close to the river Pirris. The hydro power plant is equipped with two Pelton turbines each of them producing 70 MW. The division of the water supply to the turbines occurs in a symmetrical Y-bifurcator. The branching angle is $40°$. The main pipe has a diameter of 2 m and downstream, after the Y-branch and the confusor, the branching pipes have diameters of 1 m. The design discharge rate for each Pelton turbine is 9 m^3/s. 37 m before the Y-Branch a $42.96°$ bend is placed in the penstock. The total length of the penstock is 11.3 km. The main task of this hydraulic model test is to investigate the losses of the bifurcation in a small-scale hydraulic model. Two papers (Dobler et al. [2010a] and Dobler and Zenz [2011]) have been published about this model test.

3.1 Scaling law

Due to the geometrical size of the penstock and due to the restricted discharge capacity in the hydraulic laboratory it is not feasible to do tests on a full scale model. Instead, a down-scaling of the model to a reasonable size is necessary. For full similarity between the prototype and the model three conditions have to be fulfilled (Kobus [1984]):

1. Geometric similitude, whereby the ratio of the length dimension are equal in the model and prototype

2. Kinematic similitude, whereby the ratio of velocities and accelerations are equal in the model and prototype

3. Dynamic similitude, whereby the ratio of the forces are equal in the model and prototype

It is very difficult or even impossible to achieve similarity for geometric, kinematic and dynamic similitude between prototype and model. Therefore, it is essential to identify the primary process in the hydraulic model test. For pipe flow the ratio of the inertia forces to viscous forces are of predominant importance and therefore the model is scaled after the Reynolds number Re (Eq. 3.1) which can be written as:

$$Re = \frac{L\,V}{\nu} \tag{3.1}$$

Whereas L is a characteristic length scale (e.g. pipe diameter D for pipe flow), V is the velocity (e.g. mean velocity in a pipe) and ν the dynamic viscosity.

Due to the available size in the laboratory of *TU-Graz* the following scaling ratio (Eq. 3.4) has been used:

$$Re_{pr} = Re_{mo} \tag{3.2}$$

$$L_r = \frac{L_{pr}}{L_{mo}} = 8.13 \tag{3.3}$$

$$V_r = \frac{1}{L_r} \tag{3.4}$$

$$Q_r = L_r \tag{3.5}$$

Whereas the subscript *pr* and *mo* represent prototype and model values, respectively. The subscript *r* denotes the ratio between prototype and model.

.

3.2 Model set up

In the hydraulic model test the Y-bifurcator consists of a main pipe with an inner diameter of 246 mm and two branching pipes with an inner diameter of 172 mm, respectively. The branching angle of the symmetrical Y-bifurcator is 40° and a stiffener is used for statical reason. 18 diameters ($18 \cdot D$) upstream of the Y-bifurcator a bend with an angle of 42° is located and after this bend exists a $12 \cdot D$ long pipe which ends in a flow conditioner (see Figure 3.1). Downstream of the Y-bifurcator, there is a $10 \cdot D$ long pipe with a inner diameter of 123 mm and a confuser for each branch.

The flow conditioner (see Figure 3.2) consists of a pipe bundle to smooth the incoming flow and to create a fully developed turbulent approach flow. The bend itself consists of 5 segments each of them rotated by 8.4°. The Y-bifurcator consists of three cone-shaped volumes and a stiffener. After the confuser two Pelton turbines are located in the prototype. Instead of the Pelton turbines a $10 \cdot D$ long pipe is installed in the hydraulic model to get a fully redeveloped turbulent flow.

The water for the model test is supplied by a reservoir in the laboratory. The water level in the reservoir is 13 m above the symmetry axes of the Y-bifurcator. With this water head a maximum discharge rate of 0.12 m³/s is possible. Using pumps, a discharge rate of 0.2 m³/s is possible and the maximum allowable pressure of 1.3 bar, due to the strength of the plexiglass-pipe, is achieved in the installation. After passing the model test, the water enters another reservoir which is located below the model.

Due to the length ratio of 8.13 it is possible to use prefabricated pipes with an inner diameter of 123 mm for the downstream part of the Y-branch. Upstream, handmade plexiglass
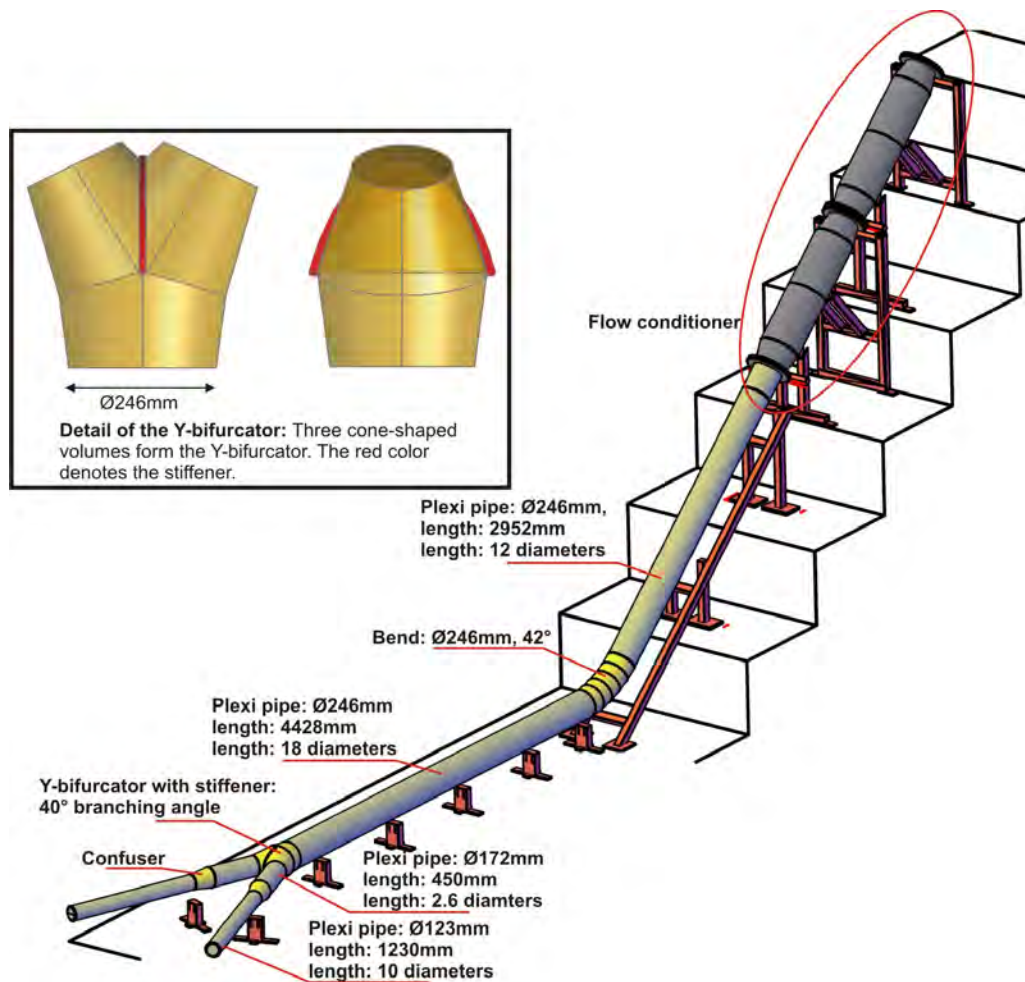
Figure 3.1: *View of the model test Pirris.*

Figure 3.2: *Flow conditioner: Assembling of smaller pipe bundles to smooth the incoming flow*

pipes are manufactured with an inner diameter of 246 mm. Generally, a manufactured pipe consists of two half pipes which are wrapped around a wooden pipe model. This can only be achieved with a heated plexiglass plate in an oven (Figure 3.3).

The same procedure is also used for the Y-branch. Again a wooden model is used to give the plexiglass plate a conical form (Figure 3.4).

Figure 3.3: *Manufacturing of a pipe: Firstly, the plexiglass-pipe is wrapped around a wooden model. After cooling, the pipe keeps its shape. Finally, the half shells are glued together*

Figure 3.4: *Manufacturing of the Y-bifurcator: Three conical plexiglass shapes are needed to assemble the Y-bifurcator*

Figure 3.5: *Final form of the Pirris hydraulic model*

Finally, all the plexiglass parts are flanged together to give the final form of the Pirris hydraulic model (Figure 3.5 and Figure 3.6). The additional parts downstream of the Y-bifurcator, that is the Howell-Bunger valves and the flow meters, will be explained later.

3.2.1 Load Cases

Seven load cases with corresponding discharge ratios for the model test are defined (see Table 3.1). The theoretical maximum discharge rate based on the Reynolds law is Q_{main}/L_r = 18/8.13=2.2 m^3/s. Note, the discharge for the prototype is 18 m^3/s.
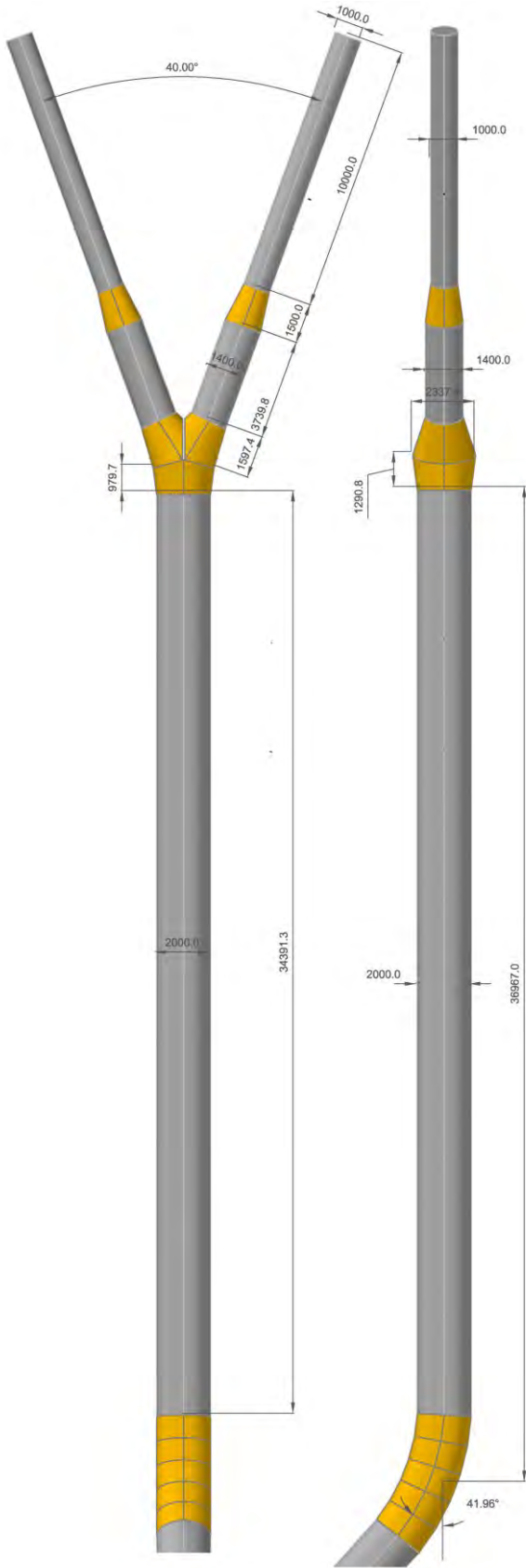
Figure 3.6: *Dimensions of the Y-bifurcator (model size [mm])*

Table 3.1: *Flow distributions*

LC1-left	LC2-right	LC2-left	LC3-right	LC3-left	LC4-right	LC4-left
-	-	-	-	-	-	-
$\frac{Q_{left}}{Q_{main}} = 1.0$	$\frac{Q_{right}}{Q_{main}} = 0.33$	$\frac{Q_{left}}{Q_{main}} = 0.67$	$\frac{Q_{right}}{Q_{main}} = 0.42$	$\frac{Q_{left}}{Q_{main}} = 0.57$	$\frac{Q_{right}}{Q_{main}} = 0.50$	$\frac{Q_{left}}{Q_{main}} = 0.50$

3.3 Instrumentation and measuring devices

For the measurement of the loss coefficient ζ two quantities have to be recorded by a data acquisition device. The first quantity is the piezometer differential pressure between two control sections and the second quantity is the discharge rate. The measuring device "Particle Image Velocimetry" will be introduced in Chapter 4.

3.3.1 Control section

For the measurement of differential pressures several control sections are necessary. Each control section consists of 8 burr-free, equi-distant and sharp edged bore holes with a diameter of 1 mm as shown in Figure 3.7.

All eight holes are connected together to get one average value. The distance between the control sections is approximately 3 times the diameter for the main pipe and 2 times the diameter for the branching pipes, respectively (see Figure 3.8).
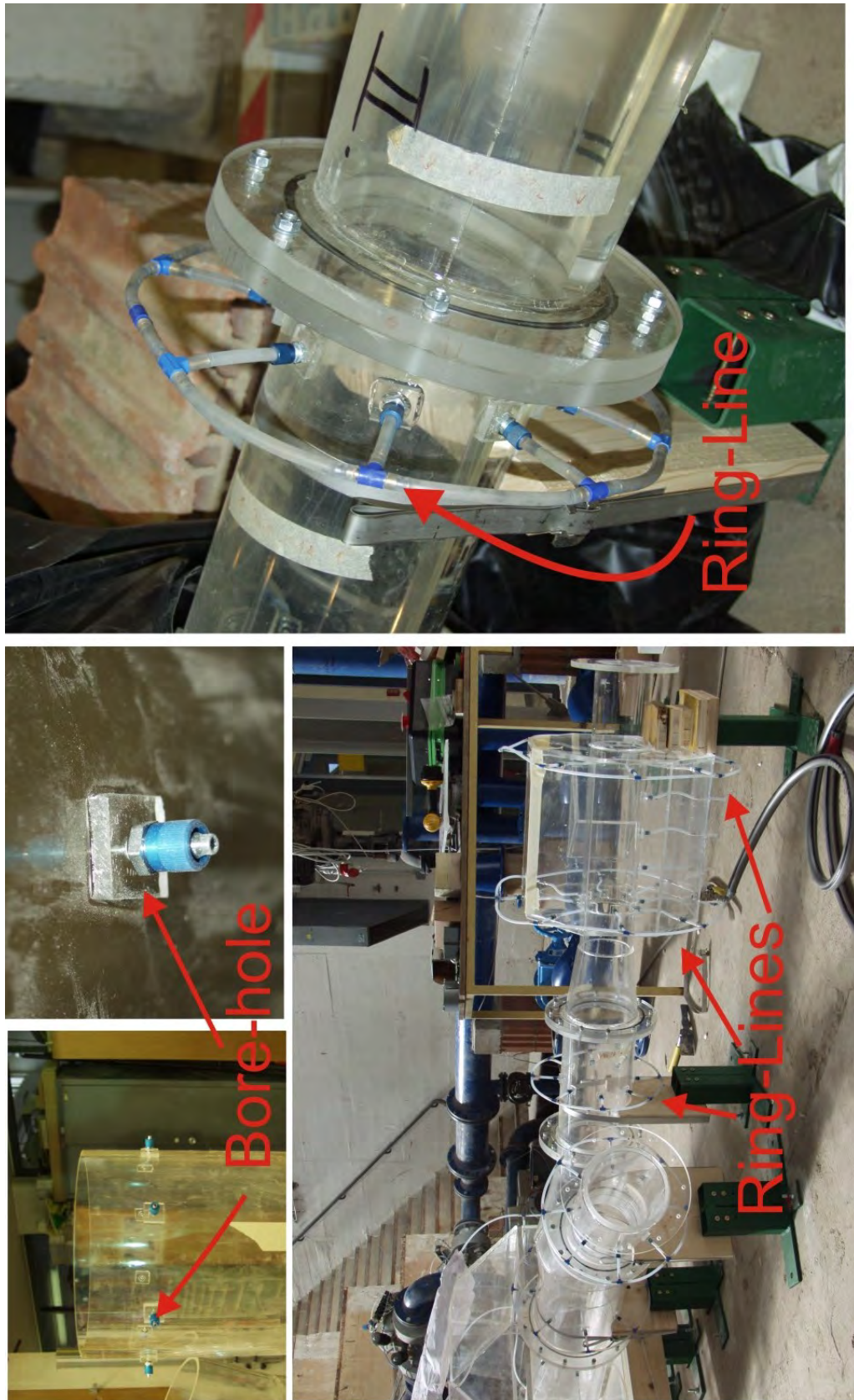
Figure 3.7: *Ring-Lines and bore holes of the model test*
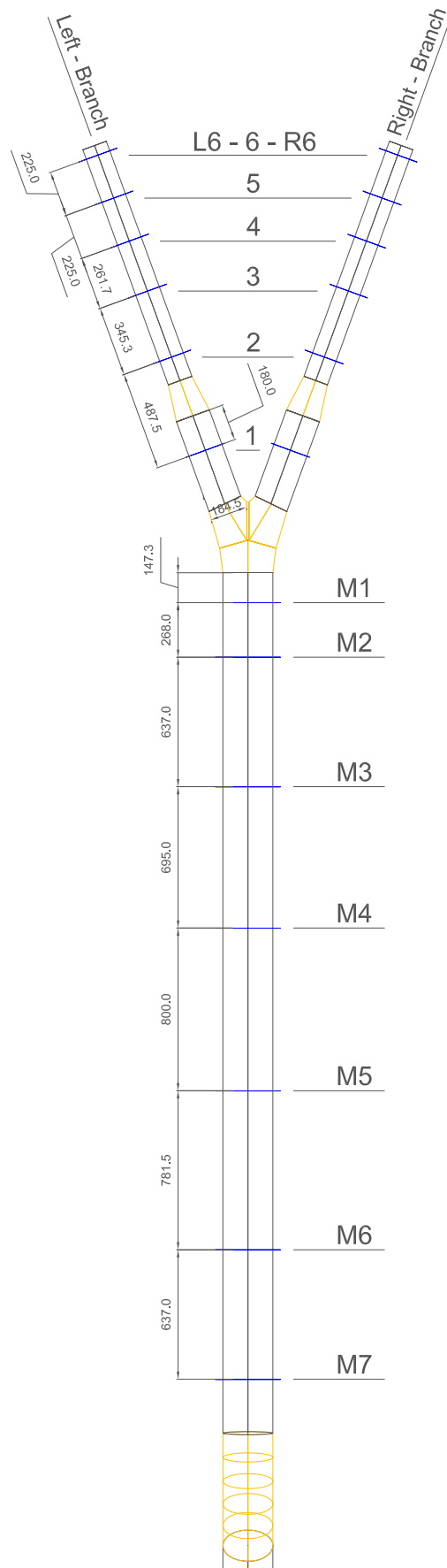
Figure 3.8: *Control sections along the pipe: M stands for main, L for left and R for right branch. [mm]*

3.3.2   Sampling rate

For all measurements the sampling rate was 1 kHz. The time length of one measurement was 60 seconds. This time length guarantees that the calculated mean value of the discharge rates and the pressure differences of the 60 000 data points are representative values. Figure 3.9 and Figure 3.10 show the influence of the time length of the sampling rate. Beginning with a time length of 300 seconds a mean value of 214.6 mbar is achieved. Unfortunately, it is not feasible to carry out the measurements with a time length of 300 seconds and therefore a reduction of the time length is necessary. If reducing the time length to 60 seconds a mean value of 214.3 mbar is found. That means that the difference of the two time lengths are only 0.3 mbar (3 mm head level) and the time length of 60 seconds are therefore long enough for the hydraulic model test. The same consideration can be applied with Figure 3.10. Again the difference for the discharge rate between 300 and 60 seconds are smaller than 0.3%. Note, that nearly 100 measurements have been carried out; with a sampling rate of 1 kHz and the aforementioned differences of the measurements of discharge and pressure the evaluation of the data with a Matlab script takes not too long (less than 1 hour) with a time length of 60 seconds.
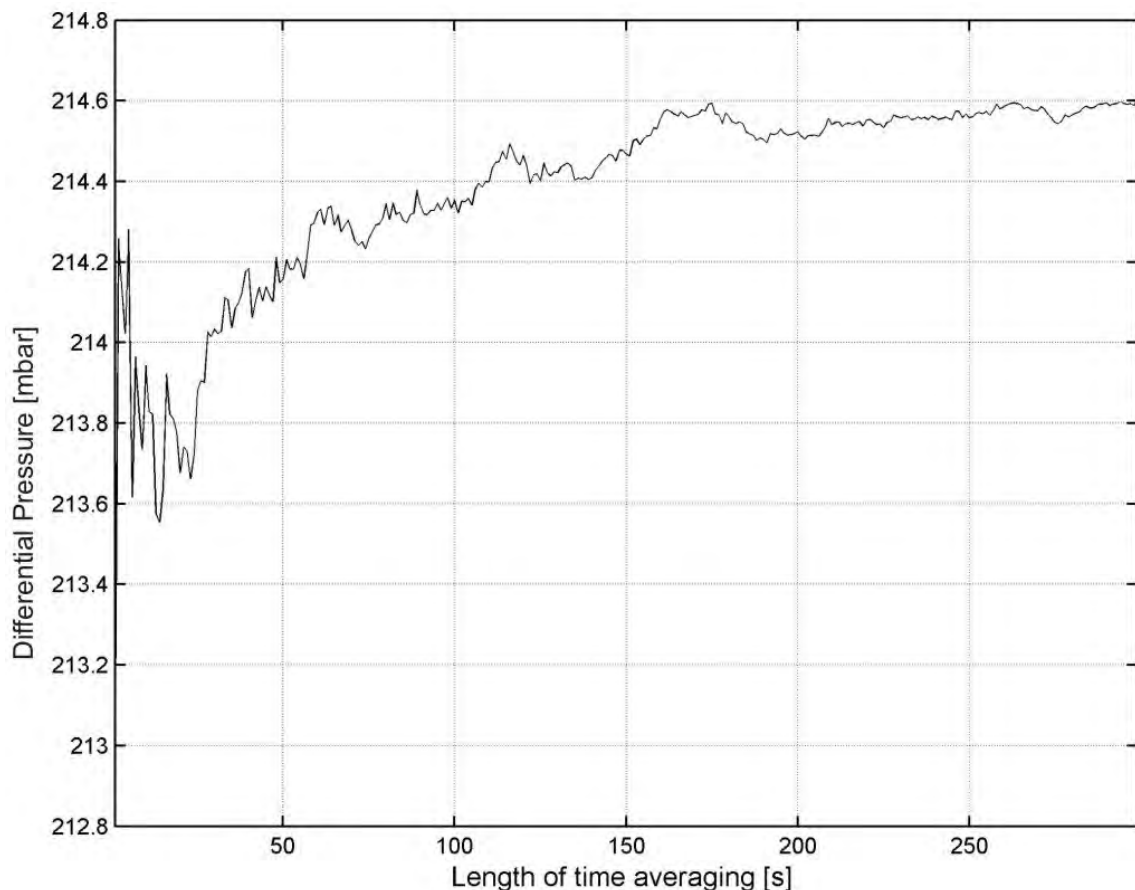
Figure 3.9: *Time dependent mean value of the total pressure difference measurement (control section M1 - L6, Q-left: 80l/s, Q-right 80 l/s*
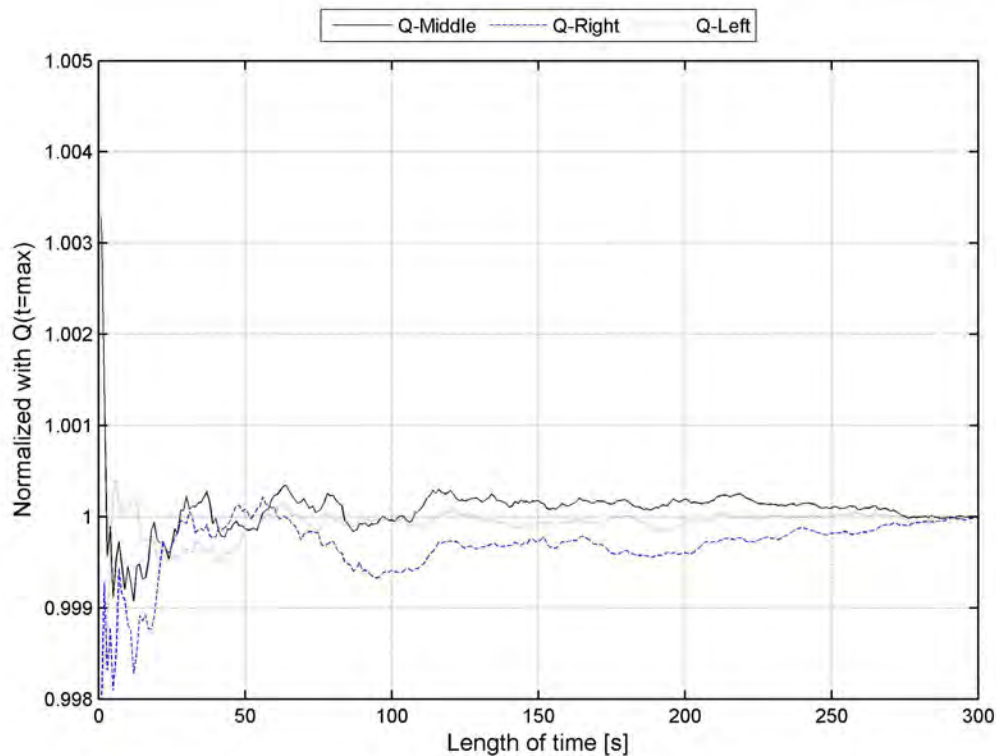
Figure 3.10: *Time dependent mean discharge rate, normalized with $Q_{t=300\ s}$ (control section M1 - L6, Q-left: 80l/s, Q-right 80 l/s)*

3.3.3 Pressure probe

The PD-23 pressure probe (Figure 3.11) from the company Keller is used. The maximum uncertainty of the pressure probe is 0.5% of the full range. With an average range of ≈ 1 m head level the uncertainty of 5 mm occurs.

Figure 3.11: *Pressure sensor PD-23 (Keller)*

3.3.4 Flow meter

Three flow meters (see also Table 3.2) are used to record the discharge rate in each branch, that is, the main branch (Ø250 mm) and the two branching pipes with a diameter of 150 mm each (flow meters are not placed in the plexiglass installation).

The measuring principle is based on electromagnetic induction where an electromagnetic
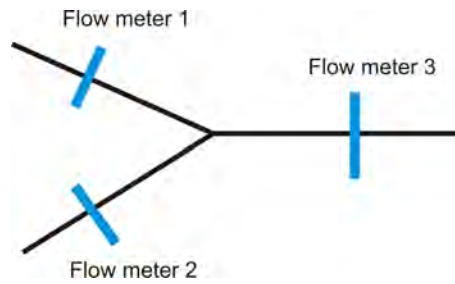
Figure 3.12: *Sketch of the position of the flow meter*

field B is used to measure the velocity in a pipe. When an electro-conductive fluid (e.g. water) in a pipe crosses the electromagnetic field which is generated by an electromagnet, a voltage U is measured between two electrodes. U is proportional to the velocity in the pipe.
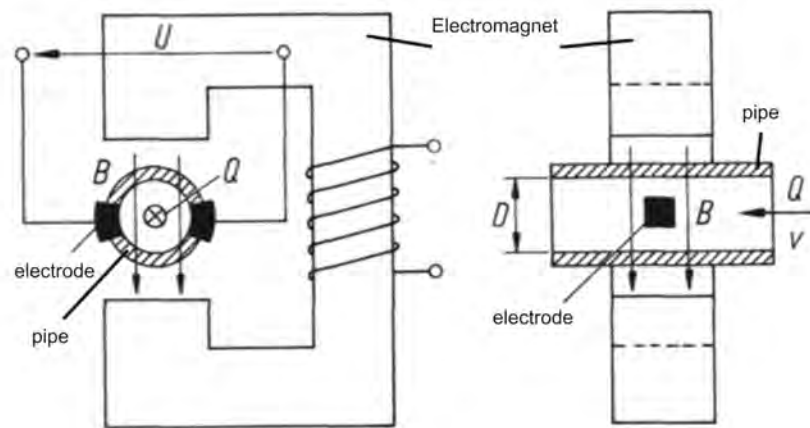
Figure 3.13: *Principle of inductive flow measurement (Goch [2008])*

The accuracy of the flow meter is a %-value of the measured discharge rate. For the highest measured discharge rate an uncertainty in the measurements occur as shown in Table 3.2.

Table 3.2: *Accuracy of the flow meters*

Flow meter No.	Type designation	Accuracy (dep. on flow rate)	Highest flow rate	Deviation
-	-	%	ℓ/s	ℓ/s
3	FXE4000(COPA-XE)	0.5	200	1
2	10DX3311G(COPA-XE)	1	100	1
1	D10D1465(COPA-XE)	0.5	100	0.5

The sample rate of the flow meter is 1 kHz. An internal damping of two seconds is set in the flow meter. That means that the flow meter calculates continuously mean values in the range of two seconds.

The discharge rate is controlled by two Howell-Bunger valves (see Figure 3.14) which have a fixed cone dispersion. With an electric motor the valves can be automatically opened or closed.

Figure 3.14: *Howell-Bunger valve (fixed cone dispersion valve) to control the discharge rate*

3.3.5 Calibration of pressure probe

Before the piezometer differential pressure measurement can be started a calibration for the pressure probe needs to be done. This is done by measuring a hydrostatic head level of 90 cm and scale the pressure probe to that height. Figure 3.15 shows the calibration device.

Figure 3.15: *Calibration of the difference pressure measurement*

Chapter 4

Particle Image Velocimetry

Particle Image Velocimetry (PIV) is an optical method to obtain instantaneous velocity vector fields of 2D-planes within a fluid. This chapter shows the set up and the positions (2D-planes for measurement) where PIV had been carried out. Also, a simple example of the evaluation of the raw-data from a PIV-measurement is demonstrated by using MATLAB R2008a (Matlab [2008]). A crucial point are the particle seeding within the flow to measure (indirectly) the flow velocity. To avoid building a second, smaller water circuit in the hydraulic laboratory where artificial seeding with a certain diameter and density could be added to the flow, the original water tanks are used instead. Therefore the whole measuring campaign was carried out by using the natural seeding of the flow itself. The diameter and the distribution of the natural seeding could be measured optically whereas an assumption had to be made that the density of the natural seeding is close to the density of water (only the floating seeding with density close to water can be drawn in by the pumps). Thus with the known diameter and density of the seeding the velocity lag as well as the minimum detectable velocity can be estimated. The results of the PIV-data, after validating the velocity vectors, have been statistically analyzed, that is, confidence intervals of the mean velocity and the standard deviations of the velocity had been checked. Finally, based on the statistical data from the PIV-measurements, several parameters of the flow can be calculated like turbulent intensity, kinetic energy, production of kinetic energy, Reynold-stress and vorticity.

4.1 Measuring Principle

Since the 1980ies considerable efforts have been undertaken to develop a Particle Image Velocimetry. Today a complete PIV device is available to investigate different flows either in air or water, mainly for research purposes. The principle of a non intrusive PIV is shown in Figure 4.1. A double pulsed Nd:YAG laser emits at 527 nm wavelength (green light) to generate a laser light which is expanded by optical lenses to a laser light sheet within the measurement area. At 1 kHz repetition rate the Nd:YAG laser has an output power of 23 mJ and therefore belongs to the safety class 4. Details on the PIV system used are given in Table 4.1.

The particle seeding flow through the laser light sheet and scatter the light which, in turn, is recorded by a high speed camera. With two images taken at t_i and t_{i+1} a cross correlation is done for each interrogation (I_1 and I_2) area of the image. For each interrogation

area one velocity vector is calculated and after carrying out the procedure for the rest of the interrogation areas a velocity vector field is achieved.

Table 4.1: *Components of PIV*

Laser	Litron Laser - Model: LDY303-PIV, Repetition rate: 0.2 - 10 kHz with 21.5 - 1.85 mJ, λ=527 nm
Camera	Photron FASTCAM SA-1 Camera, 5.4 kHz, 1024 · 1024, 16 GB Memory
Object lens	AF Micro-Nikon, 60mm f/2.8 D
Software	Dynamic Studio 2.20.18
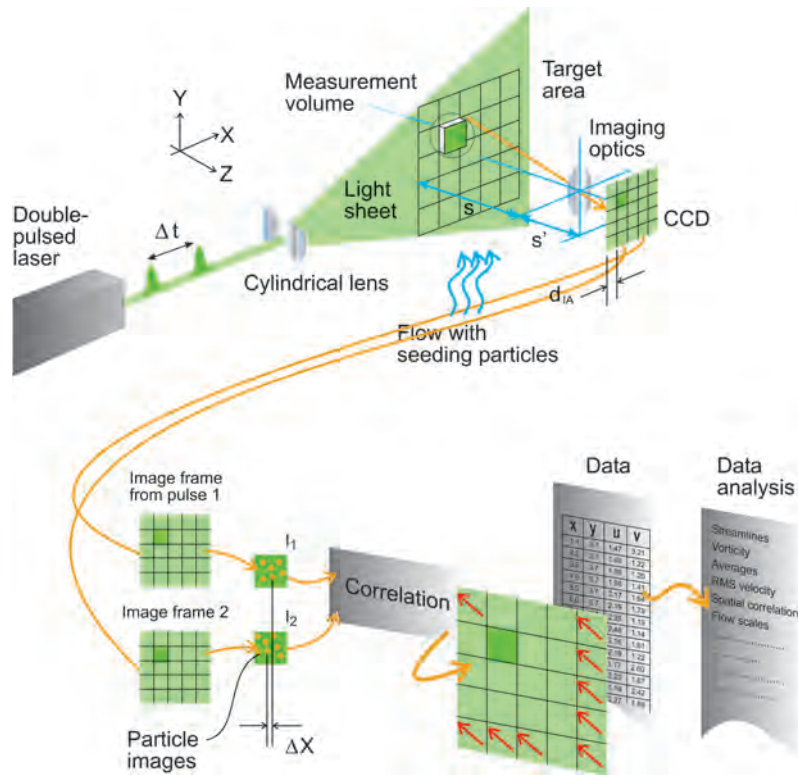
Figure 4.1: *Principle of PIV and its components (Source: Dantec Dynamics)*

4.2 PIV set-up

The position for the measurements of PIV is shown in Figure 4.3. The blue hatched boxes indicate where the laser and the camera are positioned along the pipe. In Figure 4.2 a principle set up for the camera and the laser light sheet is shown. There are 4 planes for the PIV whereby the camera is always aligned orthogonally to the laser light sheet. The reason for the water filled PIV-box is to avoid any astigmatism effects due to the curved pipe surface. The refraction index between water and plexiglass (water:1.33, plexiglass-Röhm: 1.49) is nearly the same, that is, no severe diffraction occurs.

In Table 4.2 the different load cases for PIV are shown. Several planes (Plane 1 to 4 for PIV-Box 200 to 202L; compare also with Figure 4.3) are investigated for PIV. The flow property in the hydraulic model test is indicated by the operation mode **Generating** (flow has a direction as shown in Figure 4.3) or **Swirling flow** (flow with an additional swirling flow, see also Section 5.5 on Page 102).
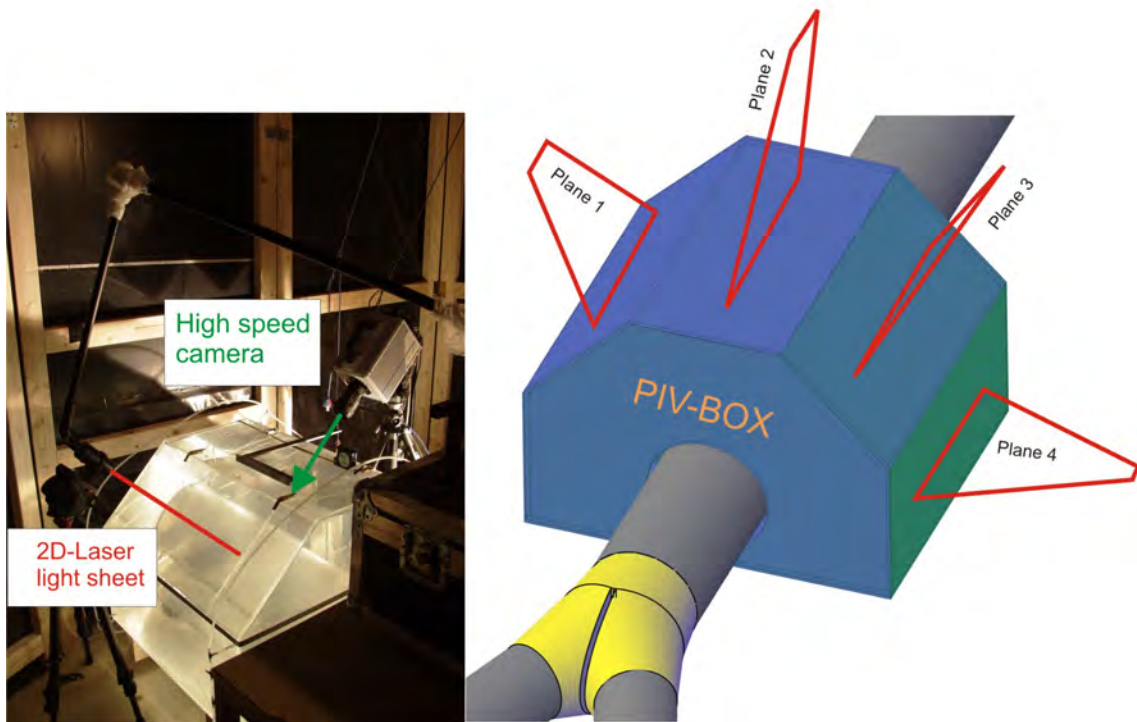
Figure 4.2: *Left Figure: typical set up for a PIV: Laser light sheet and high speed camera are orthogonally aligned. Right Figure: Four planes are used to determine the velocity vector fields*

Table 4.2: *PIV - Load cases for hydraulic model test Pirris: 40 Planes are investigated with PIV whereas 2 different discharge rates are used (80 and 40 l/s). The operation mode is either generating or swirling flow (with the use of a swirling device).*

Operation mode	Q [l/s]	PIV-Box: B200	PIV-Box: B201	PIV-Box: B202
Generating	$Q_{left} = Q_{right}=80$	Plane 1 Plane 2 Plane 3 Plane 4	Plane 1 Plane 2 Plane 3 Plane 4	Plane 1 Plane 2 Plane 3 Plane 4
	$Q_{left} = 80, Q_{right}=0$	Plane 1 Plane 2 Plane 3 Plane 4	Plane 1 Plane 2 Plane 3 Plane 4	Plane 1 Plane 2 Plane 3 Plane 4
Swirling flow	$Q_{left} = Q_{right}=40$		Plane 1 Plane 2 Plane 3 Plane 4	
	$Q_{left} = 40, Q_{right}=0$		Plane 1 Plane 2 Plane 3 Plane 4	
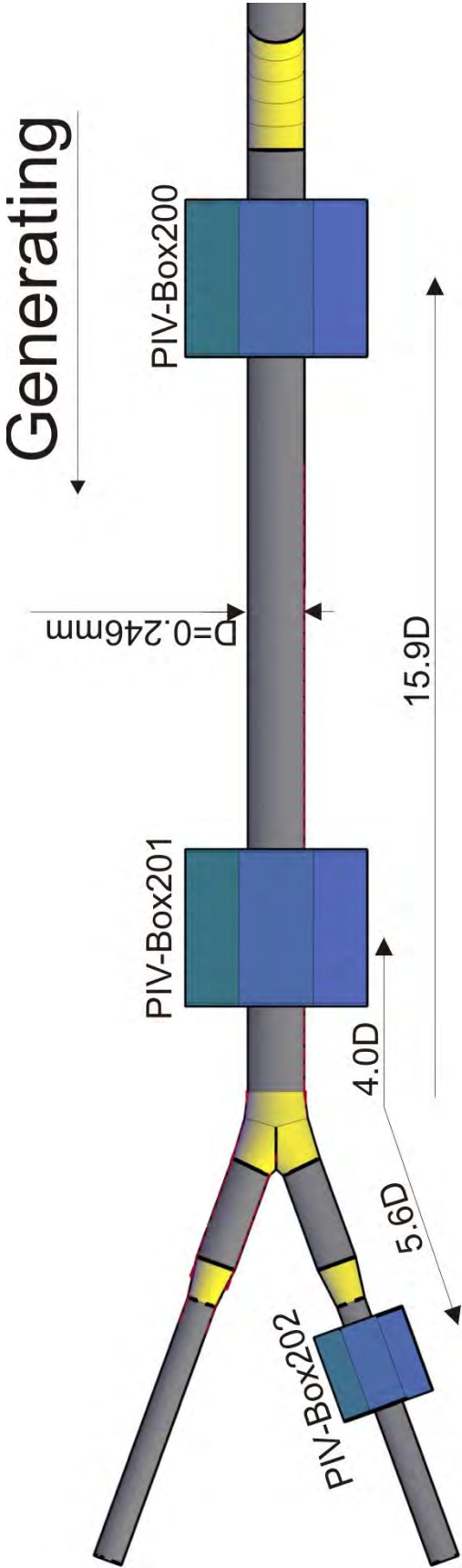
Figure 4.3: *Position for PIV along the pipe installation*

4.3 Image cross correlation principle with Matlab and Dantec

In Figure 4.5 the interrogation areas for two time steps of a PIV-measurement are shown. The interrogation areas belong to a measurement campaign of the Y-bifurcator Pirris with a sample rate of 1kHz and a size of a single pixel of 0.3 mm in x and y direction. The natural seeding can be clearly distinguished in Figure 4.5 (flow direction from left to right). Note, that the intensity for the second flash is somewhat smaller than for the first one. With the two interrogation areas a cross correlation can be carried out to find the displacement vector between the first and the second interrogation area. The correlation between two functions (x and h) is defined as:

$$z(t) = \int_{-\infty}^{-\infty} x(\xi) \cdot h(t + \xi) \cdot d\xi \qquad (4.1)$$

where t is the time and ξ is the shifting of the function. Evaluating Eq. 4.1 for two dimensional PIV pictures would be numerically very time consuming due to the multiplication and integration procedure. Alternatively, the convolution theorem is applied which states that a multiplication in the frequency domain is equivalent to a convolution in the time domain. The convolution and the cross correlation are almost identical as can be seen in Figure 4.4; the only difference is the mirroring of the function $h(\tau)$.

Therefore, as a next step, a 2-D discrete Fourier transformation into the frequency domain for the two interrogation areas will be carried out (see Figure 4.6). The syntax in Matlab2008b is simply: A =fft2(Image). Multiplication in the frequency domain with Figure 4.6, following an inverse 2-D discrete Fourier transformation (Matlab syntax: Image = ifft2(A)) to get the result in the time domain, gives the wanted peak in Figure 4.7. With a peak detection algorithm the displacement vector between the center of the image and the peak (see Figure 4.7) can be calculated (as expected the peak in Figure 4.7 is on the left of the center point).

The software of Dantec Dynamics is similar to the procedure shown above but with a more sophisticated algorithm. As a correlation method, the **adaptive correlation** of Dantec Dynamic is chosen. *The **adaptive correlation method** calculates velocity vectors with an initial interrogation area of the size N times the size of the final interrogation area and uses the intermediary results as information for the next interrogation area of smaller size, until the final interrogation area size is reached (Source: Dynamic Studio Help file*

After the adaptive correlation had been conducted three validation methods, offered by Dantec Dynamic Studio, are applied. The first one is called **peak validation**, which means that the highest peak (see peak in Figure 4.7) and the second highest peak must fulfill a minimum peak height ratio (the ratio was always 1.2). This enables to distinguish between the highest and second highest peak. The second validation method is called **range validation**. This method simply dumps every vector which has a higher absolute velocity than a certain threshold. The last method which is used to validate vector maps is called **moving average validation** by comparing each vector with the average of other vectors in a defined neighborhood. Vectors that deviate too much from their neighbors are dumped from the vector maps. Finally after the validation step, a mean vector map of all time steps is calculated by the software.
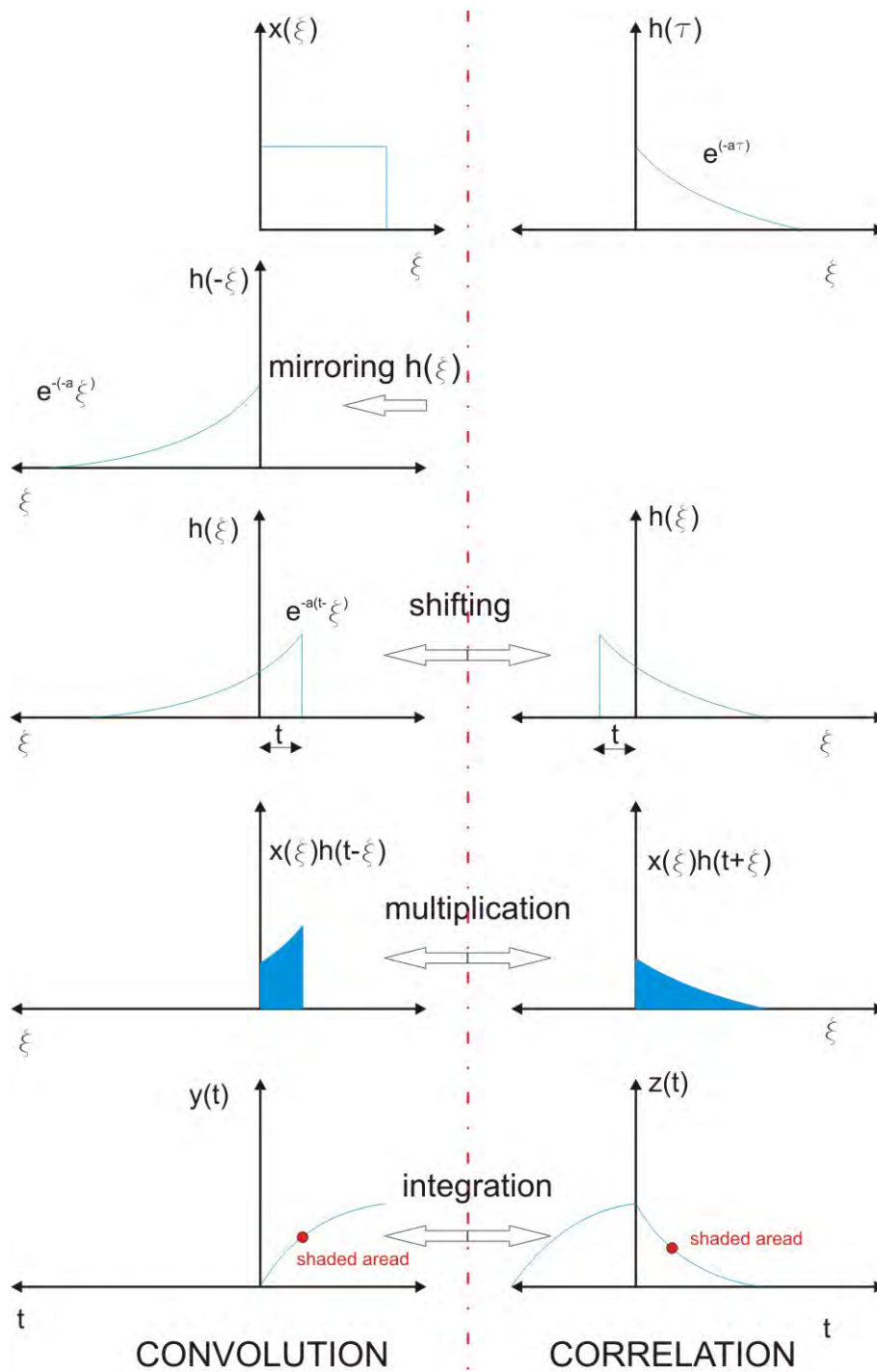
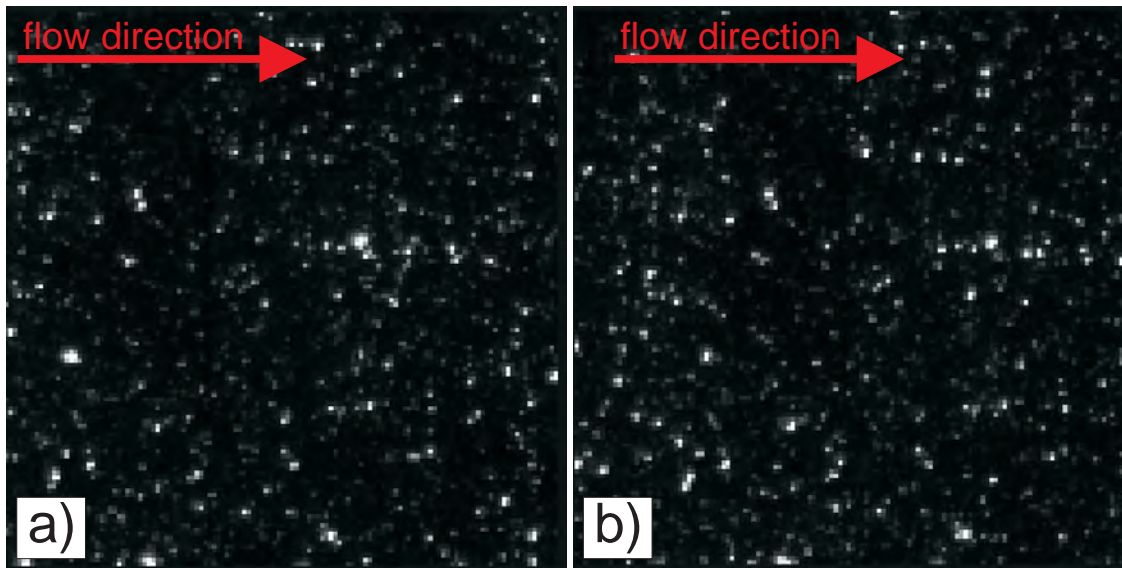**Figure 4.4:** *Relationship between convolution and correlation (taken from Brigham [1997]).*

Figure 4.5: *Interrogation area at a) t_1 and b) t_2*
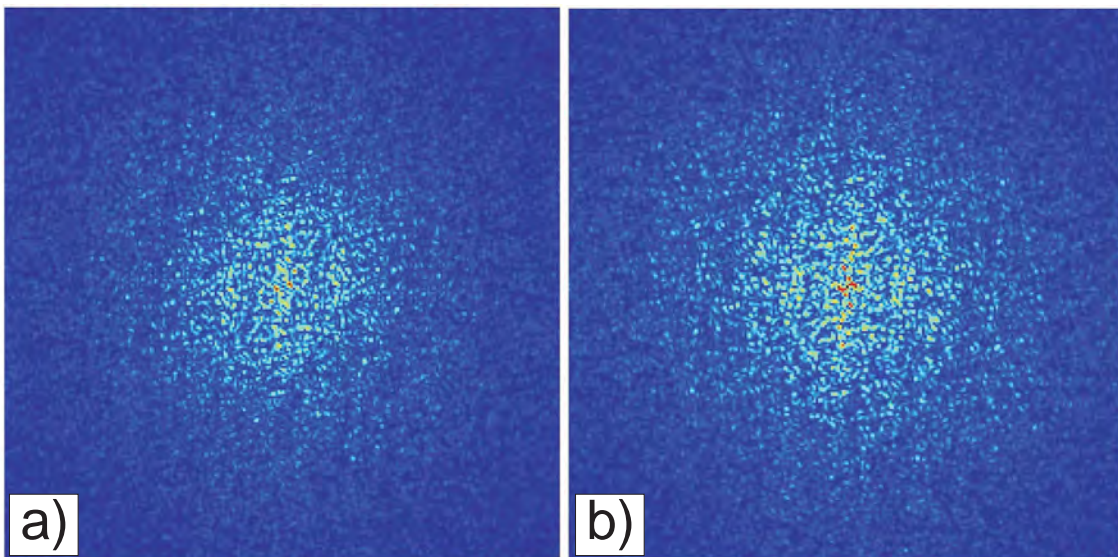
Figure 4.6: *FFT interrogation area at a) t_1 and b) t_2*
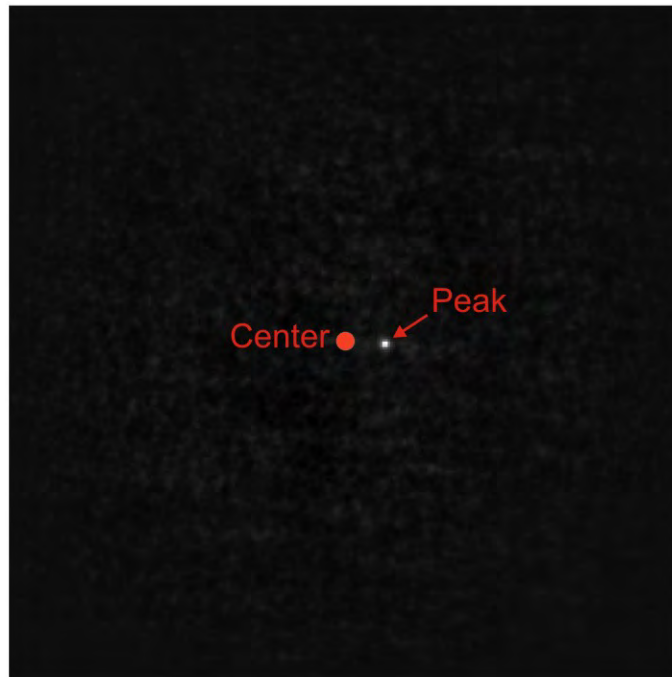
Figure 4.7: *Peak of the cross correlation*

4.4 Natural seeding

Due to the size of the hydraulic model test and the reservoir for the water supply it is not feasible to build a smaller water-circuit with artificial seeding in the flow. As an alternative, the natural seeding particles of the flow are used to detect the velocity. Obviously it is very difficult to define the density and the diameter of the natural seeding in the flow to calculate the velocity lag of the particles. Nevertheless, a reliable estimation of the velocity lag is possible.

In Figure 4.8 a representative example image of a PIV right after the bend is shown. The natural seeding can clearly be distinguished in Figure 4.8. To calculate the diameter of these particles it is necessary to divide the image into smaller parts as the working memory of the computer is restricted. One of the smaller images is presented in Figure 4.9. With this image having a gray depth of 16 bit the mean value of the gray depth of Figure 4.8 is subtracted. This reduces the background noise of the image considerably and using the threshold of 2 times the standard deviation gives the ability to distinguish between the particles and the background. The resulting particle matrix by this filtering is shown as an image in Figure 4.10 where the white space represents the background with a numeric pixel value of 0 and the black dots represent the particles with a numeric pixel value of 1. It is now possible with a Matlab script to count the seeding (black dots) and calculate the area of the seeding. This is done by stepping through the lines and columns of the particle matrix and count every conglomerate of the black dots in Figure 4.10 which represents a particle. The knowledge of the area of a pixel allows to calculate an equivalent particle diameter. Applying this procedure to the remaining image parts gives the particle distribution shown in the histogram of Figure 4.11. In the histogram a predominated class between particle diameters of 0.3159 to 0.4791 mm can be distinguished. Unfortunately, this particle diameter class is close to the pixel resolution (the area of the image is approximately 300·300 mm; with 1024·1024 pixels a length for a pixel in the image plane of 290 μm is obtained) and a microscope is used to determine the particle size. Several

probes had been taken from the reservoir and are used to check the predominated particle diameter as can be seen in Figure 4.12. The resulting diameter with the microscope is - for the most cases - between 20 and 50 μm. Therefore, for further calculations the particle size of 50 μm is used. The histogram with too big particle diameters is still useful to estimate the amount of particles in the flow which is around 12 000 for particles smaller than 600 μm. The amount of particles for each image was mostly constant, regardless of the discharge rate.
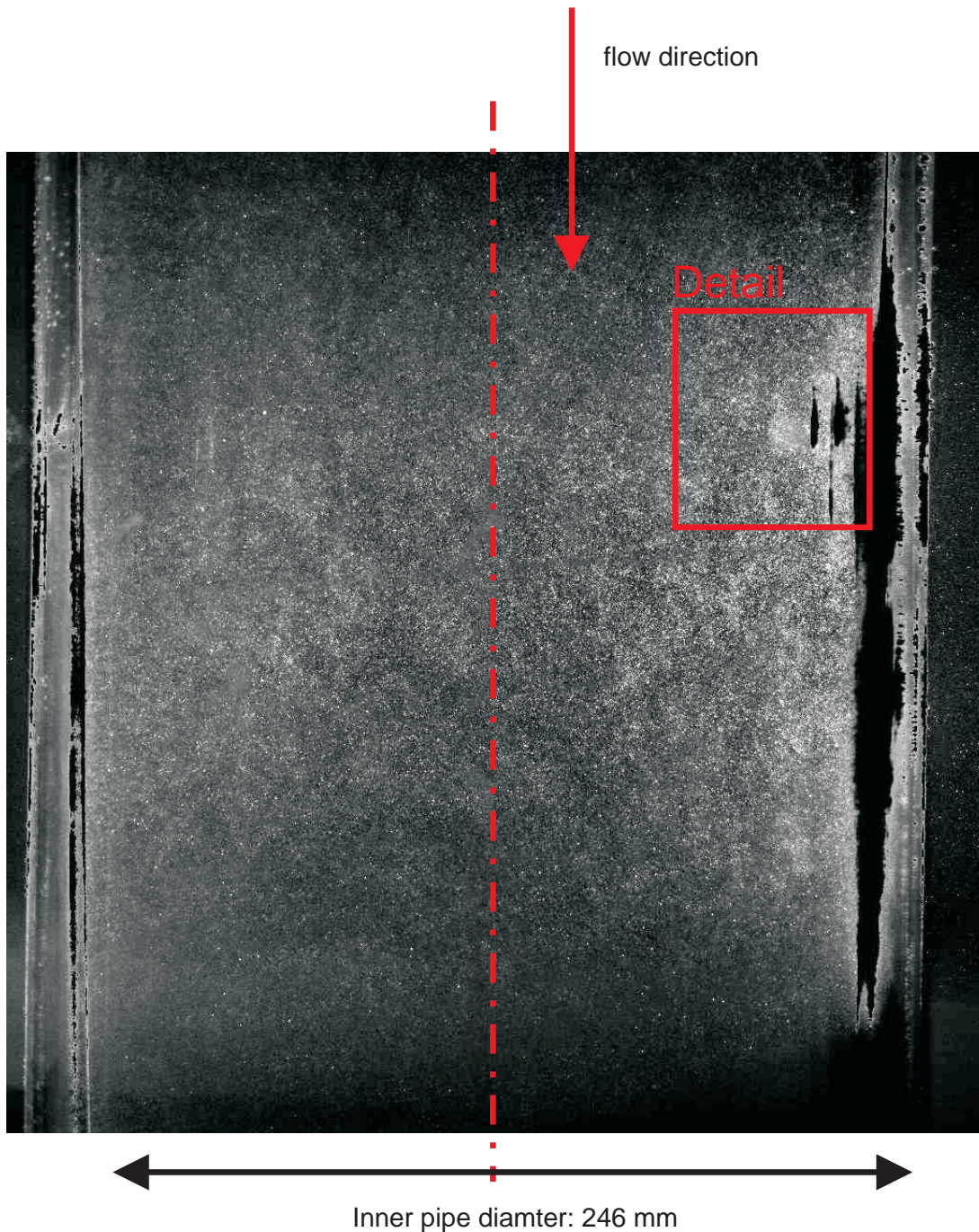
Figure 4.8: *Example image for the natural seeding of the model test. (Position: horizontal plane, right after the bend).*
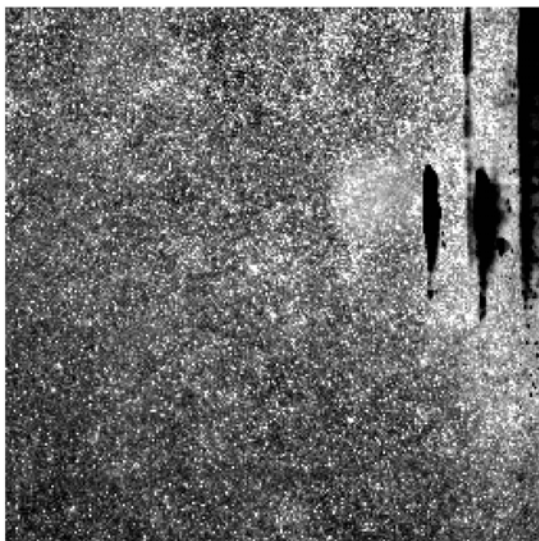
Figure 4.9: *Detail of the image in Figure 4.8*
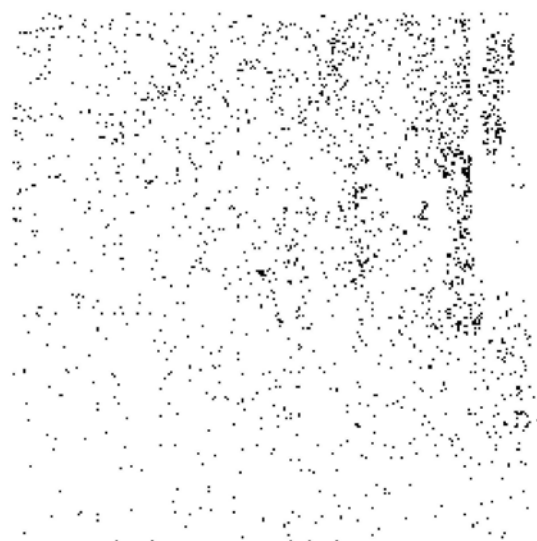
Figure 4.10: *Subtracting the mean of Figure 4.9 and filtering with 2 times the standard deviation reveals the seeding.*
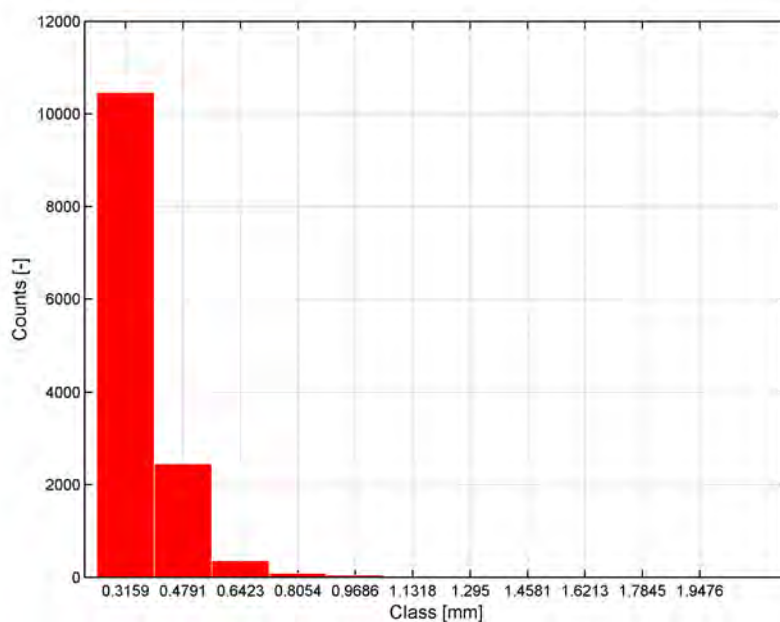
Figure 4.11: *Most particles lie in the class from diameter = 0.3159 to 0.4791. More than 12000 seeding are available per image. Note, that these particle diameters are smaller as shown in Figure 4.12*

.
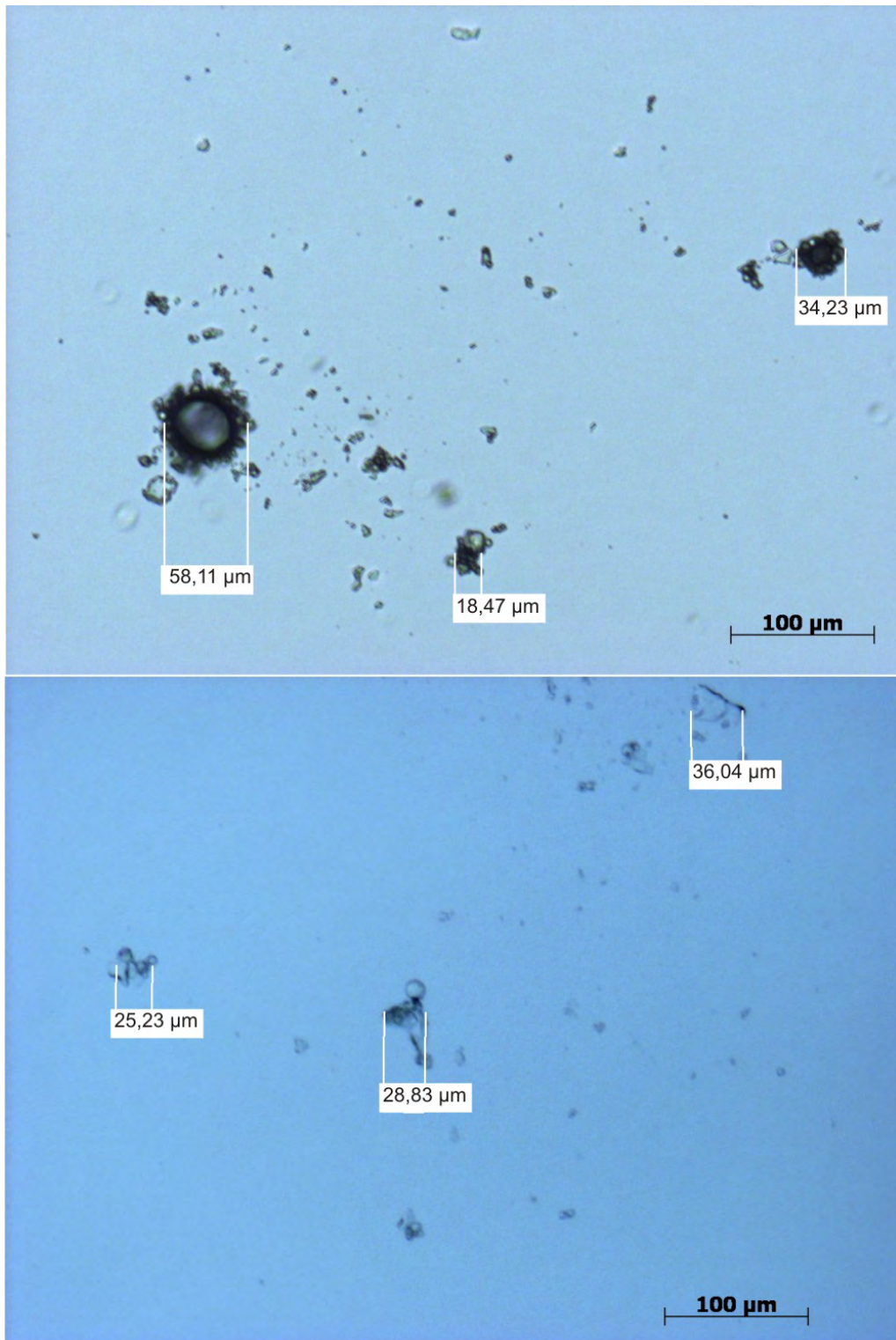
Figure 4.12: *Determine the particle size with a microscope. The predominated particle sizes are from 20 to 50 μm*

4.5   Velocity lag of the natural seeding

As mentioned in the previous section small particles (seeding) are necessary to determine the velocity field in the two-dimensional plane expanded by the PIV laser. The behavior of the seeding is of crucial importance, because PIV measures the velocity of the particles and not of the flow carrying the seeding. Depending on the size and density every particle has a velocity lag. A simple method to estimate the velocity lag of a spherical particle of radius r in a constant acceleration in a laminar flow can be made by using the law of Stokes (see also Raffel et al. [2007]).
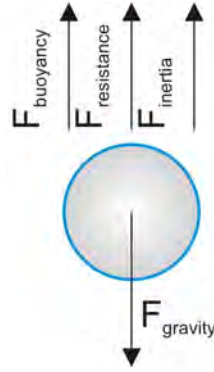
Figure 4.13: *Stokes Law of an accelerating particle in a Newtonian fluid.*

$$F_{gravity} = F_{buoyancy} + F_{resistance} + F_{inertia} \tag{4.2}$$

$$\rho_p \cdot g \cdot \frac{4}{3} \cdot \pi \cdot r^3 = \rho_f \cdot g \cdot \frac{4}{3} \cdot \pi \cdot r^3 + \frac{\rho_f}{2} \cdot \dot{x}^2 \cdot \pi \cdot r^2 \cdot \zeta + \rho_p \cdot \ddot{x} \cdot \frac{4}{3} \cdot \pi \cdot r^3 \tag{4.3}$$

where ρ_p = particle density and ρ_f = fluid density. For laminar flow the loss coefficient can be substituted by $\zeta = \frac{24}{Re} = \frac{12 \cdot \nu}{\dot{x} \cdot r}$ which yields the final ODE of 2nd order:

$$\ddot{x} + \dot{x} \cdot \frac{9 \cdot \rho_f \cdot \nu}{2 \cdot \rho_p \cdot r^2} - \left(1 - \frac{\rho_f}{\rho_p}\right) \cdot g = 0 \tag{4.4}$$

Rewriting Eq. 4.4 with $\ddot{x}$ = a = dV/dt = $\dot{V}$ and $\dot{x}$ = V yields:

$$\dot{V} + A_{const.} \cdot V = S_{const.} \tag{4.5}$$

$$with \ \ A_{const} = \frac{9 \cdot \rho_f \cdot \nu}{2 \cdot \rho_p \cdot r^2} \tag{4.6}$$

$$and \ \ S_{const} = \left(1 - \frac{\rho_f}{\rho_p}\right) \cdot g \tag{4.7}$$

To get the solution for Eq. 4.5 the following approach is used (Bartsch [1999]):

$$V = V_H + V_P \tag{4.8}$$

$$Approach \ for \ V_H : \ V = e^{\lambda \cdot t} \ \ and \ \ \dot{V} = \lambda \cdot e^{\lambda \cdot t} \tag{4.9}$$

Substituting Eq. 4.5 with Eq. 4.9 gives the homogeneous solution:

$$V_H = C_{integration} \cdot e^{-A \cdot t} \tag{4.10}$$

To get the particular solution V_P the approach $V_P = S_{const}/A_{const}$ is used (A and S are constant function and do not dependent on t). The final solution (integration constant $C_{integration} = -S_{const}/A_{const}$ at t=0) is:

$$v = \dot{x} = \frac{2 \cdot \rho_p \cdot r^2}{9 \cdot \rho_f \cdot \nu} \cdot \left(1 - \frac{\rho_f}{\rho_p}\right) \cdot g \cdot \left(1 - e^{-\frac{9 \cdot \rho_f \cdot \nu}{2 \cdot \rho_p \cdot r^2} \cdot t}\right) \tag{4.11}$$

and for $t \mapsto \infty$ the end velocity u_{end} can be written as

$$\dot{x}_{t \mapsto \infty} = u_{end} = \underbrace{\frac{2 \cdot \rho_p \cdot r^2}{9 \cdot \rho_f \cdot \nu}}_{Relaxation\ time:\ \tau_s} \left(1 - \frac{\rho_f}{\rho_p}\right) \cdot g \tag{4.12}$$

Finally, the particle velocity for every time step and applying the definition for the relaxation time τ_s gives:

$$u_p = u_{end} \cdot \left(1 - e^{-\frac{t}{\tau_s}}\right) \tag{4.13}$$

This means that the particle which is initially at rest reaches exponentially the end velocity u_{end}. As can be seen in Eq. 4.12 and Eq. 4.13 the density and diameter of the particle need to be defined. The particle diameter was determined in Section 4.4 with a value of 50 μm (a smaller particle reaches quicker the end velocity). The density could not be measured in the flow and therefore the density ρ_p is varied from 800 to 1200 kg/m^3 in Eq. 4.12 to estimate the velocity lag (only the floating particles in the reservoir with density close to water can be drawn in by the pump, heavier and lighter particles are on the ground or float up to the surface, respectively). In Figure 4.14 the result of the exponential velocity law of Eq. 4.13 is shown. When a particle is dropped in a fluid with a velocity of 1 m/s it needs, depending on the density ρ_p, $\approx 7 \cdot 10^{-4}$ s to reach the end velocity. This result can also be interpreted as having a low pass filter where every frequency which is higher than 1.4 kHz is blocked (generally, turbulent flow has a frequency range from 5 to 50 kHz, taken from Sigloch [2005], p 92). The velocity field of a PIV-measurement is therefore smoother than the real velocity field in the flow because the particles cannot follow frequencies higher than 1.4 kHz.
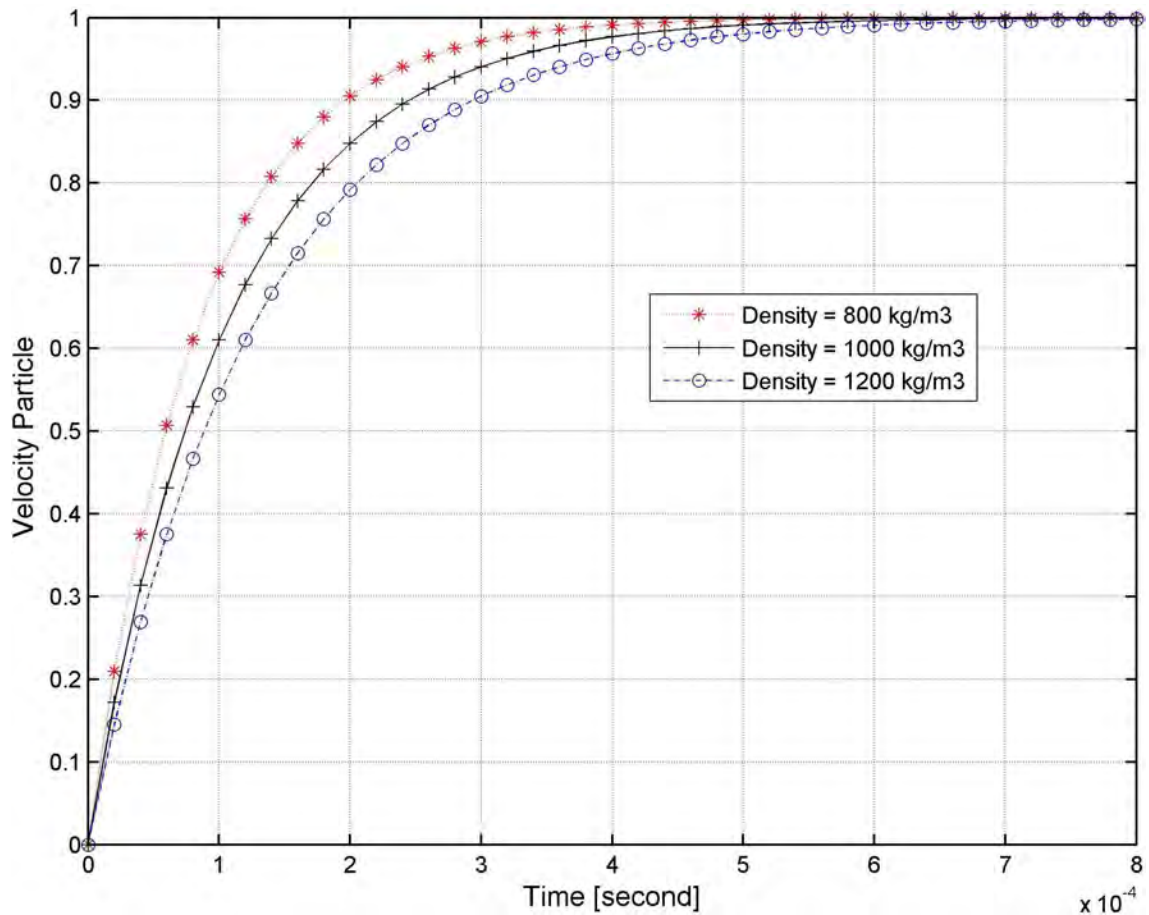
Figure 4.14: *Evaluation of Eq. 4.12 and Eq. 4.13 with* $D_p = 50\ \mu m$ *- Time response of the particle seeding.*

4.6 Minimum detectable velocity

Another error source of PIV is the diffraction due to the optical instruments. If light waves hit on a circular aperture they generate a far field diffraction pattern which is also known as Frauenhofer diffraction. By using the objective lens of the camera the far field pattern will be imaged on the sensor of the camera. The problem is now that a point in the object area (e.g. a scattering particle in a laser light sheet) does not display as a point but as a Frauenhof diffraction on the sensor of the camera (see also Raffel et al. [2007]). An example of a diffraction for a circular aperture is shown in Figure 4.16. The center of the first high intensity circle is called airy-disk. In Figure 4.15 the principle of diffraction due to the behavior of light as an electromagnetic wave is shown. Because of the phase difference Δ in Figure 4.15 interference (superposition of waves) occurs and forms the diffraction pattern on the screen behind the aperture.
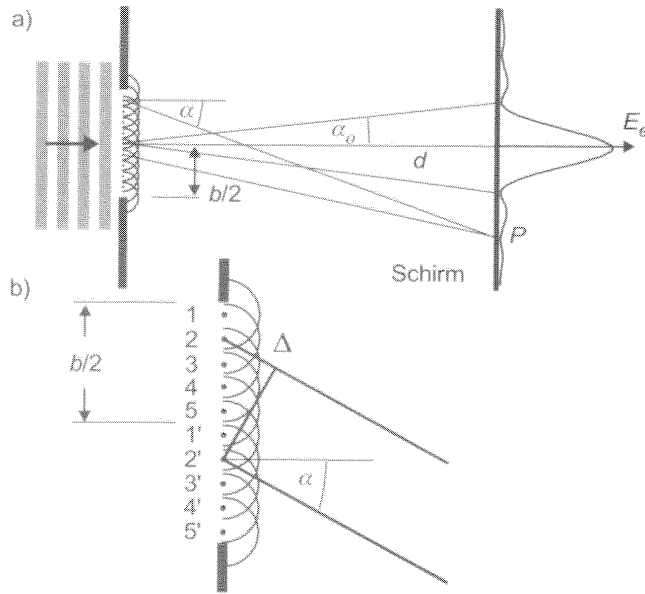
Figure 4.15: *Light is an electromagnetic wave. Due to the interference of waves, for example at a single-slit or circular aperture, diffraction occurs (Kühlke [2007]): a) general scheme, b) detail*
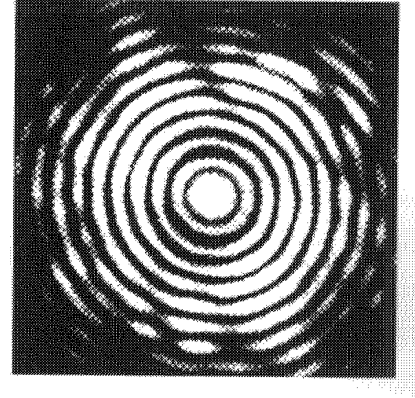
Figure 4.16: *Diffraction for a circular aperture (far-field). The center of high intensity is called Airy-disk. (Kühlke [2007])*

Raffel et al. [2007] define the diffraction-limited minimum image diameter D_{dif} as

$$D_{dif} = 2.44(M + 1) \cdot N \cdot \lambda_{wave} \qquad (4.14)$$

where M is the magnification factor between object and image plane (M=L_{image}/L_{object}=z_0/Z_0, see also Figure 4.17), N the f-number (ratio between the focal length f and the aperture diameter D_a) and λ_{wave} the wavelength.

Using the relationship for the geometrical optic (geometrical optic = wave behavior of light is neglected) the particle diameter D_p can be calculated for the particle diameter D_{geo} in the image plane:

$$D_{geo} = M \cdot D_p \qquad (4.15)$$

Combining Eq. 4.14 and Eq. 4.15 yields the effective particle image diameter D_{eff}:

$$D_{eff} = \sqrt{D_{dif}^2 + D_{geo}^2} \qquad (4.16)$$

With D_{eff} being the smallest detectable distance in the image plane the smallest detectable distance in the object plane can be calculated. Setting $L_{\Delta(image,min)} = D_{eff}$ gives the smallest length $L_{\Delta(object,min)}$:
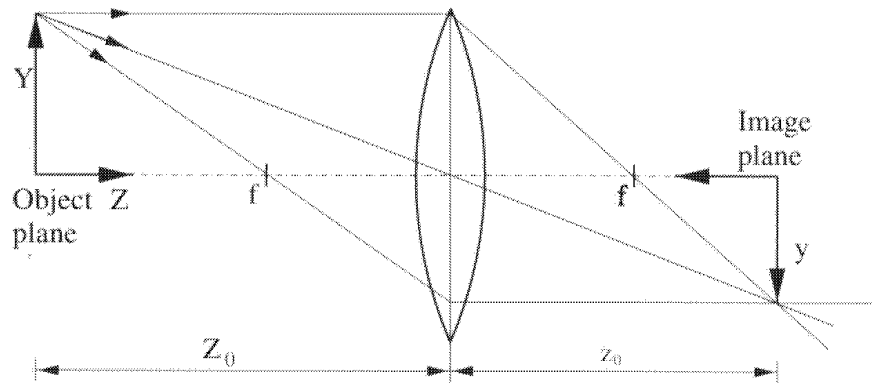
Figure 4.17: *Relationship of image and object plane for the geometrical optic ([Raffel et al. 2007])*

$$L_{\Delta(object,min)} = \frac{1}{M} \cdot D_{eff} \tag{4.17}$$

To estimate the minimum detectable distance and velocity in the hydraulic model test following representative values are chosen:

- M = 1/14.284

- N = 2.8

- D_p = 50 μm

- λ = 527 nm

- time step = 1/1kHz = 0.001 s

The results are:

- D_{diff} = 0.0039 mm

- D_{geo} = 0.0035 mm

- D_{eff} = 0.0052mm.

- $L_{\Delta(object,min)}$ = 0.0748 mm

- V_{min} = 0.0748 m/s

Therefore flow velocities which are smaller than 0.0748 m/s cannot be measured in the hydraulic model test with these input parameters (for boundary layer measurements the input parameters are different and a much smaller minimum velocity can be detected).

4.7 Confidence Interval

In Section 4.3 has been shown the way how to validate velocity vectors for each PIV measurement. With the validated velocity vectors the reliability of the mean and the standard deviation can be estimated. The confidence level is $(1-\alpha_{conf,limit}) = 90\%$. As a probability distribution the Student t-distribution is chosen. The t-distribution is a robust method and can contain more extreme sample values in the distribution than a normal distribution (see Fahrmeir and Pigeot [2007], pp304 and Woisetschläger [2008]). The confidence interval with a t-distribution is:

$$P\left[\overline{u} - t_{1-\alpha_{conf,limit}/2}\left(n-1\right)\frac{STD(u)}{\sqrt{n}},\ \overline{u}+\right.$$
$$\left. + t_{1-\alpha_{conf,limit}/2}\left(n-1\right)\frac{STD(u)}{\sqrt{n}}\right] = 1 - \alpha_{conf,limit} \tag{4.18}$$

where $1 - \alpha_{conf,limit}/2$ is the quantile of a student distribution, n is the validated vector sample size, STD(u) is the standard deviation of the velocity u and $\overline{u}$ is the mean velocity.

A confidence interval for the standard deviation can also be estimated. For that purpose a χ^2 distribution is chosen. The confidence interval for the standard deviation with normal distributed samples gives,

$$\left[\frac{(n-1)\ STD(u)^2}{\chi^2_{1-\alpha_{conf,limit}/2}(n-1)}, \frac{(n-1)\ STD(u)^2}{\chi^2_{\alpha_{conf,limit}/2}(n-1)}\right] \tag{4.19}$$

where $\alpha_{conf,limit}/2$ is the 5% quantile and $1-\alpha_{conf,limit}/2$ is the 95% quantile of a χ^2 distribution.

To demonstrate the influence of the validated sample size n of the velocity vector an example is shown in Figure 4.18 and Figure 4.19 for the reliability of the mean and the standard deviation. Evaluating Eq. 4.18 with a mean value of the velocity of 3 m/s and a Turbulence Intensity $(TU = STD(u)/MEAN(u))$ of 10% and 20%, respectively, gives the reliability of the mean value for n-samples (Figure 4.18). The same considerations are applied for Eq. 4.19; the result of the evaluation of Eq. 4.19 for n-samples are shown in Figure 4.19. As can be seen in Figure 4.18 and Figure 4.19 a high sample size n (≥ 1000) is desirable.
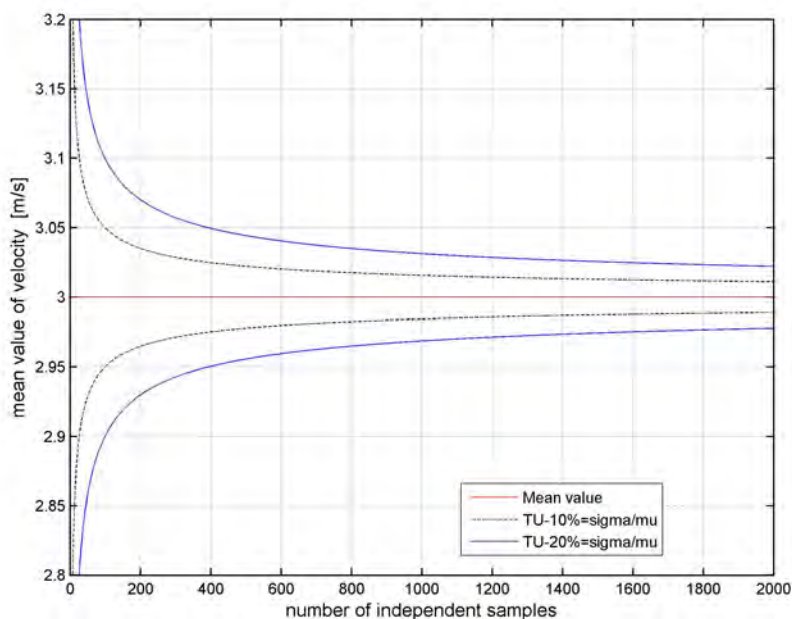
Figure 4.18: *Student distribution - reliability of the mean value*
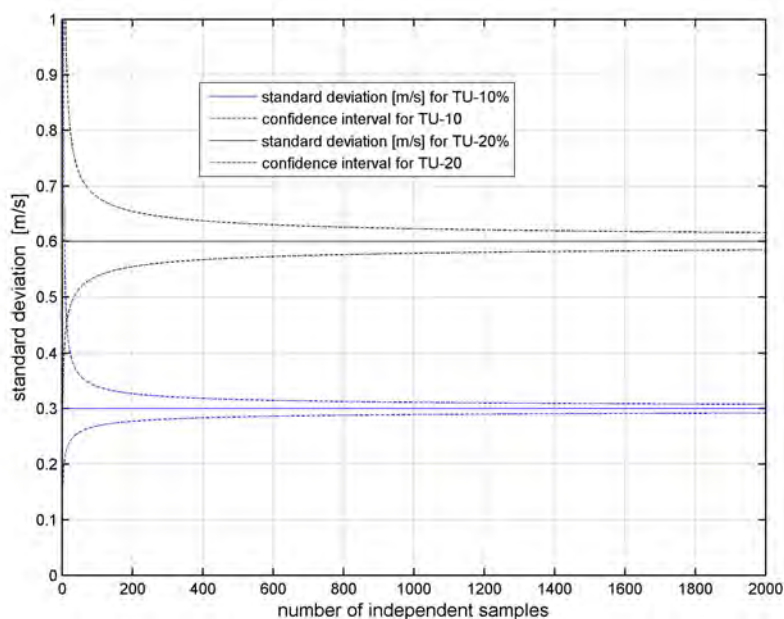
Figure 4.19: χ^2 *distribution - reliability of standard deviation*

The confidence interval is based on a normal distribution for the reliability of the mean and the standard deviation. Figure 4.21 shows a representative histogram of the velocity sample extracted at the red point in the velocity vector field of Figure 4.20 (the vector field to demonstrate the normal distribution of the velocity is located right after the bend, vertical plane). Additionally, a Probability-Probability plot of the velocity distribution is shown in Figure 4.22 which indicates whether the samples are normal distributed, that is, the distribution (blue dots in Figure 4.22) are close to the red line in Figure 4.22 or not. Both plots (Figure 4.21 and Figure 4.22) show that a nearly normal distribution of the velocity samples can be expected. For other PIV measurements in the hydraulic model
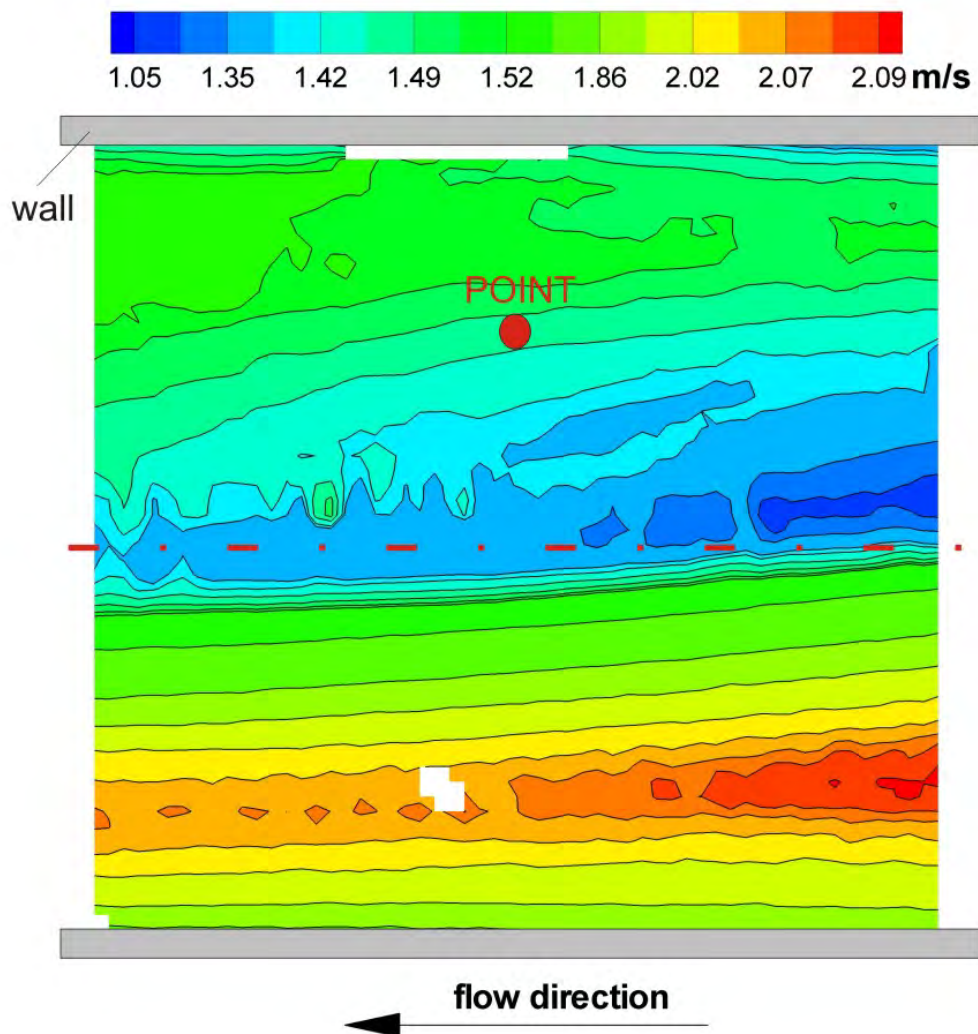
Figure 4.20: *Position for velocity sample for Figure 4.21 and Figure 4.22 (PIV-Box 200, vertical plane, asymmetric discharge rate)*

test the distribution of the velocity sample is always checked with discreet points in the vector field.

4.7.1   Result of the confidence intervals

The results of the confidence interval are shown for the vertical plane right after the bend of the PIV Box B200 (compare also with Figure 4.3 and Figure 4.2 in Section 4.2). For the other two PIV Boxes (B201 and B202L) the results are similar and not shown here.

The confidence interval of the mean value for the velocity of the X and Y components (asymmetrical discharge rate, left branch 80 l/s and right branch 0 l/s) are shown in Figure 4.23 and Figure 4.24. For better appearance the confidence interval of the mean velocities will be plotted logarithmically as a function of the ascended sorted velocity against the confidence interval (see Figure 4.25). In Figure 4.25 it can be seen that the confidence interval of the mean value is between $\approx \pm 0.007$ and ± 0.01 [m/s]. This range can also be found for the other PIV-Boxes.
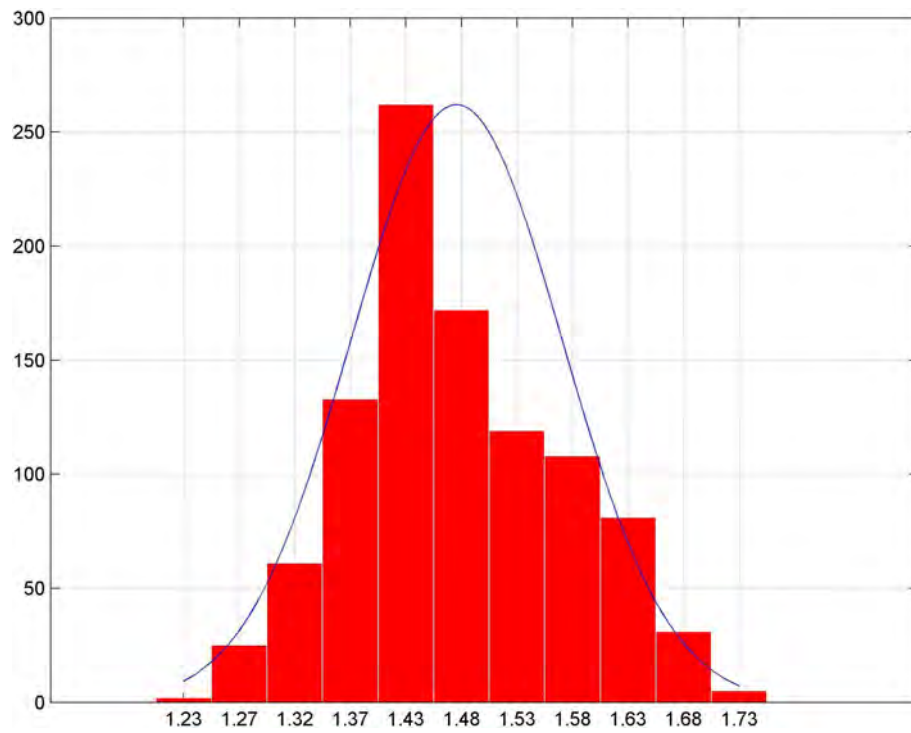
Figure 4.21: *Histogram of the X-Velocity*
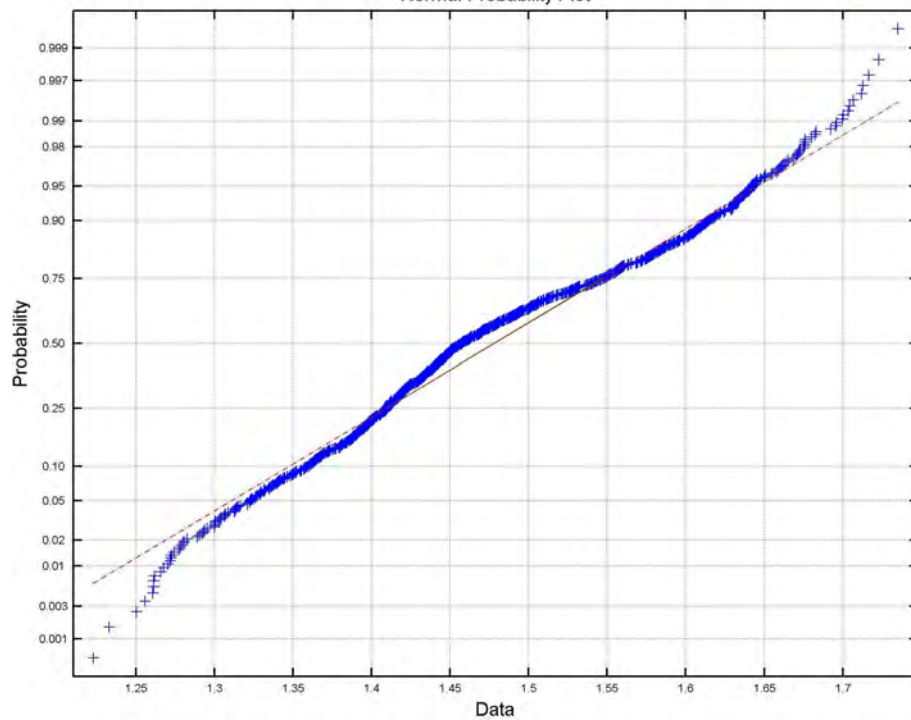
Figure 4.22: *Probability-Probability-Plot (P-P-Plot)*

The confidence interval for the standard deviation can be taken from Figure 4.26 to Figure 4.29. Generally speaking, the lower limit of the standard deviation is ≈ 0.07 and the upper limit 0.23 [m/s]. Again, the confidence interval of the standard deviations for the remaining PIV-Boxes are similar and not shown here.
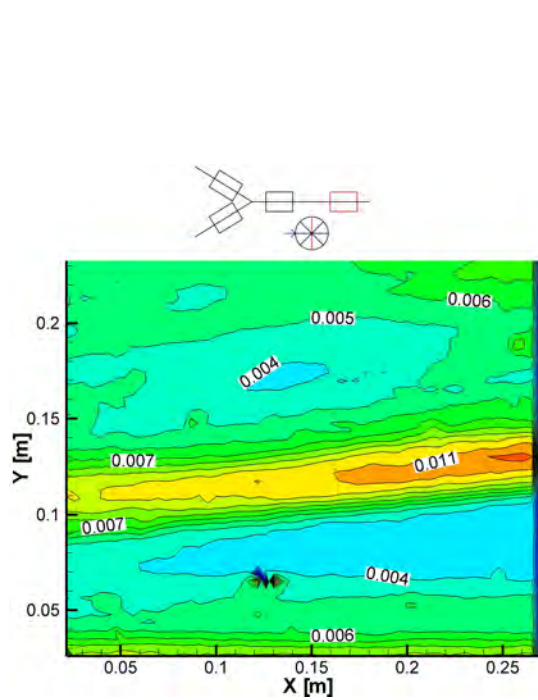
Figure 4.23: *Confidence interval [m/s] for the mean velocity in X-Direction (longitudinal velocity)*
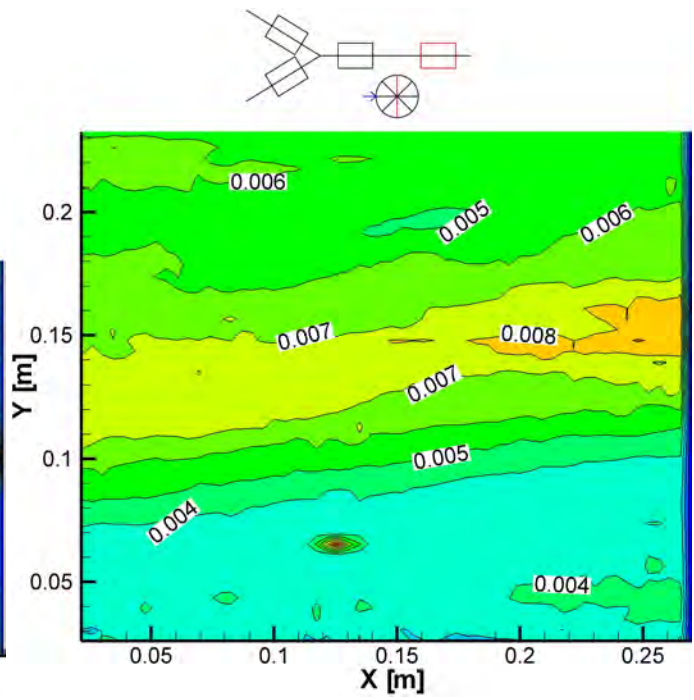
Figure 4.24: *Confidence interval [m/s] for the mean velocity in Y-Direction (lateral velocity)*
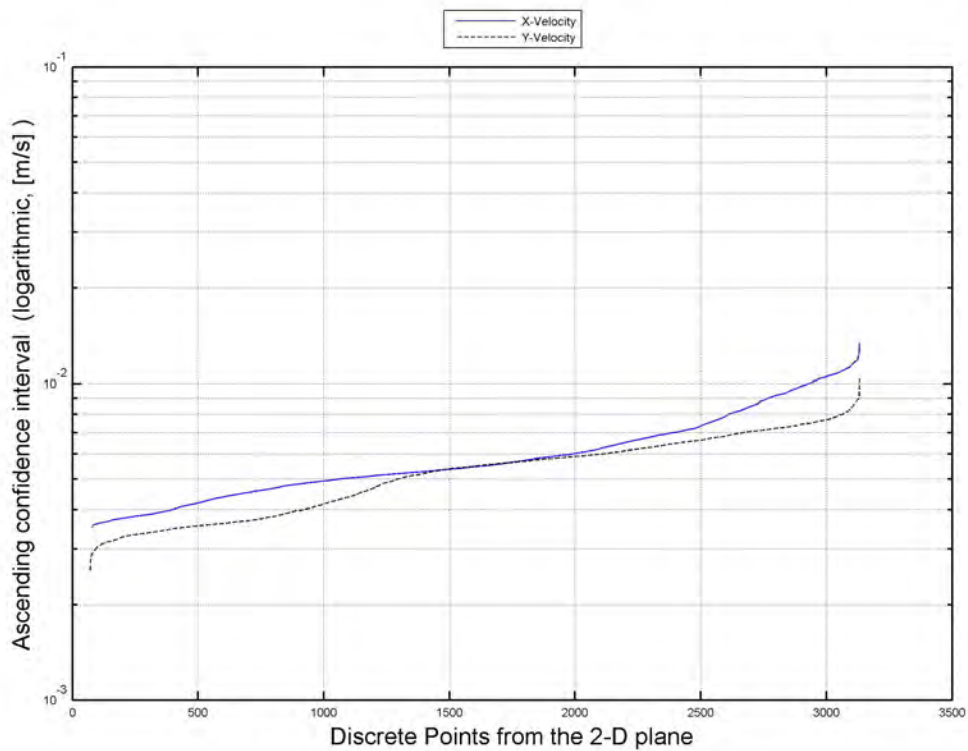
Figure 4.25: *1D-Plot of the confidence interval of the mean velocity: The discrete point velocities of the 2D-Plot (Figure 4.23 and Figure 4.23) are ascended sorted.*
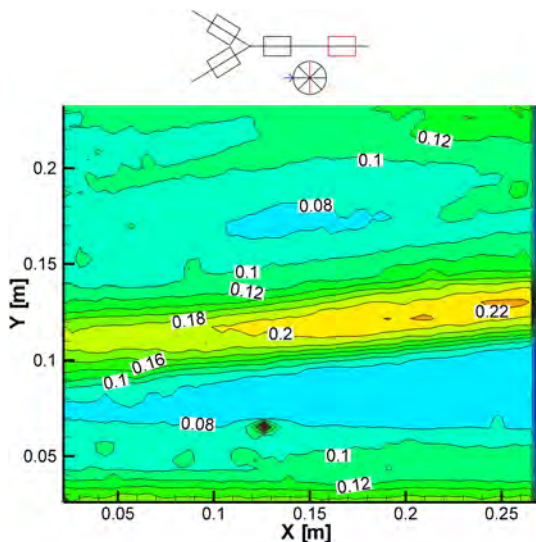
Figure 4.26: *Confidence interval [m/s] for the standard deviation of the velocity in X-Direction (longitudinal velocity), lower limit*
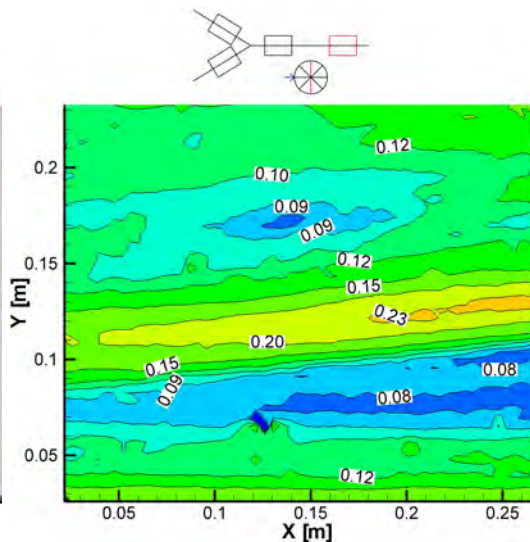
Figure 4.27: *Confidence interval [m/s] for the standard deviation of the velocity in X-Direction (longitudinal velocity), upper limit*
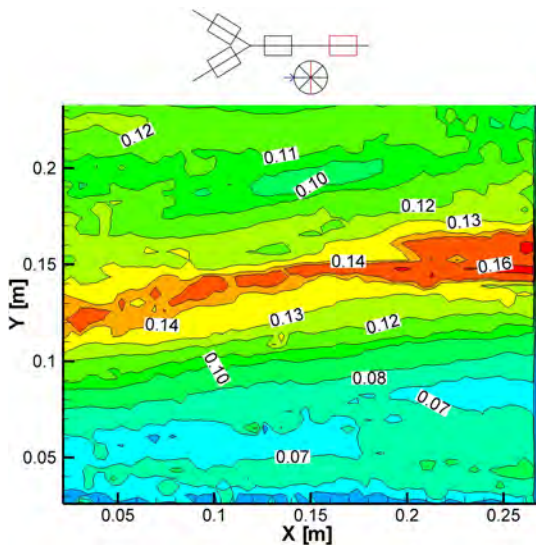
Figure 4.28: *Confidence interval [m/s] for the standard deviation of the velocity in Y-Direction (lateral velocity), lower limit*
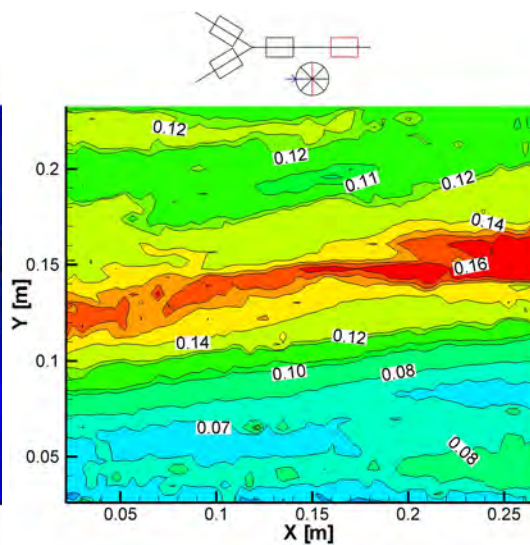
Figure 4.29: *Confidence interval [m/s] for the standard deviation of the velocity in Y-Direction (lateral velocity), upper limit*

4.8 Evaluation of the statistics

After a PIV measurement is carried out abundant data are available for further statistical investigations. The cross correlation applied on each interrogation area gives a 2D vector plot of velocities. With a sample rate between 1 and 5 kHz and the corresponding sample time of 1 second several thousand vector plots (from $t_1 \cdots t_i$) are obtained. Evaluating these plots gives the following statistical output:

With the velocity vector

$$\vec{V} = \begin{pmatrix} u \\ v \end{pmatrix} \tag{4.20}$$

a mean value can be calculated (only shown for the u-component). Thus

$$\overline{u} = \frac{1}{n} \cdot \sum_{i=1}^{n} u_i \tag{4.21}$$

with n as the sample size. Furthermore the variance which is

$$VAR(u) = \overline{u'^2} = \frac{1}{n-1} \cdot \sum_{i=1}^{n} (u_i - \overline{u})^2 \tag{4.22}$$

and the standard deviation

$$STD(u) = \sqrt{\overline{u'^2}} = \sqrt{\frac{1}{n-1} \cdot \sum_{i=1}^{n} (u_i - \overline{u})^2} = \sqrt{VAR(u)} \tag{4.23}$$

can be calculated. The covariance of u' and v' is

$$COV(u,v) = \overline{u'v'} = \frac{1}{n-1} \cdot \sum_{i=1}^{n} (u_i - \overline{u}) \cdot (v_i - \overline{v}) \tag{4.24}$$

and dividing the covariance with the standard deviations gives the correlation coefficient COR(u,v):

$$COR(u,v) = \frac{COV(u,v)}{STD(u) \cdot STD(v)} \quad \{COR(u,v) \in \Re \mid -1 \leq COR(u,v) \leq 1\} \tag{4.25}$$

4.8.1 Turbulence Intensity

Depending on the flow being 1 or 2 dimensional the turbulence intensity is defined as (Bodo [2010]):

$$TU = \frac{\sqrt{\frac{1}{2} \cdot [VAR(u) + VAR(v)]}}{\left|\vec{V}\right|} \tag{4.26}$$

$$TU = \frac{STD(u)}{\overline{v}} \tag{4.27}$$

In the Fluent Manual (ANSYS Fluent [2005]) the turbulence intensity is stated as

$$TU \approx 0.16(Re)^{-\frac{1}{8}} \tag{4.28}$$

which is a good estimation for a fully turbulent pipe flow. Values for TU below 1% are considered as a low turbulent flow whereas values above 10% are considered as a strong turbulent flow (see ANSYS Fluent [2005]).

4.8.2 Kinetic energy of the mean flow

The kinetic energy k_{tot} of the flow can be split into a mean kinetic energy K and the turbulent kinetic energy k (Bodo [2010]):

$$k_{tot} = K + k \tag{4.29}$$

$$K = \frac{1}{2} \cdot \left(\overline{u}^2 + \overline{v}^2\right) \tag{4.30}$$

In comparison to the turbulent kinetic energy k, where all three dimensions have to be considered, K can be defined with only one or two components of the velocity vector.

4.8.3 Turbulent kinetic energy of the flow

The turbulent kinetic energy k is defined as (Bodo [2010]):

$$3D: \quad k = \frac{1}{2} \cdot (VAR(u) + VAR(v) + VAR(w)) \tag{4.31}$$

$$2D: \quad k = \frac{3}{4} \cdot (VAR(u) + VAR(v)) \tag{4.32}$$

When only a 2D-Measurement system is used (e.g. PIV) the third non-measured component will be replaced by half of each of the two known components (see Eq. 4.32). Thus, an isotropic turbulence is assumed ($\overline{u'^2} = \overline{v'^2}$, $\overline{u'v'} = \overline{v'u'} = 0$).

4.8.4 Production of k

The kinetic energy of the mean flow is transferred to the turbulent flow. The term P appears in the transport equation for the mean and turbulent kinetic energy but with opposite sign. For a 3D-flow the production can be written as (Bodo [2010]):

Generally (3D)

$$P = -\overline{u_i' u_j'} \cdot S_{ij} \tag{4.33}$$

$$\tag{4.34}$$

2D:

$$P = -\left(\overline{u'^2}\frac{\partial \overline{u}}{\partial x} + \overline{u'v'}\frac{\partial \overline{v}}{\partial x} + \overline{u'v'}\frac{\partial \overline{u}}{\partial y} + \overline{v'^2}\frac{\partial \overline{v}}{\partial y} \right) \tag{4.35}$$

4.8.5 Turbulent shear stress

The turbulent shear and normal stresses (Reynolds-stress tensor) for a 2D plane is defined as (Bodo [2010]):

$$\tau_{turb} = -\rho \cdot COV(u,v) = -\rho \cdot \overline{u'v'} \tag{4.36}$$

$$\sigma_{x,turb} = -\rho \cdot VAR(u) = -\rho \cdot \overline{u'^2} \tag{4.37}$$

$$\sigma_{y,turb} = -\rho \cdot VAR(v) = -\rho \cdot \overline{v'^2} \tag{4.38}$$

Chapter 5

Hydraulic losses - Loss coefficient ζ

This chapter presents the calculation of the loss coefficient ζ. For that purpose two quantities need to be measured: the differential pressure upstream and downstream of the Y-bifurcator and the discharge rate. For the differential pressure measurement several control sections along the pipe installations are defined. Each control section consists of 8 burr-free and sharp-edged bore holes connected together by a single ring line. The discharge rate is measured by three flow meters for the main and the branching pipes. With the known diameter of the pipe the mean velocity can be calculated.

The loss coefficient ζ is defined as the total head loss Δh_{tot} divided by the kinetic head, excluding any pipe friction. This can be done by defining substitute-cylinders between two control sections and using the Colebrook and Darcy-Weisbach equations to calculate the pipe friction and subtracting it from the measured head loss Δ_{tot}. Before each measuring campaign the pressure probe is calibrated with a water column gauge glass.

The equivalent sand roughness k_s which is needed for the Colebrook-White equation to determine the pipe friction coefficient λ is measured by two different methods. The first method uses the differential pressure loss between several control sections where a linear friction gradient exists. With the known head loss Δh_{tot} the Darcy-Weisbach and the Colebrook-White equations are applied to calculate the equivalent sand roughness k_s. The other method for the k_s calculation is done via Particle Image Velocimetry (PIV). As generally known, close to the wall exists a universal law for the velocity distribution which is also known as the logarithmic law of the wall. With the measured (via PIV) axial velocity u and the corresponding distance y from the wall as well as the equation of the law of the wall for rough pipes the equivalent sand roughness k_s can be calculated. The chosen k_s value for both methods is 0.015 mm.

Due to the bend upstream of the Y-bifurcator secondary flow occurs in the pipe installation. Because of the 1D-consideration for the loss coefficient calculation (ζ) the influence of the secondary flow needs to be taken into account via a velocity correction factor α which is defined as the ratio of the kinetic energy of the axial secondary flow and the kinetic energy defined by the mean velocity. With PIV the kinetic energy of the axial secondary flow can be measured - only the last approximately three millimeters to the wall cannot be resolved with PIV due the reflection of the laser light close to the wall. This problem is solved by closing the velocity profile with a linear function. The influence of the velocity profile with the added linear function to close the gap will be further investigated (Note, the results show that a logarithmic function is not yet necessary). The results show that the influence of this procedure is marginal and the calculated α coefficients can be used for further loss calculations.

The hydraulic model test is scaled after the Reynolds law which implies that the velocity in the model test is the scale-factor times the velocity of the prototype. This yields velocities up to 43 m/s in the model test which are too high for the pumps in the laboratory. To overcome this problem the

head loss Δh as a function of the discharge rate is decomposed into a polynomial function with a quadratic, linear and constant term via the least square method. With the polynomial function the desired head loss with respect to the discharge rate can be calculated. Furthermore, a comparison is carried out whether it is better to use only the quadratic term of the polynomial function to calculate the head loss for higher discharge rates. This assumption is based on previous model tests (cf. Vogel [1926]) where the head loss as a function of the discharge rate is a pure quadratic behavior. The comparison (only the quadratic term of the polynomial function or all three terms) showed better results if only the quadratic term of the least square method is used. This is also checked by a numerical calculation where the desired discharge rate due to the Reynolds model can be set and the resulting head loss are compared with the extrapolated head losses of the model test. The comparison of the CFD-calculations and the hydraulic model test with the extrapolated values shows good agreement.

The last section of this chapter shows an attempt to reduce the loss coefficient ζ with a guide vane apparatus. The guide vane induces a swirling flow upstream of the Y-bifurcator. As a result the loss coefficient can be reduced for one flow distribution.

5.1 Hydraulic equations

5.1.1 Friction loss

Darcy and Weisbach derived an equation for the loss coefficient λ for a straight pipe and steady state flow (Preissler and Bollrich [1985]).
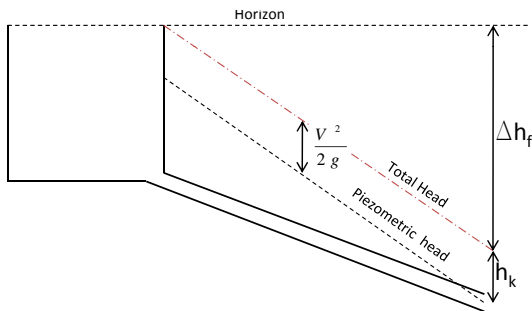
Figure 5.1: *Head loss Δh_f for a gravitational driven pipe flow*
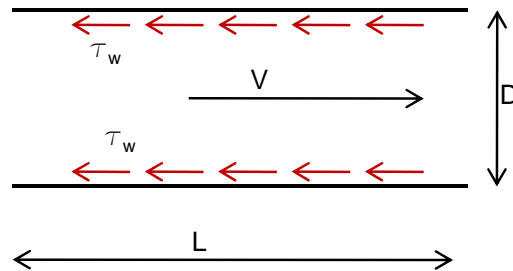
Figure 5.2: *Friction loss along the wall*

The friction energy loss E_f due to the pipe friction for the length L is defined as (cf. Figure 5.1 and Figure 5.2):

$$E_f = \Delta h_f \cdot m \cdot g = \Delta h_f \cdot \rho \cdot L \cdot \frac{\pi \cdot D^2}{4} \cdot g \tag{5.1}$$

where m stands for mass, D for pipe diameter, ρ for density and Δh_f for friction loss. Eq. 5.1 is also equivalent to the loss of potential energy between two cross sections. The friction energy loss E_f can also be derived from Figure 5.2 with an additional assumption (experiments showed that this assumption, especially for strong turbulent flows, is valid):

$$\tau_w \sim V^2 \tag{5.2}$$

To get a shear stress with the units $\frac{N}{m^2}$ one needs to multiple the right side of Eq. 5.2 with ρ and a constant factor $\frac{\lambda}{8}$. Eq. 5.2 then yields:

$$\tau_w = \frac{\lambda}{8} \cdot \rho \cdot V^2 \qquad (5.3)$$

The friction force for Eq. 5.3 yields:

$$F_f = \tau_w \cdot A = \frac{\lambda}{8} \cdot \rho \cdot V^2 \cdot D \cdot \pi \cdot L \qquad (5.4)$$

and the friction energy along the stretch of length L is then

$$E_f = F_f \cdot L = \frac{\lambda}{8} \cdot \rho \cdot V^2 \cdot D \cdot \pi \cdot L^2 \qquad (5.5)$$

If Eq. 5.1 and Eq. 5.5 are combined to

$$\Delta h_f \cdot \rho \cdot L \cdot \frac{\pi \cdot D^2}{4} \cdot g = \frac{\lambda}{8} \cdot \rho \cdot V^2 \cdot D \cdot \pi \cdot L^2 \qquad (5.6)$$

and after some rearrangement one gets the Darcy and Weisbach equation:

$$\Delta h_f = \lambda \cdot \frac{L}{D} \cdot \frac{V^2}{2 \cdot g} \qquad (5.7)$$

Depending on the flow condition (laminar or turbulent) λ can either be calculated exactly for laminar flow or from experimentally determined relationships for turbulent flow. In case of the hydraulic model test only turbulent flow is predominant. The factor λ is called the friction coefficient.

5.1.2 Friction coefficient λ

Based on the work of Colebrook [1938] a semi-empirical equation can be derived for the friction coefficient λ. Generally λ depends on the Reynolds Number (Re) and the relative roughness of the pipe k$_s$/D with k_s as the equivalent sand roughness. This can also be shown in Figure 5.3 where three areas can be distinguished:

1. Hydraulic smooth: $\lambda(Re)$

2. Transition: $\lambda(Re, k_s/D)$

3. Hydraulic rough: $\lambda(k_s/D)$

Colebrook developed one single equation for all three areas. This equation is used to calculate the friction coefficient λ:

$$\frac{1}{\sqrt{\lambda}} = -2.0 \cdot lg \left(\frac{2.51}{Re \cdot \sqrt{\lambda}} + \frac{k_s/D}{3.71} \right) \qquad (5.8)$$

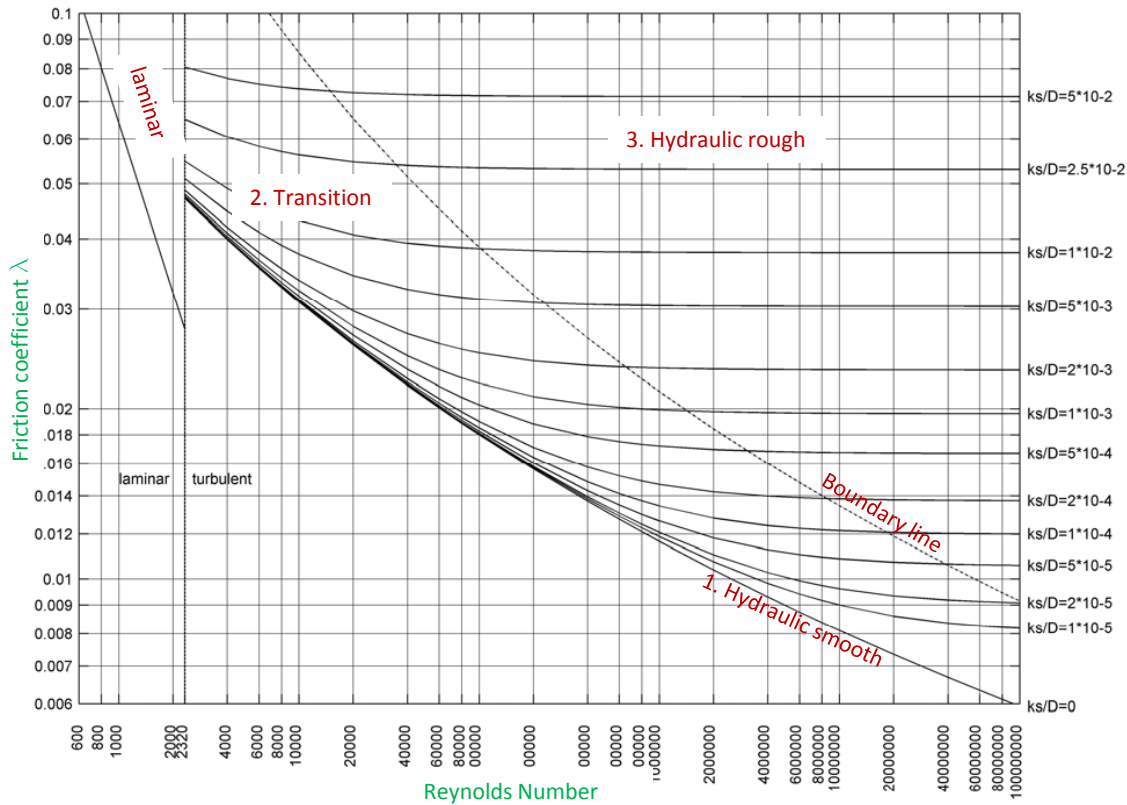with $Re = D \cdot V/\nu$ as the Reynolds number.

Figure 5.3: *Diagram of Moody*

5.1.3 Definition of the local loss coefficient ζ

Figure 5.4 shows the definition of the loss coefficient ζ. The difference between a pipe with no installed component and the very same pipe with an installed component is defined as

$$\zeta = \frac{\Delta h_{local}}{\frac{V^2}{2g}} \tag{5.9}$$

The position for the Δh_{local} measurement is always between the redeveloped friction gradients (upstream and downstream of the component).

In Figure 5.4 a redeveloping friction gradient can be seen which needs a certain distance downstream of the component. This makes sure that no secondary flow exists in the cross sections where the energy budget will be balanced for further calculation. With this definition the loss coefficient calculation can be based on a 1D-consideration.

The necessary distance to get a redeveloped friction gradient in a pipe after a disturbance can be estimated by Idelchik [1994] (cf. with Figure 5.5):

$$\frac{L_{st}}{D} = 7.88 \cdot log(Re) - 4.35 \tag{5.10}$$

whereas L_{st} is the developing length and Re is the Reynolds number.

As mentioned in previous sections the hydraulic model test consists of a bend before the Y-bifurcator. The length between the Y-bifurcator and the bend is 4.23 m. Applying Eq. 5.10 with the maximum velocity in the main branch of V = 4.4 m/s, a diameter of D = 0.246 m and a kinematic viscosity of $1 \cdot 10^{-6}$ m/s^2 yields a developing length of $L_{st} = \approx 10.6$ m. Therefore, due to
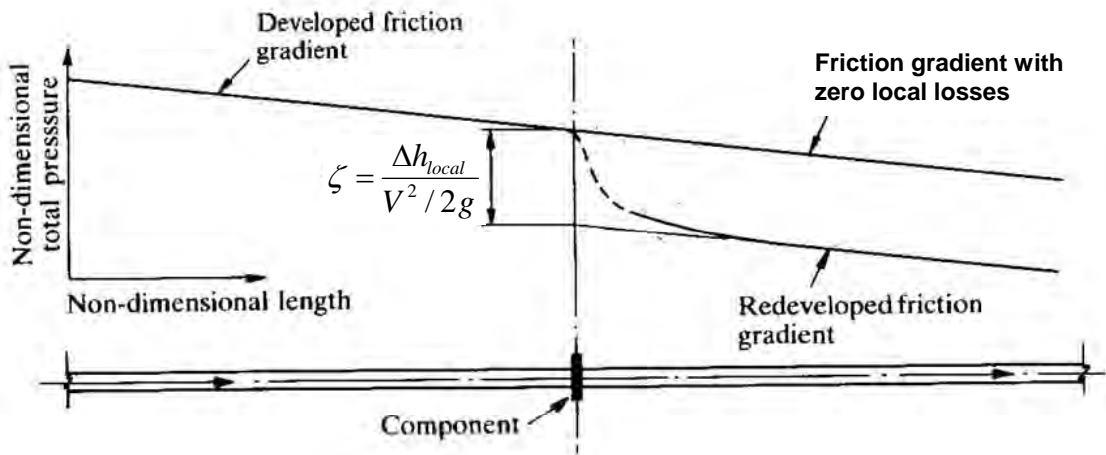
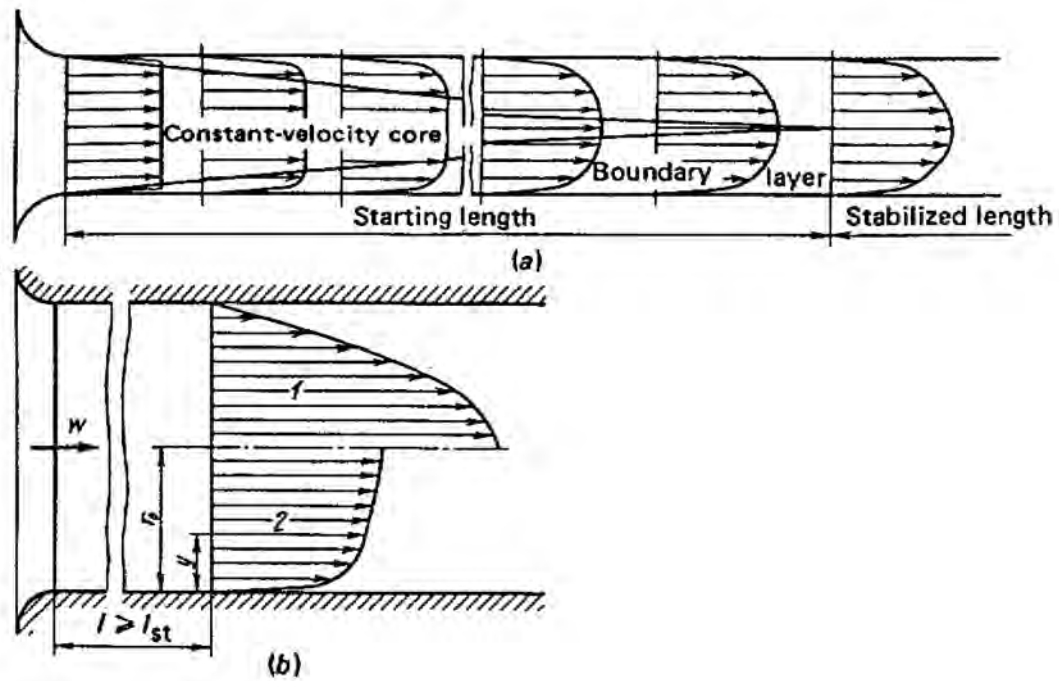**Figure 5.4:** *Definition according to Miller [1990]*

Figure 5.5: *Developing length L_{st} for turbulent flow (Idelchik [1994])*

the too short developing length of the hydraulic model test the secondary flow has to be taken into account by means of PIV and the resulting velocity correction factor α.

5.1.4 Energy budget between two control sections for 1D consideration

As is general known the energy budget between two control sections consist of the following energy terms (frictionless)

$$E_{tot} = \underbrace{m\, g\, z}_{Potential\ energy} + \underbrace{m\, \frac{P}{\rho}}_{Pressure\ energy} + \underbrace{m\, \frac{V^2}{2}}_{Kinetic\ energy} \tag{5.11}$$

Eq. 5.11 has the unit of energy [Nm]; if on divides Eq. 5.11 by $(m\ g)$ the well known Bernoulli equation is obtained in terms of heights:

$$\frac{E_{tot}}{m\ g} = \underbrace{z}_{Height} + \underbrace{\frac{P}{g\,\rho}}_{Piezometer\ head\ h} + \underbrace{\frac{V^2}{2g}}_{Kinetichead\ h_k} \tag{5.12}$$

Due to hydraulic losses the total head is not a horizontal line but a a slope as shown in Figure 5.6. Generally, for the hydraulic model test the following form of the Bernoulli equation is used for a horizontal pipe (including hydraulic losses):

$$h_1 + \alpha_1 \cdot h_{k,1} = h_2 + \alpha_2 \cdot h_{k,2} + \Delta h_{tot} \tag{5.13}$$

Since the differential pressure is measured between two control sections the resulting piezometer head is $\Delta h = h_1 - h_2$ and introducing the variable $\Delta K = \alpha_1 \cdot h_{k,1} - \alpha_2 \cdot h_{k,2}$ one can rewrite Eq. 5.13:

$$\Delta h_{tot} = \Delta h + \Delta K \tag{5.14}$$

whereas

- Δh_{tot} is the total head differential

- h_k is the kinetic head

- Δh is the piezometer head differential

- ΔK is the kinetic head differential

- α is the velocity correction factor (shown later in Section 5.3 at Page 89)

The total head differential Δh_{tot} can also be defined as:

$$\Delta h_{tot} = \Delta h_{local} + \Delta h_f \tag{5.15}$$
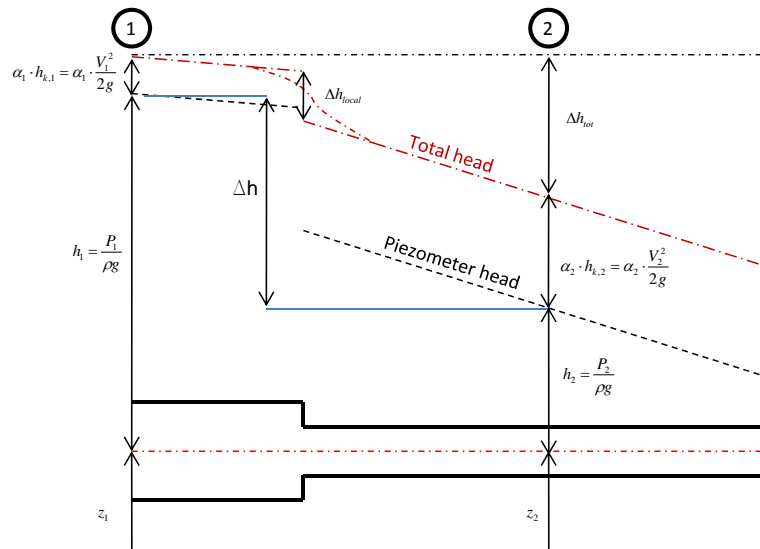
Figure 5.6: *Energy budget between cross section 1 and 2*

whereas Δh_f is the hydraulic losses due to pipe friction and Δh_{local} are the losses due to built-in components. The friction loss Δh_f can be calculated by using the Colebrook equation as given by Eq. 5.8 and the Darcy Weisbach equation given by Eq. 5.7. To have the ability to use Eq. 5.8 one needs to define substitute cylinders with a certain diameter D and length L as shown in Figure 5.7 and Table 5.1. The chosen diameters and lengths represent as close as possible the pipe friction in the hydraulic model test (Note, the loss coefficient for the prototype, derived from the model test, can only be used when the plexiglass friction of the model is subtracted).

Table 5.1: *Lengths and diameters for the substitution cylinders*

No. in Figure 5.7	Diameter	Lenght
-	mm	mm
Z 1	246	415
Z 2	262	140
Z 3	185	234
Z 4	172	543
Z 5	123	1272

Finally, with the known pipe frictions Δh_f, the measured piezometer differential Δh, the measured kinetic head differential (via flow meter) ΔK and combining equation Eq. 5.14 and Eq. 5.15 one can calculate Δh_{local}. To get the hydraulic losses in dimensionless form Δh_{local} is divided by the kinetic head of the main pipe in the hydraulic model test which is

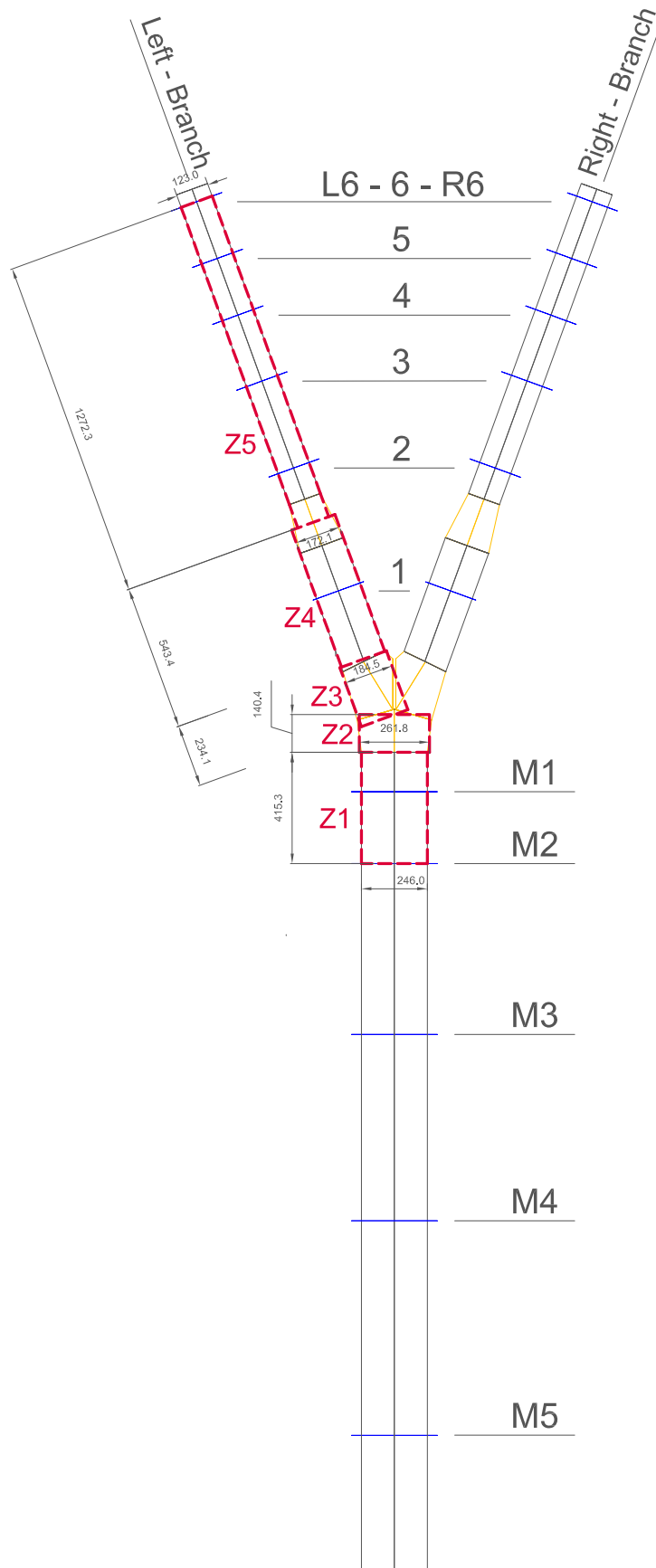$$\zeta = \frac{\Delta h_{local}}{\frac{V_{main\ pipe}^2}{2g}} \tag{5.16}$$

Figure 5.7: *Substitution cylinders in the hydraulic model test to calculate Δh_f - Load Case Generating (Units [mm])*

5.2 Determination of the pipe roughness

As explained in the previous sections it is essential to determine the pipe friction Δh_f as exactly as possible to calculate the local head loss Δh_{local}. The main parameter for the roughness is the equivalent sand roughness k_s in the Colebrook equation (Eq. 5.8). Normally, k_s =0.0015 mm for plexiglass, but due to the built-in component like flange, bore-holes, etc. the roughness increases. Two independent ways will be shown in the next two sections for the calculation of the actual roughness in the hydraulic model test.

5.2.1 Roughness - Pressure differential measurement

In flow regions where the pressure gradient is a linear function it is possible to determine the equivalent sand roughness k_s. In Figure 5.8 two possible positions for the calculation of the roughness k_s are shown: between the bifurcator and the bend and downstream of the bifurcator.
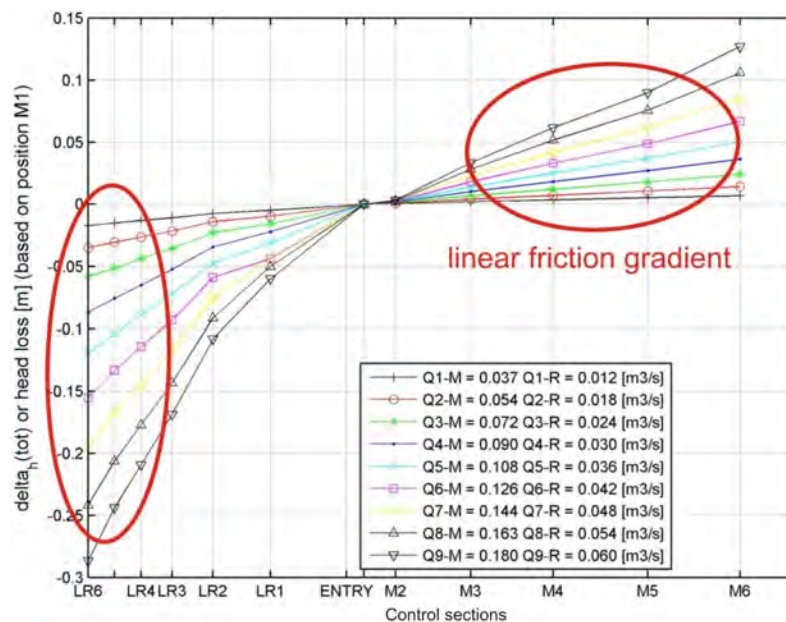

Figure 5.8: *Example for the roughness calculation. The right branch is shown for an asymmetrical flow distribution. The discharge rate starts from 37 ℓ/s up to 180 ℓ/s for the main branch (in the legend M stands for Main branch and R for the right branch)*

With the known friction loss Δh_f from Figure 5.8, velocity V (via flow meter) and the geometry (L and D) the Darcy-Weisbach equation (Eq. 5.7) can be used to calculate the friction coefficient λ. Eventually, the Colebrook equation (Eq. 5.8) is applied to determine the equivalent sand roughness k_s. This procedure is repeated for all other of the measurements and is summarized in Figure 5.9. The equivalent sand roughness k_s reaches asymptotically the value of 0.019 and 0.01 mm, respectively. If one takes a closer look of the roughness of the *main pipe* and the *branching pipes* it can be seen that k_s has an asymptotical characteristic which, at first glance, is inconsistent with the Moody-diagram (see Figure 5.3) where k_s is a constant value.

The reason for that is that every measurement - also those with slow velocities and thus a viscous sublayer which is bigger as the actual roughness peaks - are evaluated. For higher velocities (this is from the transition region up to the hydraulic rough area as shown for example in Figure 5.22) the roughness peaks have a significant influence and tend to a single constant value.
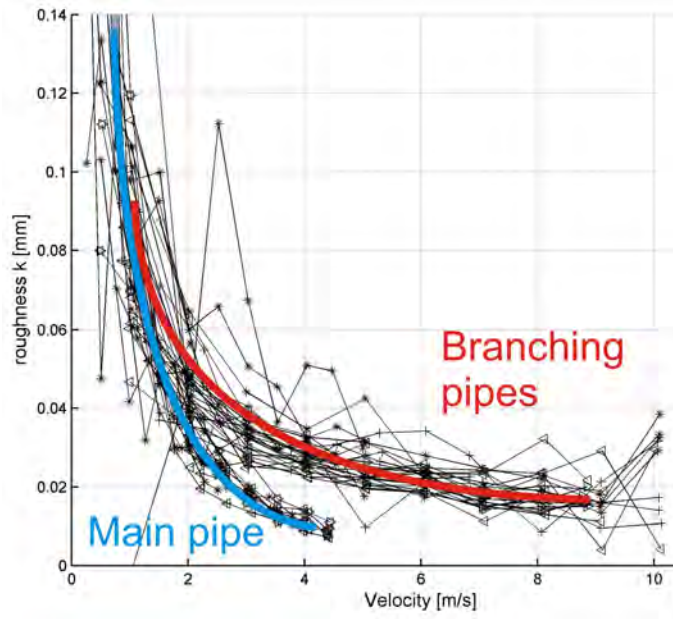
Figure 5.9: *Evaluation of Darcy Weisbach and Colebrook equation: The branching pipe reaches asymptotically the roughness of 0.019 and the main pipe 0.008 mm.*

5.2.2 Roughness - Particle Image Velocimetry

The other method to estimate the equivalent sand roughness is the use of the logarithmic law of the wall by von Kármán [1930]. The shear stress near to the wall is:

$$\tau(y) = \left(\mu + \rho \cdot \ell_m^2 \cdot \left| \frac{d\overline{u}}{dy} \right| \right) \frac{d\overline{u}}{dy} \tag{5.17}$$

whereas $\ell_m^2 \cdot \left| \frac{d\overline{u}}{dy} \right| = \nu_t$ is the eddy viscosity based on the mixing length ℓ_m of Prandtl [1925], μ is the dynamic viscosity, $\frac{d\overline{u}}{dy}$ the velocity gradient and ρ the density. Close to the wall the turbulent fluctuations decay to zero and thus ℓ_m=0. Eq. 5.17 evolves then to the shear stress for the viscous sublayer after integrating and normalizing by the shear velocity u_τ

$$u_\tau = \sqrt{\frac{\tau_w}{\rho}} \tag{5.18}$$

and also includes the effect that close to the wall $\tau(y) = \tau_w$ (see Herwig [2006],p228 and Figure 5.10) gives

$$u^+ = y^+ \tag{5.19}$$

whereas

$$u^+ = \frac{\overline{u}}{u_\tau} \tag{5.20}$$

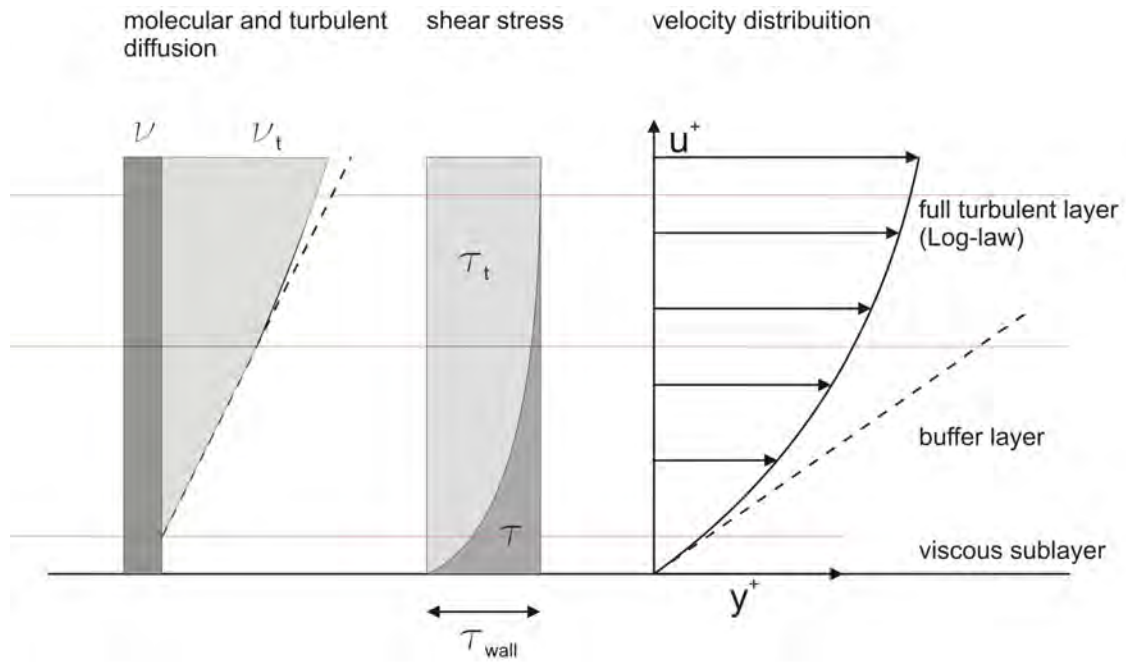$$y^+ = \frac{u_\tau \cdot y}{\nu} \tag{5.21}$$

Figure 5.10: *Turbulent and molecular diffusion, shear stress close to the wall and the corresponding velocity gradient (Herwig [2006])*

Further away from the wall the viscose forces decay ($\nu \cdot \ll \cdot \nu_\tau$) and the turbulence gets stronger and stronger. With the experimental data from von Kármán [1930] where the mixing length $\ell_m = \kappa \cdot y$ (close to the wall) Eq. 5.17 evolves to the logarithmic law of the wall (after normalizing the equation again with the friction velocity u_τ and integrating it):

$$u^+ = C + \frac{1}{\kappa} \cdot \ln y^+ \tag{5.22}$$

$$u^+ = C + 5.75 \cdot \log y^+ \tag{5.23}$$

whereas $\kappa = 0.41$ is the von Kármán-Constant and C is an integration constant which is determined experimentally from Figure 5.11 whereas C is the intersection point of the ordinate.

The final form of the logarithmic law of the wall for a **smooth wall** is then:

$$u^+ = 5.5 + 5.75 \log y^+ \tag{5.24}$$

For a **rough wall** the function $y^+ = \frac{y \cdot u_\tau}{\mu}$ is normalized by the sand roughness k_s yielding:

$$u^+ = 8.5 + 5.75 \log \frac{y}{k_s} \tag{5.25}$$

From PIV-results close to the wall (discrete wall distance y_i and the corresponding axial velocity u_i) the sand roughness can be calculated from Eq. 5.25 and Eq. 5.18, which is valid between $20 \leq y^+ \leq 300$ (see ANSYS Fluent [2005]):

$$\frac{u_i}{5.75 \cdot \log \frac{y_i}{k_s} + 8.5} = \frac{u_{i+1}}{5.75 \cdot \log \frac{y_{i+1}}{k_s} + 8.5} \tag{5.26}$$
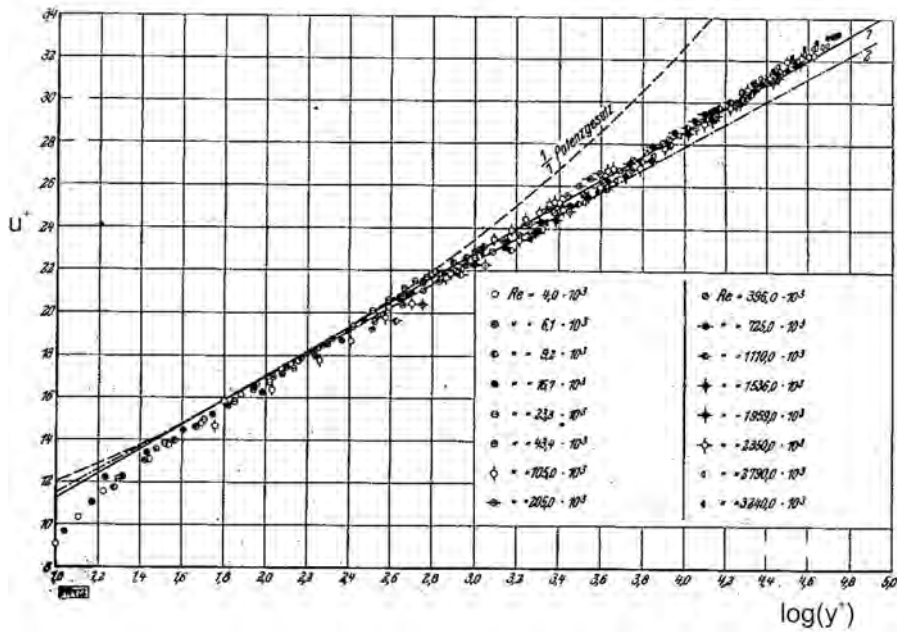
Figure 5.11: *Experimental results of Nikuradse [1932] of the logarithmic law of the wall*
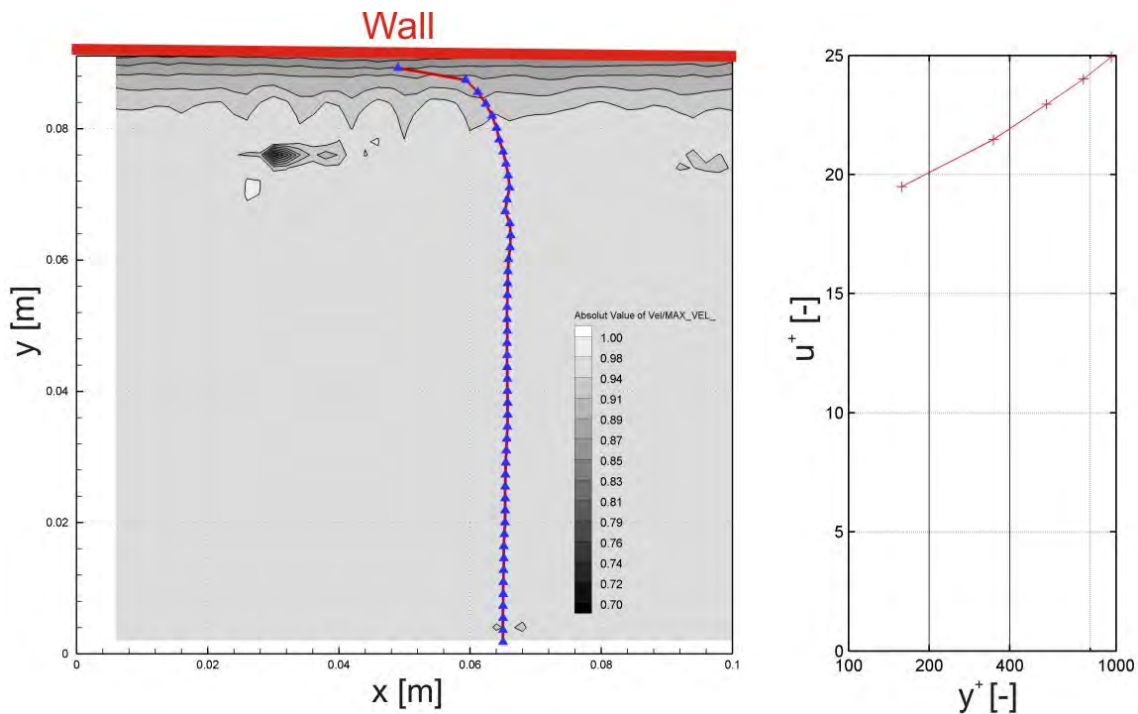

Figure 5.12: *Left: Velocity profile (blue line) and contour plot close to the wall at Position PIV-BOX: B201 (main pipe) in Figure 4.3. Right: Evaluation of Eq. 5.26 and normalizing with u_τ. Q = 160 l/s, D = 0.246 m, V = 3.36 m/s and Re = $8.3 \cdot 10^5$*

The first point of the function F(y^+, u^+) in Figure 5.12 is still in the valid logarithmic range (20 $\leq y^+ \leq$ 300) and therefore the following quantities can be calculated for the main pipe:

1. k_s = 0.0187 mm

2. u_τ = 0.103 m/s

3. τ_w = 10.67 N/m^2

The resulting roughness is in acceptable agreement with the results of the roughness due to pressure differential measurements with 0.019 (branching pipe) and 0.01 (main pipe) mm, respectively. The roughness for the whole plexiglass installation will be set to **0.015 mm**. The calculated values for u_τ and τ_w of the pipe flow can be double checked with Sigloch [2005], p144 (cp. also with Figure 5.12):

$$u_\tau \approx 0.2 \cdot Re^{-0.125} \cdot V \approx 0.12 m/s \qquad (5.27)$$

The distance (in [mm]) for the first point in Figure 5.12-right by using Eq. 5.21 with the values u_τ = 0.103 m/s, y^+ = 157 and $\nu = 1 \cdot 10^{-6}$ m^2/s gives 1.5 mm (cf. also with Figure 5.13). The distance where the logarithmic law of the wall is not valid anymore would be at $y^+ >$ 300 which is 2.9 mm or 2.4 % of the pipe radius.
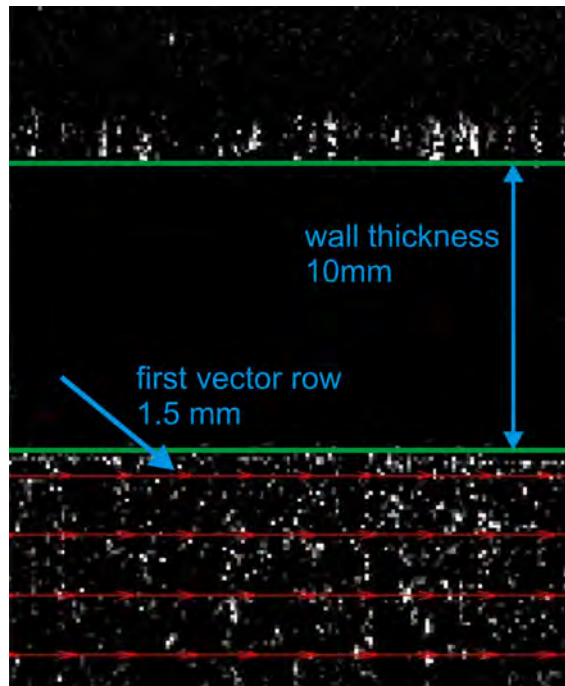

Figure 5.13: *Distance between the first row of vectors and the wall of a PIV*

5.3 Determination of the velocity correction factor α

Due to the bend upstream of the Y-bifurcator and the short pipe between the bend and the Y-bifurcator (18 · D) a weak secondary flow is still presented. The simple 1D-consideration of the

Bernoulli equation is not valid anymore and a velocity correction factor α is introduced to quantify the secondary flow with PIV. The α factor in this theses deals only with the secondary flow of the axial velocity and any weak spiral flow within the cross section cannot be measured with PIV having only one camera (although with a second camera it would be possible). With the known α factor the Bernoulli equation for 1D-flow can again be used.

The definition of the α factor is (Preissler [1973]):

$$\alpha = \frac{E_{k,real}}{E_{k,theoretical}} \tag{5.28}$$

whereas $E_{k,real}$ is the real kinetic energy of a control section calculated with the axial velocity u which is

$$dE_{k,real} = dm \cdot \frac{u^2}{2} = \frac{\rho \cdot dt}{2} \cdot u_A^3 \cdot dA \tag{5.29}$$

and $E_{k,theoretical}$ is the theoretical energy of the control section calculated with the mean axial velocity V which is:

$$dE_{k,theoretical} = \frac{\rho \cdot dt}{2} \cdot V^3 \cdot A \tag{5.30}$$

Substituting Eq. 5.28 with Eq. 5.29 and Eq. 5.30 gives

$$\alpha = \frac{1}{V^3 \cdot A} \cdot \int^A u_A^3 \cdot dA \tag{5.31}$$

Eq. 5.31 is the general form of the velocity correction factor α. With PIV measurements 2D velocity profiles can be measured as shown in Figure 5.14 for the vertical plan.

For each PIV-Box four planes are used to calculate the velocity correction factor α (cf. with Figure 4.3 and Figure 4.2). To evaluate Eq. 5.31 for a 2D velocity profile following modification needs to be done:

$$\alpha = \frac{1}{V^3 \cdot A} \cdot \int_{-R}^{R} \cdot u(y)^3 \cdot \pi \cdot y \cdot dy \tag{5.32}$$

with

- $V = \overline{u}$ (mean velocity)

- A = cross section area

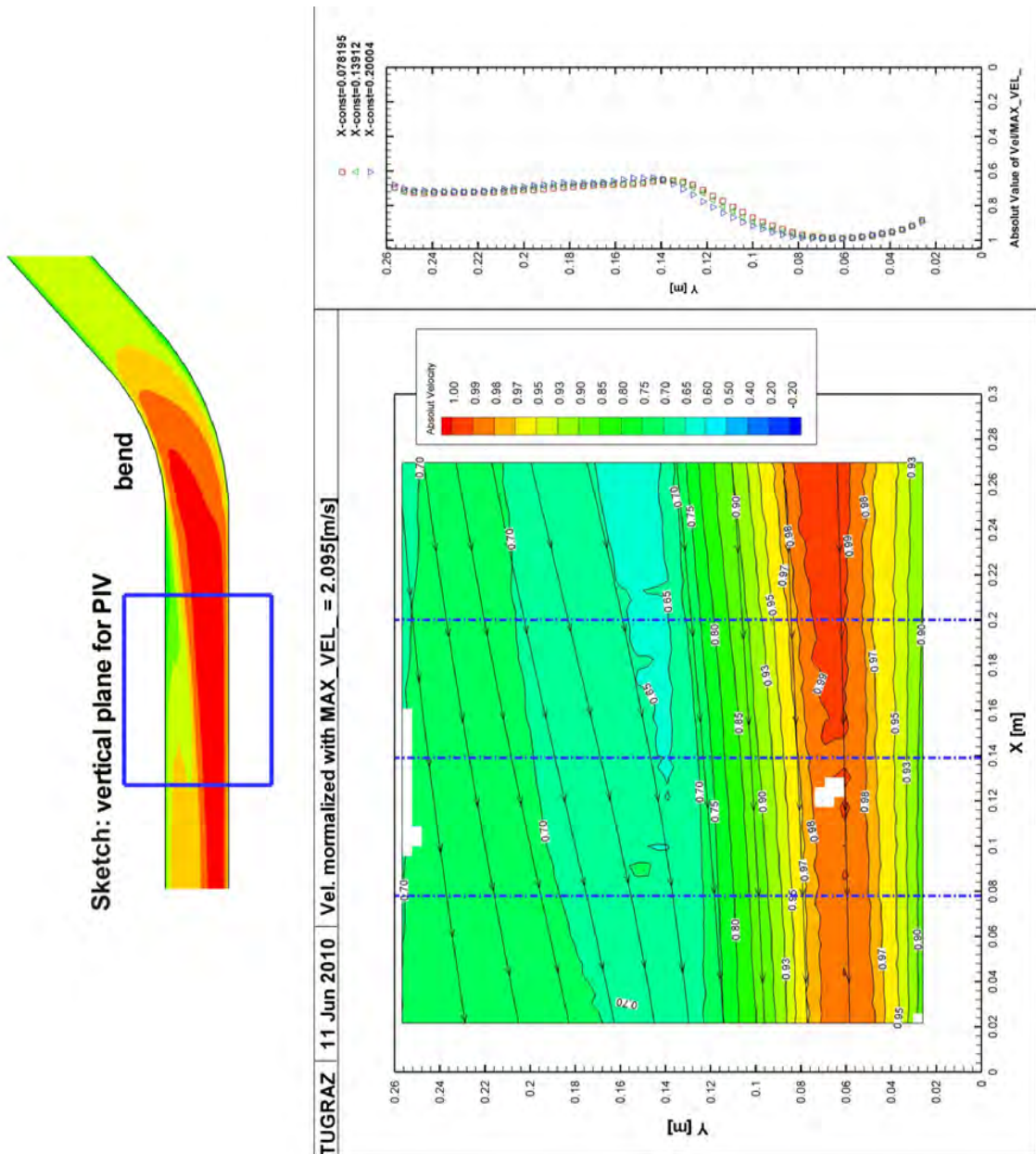- and u = axial velocity as function of the distance y

Figure 5.14: *Example of a PIV measurement right after the bend - vertical plane. Discharge rate 80 ℓ/s. The three dashed lines show the position of the velocity plot on the left side.*

The α factor for a velocity profile in a pipe flow can now be calculated. Before the results are shown two further comments are necessary: (1) Due to the reflecting laser light on the surface of the plexiglass installation the last $\approx$ 3 mm from the boundary cannot be resolved with PIV. Therefore a linear function is used to close the gap in the profile. Also, (2) the mean value of the four investigation planes are used to describe the behavior of the three-dimensional velocity profile. To check the accuracy of the calculated α factors as mentioned in (1) and (2), a 2D-plane from the numerical solution is chosen as can be seen in Figure 5.15 and Figure 5.16.
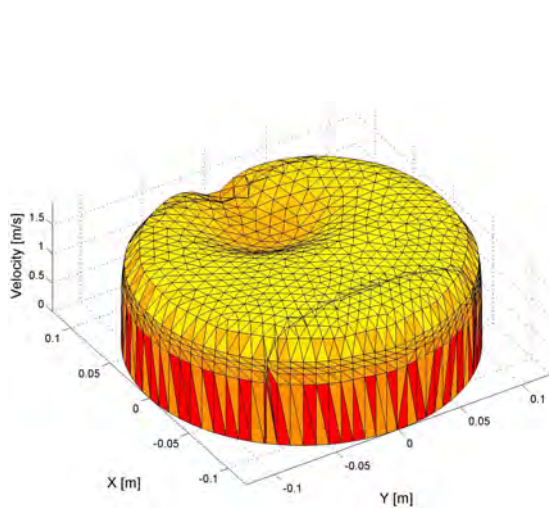

Figure 5.15: *Cross section cut from the numerical simulation: The secondary flow due to the bend can clearly be seen.*
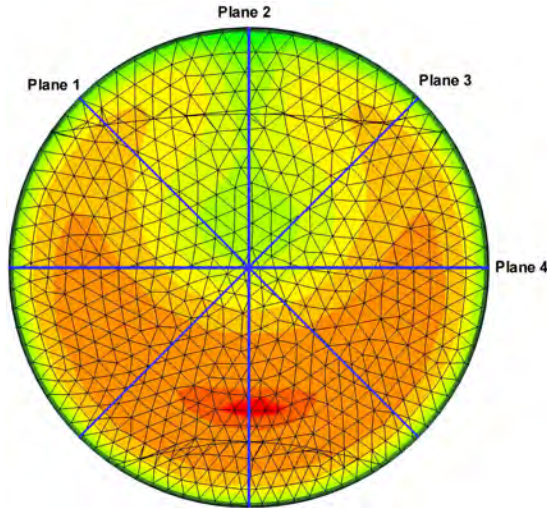
Figure 5.16: *At the exact same position as in the PIV-measurements 4 profile plots are extracted from the numerical simulation to calculate the α factor.*

As already mentioned above, the last part of the velocity profile, which cannot be resolved with PIV, will be closed with a linear function. To see the influence of this procedure the velocities of Figure 5.15 will be replaced with the logarithmic velocity profile from Schlichting and Gersten [1997] (taken from Sigloch [2005], p138):

$$\frac{V_{max} - u(r)}{u_\tau} = -\frac{1}{\kappa} \cdot \left[\ln \left(1 - \sqrt{\frac{r}{R}} \right) + \sqrt{\frac{r}{R}} \right] \tag{5.33}$$

where u_τ is the friction velocity (see Eq. 5.27), $\kappa = 0.41$ the von Kármán-Constant , R=0.123 m the radius and r the variable radius from r=0 to r=R.

The influence for the linear instead of the logarithmic term is shown in Figure 5.19. As can be seen more and more of the logarithmic function will be replaced with a linear function up to the theoretical condition of a conical velocity profile (see also Figure 5.17 and Figure 5.18). The resulting α factor is the ordinate in Figure 5.19 and the percentage of the replacement of the logarithmic/linear function is the abscissa (0% means no replacement; 100 % means all of the logarithmic function is replaced by a linear function). For better illustration the absolute position for the transition of the logarithmic/linear function is also plotted in Figure 5.19 on the right side.

The results of the α factors from Figure 5.19 show the strong influence of the replacement of the linear term close to the wall. If one takes the α factor 1.024 (at Clipping in percentage = 0! in Figure 5.19) as the assumed true value (according to Schlichting and Gersten [1997]) the α factor yields already a value of 1.162 at a clipping percentage of 10%. Fortunately, the PIV-measurements nearly reach the wall and only the last 3 mm are missing which corresponds to a 2.4 % of the radius (see Figure 5.20). This gives a α factor of 1.044 which is only about 2 % larger
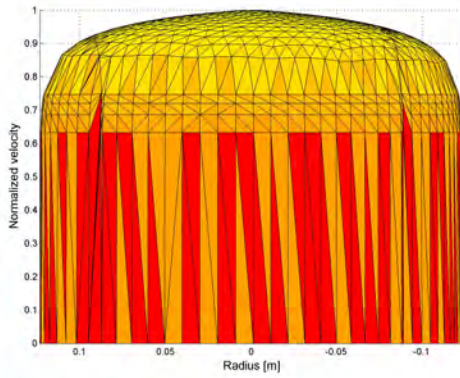
Figure 5.17: *Logarithmic velocity profile for Re = $1.1 \cdot 10^6$ without any linear term*
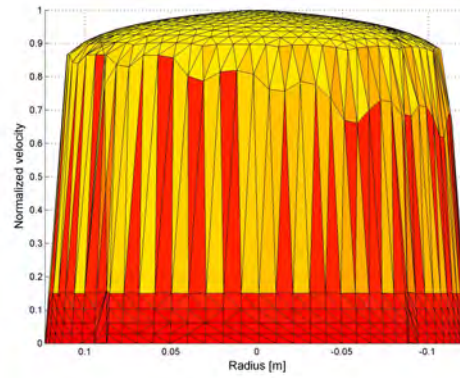

Figure 5.18: *Logarithmic velocity profile for Re = $1.1 \cdot 10^6$ with a linear term for the last 10% of radius R.*

than the assumed true value with 1.024. The final conclusion is that the error which is introduced by filling up the last 3 mm of the velocity profile with a linear term is small and can be neglected. This investigation is also carried out for smaller pipes downstream of the Y-bifurcator and similar results are obtained. Note, that the gap could also be closed with a logarithmic function but in this measurement series the gaps had been small enough and the influence are negligible.

The second questioned which needs to be answered is the quality of the mean value for the four profiles. As can be seen in Figure 5.16 four planes from the PIV - measurements are used to calculate the α factor of the 3D-velocity distribution of Figure 5.15. With the 3D-velocity profile from the numerical simulation and using Eq. 5.31 the real α factor can be calculated. Also, with velocity profiles extracted from the 3D-velocity distribution in Figure 5.16 (blue lines), the α factor can be calculated from Eq. 5.32 and compared with the result of the 3D-velocity distribution. Table 5.2 shows the results of the comparison: For the 3D velocity distribution the factor is 1.043 and for the mean value of α of the very same 3D velocity distribution is 1.042 which is only about 0.1 % percent lower. This investigation is also carried out for smaller pipes downstream of the Y-bifurcator and similar results are obtained.

Table 5.2: *Comparison of the α factor of the 3D-velocity distribution and the extracted four velocity profiles of the numerical calculation*

3D-Velocity Profile	Plane 1 - diagonal left	Plane 2 - vertical	Plane 3 - diagonal right	Plane 4 - horizontal	Mean of Plane 1 to 4
-	-	-	-	-	-
1.043	1.026	1.098	1.026	1.018	1.042

The final results for all α factors are presented in Figure 5.21: The α factor right after the bend amounts to 1.06, shortly before the Y-bifurcator to 1.037 and downstream of the Y-bifurcator to 1.030 for asymmetrical discharge rate (for symmetrical discharge rate similar results are obtained). These values are used for the calculation of the loss coefficient ζ.
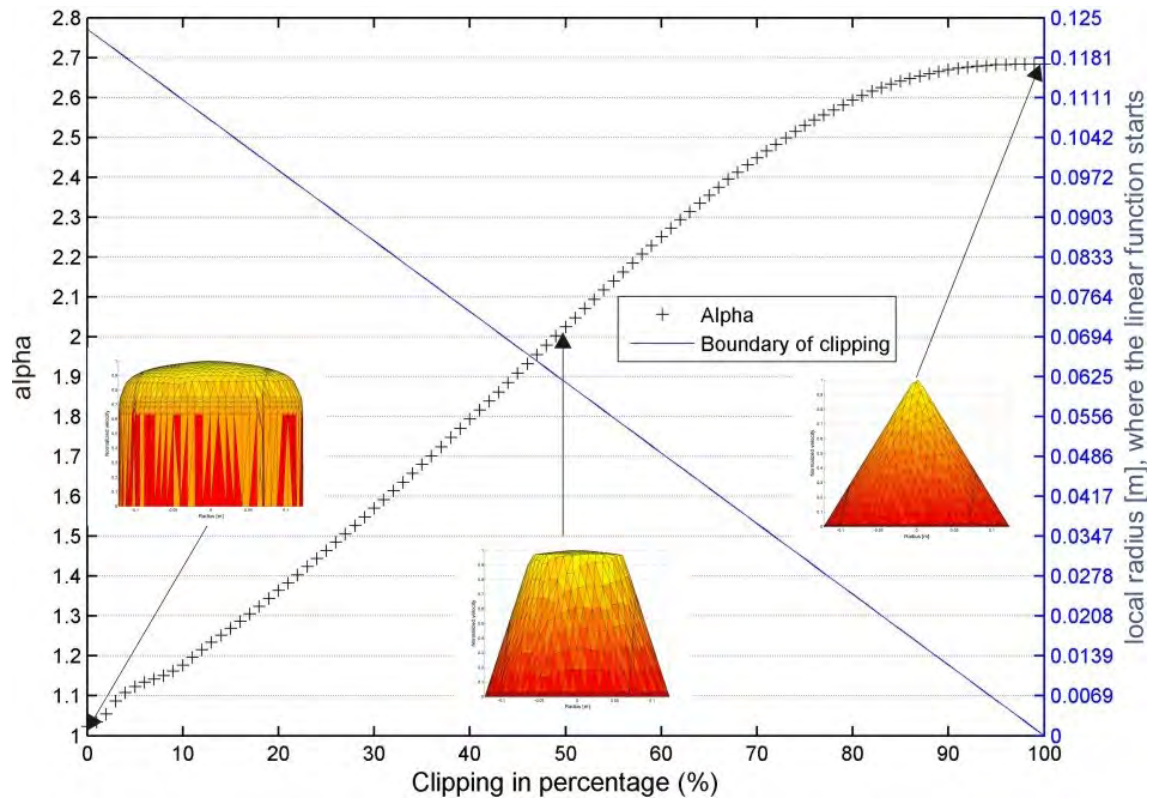
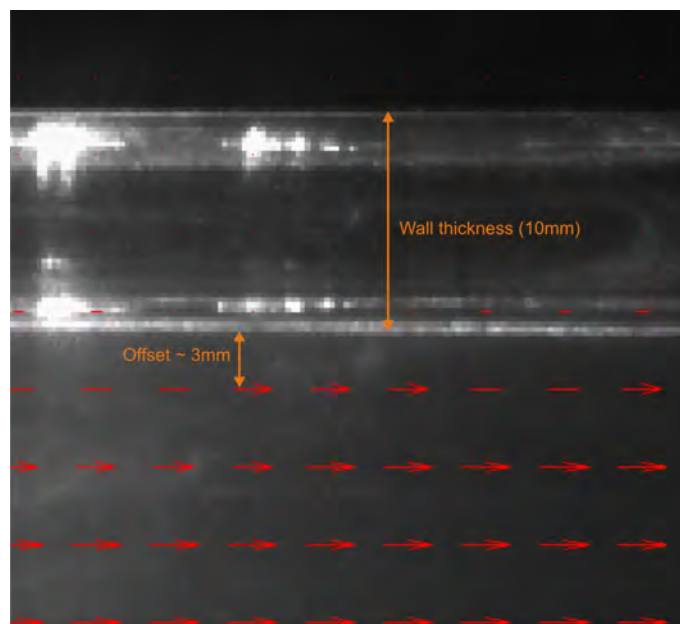**Figure 5.19:** *Result of α factors as function of the percentage of the linear replacement.*

Figure 5.20: *Close-up view of the velocity profile for the pipe diameter of 0.246 m: The last 3 mm or 2.4 % of the radius cannot be measured with PIV.*
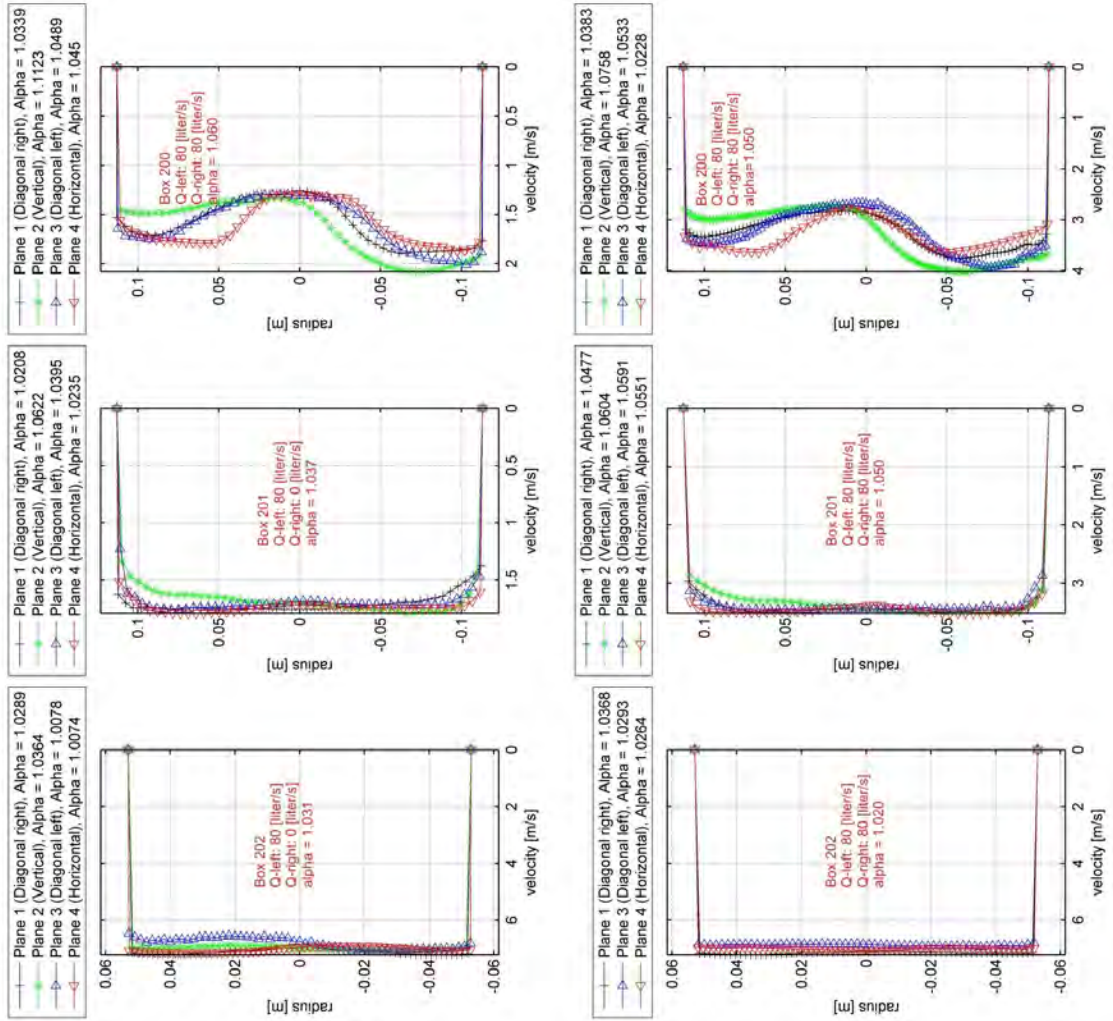
Figure 5.21: *Result of α-factors for the three PIV-Boxes and planes*

5.4 Extrapolation method for the loss coefficient ζ

In Section 5.1 at Page 78 the hydraulic equations for the loss coefficient ζ have been presented. Unfortunately, due to the law of Reynolds the velocity in the hydraulic model test V_{mo} must be larger than the prototype velocity V_{pr} by the scaling factor of the model. The highest resulting velocity V_m in the hydraulic model test would be 46.58 m/s which is impossible to achieve. Nevertheless, there exists a way to obtain the loss coefficient ζ for the prototype: If the hydraulic losses for the prototype are in the hydraulic rough area (see also Figure 5.3) than it is satisfying when the losses for the hydraulic model test are also in the hydraulic rough area (Kobus [1984], p237). This implies that the Reynolds number must at least reach the beginning of the hydraulic rough area. If this is not possible the discharge rate as function to the hydraulic losses need to be extrapolated into the hydraulic rough are (see Figure 5.22).
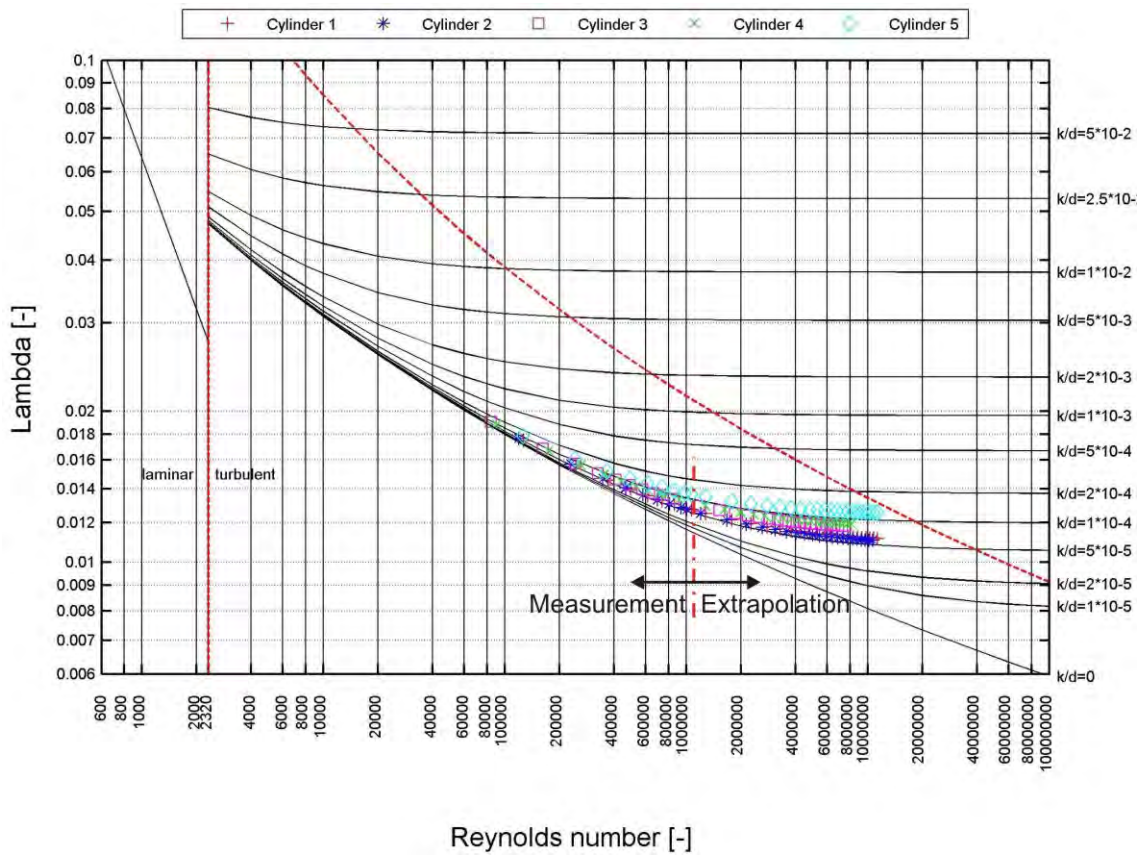

Figure 5.22: *Applying the Darcy and Weisbach equation for the substitution cylinders with different Reynolds numbers. The measured local losses Δh_{local} (not shown in the figure) need to be extrapolated (see Figure 5.7)*

The extrapolation method is based on the method of least squares assuming that the best-fit curve is the curve that has the minimal sum of the deviations squared from a set of measured data. Thus one can write (Bartsch [1999], p572):

$$\Pi = \sum_{i=1}^{n} [y_i - f(x_i)]^2 \qquad (5.34)$$

For the best fit curve f(x) a polynomial of second order will be used:

$$\Pi = \sum_{i=1}^{n} \left[y_i - (a + b \cdot x_i + c \cdot x_i^2) \right]^2 \tag{5.35}$$

Eq. 5.35 needs to be partially differentiated with respect to ∂a, ∂b and ∂c. This gives three linear equations which can be solved for the unknown coefficients a, b and c. An example for the extrapolation method for symmetrical discharge rate is shown in Figure 5.23 and Figure 5.24; the head losses and the corresponding loss coefficient ζ are measured for the highest possible discharge rate in the hydraulic model test, beyond that, the values will be extrapolated into the hydraulic rough are where the loss coefficient ζ is independent of the Reynolds number (the loss coefficient is normalized with ζ_{max} due to data protection).

As already mentioned by Vogel [1926] the discharge rate as function of the head loss is a pure quadratic relationship (the quadratic behavior can also be seen in Figure 5.24). It is therefore obvious to conduct the extrapolation method only with the quadratic term in Eq. 5.35. The resulting coefficients a and b of the least square method will be set to zero and only the coefficient c is used. The difference between using only the term c for the quadratic function and omitting the a (constant function) and b (linear function) coefficients or using all three coefficients is shown in Figure 5.25 and Figure 5.26. Figure 5.25 presents the results of the loss coefficient ζ in the hydraulic rough area for several control sections. These control sections are M1-L3/R3, M3-L3/R3, M4-L4/R4, M5-L5/R5 and M6-L6/R6 (cf. with Figure 3.8). The definitions for the load cases are in Table 3.1. For a flow without any secondary flow the loss coefficient (excluding pipe friction) should collapse to a single curve in Figure 5.25 and Figure 5.26. Obviously, this is not the case for Figure 5.25 where for Load case 1-left and Load case 2-left stronger deviations occur - especially for those control sections (M5-L5/R5 and M6-L6/R6) which are close to the bend with its strong secondary flow. The comparison clearly shows that omitting the linear and constant coefficients of the least square method yields better results.

Another way to check the accuracy of the extrapolation method is done by using a CFD calculation (for the details of the numerical simulation see Chapter 6 at Page 105). With the necessary model discharge rates (e.g. load case 4 = Q_{main}/L_r = 18/8.13=2.2 m^3/s, see also Table 3.1) the resulting total head loss differential (without secondary flow) between extrapolation method and CFD calculation [in %] depicts the following behavior as shown in Figure 5.27 and Figure 5.28 (the absolute values cannot be shown; data protection at the request of HYDRO - Andritz, the founder of the project). The difference for the control section M1-L/R3, M3-L/R3 and M4-L/R4 are lower (5%) than for control section M5-L/R5 and M6-L/R6 in Figure 5.27. The possible reason for this behavior is shown in Figure 5.29 where a strong secondary flow occurs right after the bend for control section M5 and M6. Again, if only the quadratic term is used of the least square method the results for the total head loss differential get much better as can be seen in Figure 5.28.
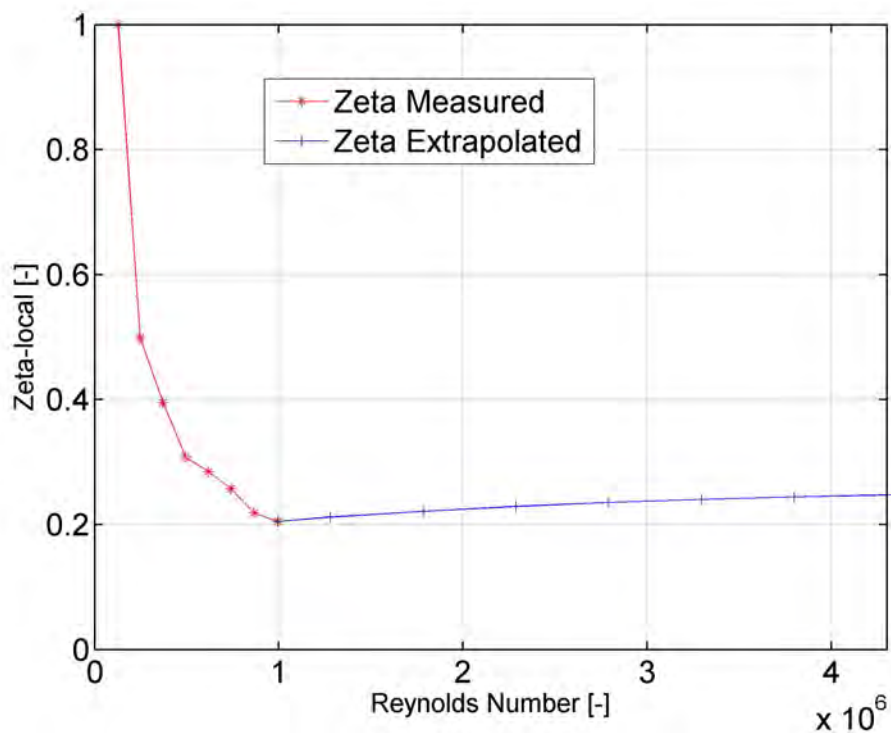
Figure 5.23: *Extrapolation of the function(Re,ζ), normalized with max(ζ)*
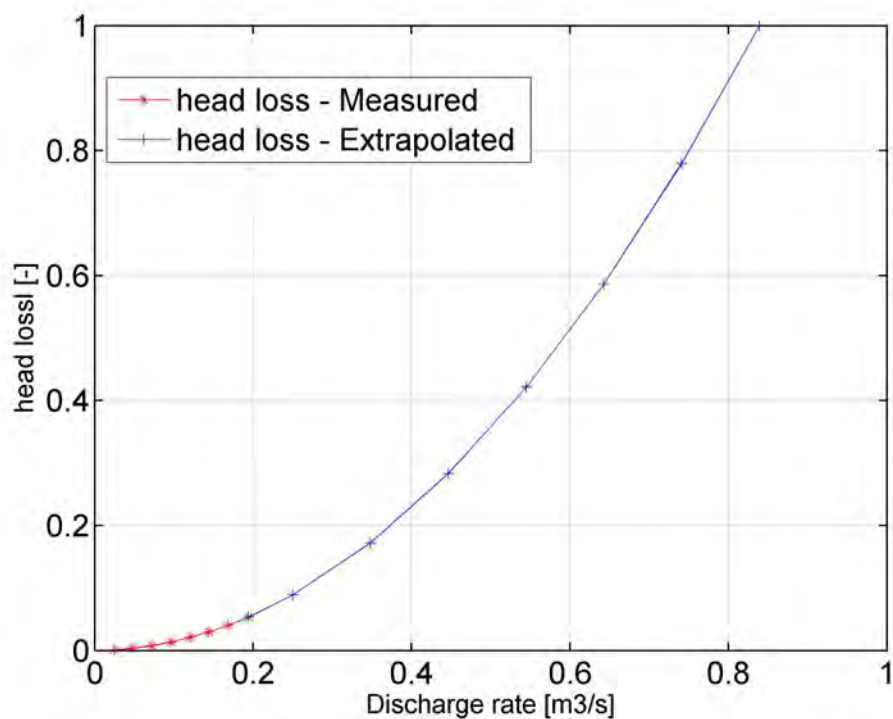

Figure 5.24: *Extrapolation of the function(Q_{main}, Δh), normalized with max(head loss)*
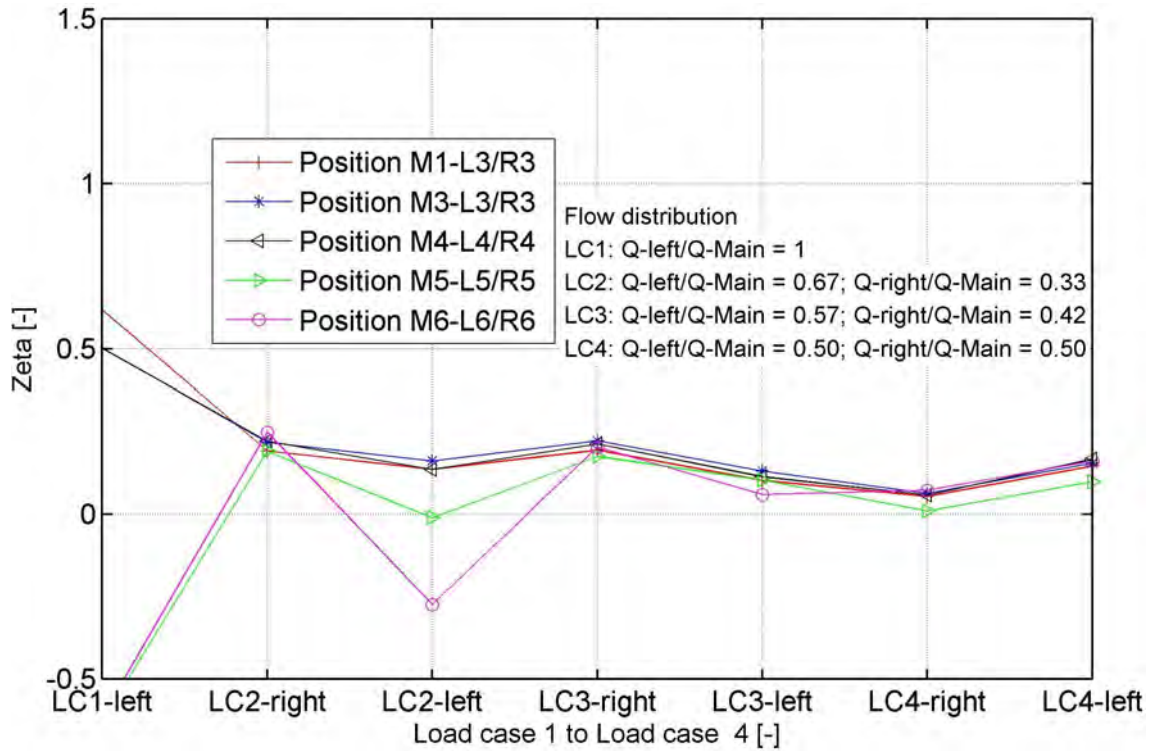
Figure 5.25: *Resulting loss coefficient ζ for several control sections and flow distributions (see Table 3.1 for LC1-left etc.). Quadratic extrapolation with all three coefficients a, b and c (see Eq. 5.35)*
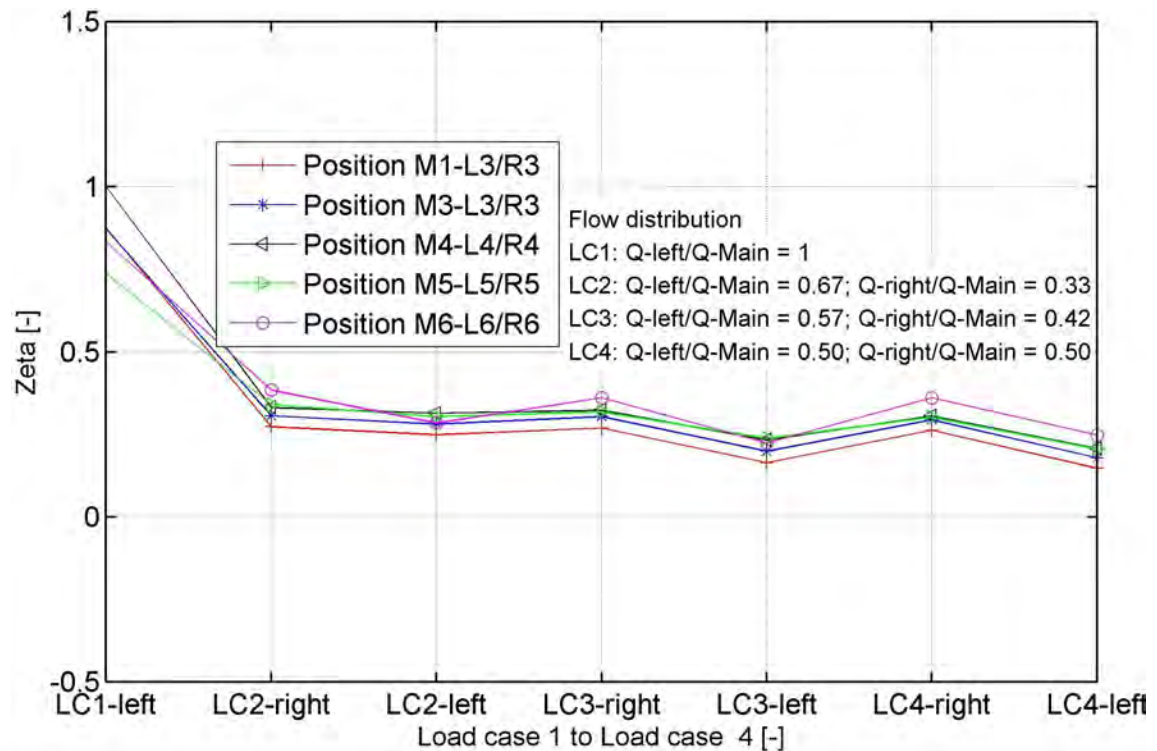

Figure 5.26: *Resulting loss coefficient ζ for several control sections and flow distributions (see Table 3.1 for LC1-left etc.). Quadratic extrapolation with coefficient c only (see Eq. 5.35)*
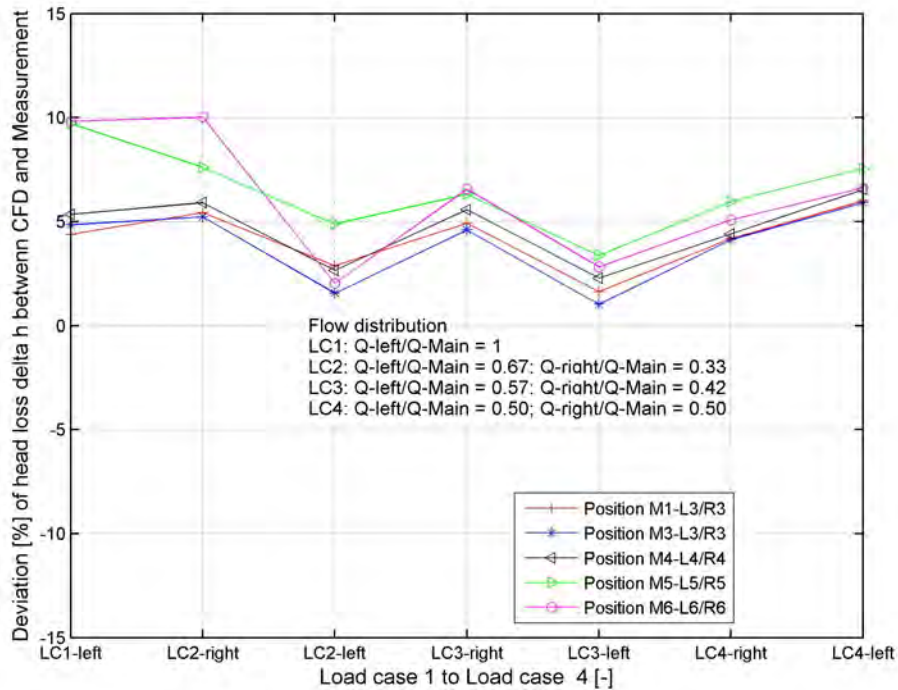
Figure 5.27: *Comparison of total head losses between the extrapolation method (with quadratic, linear and constant term of the least square method) and the numerical simulation for $Re_{prototype} = Re_{model}$.*
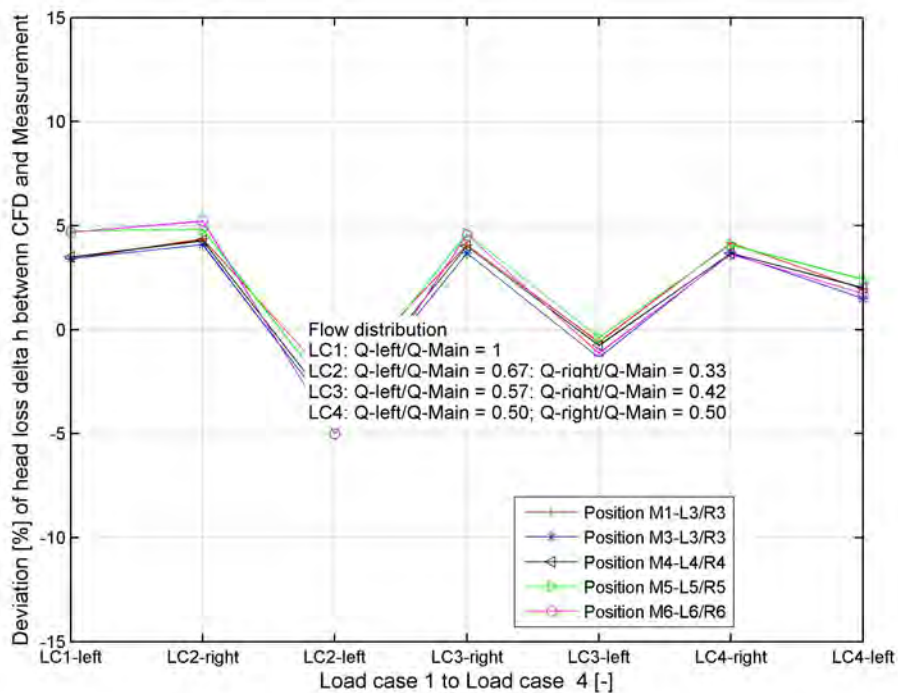

Figure 5.28: *Comparison of total head losses between the extrapolation method (only with the quadratic term of the least square method) and the numerical simulation for $Re_{prototype} = Re_{model}$.*
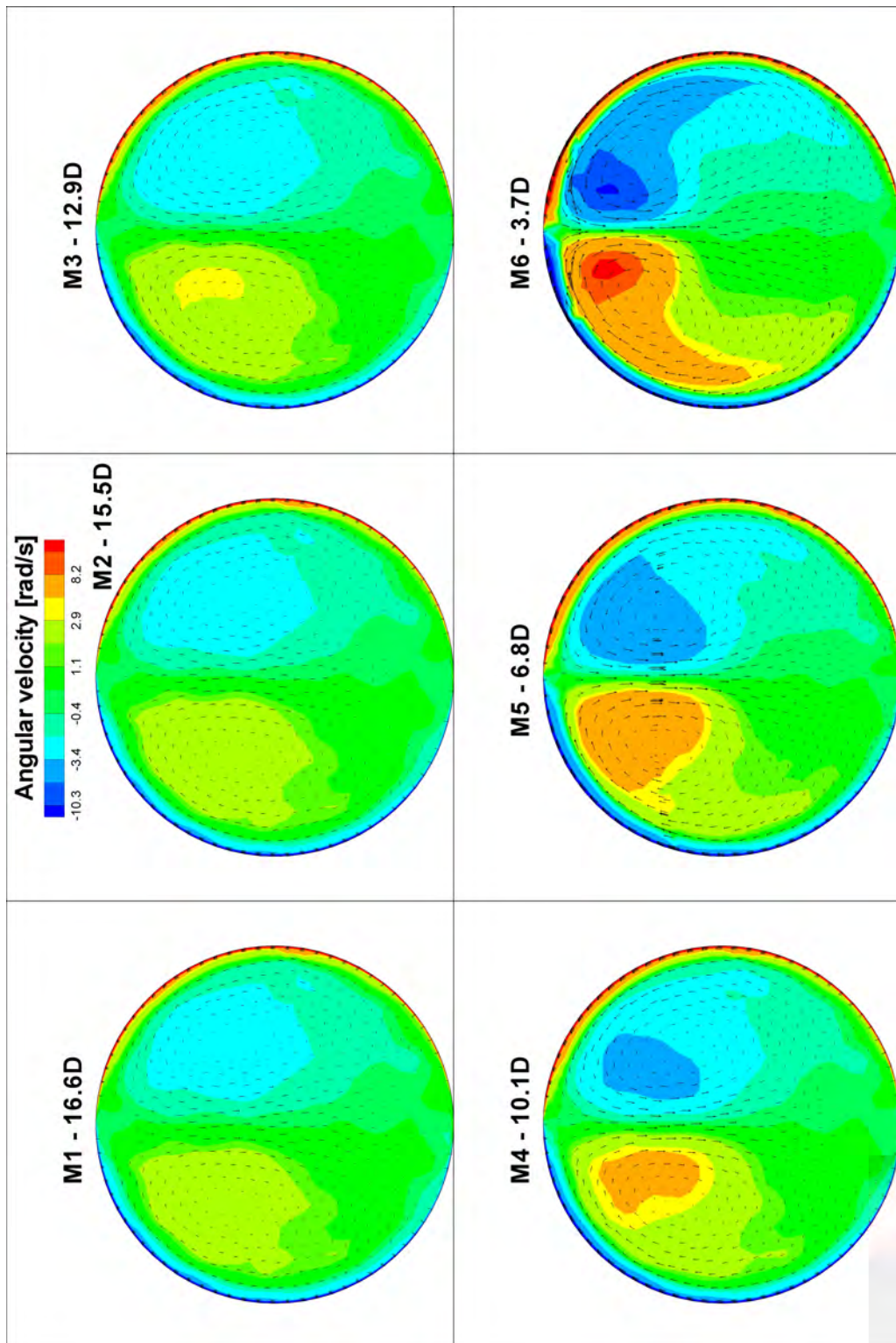
Figure 5.29: *Visualization of the in-plane secondary flow between the bend and the Y-bifurcator with a numerical simulation (symmetrical discharge rate, Q=160 ℓ/s): At control section M6 and M5 (3.6 or 6.8-D after the bend) a strong secondary flow is induced which is also shown by the angular velocity. Further away, the secondary flow decreases*

5.5 Swirling flow

In the thesis of Mayr [2009] a study of a trifurcator is presented. In this hydraulic model test an attempt was made to reduce the losses by a swirling flow. This idea has also been applied on the current bifurcator with a guide vane apparatus from the neighboring mechanical engineering department. A picture of this is shown in Figure 5.30; the guide vane apparatus consists of 16 guides and three fixed guide vanes. The apparatus is installed 6 · D upstream of the Y-bifurcator.
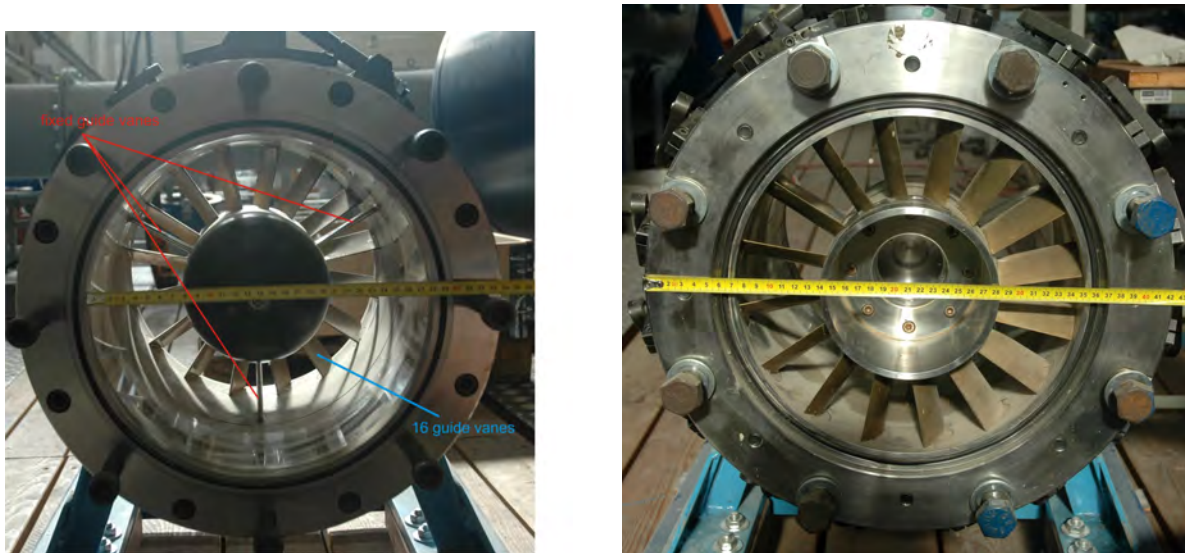

Figure 5.30: *Guide vane apparatus; Left picture: View in flow direction, Right picture: View ageist the flow direction*

As can be seen in Figure 5.32 a yellow bulb is installed downstream of the guide vanes (the guide vane apparatus is connected to a Kaplan-Turbine for its original use, thus the yellow bulb replaces the Kaplan Turbine). The geometrical form of the bulb corresponds to an airfoil wing; the geometry is taken from Idelchik [1994] (see Figure 5.31 and Table 5.3):

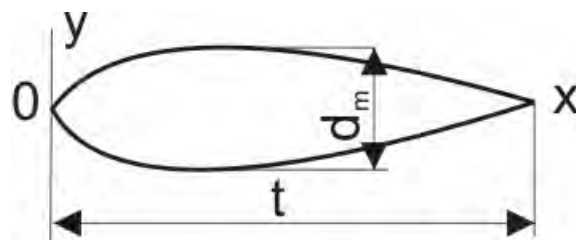**Figure 5.31:** *Sketch of the wing for the coordinates given in Table 5.3*

Figure 5.32: *Built-in Guide vane apparatus to induce a swirling flow*

Table 5.3: *Coordinates 2y/d$_m$ of the streamlined profile (Idelchik [1994], p 597)*

					Airfoil Wing						
x/t	0	0.05	0.1	0.2	0.3	0.4	0.5	0.6	0.7	0.8	0.9	1
2y/d$_m$	0	0.528	0.720	0.917	0.987	1	0.960	0.860	0737	0.568	0.340	0

5.5.1 Resulting loss coefficient of the swirling flow

The resulting loss coefficient is shown in Figure 5.33: The flow distributions are the same as given in Figure 5.25 and Figure 5.26. The control sections for differential pressure measurements are M5 to L6 and R6 respectively (cf. with Figure 3.8). As can be seen in Figure 5.33, the loss coefficient of the swirling flow (blue line) is higher than the loss coefficient of the original non-swirling flow. The higher loss coefficient for the swirling flow is due to the relatively high local losses of the guide vane apparatus. If one subtracts the losses of the guide vane apparatus from the losses of the swirling flow the magenta line is obtained. Thus, the magenta line includes only the pipe friction and the losses of the Y-bifurcator due to the swirling flow without any losses of the guide vane apparatus itself. This results in Figure 5.33 in a lower loss coefficient ζ for load case LC2-left.

Finally, to visualize the swirling flow a PIV-measurement has been carried out (see Figure 4.3).
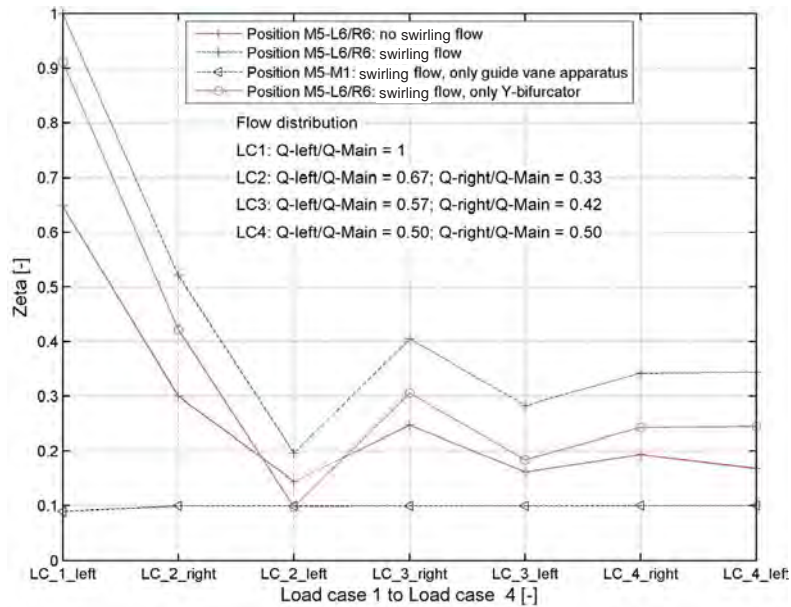
Figure 5.33: *Resulting loss coefficient ζ: Red line is the original loss coefficient without any swirling flow, blue line is the loss coefficient for the swirling flow, black line is the loss coefficient for the guide vane apparatus without the local loss of the Y-bifurcator and finally, the magenta line is the loss coefficient of the swirling flow without the local loss of the guide vane apparatus. All losses include also the pipe friction.*
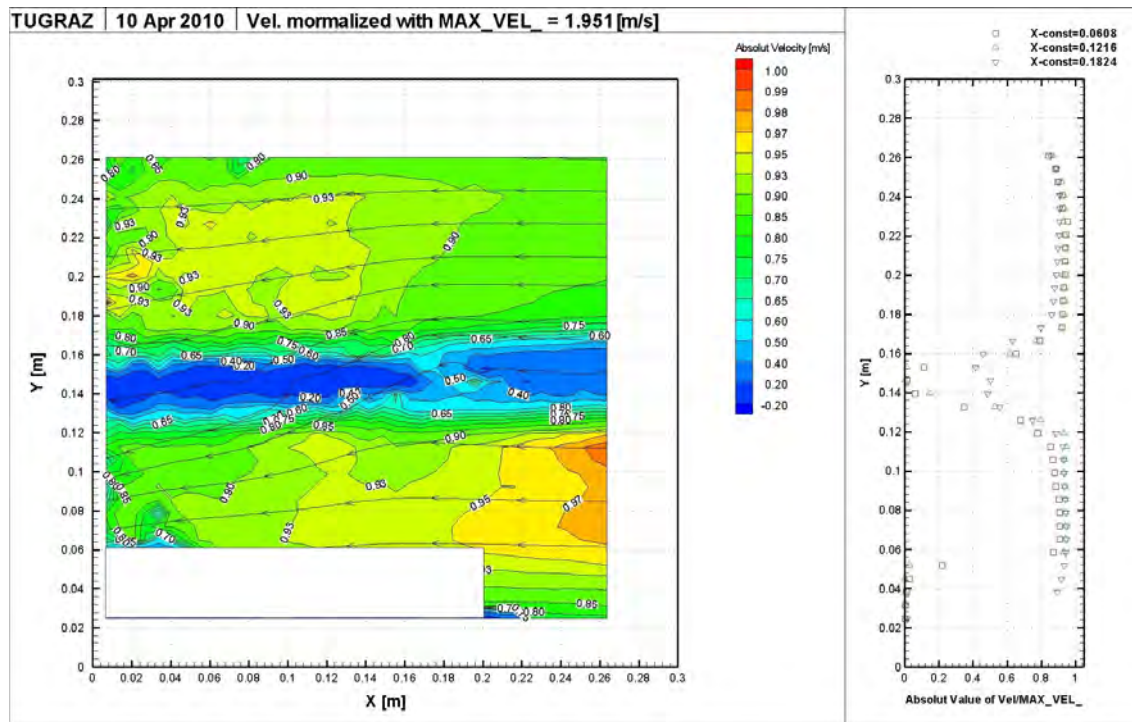

Figure 5.34: *Horizontal PIV-measurement of the swirling flow at position: PIV-Box B201 (see Figure 4.3 at Page 55). Symmetrical discharge rate with 40 ℓ/s. The velocity is normalized with v_{max}.*

Chapter 6

Computational Fluid Dynamics

6.1 Computational Fluid Dynamics with Fluent (Ansys)

In this chapter the decomposition of the Navier-Stokes and the continuity equation for an incompressible flow is presented. As a result, the Reynolds-averaged Navier-Stokes equation is obtained with an additional stress term, the so called *Reynolds-stress*. The *Reynolds-stress* term is the starting point of turbulence modeling where, due to the molecular-diffusion hypotheses of Boussinesq, an eddy viscosity as a model parameter is introduced. The set of equations are for the most flow conditions on the one hand the RANS equations (**R**eynolds-**A**veraged **N**avier-**S**tokes equations) and on the other hand the eddy viscosity with additional transport equations. The turbulence model which is used in this thesis is the k-ϵ model. The transport equations for the k-ϵ model are the turbulent kinetic energy k and the dissipation rate ϵ. Some terms of the k-ϵ model can be measured with Particle Image Velocimetry (see Section 4), namely:

- Kinetic energy K of the mean flow

- Turbulent kinetic energy k (Thus: $k_{tot} = K + k$) (see Eq. 6.24)

- Reynolds-stress tensor (see: Eq. 6.22)

- Production of turbulent kinetic energy P (see: Eq. 6.28)

As a preprocessor, Gambit is used to create the mesh and the desired boundary layer in the range of $20 \leq y^+ \leq 300$. Thus the standard wall function to bridge the boundary layer can be used. The grid independence is checked with several mesh sizes and as a result, meshes with more than 600 000 elements are necessary.

The CFD calculations are carried out with the commercial program Fluent (6.3.26 by Ansys). The discretization method of the program is the finite volume method. The setting for the simulations are the unsteady second order implicit method. For the turbulence the k-ϵ model is used.

Together with the results of the numerical calculations a comparison for the hydraulic model test can be done (see chapter Section 7), which shows good agreement.

6.1.1 Transport equations

The derivation of the Navier-Stokes equation will be shown by means of transport equations. The principle for these transport equations are the rate of change of $\Delta \Phi$, which is transported by

fluid motion into and out of a fixed volume in space (see Figure 6.1). Φ is the representative for example of heat, mass or the components of the momentum (see also Schröder and Zanke [2003]). The mechanism for the rate of change of $\Delta\Phi$ are:

C   Convection of Φ

Di   Diffusion of Φ

S   Net rate of change of Φ due to a sink or source in the volume

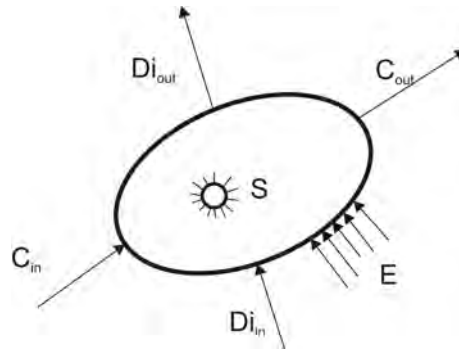**E**   Effects on the surface of the volume depending on Φ

Figure 6.1: *General transport process (taken from Schröder and Zanke [2003]).*
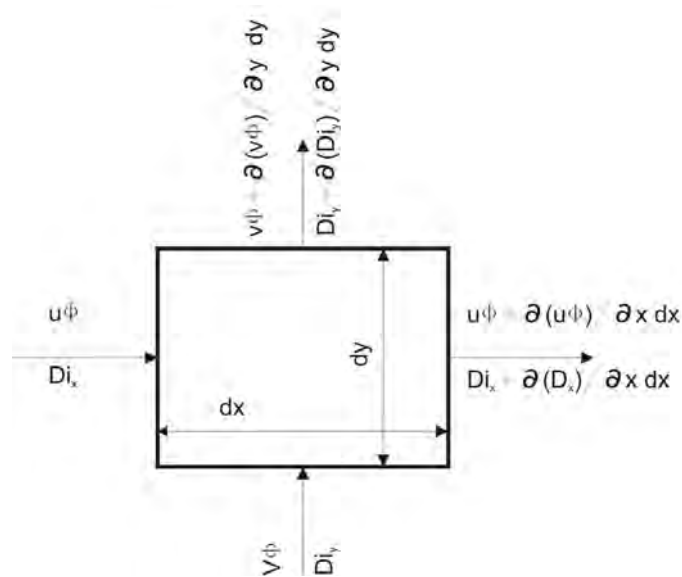

Figure 6.2: *Transport process in cartesian coordinate system.*

With these qualitative variables Eq. 6.1 can be written for the rate of change of $\Delta\Phi$:

$$\Delta\Phi = (C_{in} - C_{out}) + (Di_{in} - Di_{out}) + S + E \qquad (6.1)$$

If a Cartesian coordinate system is used, as shown in Figure 6.2, the qualitative transport equation can be written more precisely. With dV=dx dy dz one can rewrite the convection (Eq. 6.2) and the diffusion (Eq. 6.3) equation as:

$$-\left[\frac{\partial}{\partial x}\left(u\,\Phi\right) + \frac{\partial}{\partial y}\left(v\,\Phi\right) + \frac{\partial}{\partial z}\left(w\,\Phi\right)\right] \;\widehat{=}\; Convection \tag{6.2}$$

$$-\left[\frac{\partial}{\partial x}\,Di_x + \frac{\partial}{\partial y}\,Di_y + \frac{\partial}{\partial z}\,Di_z\right] \;\widehat{=}\; Diffusion \tag{6.3}$$

The convection term in Eq. 6.2 can also be summarized as $\nabla \cdot \left(\vec{V}\Phi\right)$ which is mathematically the divergence of $\vec{V}\Phi$. For the diffusion term in Eq. 6.5 the law of Fick is applied and one can write:

$$Di_x = -\Gamma\,\frac{\partial}{\partial x}\,\left(\frac{\Phi}{\rho}\right) \tag{6.4}$$

whereas Γ is the diffusion coefficient. Thus Eq. 6.4 can be rewritten as

$$\Gamma\,\left[\frac{\partial^2}{\partial x^2}\left(\frac{\Phi}{\rho}\right) + \frac{\partial^2}{\partial y^2}\left(\frac{\Phi}{\rho}\right) + \frac{\partial^2}{\partial z^2}\left(\frac{\Phi}{\rho}\right)\right] = \Gamma\,\Delta\,\left(\frac{\Phi}{\rho}\right) \tag{6.5}$$

whereas Δ is the Laplace operator which is defined as the divergence $\nabla\cdot$ of the gradient ∇ of $\frac{\Phi}{\rho}$.

Finally, replacing $\Delta\Phi$ in Eq. 6.1 with the time rate of change $\frac{\partial\Phi}{\partial t}$ and due to dimensional reasoning adding the density ρ to the net rate of change **S**, gives the transport equation Eq. 6.6.

$$\frac{\partial\Phi}{\partial t} + \nabla \cdot \left(\vec{V}\Phi\right) = \Gamma\,\Delta\,\left(\frac{\Phi}{\rho}\right) + \rho \cdot \vec{S} + \vec{E} \tag{6.6}$$

6.1.1.1   Continuity equation

If the transported quantity ϕ is substituted by the density the transport equation evolves to the continuity equation. For incompressible flow (ρ=constant) $\vec{E}$, $\vec{S}$, the time derivate and the diffusion process do not influence the transport of mass and therefore one can write:

$$\nabla \cdot \vec{V} = 0 \tag{6.7}$$

6.1.1.2   Momentum equation

The transport of the vector momentum is shown component by component. For the x-component the transport variable Φ is (ρu). Additionally, to fulfill the balance of forces the gravitation with $S = G_x$ and the pressure gradient E=-$\frac{\partial P}{\partial x}$ will be included in the transport equation (Eq. 6.6).

$$\frac{\partial(\rho\,V_x)}{\partial t} + \nabla \cdot \left(\rho\,V_x\,\vec{V}\right) = \Gamma\,\Delta\,V_x + \rho\,G_x - \frac{\partial P}{\partial x} \tag{6.8}$$

For the diffusion coefficient Γ the molecular diffusion coefficient ν due to Newton's law of viscosity will be applied. Finally, for an incompressible fluid ($\rho = const.$) and the vector identity $\nabla \cdot \left(V_x \, \vec{V} \right) = V_x \left(\nabla \cdot \vec{V} \right) + \vec{V} \cdot \left(\nabla \, V_x \right)$ and the use of the continuity equation with $\nabla \cdot \vec{V} = 0$ one can rewrite the x-component:

$$\frac{\partial (V_x)}{\partial t} + \vec{V} \cdot \left(\nabla \, V_x \right) = \nu \, \Delta \, V_x + G_x - \frac{1}{\rho} \frac{\partial P}{\partial x} \tag{6.9}$$

If the same considerations are applied for the y and z component the momentum equation gets its final form (in braces are the physical meaning of each term):

$$\underbrace{\frac{\partial \left(\vec{V} \right)}{\partial t}}_{local\ derivate} + \underbrace{\left(\vec{V} \cdot \nabla \right) \vec{V}}_{convective\ derivate} = \underbrace{\nu \, \Delta \, \vec{V}}_{diffusion\ derivate} + \underbrace{\vec{G}}_{body\ force} - \underbrace{\frac{1}{\rho} \nabla P}_{surface\ force} \tag{6.10}$$

whereas:

- $\vec{V} = \vec{V} \left(\vec{r} \right) = \vec{V} \left(x, \, y, \, z \right) = \begin{pmatrix} V_x(x,y,z) \\ V_y(x,y,z) \\ V_z(x,y,z) \end{pmatrix}$ Velocity vector

- $\vec{G} = (G_x \, G_y \, G_z)$ Body force vector

- $\vec{P} = (P_x \, P_y \, P_z)$ Pressure vector

- $\vec{V} \cdot (\nabla u) = u \cdot \frac{\partial u}{\partial x} + v \cdot \frac{\partial u}{\partial x} + w \cdot \frac{\partial u}{\partial x}$ Convective derivate; only for the x-component

- $\nabla = \frac{\partial}{\partial x} \, \frac{\partial}{\partial y} \, \frac{\partial}{\partial z}$ Nabla Operator

- $\Delta = \nabla^2 = \frac{\partial^2}{\partial x^2} + \frac{\partial^2}{\partial y^2} + \frac{\partial^2}{\partial z^2}$ Laplace Operator

- $\nu = \frac{\mu}{\rho}$ Kinematic viscosity

6.1.1.3 Momentum equation in tensor form

The momentum equation can also be written in a very compact tensor form (see also Pope [2006]):

$$\rho \frac{du_j}{dt} = \frac{\partial \tau_{ij}}{\partial x_i} - \rho \frac{\partial \Psi}{\partial x_j} \tag{6.11}$$

whereas (only for j=1)

$$\underbrace{\frac{du}{dt}}_{Lagrange} = \underbrace{\frac{\partial u}{\partial x} u + \frac{\partial u}{\partial y} v + \frac{\partial u}{\partial z} w + \frac{\partial u}{\partial t}}_{Euler} \tag{6.12}$$

is the total derivate of u (Lagrange reference system) which is equal to the local plus the convective derivate (Euler reference system). The stress tensor τ_{ij} in Eq. 6.11 can be written as

$$\tau_{ij} = -P \cdot \delta_{ij} + \mu \cdot \left(\frac{\partial u_i}{\partial x_j} + \frac{\partial u_j}{\partial x_i} \right) \tag{6.13}$$

and for the gravity as the only body force a gravitational field $\vec{g} = -\nabla\Psi$ with $\Psi = gz$ can be defined in Eq. 6.11. Again with a constant density and thus

$$\frac{\partial^2 u_i}{\partial x_i \cdot \partial x_j} = \frac{\partial}{\partial x_j} \frac{\partial u_i}{\partial x_i} = 0 \tag{6.14}$$

Eq. 6.11 can be written as

$$\frac{du_j}{dt} = -\frac{\partial P}{\partial x_j} + \mu \cdot \frac{\partial^2 u_j}{\partial x_i x_i} - \rho \frac{\partial \Psi}{\partial x_j} \tag{6.15}$$

which is equivalent to Eq. 6.10, except for the gravitational field. The last simplification is to merge the gravitational potential Ψ with the pressure (both are isotropic stresses), that is,

$$p = P + \rho\Psi \tag{6.16}$$

which gives the final form for the momentum equation in tensor form (Pope [2006])

$$\frac{du_j}{dt} = -\frac{\partial p}{\partial x_j} + \mu \cdot \frac{\partial^2 u_j}{\partial x_i x_i} \tag{6.17}$$

(Note: Einstein's notation is used: when an index appears twice in a single term a summation is applied. For example, only for j=1: $\frac{\partial^2 u_j}{\partial x_i x_i} = \frac{\partial^2 u_1}{\partial x_1{}^2} + \frac{\partial^2 u_1}{\partial x_2{}^2} + \frac{\partial^2 u_1}{\partial x_3{}^2}$)

6.1.2 Reynolds-averaged Navier-Stokes equation (RANS)

With Eq. 6.17 it is possible to carry out a decomposition into a mean part (over line) and a fluctuating part (prime), that is:

$$\vec{V}_j = \overline{\vec{V}_j} + \vec{V}_j{}' \tag{6.18}$$
$$p_j = \overline{p_j} + p_j' \tag{6.19}$$

The final decomposition (the procedure can be found in Pope [2006]) of Eq. 6.17 is the RANS equation

$$\rho \cdot \frac{d\overline{u_j}}{dt} = -\frac{\partial \overline{P}}{\partial x_j} + \mu \frac{\partial^2 \overline{u_j}}{\partial x_i \, \partial x_i} - \frac{\partial \rho \overline{u_i' u_j'}}{\partial x_i} \tag{6.20}$$

and the continuity equation is

$$\nabla \cdot \vec{V} = 0 \tag{6.21}$$

The RANS equation looks almost the same as the Navier Stokes equation, except for the term $\rho \overline{u_i' u_j'}$ which is also known as the *Reynolds-stress*. The *Reynolds-stress* is a second order tensor with normal and shear stresses that is:

$$\rho \overline{u_i' u_j'} = \begin{bmatrix} \rho \overline{u'^2} & \rho \overline{u'v'} & \rho \overline{u'w'} \\ \rho \overline{v'u'} & \rho \overline{v'^2} & \rho \overline{v'w'} \\ \rho \overline{w'u'} & \rho \overline{w'v'} & \rho \overline{w'^2} \end{bmatrix} \tag{6.22}$$

One of the primary tasks in fluid mechanics is to model the *Reynolds-stress* by a turbulent model. An early attempt to solve this problem was introduced by Boussinesq in 1877 which is analogous to the stress-rate of strain relation for a Newtonian fluid. This analogy can be written as:

$$\rho \cdot a_{ij} \equiv \rho \overline{u_i' u_j'} - \frac{2}{3} \cdot \rho \cdot k \cdot \delta_{ij} = -\rho \cdot \nu_t \left(\frac{\partial \overline{u_j}}{\partial x_i} + \frac{\partial \overline{u_i}}{\partial x_j} \right) = -2 \cdot \nu_t \cdot \overline{S}_{ij} \tag{6.23}$$

whereas the variable a_{ij} represents the deviatoric and $\frac{2}{3} \cdot k \cdot \delta_{ij}$ the isotropic part. The turbulent kinetic energy is defined as

$$k = \overline{k'} = \frac{1}{2} \overline{u_i' u_i'} \tag{6.24}$$

The model parameter ν_t, also called the eddy viscosity, is the link between the deviatoric part and the deformation tensor

$$\overline{S}_{ij} = \frac{1}{2} \left(\frac{\partial \overline{u_j}}{\partial x_i} + \frac{\partial \overline{u_i}}{\partial x_j} \right) = \begin{pmatrix} \frac{\partial u}{\partial x} & \left[\frac{\partial v}{\partial x} + \frac{\partial u}{\partial y} \right] & \left[\frac{\partial u}{\partial z} + \frac{\partial w}{\partial x} \right] \\ \left[\frac{\partial v}{\partial x} + \frac{\partial u}{\partial y} \right] & \frac{\partial v}{\partial y} & \left[\frac{\partial w}{\partial y} + \frac{\partial v}{\partial z} \right] \\ \left[\frac{\partial u}{\partial z} + \frac{\partial w}{\partial x} \right] & \left[\frac{\partial w}{\partial y} + \frac{\partial v}{\partial z} \right] & \frac{\partial w}{\partial z} \end{pmatrix} \tag{6.25}$$

A solution to model ν_t is the relationship first introduced by Jones and Launder [1972],

$$\nu_t = C_\mu \frac{k^2}{\epsilon} \tag{6.26}$$

whereas C_μ is one of the model constants, k is the turbulent kinetic energy and ϵ is the dissipation rate (see also Knoblauch [1995]). With the additional eddy viscosity the RANS equation becomes:

$$\frac{d\overline{u_j}}{dt} = \frac{\partial}{\partial x_i} \left[\nu_{eff} \left(\frac{\partial \overline{u_i}}{\partial x_j} + \frac{\partial \overline{u_j}}{\partial x_i} \right) \right] - \frac{1}{\rho} \cdot \frac{\partial}{\partial x_j} \cdot \left(\overline{p} + \frac{2}{3} \cdot \rho \cdot k \right)$$

whereas $\nu_{eff} = \nu + \nu_t$.

The exact derivation for the transport equation of k and ϵ are given in Pope [2006]. For the turbulence modeling of k and ϵ, the so called k-ϵ model, the following transport equation are used (compare also with Table 6.1):

$$\frac{\partial (\Phi)}{\partial t} + \frac{\partial}{\partial x_i} (\Phi \overline{u_i}) = \frac{\partial}{\partial x_i} \left(\Gamma \frac{\partial \Phi}{\partial x_i} \right) + S \tag{6.27}$$

Table 6.1: *Transport coefficient for the k-ϵ model (Versteeg and Malalasekera [2007])*

Equation	Φ	Γ	S
k-equ.	k'	$\frac{\mu_t}{\sigma_k}$	$P - \epsilon$
ϵ-equ.	ϵ	$\frac{\mu_t}{\sigma_\epsilon}$	$C_{1\epsilon}\,P - C_{2\epsilon}\,\epsilon$

The variable P in Table 6.1 is the production of turbulence that is (see also Durst [2006]):

$$P = -\overline{u_i' u_j'} \cdot \frac{\partial \overline{u}_j}{\partial x_i} = \nu_t \left(\frac{\partial \overline{u}_j}{\partial x_i} + \frac{\partial \overline{u}_i}{\partial x_j} \right) \frac{\partial \overline{u}_j}{\partial x_i} \tag{6.28}$$

$$P = exact\ term\ = modelling\ term$$

The exact term of the dissipation ϵ requires to process into the dissipative (small scale) range. (see Pope [2006], p375). Therefore the transport equation for ϵ in Table 6.1 is entirely empirical. With the eddy viscosity (Eq. 6.26) and the model constants μ_t, σ_k, C_μ, σ_ϵ, $\sigma_{1\epsilon}$ and $\sigma_{2\epsilon}$ the $k - \epsilon$ turbulence model is completed.

The results of the Particle Image Velocimetry (PIV) in Section 4 can be compared with the afore-mentioned quantities (K, k, Reynolds-stress and P).

6.1.3   The SIMPLE Scheme

One of the major problems (beside non-linearities) of the incompressible Navier-Stokes equation (see Eq. 6.10) is that there is no transport equation for the pressure as it is available for the compressible flow (equation of state for p=p(ρ,T)). If the pressure field was a priori known the velocity field could be simply solved by using for example central or upwind differencing schemes. Unfortunately, the pressure field is not known a priori and an iterative solution strategy such as the SIMPLE (Semi-Implicit Method for Pressure-Linked Equations) algorithm is used (Patankar and Spalding [1972]). The SIMPLE algorithm is applied on a staggered grid, that is, all scalar variables like pressure, temperature etc., are located at nodal points whereas the velocity is located at the cell faces. This arrangement avoids that a highly non-uniform pressure field acts like a uniform pressure field (see Versteeg and Malalasekera [2007], p 180). The SIMPLE algorithm can basically be described (see Anderson [1995]) as:

1. Start the iterative process by guessing the pressure field p^*.

2. Use the values of p^* to solve the momentum equation to get u^*, v^*, w^*.

3. Check if the continuity equation ($\nabla \cdot \vec{U}$=0) is satisfied; if not

4. construct a pressure correction p' to correct the pressure (p=p^*+p') to bring the velocity field more into agreement with continuity.

5. Corresponding velocity corrections u', v', w' can be obtained from p' such that u=u^* + u', v=v^* + v' and w=w^* + w'.

6. With the corrected values repeat the procedure until the velocity field satisfies the continuity equation.

The SIMPLE algorithm is implemented in Fluent and *OpenFoam*. In *OpenFoam* the algorithm is called **simpleFoam**.

6.1.4 Geometry and Mesh of the domain

For the hydraulic model test a numerical simulation has been carried out. The domain of the numerical calculation includes the bend, the Y-bifurcator and the two confusers after the Y-bifurcator (cf. with Figure 3.1). The geometry is created with Autocad 2008 and exported as an IGES file. Afterwards, the IGES file is imported into the preprocessor Gambit (Gambit 2.4.6) to mesh the boundary layer and the core flow of the pipe installation.

6.1.4.1 Dimensionless wall distance y^+

Due to the no-slip condition at the wall (V_{Wall}=0) high velocity gradients occur and thus a very dens mesh is necessary. To avoid this uneconomical finer mesh at the wall the logarithmic law of the wall (further details are given in Section 5.2.2 at Page 86) to bridge the turbulent boundary layer will be used. This means that the dimensionless distance y^+ must be in the range of $20 \leq y^+ \leq 300$ (see Figure 6.3). The first row of the boundary layer is 0.4 mm away from the wall and starts to grow up tp 2.15 mm. In total, there are four boundary rows before the mesh of the core flow begins. The equivalent sand roughness of the wall is 0.015 mm.
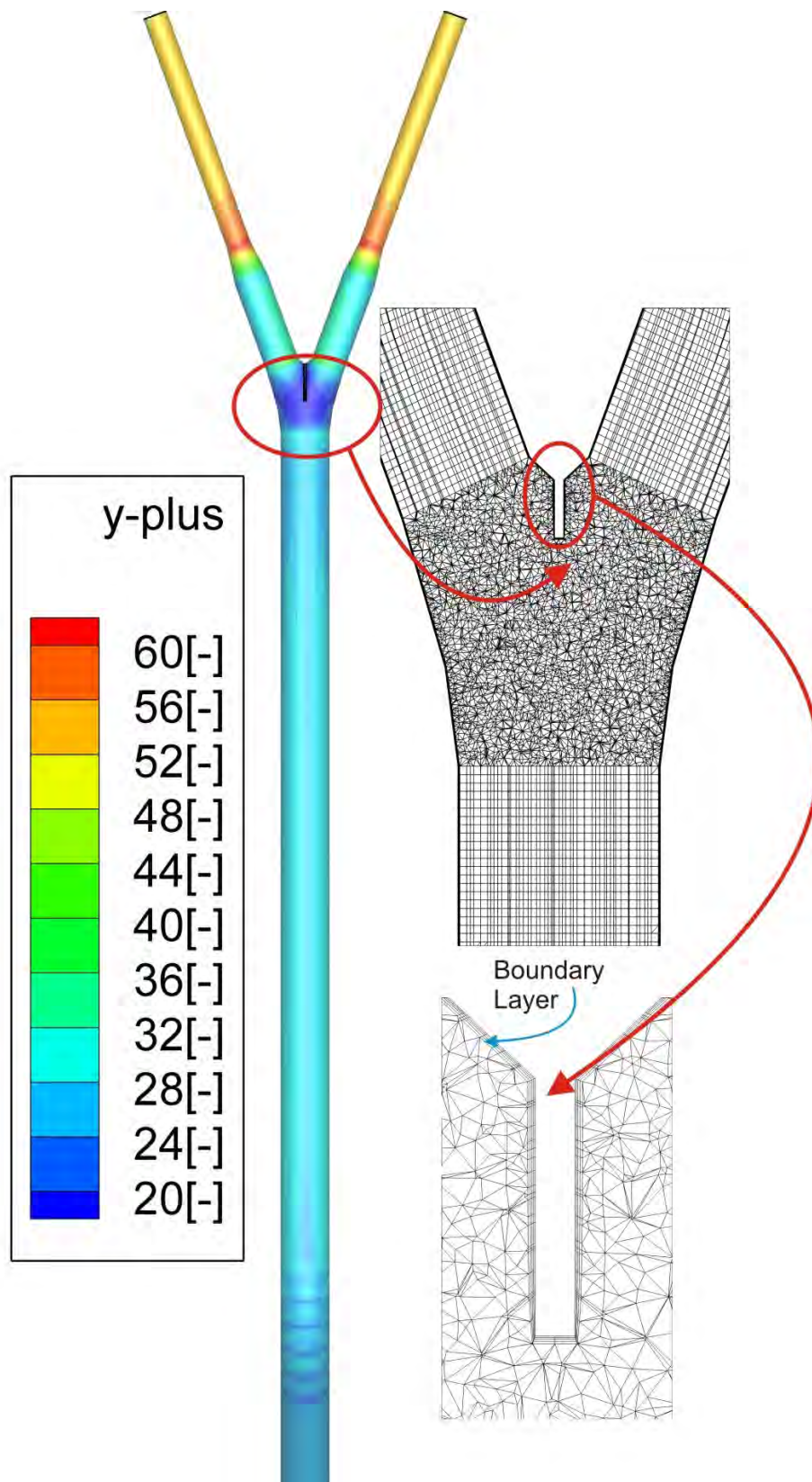
Figure 6.3: *Contour plot of the dimensionless wall distance y^+ and a detailed plot of the mesh and boundary layer.*

6.1.4.2 Grid size

The next step is to check if the solution of the CFD calculation is independent of the grid size. This means that several meshes - with different grid sizes - are numerically solved and compared to each other. If the solution does not show any difference between the mesh and the next finer mesh, grid independence is achieved. In Figure 6.4 the velocity and the static pressure for 40000 discrete points and four different meshes are shown. As can be seen Grid 2 to Grid 4 show almost no difference between each other in Figure 6.4; therefore grid 2 with 603813 elements is chosen. Grid 2 has generally an element size of 10 mm (except in the boundary layer) and the shape of hexahedron or tetrahedron elements.
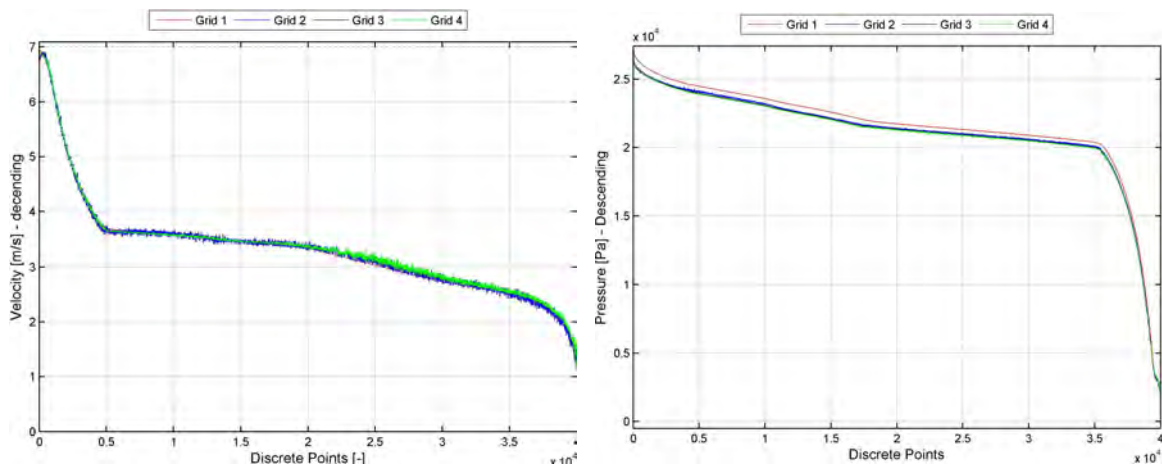
Figure 6.4: *Descending velocity and static pressure at 40000 discrete points in the domain for four different meshes: Grid 1 with 293195, Grid 2 with 603813, Grid 3 with 1 791714 and Grid 4 with 2800000 elements*

6.1.5 Boundary conditions

The CFD calculation has three inlet/outlet boundaries. With the hydraulic diameter and the turbulence intensity Fluent can estimate the turbulence at the boundary (see Table 6.2).

Table 6.2: *Boundary conditions for the CFD calculation; mass flow is either 80 ℓ/s for left and 80 ℓ/s for right branch or 80 ℓ/s for left and 0 ℓ/s for right branch*

Type	Turbulence intensity	Hydraulic Diameter
-	[%]	mm
Mass flow inlet	10	246
Pressure outlet-left	10	123
Pressure outlet-right	10	123

6.1.6 Fluent - Solver

The calculation is done with Fluent (6.3.26). The settings for the models are as follows:

The discretization schemes for the CFD calculation is as follows:

Table 6.3: *Setting of the models for the CFD calculation*

Model	Settings
-	-
Space	3D
Time	Unsteady, 2nd-Order Implicit
Time step	0.01 second
Viscous	Standard k-ϵ turbulence model
Wall treatment	Standard wall function

Table 6.4: *Discretization Scheme*

Variable	Scheme
-	-
Pressure	second order
Momentum	second order upwind
Turbulent Kinetic Energy	second order upwind
Turbulent Dissipation Rate	second order upwind

The CFD calculation is carried out for different roughnesses and different turbulence models to check which setting is the best for the current project. The parameter for the comparison was either the velocity field of the PIV measurements or the measured head losses along the pipe installation. The best result is achieved with a pipe roughness of 0.015mm and the k-ϵ turbulence model. The setting will be used for further investigations (see Chapter 7).

6.2 Computational Fluid Dynamics with *OpenFoam*

This chapter shows the comparison between Fluent (Version 6.3.26) and *OpenFoam* (Version 1.7.1) for the symmetrical (80 ℓ/s per branch) and asymmetrical (only 80 ℓ/s for the left branch) discharge rates. The numerical simulation is done with a steady state simulation and a solver for incompressible fluids. The k-ϵ and the standard wall function are applied. The results for the piezometer head as well as for the velocity along the center line of the pipe show good agreement between Fluent and *OpenFoam*. The results for the symmetrical discharge rate are also double-checked with measurements of the hydraulic model test. Due to the promising outcome of *OpenFoam* which is a non- commercial, open source software, it is expected that this software will be more and more applied in the industry.

In Chapter 6 the numerical simulation was carried out with the commercial software Fluent (Ansys). Two simulations will be repeated with two different discharge rates which are

- Symmetrical discharge rate - $Q_{left} = Q_{right} = 80\ell/s$ and

- Asymmetrical discharge rate - $Q_{left} = 80\ell/s$, $Q_{right} = 0\ell/s$

to show that a highly sophisticated and reliable solution with *OpenFoam* can be achieved. Open-Foam uses the finite volume method to solve the Navier-Stokes equation on an arbitrary, unstructured 3D mesh of polyhedral elements. The fluid flow solvers are developed within a robust, implicit, pressure-velocity, iterative solution framework (OpenFoam [2010]). The newest version (Version 1.7.1, released 26/08/10) has been used on a Linux-Ubuntu system (Version 10.04 LTS - Lucid Lynx). The available computational resources are two Intel (T7500) 2.2 Ghz processors with 2 GB memory (ordinary Laptop). The mesh for the simulation is the same as for the Fluent case. The file structures for this case are in the appendix (Table 10.1).

6.2.1 Folder 0: Boundary conditions

The positions for the boundary conditions are shown in Figure 6.5:
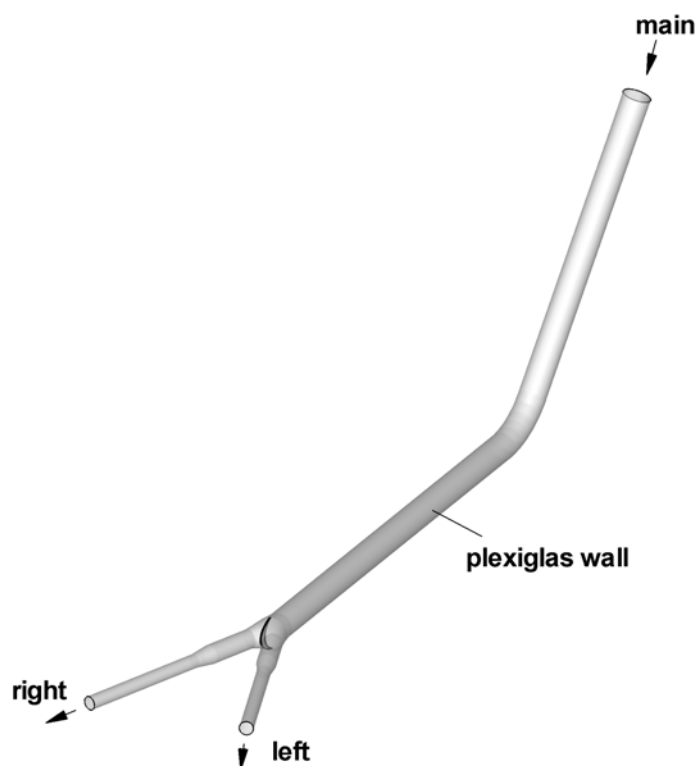
Figure 6.5: *Boundary conditions for the numerical simulation:* **main** *is the inlet boundary,* **left** *and* **right** *are the outlet boundaries and finally* **plexiglass wall** *is the wall boundary*

6.2.1.1 File: epsilon

The dissipation rate ϵ will be initialized with a guessed value of $1\ m^2/s^3$. For the inlet boundary *main*, a turbulent length scale ℓ_0 related to the larger eddies will be defined. In fully-developed pipe flow, the length scale is restricted to the pipe diameter, since the eddies cannot be larger than the pipe diameter. An approximate relationship between ℓ_0 and the physical size of the duct is (taken from ANSYS Fluent [2005])

$$\ell_0 = 0.07 \cdot D \tag{6.29}$$

where D is the pipe diameter. The pipe diameter for the numerical simulation is 0.25 m (at the entrance there is a confuser which reduces the pipe diameter from 0.25 to 0.246m) and therefore the length scale becomes $\ell_0 = 0.0175$ m. With this length scale the dissipate rate ϵ at the inlet can be estimated:

$$\epsilon = C_\mu^{3/4} \cdot \frac{k^{3/2}}{\ell_0} \tag{6.30}$$

whereas C_μ is a constant of the k-ϵ model (approximately 0.09) and k is the turbulent kinetic energy.

For the outlets **left** and **right** an inlet-outlet boundary condition is used (see also OpenFoam [2010]). If the velocity vector at the boundary points outward of the domain then a Neumann boundary condition is used ($\partial \epsilon / \partial n = 0$), if the velocity vector points inward to the domain then a Dirichlet boundary condition is used ($\epsilon = const.$)

For the wall boundary **plexiglass-wall** the epsilon wall function is used. With Eq. 6.30 and the mixing length $\ell_m = \kappa \cdot y$ as the turbulent length scale in the boundary layer, ϵ can be calculated as:

$$\epsilon = C_\mu^{3/4} \cdot \frac{k^{3/2}}{\kappa \cdot y} \tag{6.31}$$

where κ is the von Kármán-constant and y is the distance from the wall.

6.2.1.2 File: Turbulent kinetic energy

The turbulent kinetic energy at the **inlet** is defined by a turbulent intensity TU and the inlet velocity magnitude $\left| \vec{V} \right|$:

$$k = \frac{3}{2} \cdot \left(\left| \vec{V} \right| \cdot TU \right)^2 \tag{6.32}$$

The turbulent intensity TU = 5% which corresponds to a medium turbulence at the inlet boundary.

For the outlets **left** and **right** an inlet-outlet boundary condition is used as described in Section 6.2.1.1. For the wall function the turbulent kinetic energy is solved in the whole domain including the near wall region where the kinetic energy is:

$$\frac{\partial k}{\partial n_w} = 0 \tag{6.33}$$

6.2.1.3 File: Turbulent eddy viscosity

The turbulent eddy viscosity is solved together with two transport equations for k and ϵ. At **all boundary conditions** a zero gradient condition is used.

6.2.1.4   File: Pressure

The domain is initialized with zero gauge pressure. At the **outlets** zero gauge pressure is defined. For the **inlet** and the **wall boundary** a zero gradient pressure is used.

6.2.1.5   File: Velocity

The inlet velocity is defined by the boundary condition **surfaceNormalFixedValue** (see also OpenFoam [2010]). The inlet velocity is 3.26 m/s for symmetrical discharge and 1.63 m/s for asymmetrical discharge. For the outlets a **inlet-Outlet**, as described in Section 6.2.1.1, is used. The velocity at the wall is zero due to the no-slip condition for viscous flow.

Chapter 7

Comparison of CFD and PIV

In this chapter the comparison between the PIV-Measurements and the numerical simulations is presented. As a result, the accuracy of the CFD calculation, like secondary flow or the head loss along the pipe installation, can be quantified. The results of the PIV measurements are similar to a Large Eddy Simulation (LES) where the big eddies are numerically resolved and the smaller eddies are modeled with a turbulence model. The turbulence model for the numerical simulation presented in this thesis is the k-ϵ model which models to whole turbulent spectrum (including also the big eddies). Therefore, the comparison between the PIV measurements and the CFD simulations could be improved if a LES simulation is applied.

The velocity distribution along the hydraulic model shows good agreement between PIV and CFD as long as no strong secondary flow occurs: For example in Figure 7.1 (PIV-Box-200) a strong secondary flow is initialized after the flow passes the bend and the results between PIV - CFD do not match properly. However, the results of the comparison (see Figure 7.1 PIV-Box 201 and 202L) get much better when the secondary flow decays as indicated in Figure 7.4. The influence of the secondary flow on the pressure distribution along the pipe and thus the head loss of the pipe installation can be seen in Figure 7.5: After the bend the total head losses of the numerical simulation (k-ϵ, standard wall function) and the pressure loss measurements are almost the same. This means, if only the loss coefficient ζ is of interest a numerical simulation without a model test could be sufficient in simple pipe flows and bifurcations.

In Figure 7.6 to Figure 7.7 the kinetic energy of the mean flow and the turbulent flow are shown. The location of the presented quantities is right after the Y-bifurcator (PIV-Box: 202L) and the comparison between PIV and CFD shows an acceptable agreement. The turbulent kinetic quantity is also an important value for turbulence modeling: The kinetic energy of the mean flow is transfered via the production term (see Figure 7.11) to the turbulent kinetic energy which is one of the quantities of the k-ϵ turbulence model.

Further comparisons between PIV and CFD are shown in Figure 7.8 to Figure 7.10. These plots present the Reynold stress tensor (normal and shear stress) of the pipe flow right after the Y-bifurcator. Again, the comparison between PIV and CFD looks reasonable, although a slight deviation at the upper part of the pipe flow occurs. The isotropic normal stress of the CFD-calculation due to the Boussinesq hypotheses can also be seen for the normal stresses in lateral and longitudinal direction. However, the PIV-measurements for the lateral and longitudinal normal stresses do not fully show the isotropic behavior which reveals one of the well known shortcomings of the k-ϵ turbulence model.

7.1 Velocity

Figure 7.1 and Figure 7.2 show the velocity distribution for symmetrical discharge rate (each branch 80 ℓ/s) for the horizontal and vertical plane, respectively. On the left side the PIV and on the right side the CFD results are shown. The secondary flow caused by the bend is qualitatively predicted by the numerical simulation but it does not match the PIV results quantitatively (compare the PIV-Box: 200 of Figure 7.1 and Figure 7.2). The secondary flow induced by the bend is reduced along the pipe installation and reasonably well predicted further downstream in the numerical simulation(see PIV-Box: 201 and PIV-Box: 202L).

The secondary flow is also shown in Figure 7.3 where the ill-predicted secondary flow right after the bend in the numerical simulation can clearly be seen for the PIV-Box: 200.

The development of the secondary flow along the pipe installation (PIV and CDF) up to the Y-bifurcator is shown in Figure 7.4. The reduction of strength of the secondary flow is shown along the pipe installation but does not vanish before the flow enters the Y-bifurcator. This is the principle reason why the velocity correction factor α needs to be determined for the loss coefficient ζ.
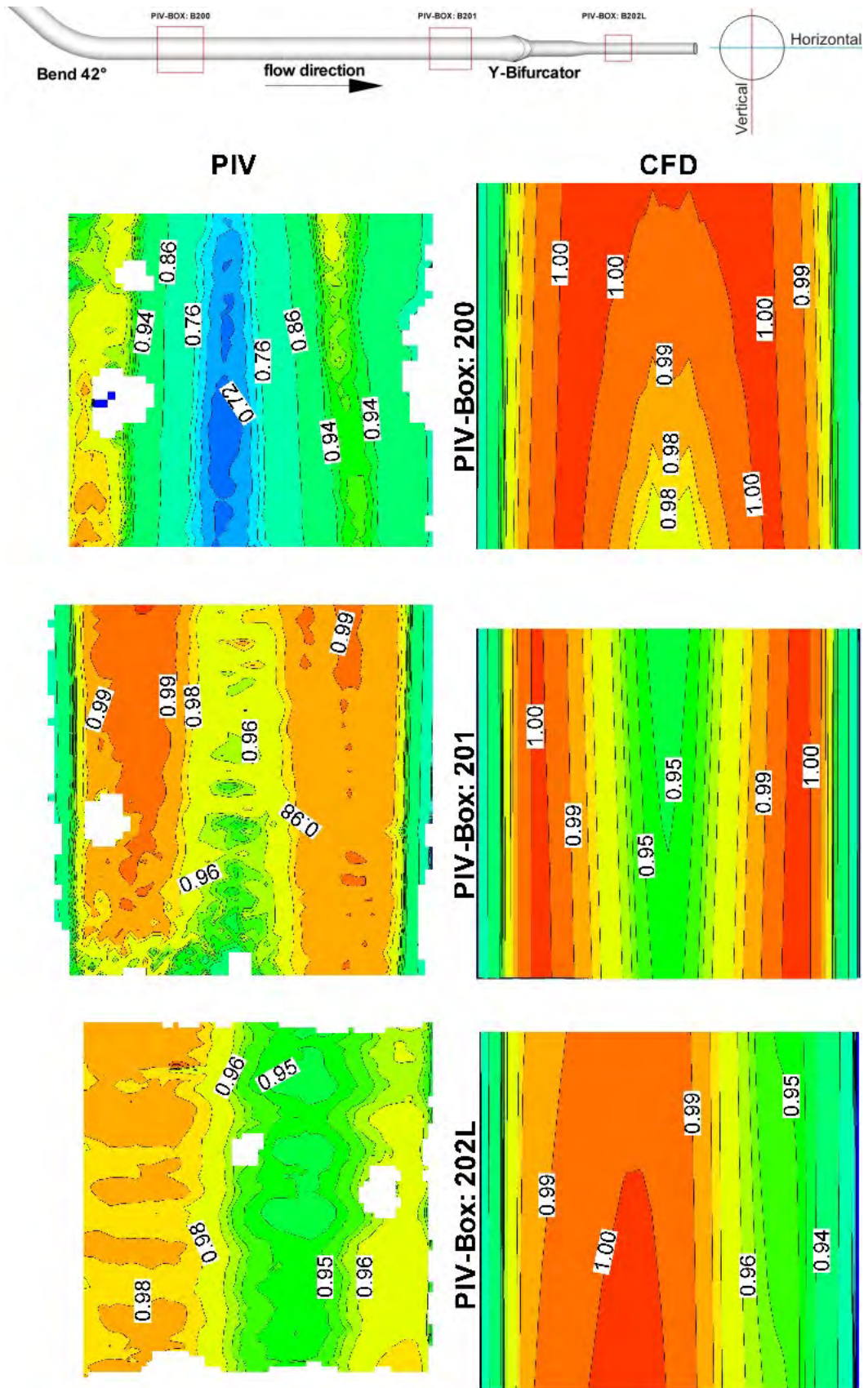
Figure 7.1: *Comparison of PIV-CFD velocity distributions (normalized with v_{max}), symmetrical flow with Q_{main} = 160 ℓ/s - horizontal plane*
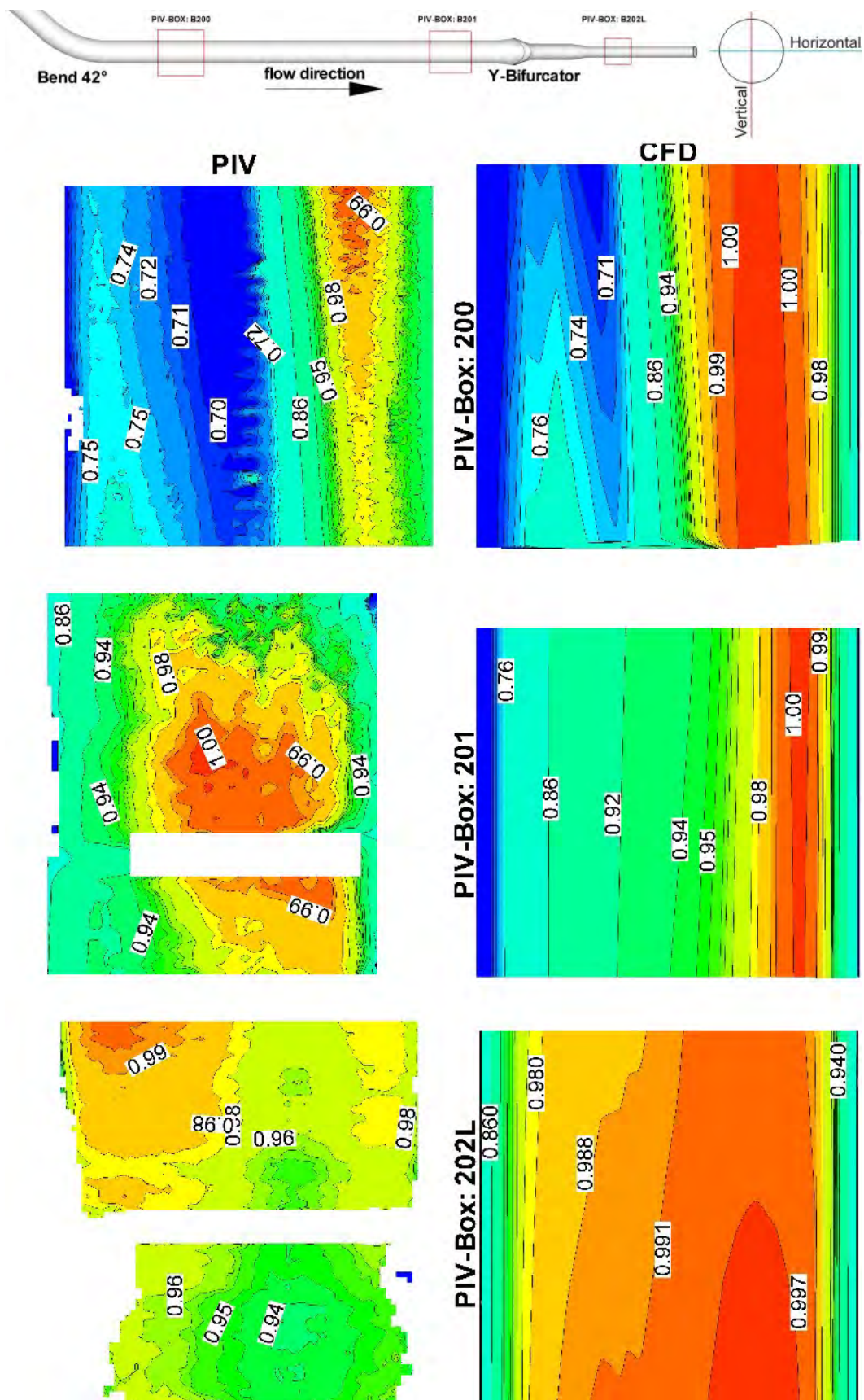
Figure 7.2: *Comparison of PIV-CFD velocity distributions (normalized with v_{max}), symmetrical flow with $Q_{main} = 160 \; \ell/s$ - vertical plane*
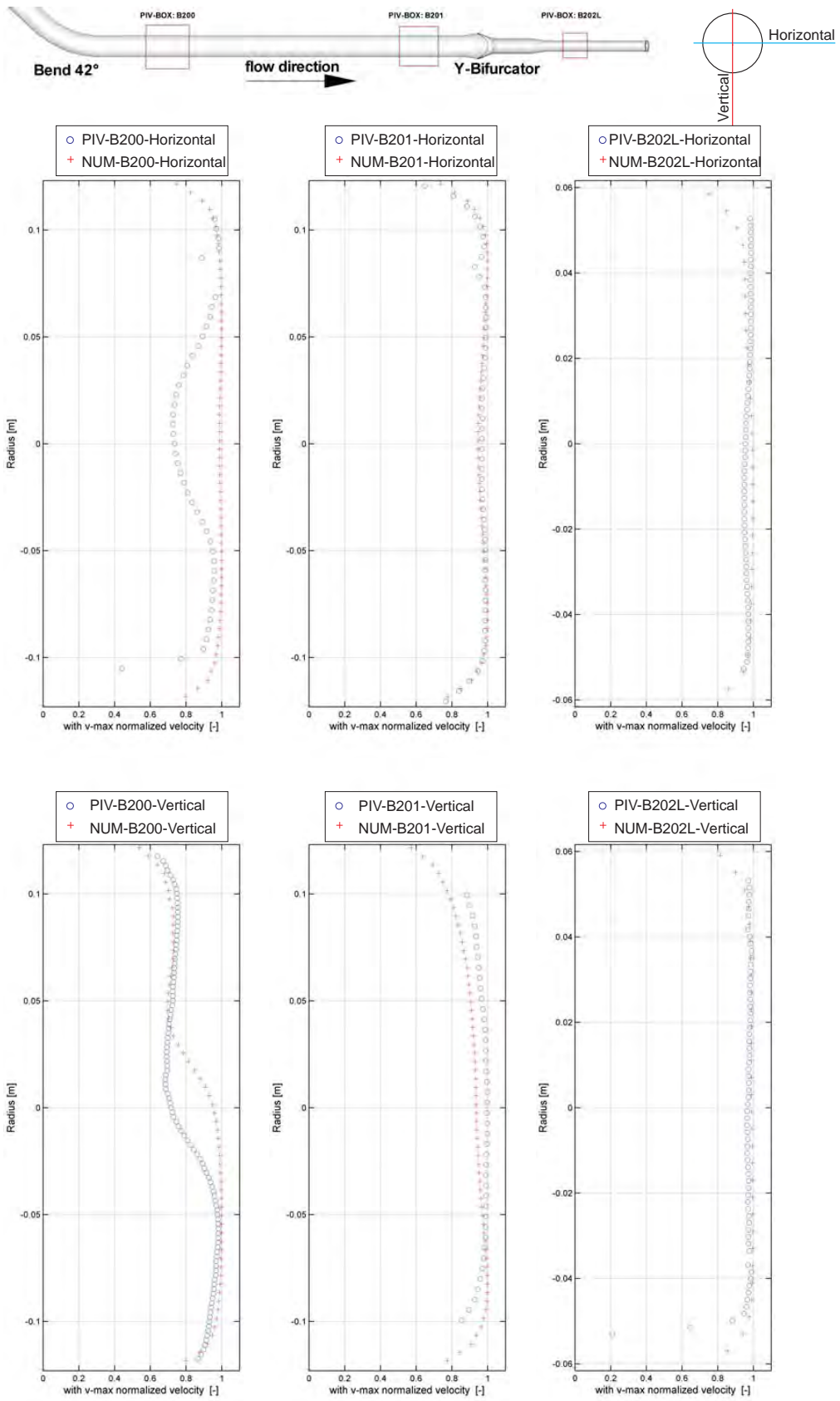
Figure 7.3: *Comparison of PIV-CFD for horizontal and vertical velocity profiles (normalized with v_{max}), symmetrical flow with $Q_{main} = 160 \, \ell/s$*
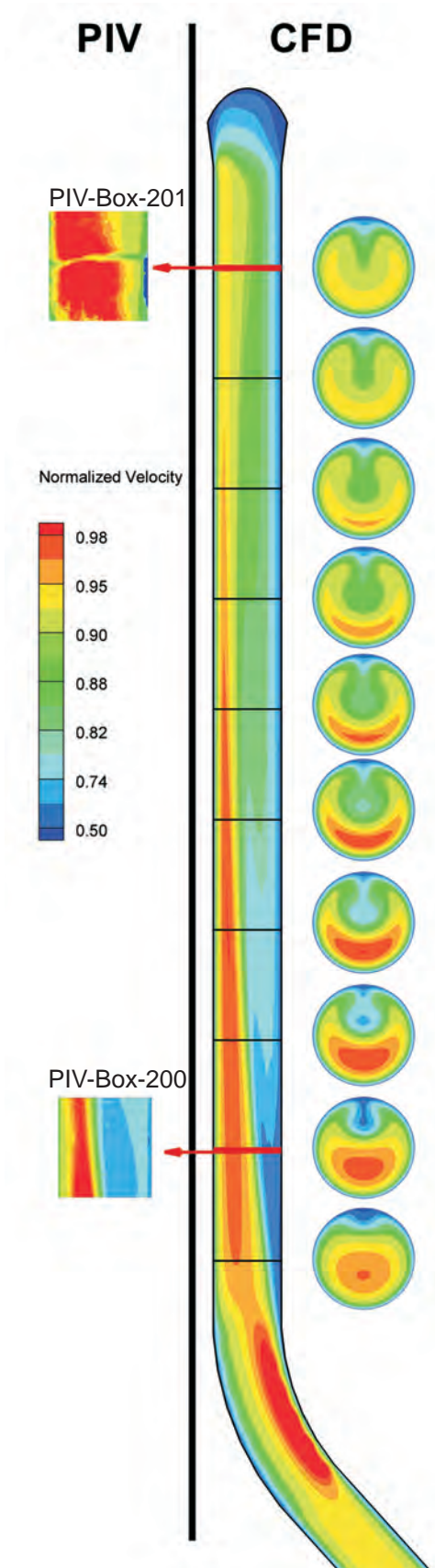
Figure 7.4: *Comparison of the secondary flow: PIV-CFD for vertical velocity with Q_{main} = 160 ℓ/s, flow direction from bottom to top*

7.2   Total head

The differential total head based on the control section M1 (see Figure 3.8) is shown in Figure 7.5. The differential pressure in the numerical simulation is extracted at the pipe-surface and compared with the results of the hydraulic model test. As can be seen, there is a good agreement between the numerical simulation and the model test. The slight asymmetry between branch left and branch right in the model test could not be avoided even though the model set up was done carefully (to avoid the asymmetry of the total head loss for 80 ℓ/s per branch a deviation of 1 ℓ/s is necessary. The deviation of 1 ℓ/s is within the accuracy of the flow meter; see Table 3.2). The good results of the comparison in Figure 7.5 indicate that even with a simple k-ϵ turbulence model the necessity of a hydraulic model test is questionable and could be omitted.
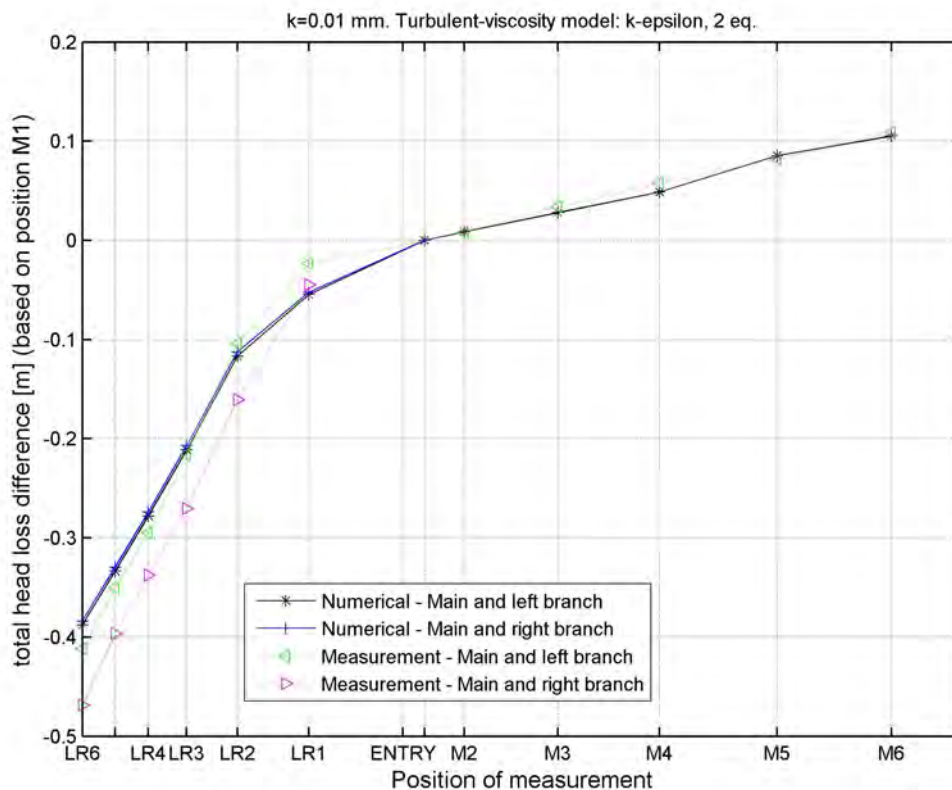
Figure 7.5: *Comparison of differential total head loss based on control section M1 with* $Q_{left} = Q_{right} = 80 \, \ell/s$

7.3   Kinetic Energy

7.3.1   Kinetic energy of the mean flow

The kinetic energy of the mean flow is shown in Figure 7.6 for the plane which is rotated by 45° against the vertical plane (other planes are also evaluated, but have some missing velocity vectors). The CFD-PIV comparisons are in reasonable agreement for the PIV-Box 200L.
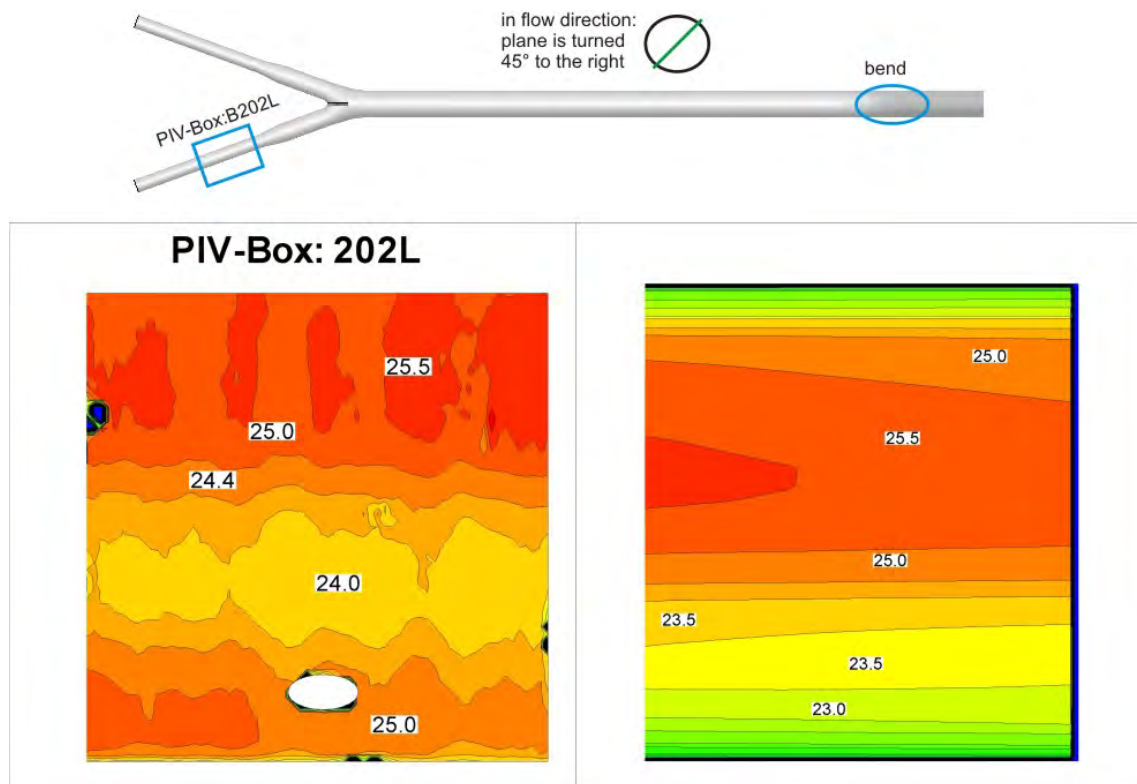
Figure 7.6: *Comparison of the kinetic energy of the mean flow ($\frac{m^2}{s^2}$ per unit mass [kg]) for Q_{main} = 160 ℓ/s, PIV-Box B202L*

7.3.2 Kinetic energy of the turbulent flow

The energy of the mean flow will be transferred via the production P (see Figure 7.11) to the turbulent kinetic energy (see Figure 7.7).
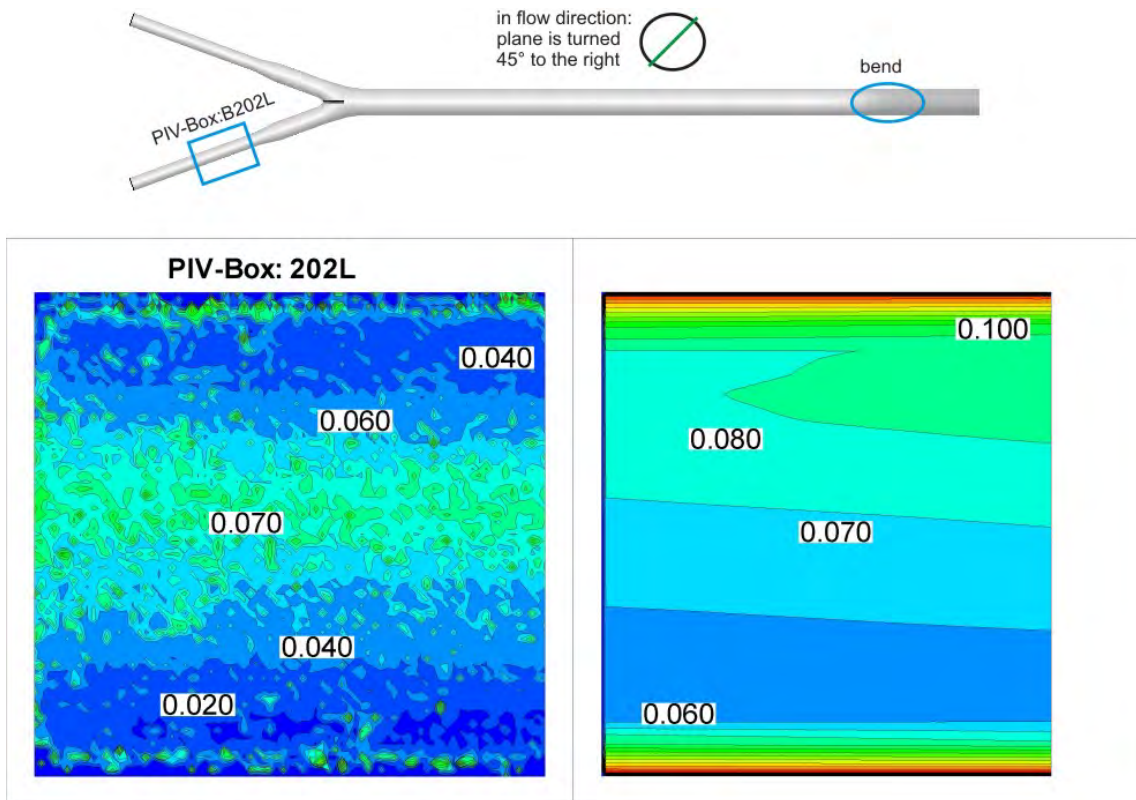
Figure 7.7: *Comparison of the turbulent kinetic energy ($\frac{m^2}{s^2}$ per unit mass [kg]) for Q = 160 ℓ/s, PIV-Box B202L*

7.4 Reynolds stress

The normal and shear stresses are shown in Figure 7.8, Figure 7.9 and Figure 7.10. From the bottom to the middle of the PIV-planes the normal and shear stresses of the PIV-measurements match the CFD results; above the symmetry line a deviation occurs. The presumably reason, as already mentioned at the beginning of the chapter, is that the PIV-measurements are similar to a LES calculation and thus, more accurate than a CFD simulation with the k-ϵ model. Note, that the k-ϵ model calculates isotropic stresses as shown in Figure 7.8 and Figure 7.9 which is not always true in real flows (this behavior is also mentioned in several books, like Pope [2006] or Laurien and Oertel [2009]).

7.4.1 Normal stress
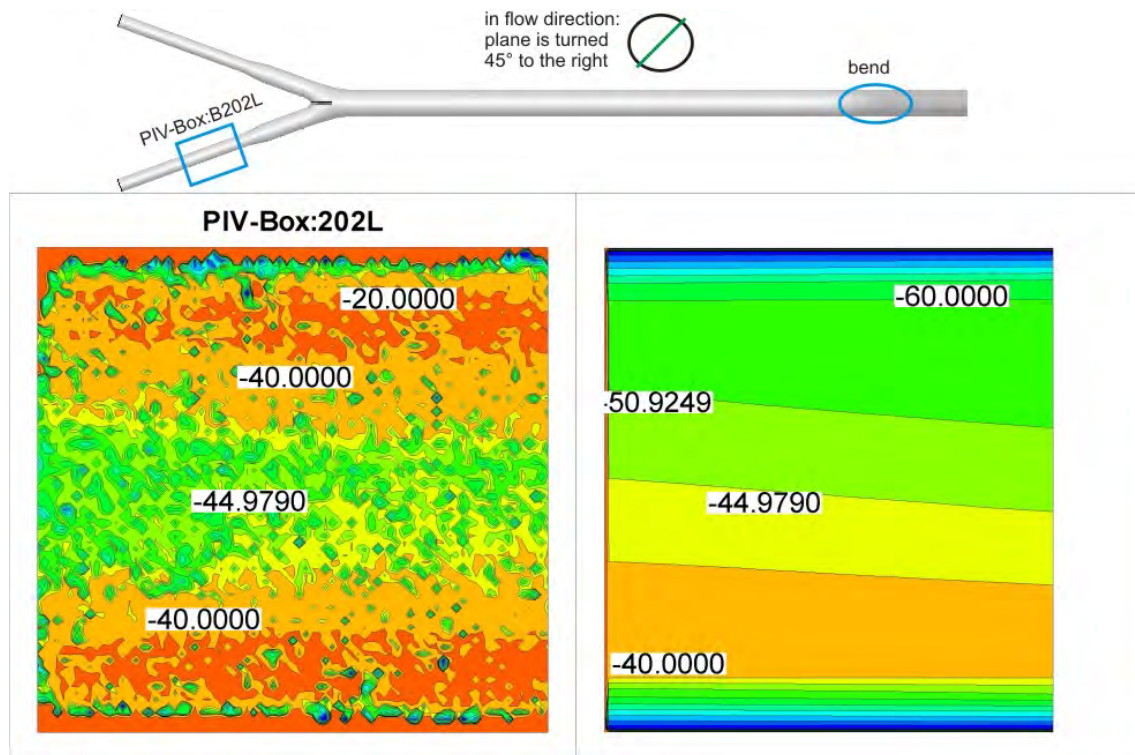
Figure 7.8: *Comparison of the Reynolds stress in longitudinal direction ($\frac{N}{m^2}$) for Q_{main} = 160 ℓ/s , PIV-Box B202L*
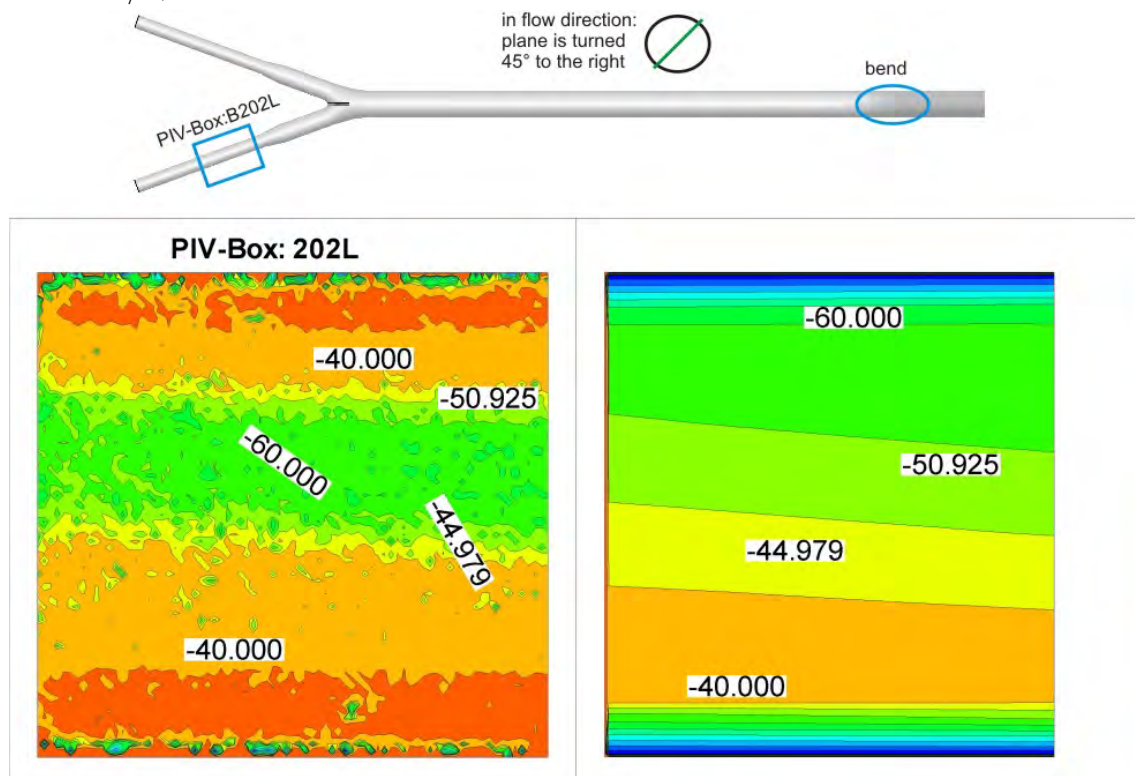
Figure 7.9: *Comparison of the lateral Reynolds stress ($\frac{N}{m^2}$) for Q_{main} = 160 ℓ/s , PIV-Box B202L*

7.4.2 Shear stress
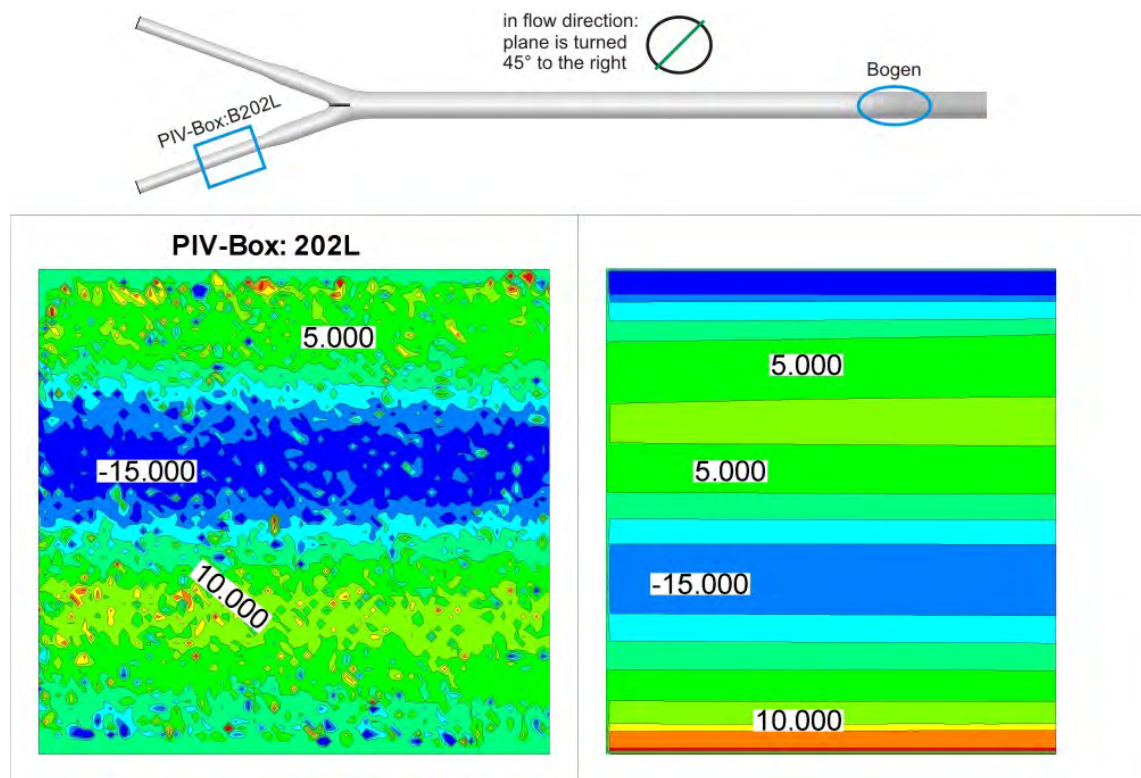
Figure 7.10: *Comparison of the Reynolds shear stress ($\frac{N}{m^2}$) for Q_{main} = 160 ℓ/s , PIV-Box B202L*

7.5 Production

In Figure 7.11 the results for the production of turbulent kinetic energy of the PIV-measurements and CFD-calculations are shown. One of the main difference between the methods is the negative sign of the production in the PIV-measurement which cannot be explained with the turbulent-viscosity hypothesis (there can only be a positive sign). This means that energy is transferred from the turbulent kinetic energy to the mean flow. This behavior is also found in other flows, e.g. in turbulent mixing layers (see Pope [2006]).
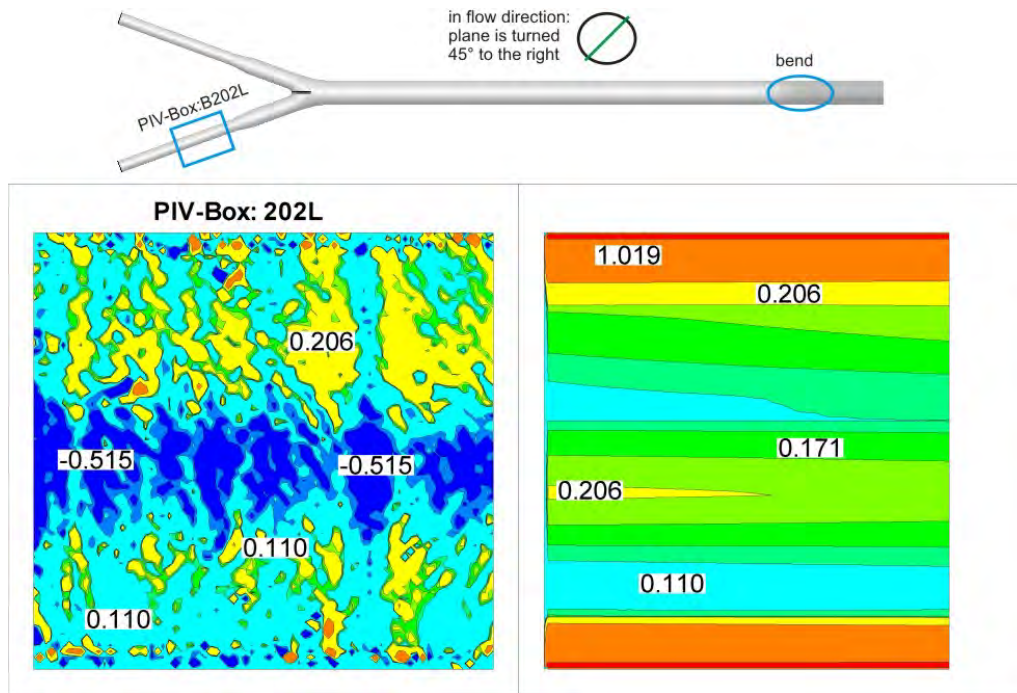
Figure 7.11: *Comparison of the production of turbulent kinetic energy ($\frac{m^2}{s^3}$ per unit mass [kg]) for Q = 160 ℓ/s , PIV-Box B202L*

7.6   Comparison of Fluent with *OpenFoam*

The comparison of **OpenFoam** with Fluent and with measurements in the hydraulic lab is shown in Figure 7.12 to Figure 7.15: The first two pictures show the piezometric head along the left and the main pipe. The numerical simulations show the same results and are in good agreement with the measured piezometer head in the hydraulic model test (see Figure 7.12). The velocity results along the hydraulic model test in the center line show also good agreement between **OpenFoam** and Fluent (see Figure 7.14 Figure 7.15). The secondary flow can also be seen in the velocity plot; after the bend the velocity shows no constant value due to the influence of the bend. The secondary flow which is induced by the bifurcator is smoothed out by the confuser.
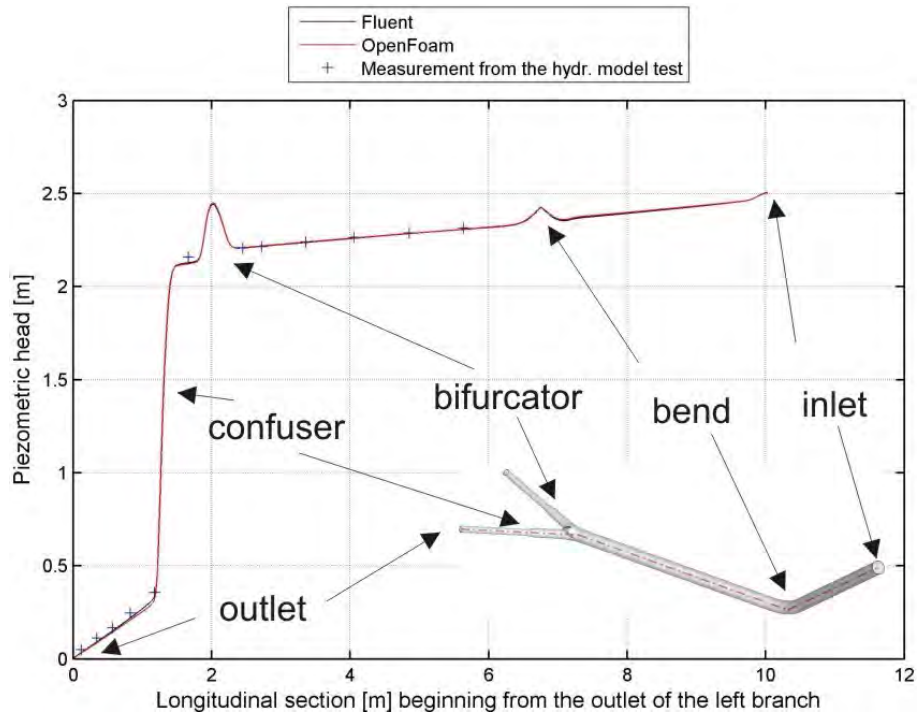
Figure 7.12: *Comparison of the piezometric head of the Fluent and OpenFoam simulations, symmetrical discharge rate with $Q_{main} = 160 \; \ell/s$*
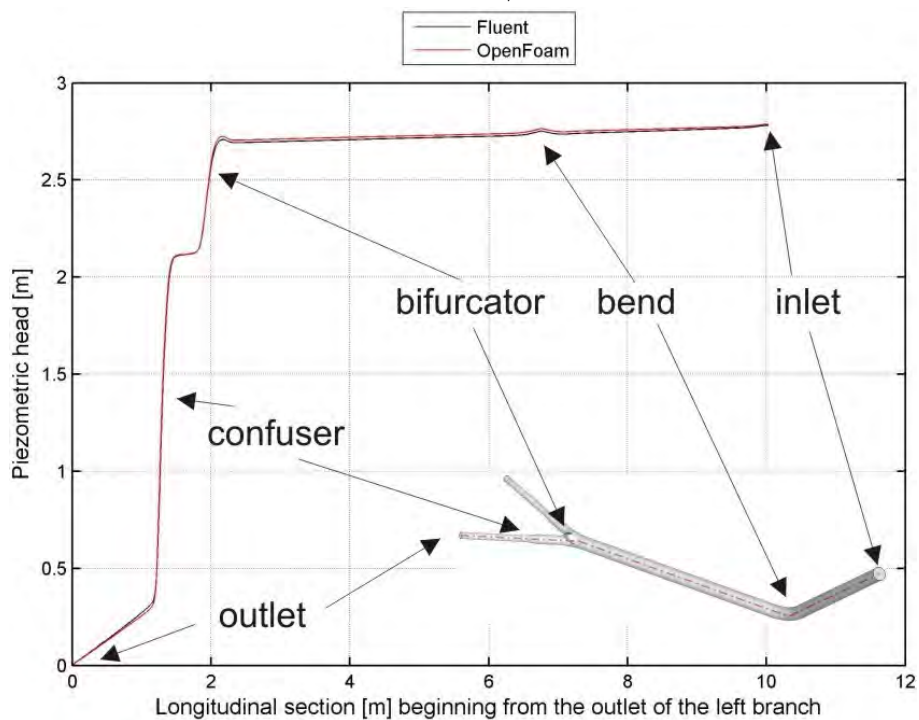
Figure 7.13: *Comparison of the piezometric head of the Fluent and OpenFoam simulations, asymmetrical discharge rate with $Q_{main} = Q_{left} = 80 \; \ell/s$*
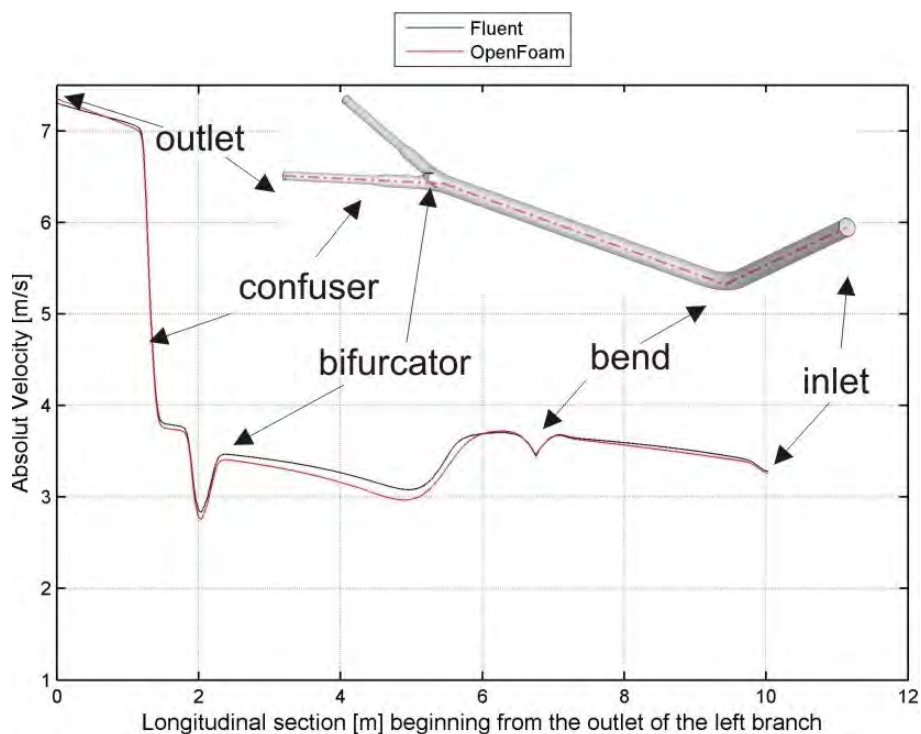
Figure 7.14: *Comparison of the velocities of the Fluent and OpenFoam simulations, symmetrical discharge rate with $Q_{main} = 160 \, \ell/s$*
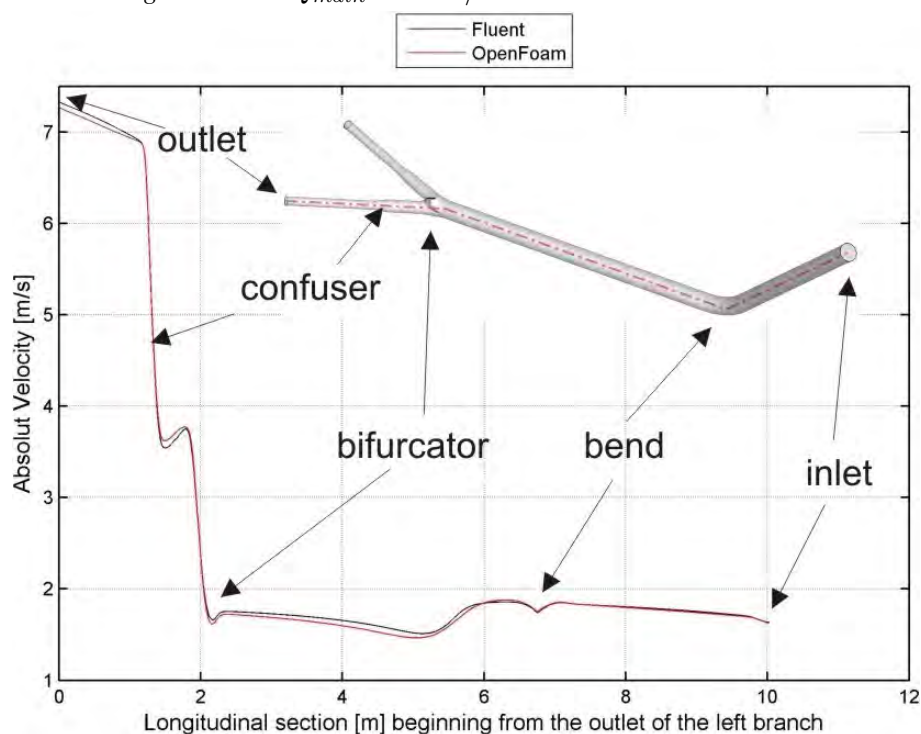
Figure 7.15: *Comparison of the velocities of the Fluent and OpenFoam simulations, asymmetrical discharge rate with $Q_{main} = Q_{left} = 80 \, \ell/s$*

Chapter 8

Water Hammer calculation of Pirris hydro power plant

This chapter presents a water hammer calculation of the Pirris power plant (see Figure 8.1 and Figure 8.2). The whole pipe installation will be discretized and numerically solved with the method of characteristics. The numerical simulation is written as a Matlab/Octave script. The input data for the water hammer calculation (like pressure wave speed, operating level, discharge etc.) are kindly provided by Andritz-Hydro. Two load cases will be simulated

1. Opening in 100 seconds, linearly

2. Closing in 150 seconds, linearly

The goal of the numerical simulation is the calculation of the highest and lowest pressure height in the Y-bifurcator for the load cases. The penstock has no surge chamber. With the known pressure, a design of the Y-bifurcator is possible. The simulation will be double-checked with the commercial software Wanda (Version: 3.72.851). The results of the comparison show good agreement between Wanda and the Matlab/Octave script.
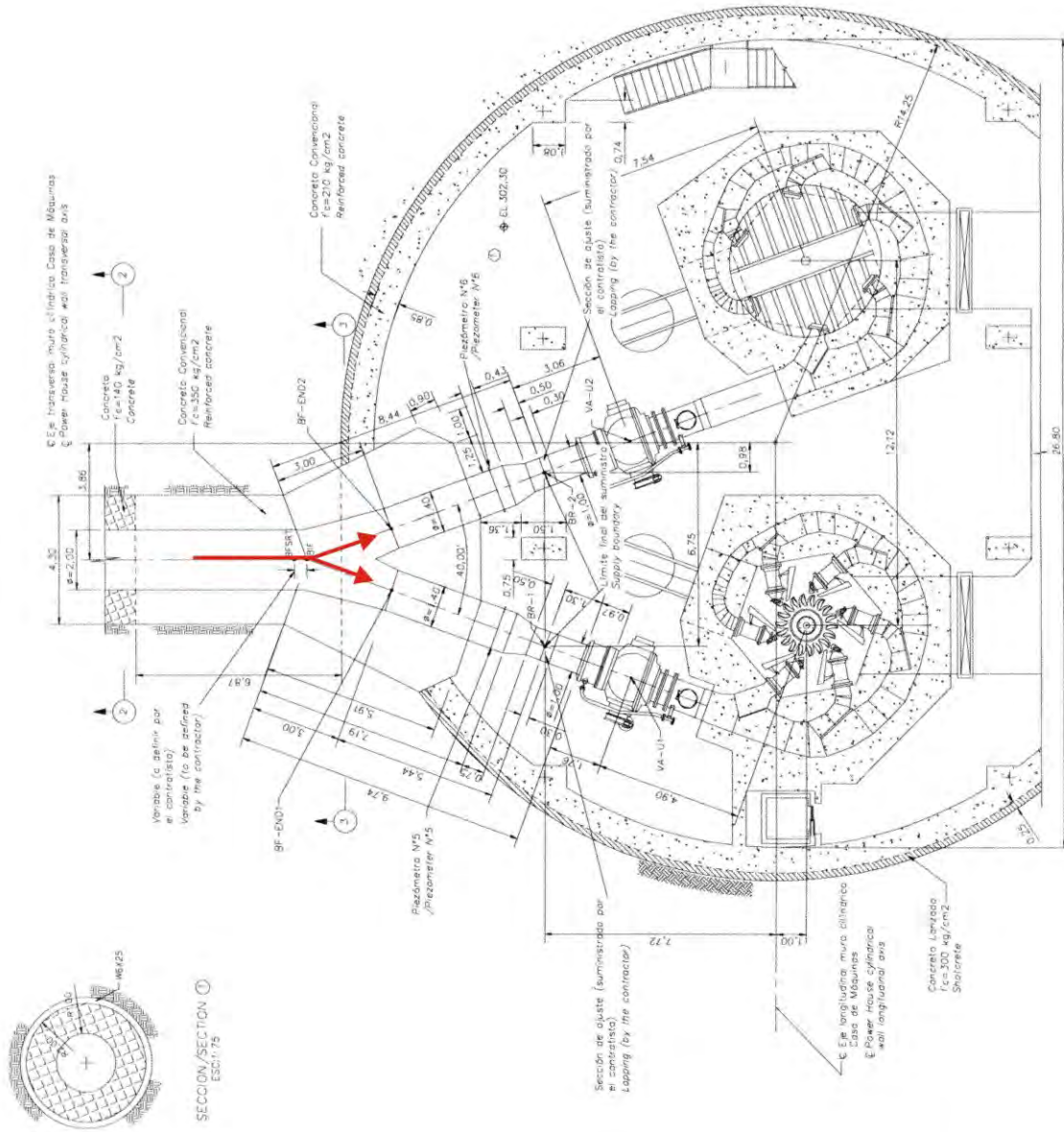
Figure 8.1: *Plan view of the Y-bifurcator*
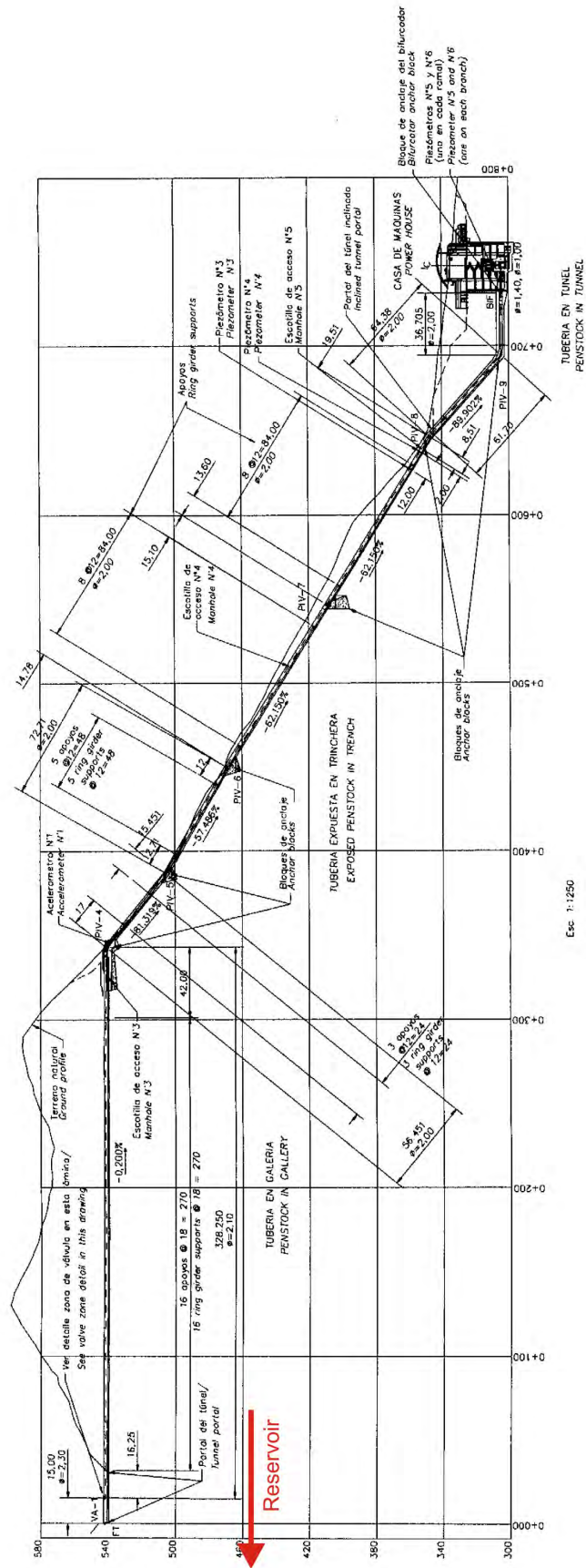
Figure 8.2: *Longitudinal section of the pipe installation*

8.1 Theoretical background for water hammer

If the discharge rate is changed, typically by the turbine or a valve, a water hammer is induced in the penstock. The kinetic energy, when closing a valve, will be changed into pressure energy which can destroy the pipe. However, if the valve opens, pressure energy will be converted into kinetic energy and can cause serious cavitation in the pipe installation. The water hammer is therefore an inertia force due to the change of rate of momentum.

For better convenience, the complete derivations of the equations for the water hammer calculations are in the appendix (see Section 10.2). The resulting equations of the derivations for the pressure height H_P at point p is:

$$H_P = h_U + B \cdot (Q_U - Q_P) - R \cdot (Q_P \cdot |Q_U|)$$
$$H_P = h_R - B \cdot (Q_R - Q_P) + R \cdot (Q_P \cdot |Q_R|) \tag{8.1}$$

With the abbreviations:

$$B = \frac{a}{g \cdot A}$$
$$R = \frac{\Delta x \cdot \lambda}{2 \cdot g \cdot D \cdot A^2} \tag{8.2}$$

where a = pressure wave speed $[m/s]$, g t = acceleration of gravity $[m/s^2]$, A = cross sectional area of the pipe $[m^2]$, Δx = length $[m]$, λ = friction coefficient $[-]$, D = pipe diameter [m] and finally Q = discharge $[m/s^3]$. The indexes U and R stand for a position before and after the index P, respectively.

8.1.1 Time step

The time step is regarded implicitly for the characteristic method. With the length L, which is divided by n integer number elements Δx , one obtains:

$$\Delta t = \frac{\Delta x}{a} \tag{8.3}$$

When more than one pipe element is considered (with different Δx), the time step needs also to be divided into sub-time steps. The sub-time step is a multiple of the global time step (e. g. $t_{global} = 0.1$ s the sub-time step could be: $t_{sub} = 0.05$ s or $t_{sub} = 0.025$ s ; with 2 or 4 iterations the global time step is reached). Therefore, for more than one pipe element either the element length Δx or the pressure wave velocity **a** deviates more or less from the actual value. For all calculations the pressure wave velocity **a** will be slightly modified to fulfill Eq. 8.3 .

8.1.2 Boundary Conditions

For the water hammer calculations 6 boundary conditions are defined; surge chamber, constant discharge or height (e. g. operation level in the reservoir), resistance in the pipe installation, connection between pipes and bifurcation.

8.1.2.1 Constant height

Depending whether the start or the end point of the pipe is considered, a forward or a backward characteristic for the discharge Q is used. With Eq. 8.1 the discharge can be calculated with a backward characteristic for the **pipe-end** point:

$$Q_P = \frac{H_P - h_R + B \cdot Q_R}{B + R \cdot |Q_R|} \tag{8.4}$$

For the **pipe-start** point the forward characteristic gives:

$$Q_P = \frac{H_P - h_U - B \cdot Q_U}{-B + R \cdot |Q_U|} \tag{8.5}$$

8.1.2.2 Constant discharge Q

Depending whether the start or the end point of the pipe is considered, a forward or a backward characteristic for the height H is used. With Eq. 8.1 the height can be calculated with a backward characteristic for the **pipe-end** point:

$$H_P = H_R + B \cdot (Q_P - Q_R) + R \cdot Q_P \cdot |Q_R| \tag{8.6}$$

For the **pipe-start** point the forward characteristic gives:

$$H_P = H_U - B \cdot (Q_P - Q_U) - R \cdot Q_P \cdot |Q_U| \tag{8.7}$$

8.1.2.3 Y-Bifurcation

For the Y-Bifurcation two equations need to be satisfied:

$$\sum Q = Q_{Pipe1} + Q_{Pipe2} + Q_{Pipe3} = 0 \tag{8.8}$$

$$h = h_{Pipe1} = h_{Pipe2} = h_{Pipe3} \tag{8.9}$$

Depending whether the start or the end point of the bifurcation is considered, Eq. 8.9 will be rewritten with the characteristic equations (Eq. 8.1). The following terms are obtained (from A_{Bif} to D_{Bif}):

$$A_{Bif} = -H_{(Pipe1,Position)} - Vz_1 \cdot B \cdot Q_{(Pipe1,Position)} \tag{8.10}$$

$$B_{Bif} = -B \cdot Vz_1 - R \cdot Vz_1 \cdot \left|Q_{(Pipe1,Position)}\right| \tag{8.11}$$

$$C_{Bif} = -H_{(Pipe2,Position)} - Vz_2 \cdot B \cdot Q_{(Pipe2,Position)} \tag{8.12}$$

$$D_{Bif} = -B \cdot Vz_2 - R \cdot Vz_2 \cdot \left|Q_{(Pipe2,Position)}\right| \tag{8.13}$$

$$E_{Bif} = -H_{(Pipe3, Position)} - Vz_3 \cdot B \cdot Q_{(Pipe3, Position)} \qquad (8.14)$$

$$F_{Bif} = -B \cdot Vz_3 - R \cdot Vz_3 \cdot \left| Q_{(Pipe3, Position)} \right| \qquad (8.15)$$

where *Position* indicates if the pipe-end or the pipe start point is considered. The variable Vz, which stands for the sign (- or +), is automatically determined with the *Position*. B and R are defined from Eq. 8.2. Finally, the terms A_{Bif} to D_{Bif} can be used to calculate the pressure height h and the discharge Q:

$$h = \frac{-\frac{A_{Bif} \cdot Vz_1}{B_{Bif}} - \frac{C_{Bif} \cdot Vz_2}{D_{Bif}} - \frac{E_{Bif} \cdot Vz_3}{F_{Bif}}}{\frac{Vz_1}{B_{Bif}} + \frac{Vz_2}{D_{Bif}} + \frac{Vz_3}{F_{Bif}}}$$

$$Q_{(Pipe1)} = \frac{h + A_{Bif}}{B_{Bif}}$$

$$Q_{(Pipe2)} = \frac{h + C_{Bif}}{D_{Bif}}$$

$$Q_{(Pipe3)} = \frac{h + E_{Bif}}{F_{Bif}} \qquad (8.16)$$

8.1.2.4 Pipe Connection

For a pipe-connection (e. g. Pipe 1 with Pipe 2) two equations are necessary:

$$Q = Q_{Pipe1} = Q_{Pipe2} \qquad (8.17)$$

$$h = h_{Pipe1} = h_{Pipe2} \qquad (8.18)$$

A forward and a backward characteristic is used for h_{Pipe1} and h_{Pipe2}, respectively. Solving the equation for Q and h yields:

$$Q = \frac{h_{(Pipe1)} + B \cdot Q_{(Pipe1)} - h_{(Pipe2)} + B \cdot Q_{(Pipe2)}}{B + R \cdot \left| Q_{(Pipe1)} \right| + B + R \cdot \left| Q_{(Pipe2)} \right|}$$

$$h = \frac{\left(B + R \cdot \left| Q_{(Pipe2)} \right| \right) \cdot \left(h_{(Pipe1)} + B \cdot Q_{(Pipe1)} \right) - \left(B + R \cdot \left| Q_{(Pipe1)} \right| \right) \cdot \left(h_{(Pipe2)} - B \cdot Q_{(Pipe2)} \right)}{B + R \cdot \left| Q_{(Pipe2)} \right| + B + R \cdot \left| Q_{(Pipe1)} \right|}$$

$$(8.19)$$

whereas B and R are defined from Eq. 8.2.

8.1.2.5 Pipe Connection with a resistance

Similar to the equations for the pipe-connection an additional term is included for the pressure height:

$$Q = Q_{Pipe1} = Q_{Pipe2} \qquad (8.20)$$

$$\Delta h = h_{Pipe1} - h_{Pipe2} \qquad (8.21)$$

and for Δh, the additional head loss, one can write:

$$\Delta h = \zeta_{Resistance} \cdot \frac{V^2}{2 \cdot g} \tag{8.22}$$

A forward and a backward characteristic is used for h_{Pipe1} and h_{Pipe2}, respectively. Solving the equation for Q and h yields:

$$
\begin{aligned}
Term_1 &= \frac{\zeta_{Resistance}}{2 \cdot g \cdot A_{throttle}^2} \\
Term_2 &= -B - R \cdot |Q_{Pipe1}| - B - R \cdot |Q_{Pipe2}| \\
Term_3 &= H_{Pipe1} + B \cdot Q_{Pipe1} - H_{Pipe2} + B \cdot Q_{Pipe2}
\end{aligned}
\tag{8.23}
$$

whereas B and R are defined for Eq. 8.2, Q is the discharge, H is the height, g is the acceleration and $A_{throttle}$ is the throttle cross section. $Term_1$ to $Term_3$ are used to solve the quadratic equation:

$$
\begin{aligned}
Solution_1 &= \frac{-Term_2 + \sqrt{Term_2^2 - 4 \cdot Term_1 \cdot Term_3}}{2 \cdot Term_1} \\
Solution_2 &= \frac{-Term_2 - \sqrt{Term_2^2 - 4 \cdot Term_1 \cdot Term_3}}{2 \cdot Term_1} \\
Q &= Solution_{1,2} \\
\Delta h &= \frac{Q \cdot |Q|}{A_{throttle}^2 \cdot 2 \cdot g} \cdot \zeta_{throttle}
\end{aligned}
\tag{8.24}
$$

8.1.2.6 Surge chamber

For the surge chamber the condition (Giesecke and Mosonyi [1997]):

$$dV = A_W \cdot dz = A_W \cdot (z_P - z_3) \tag{8.25}$$

is used, whereas z_P is the actual height (at time step j) and z_3 is the former height (at time step j-1) in the surge chamber. A_W $[m^2]$ is the cross sectional area of the surge chamber. Rewriting Eq. 8.25 yields:

$$(z_P - z_3) = \frac{Q_p + Q_3}{2 \cdot A_W} \cdot \Delta t \tag{8.26}$$

whereas Q_P is the actual discharge rate into the chamber and Q_3 the former discharge. For the new height z_P Eq. 8.26 can be written as:

$$z_P = z_3 + \frac{\Delta t}{2 \cdot A_W} \cdot Q_P + \frac{\Delta t}{2 \cdot A_W} \cdot Q_3 \tag{8.27}$$

If a throttle is used in the surge chamber an additional term is defined for Eq. 8.27:

$$h_{throttle} = \pm \frac{\zeta_{throttle}}{2 \cdot g \cdot A_{throttle}^2} \cdot Q_{throttle}^2 \qquad (8.28)$$

where, $h_{throttle}$ = loss of height, $\zeta_{throttle}$ = loss coefficient, $A_{throttle}$ = cross section and $Q_{throttle}$ = discharge rate of the throttle. Further details about water chambers can be found in Richter and Dobler [2011], Richter et al. [2012], Gabl et al. [2011] and Heigerth [1970].

8.2 Calculation procedure and results

8.2.1 Input data

The input data to calculate the water hammer of the Pirris hydro power plant is provided by Andritz-Hydro. The general pipe installation is shown in Figure 8.3; for the main Pipe between the reservoir and the bifurcation 20 pipe elements are defined. Downstream of the bifurcation, two pipe elements for each branch are defined. The whole installation can also be seen in Figure 8.1 and Figure 8.2.

The detailed input data for the water hammer calculation are given in Table 8.1.
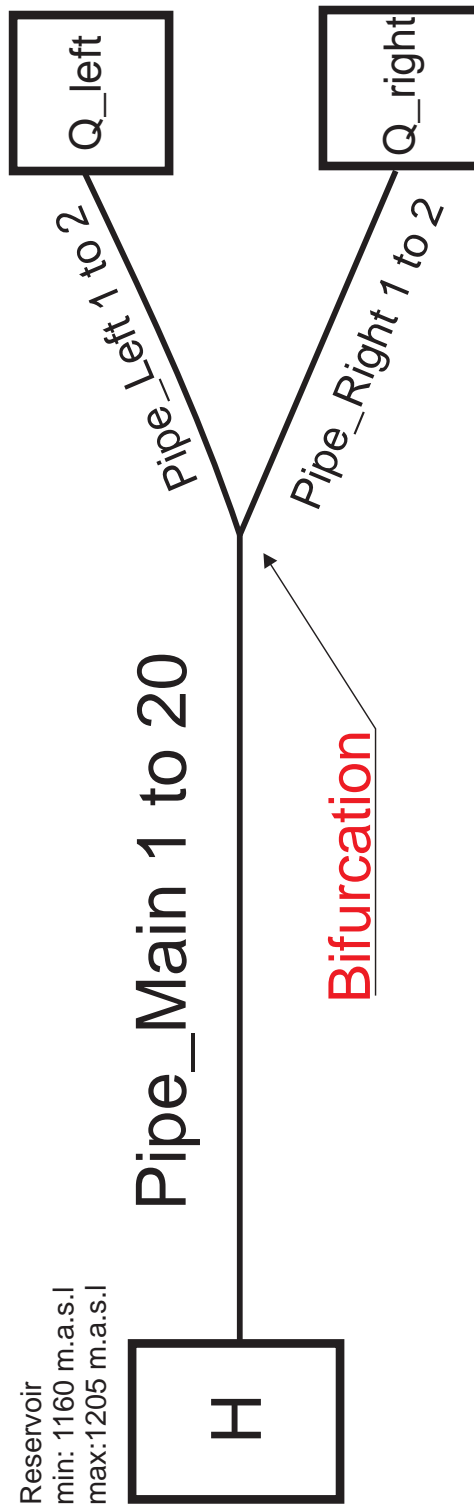
Figure 8.3: *Sketch of the pipe elements*

Table 8.1: *Input Data for the pipe elements: dx = length of element, Knots = number of knots, a theo = theoretical pressure wave speed, a actual = actual pressure wave speed, ratio of theoretical and actual pressure wave speed, Length = length of pipe, Diameter = diameter of pipe, ks = sand roughness and H1, H2 = geodetic height of pipe.*

Name	dx	Knots	a theo	a actual	1-theo/actual	Length	Diameter	k_s	H1	H2
	[m]	[-]	[m/s]	[m/s]	[%]	m	m	mm	m. a. s. l.	m. a. s. l.
Pipe_Main_1	6.250	137	1200	1250.0	4.00	850.0	3.90	0.8	1120.00	1106.00
Pipe_Main_2	5.172	59	1000	1034.5	3.33	300.0	3.90	0.8	1106.00	1101.64
Pipe_Main_3	6.250	21	1200	1250.0	4.00	125.0	3.40	0.8	1101.64	1099.64
Pipe_Main_4	6.250	69	1200	1250.0	4.00	425.0	3.90	0.8	1099.64	1092.85
Pipe_Main_5	6.306	223	1200	1261.3	4.86	1400.0	4.60	0.8	1092.85	1070.49
Pipe_Main_6	6.250	17	1200	1250.0	4.00	100.0	3.90	0.8	1070.49	1068.90
Pipe_Main_7	6.129	63	1200	1225.8	2.10	380.0	3.40	0.8	1068.90	1062.83
Pipe_Main_8	6.301	147	1200	1260.3	4.78	920.0	3.90	0.8	1062.83	991.85
Pipe_Main_9	6.295	557	1200	1259.0	4.69	3500.0	3.90	0.8	991.85	721.82
Pipe_Main_10	6.250	137	1200	1250.0	4.00	850.0	2.67	0.8	721.82	656.25
Pipe_Main_11	5.750	21	1200	1150.0	4.34	115.0	2.30	0.8	656.25	647.37
Pipe_Main_12	3.400	11	1360	1360.0	0.00	34.0	2.30	0.8	647.37	644.75
Pipe_Main_13	6.290	241	1200	1258.0	4.61	1509.6	2.30	0.8	644.75	542.00
Pipe_Main_14	6.129	57	1200	1225.7	2.10	343.2	2.11	0.8	542.00	541.32
Pipe_Main_15	5.650	11	1100	1130.0	2.66	56.5	2.00	0.8	541.32	505.70
Pipe_Main_16	2.796	27	1100	1118.5	1.65	72.7	2.00	0.8	505.70	469.47
Pipe_Main_17	6.128	15	1200	1225.7	2.10	85.8	2.00	0.8	469.47	428.77
Pipe_Main_18	5.363	17	1100	1072.5	2.56	85.8	2.00	0.8	428.77	388.08
Pipe_Main_19	5.682	23	1100	1136.4	3.20	125.0	2.00	0.8	388.08	304.50
Pipe_Main_20	1.373	27	1098	1098.5	0.04	35.7	2.00	0.8	304.50	304.50
Pipe_Left_1	2.875	5	1100	1150.0	4.35	11.5	1.19	0.8	304.50	304.50
Pipe_Left_2	1.875	5	1500	1500.0	0.00	7.5	1.00	0.8	304.50	304.50
Pipe_Right_1	2.875	5	1100	1150.0	4.35	11.5	1.18	0.8	304.50	304.50
Pipe_Right_2	0.917	7	1447	1466.7	1.34	5.5	1.00	0.8	304.50	304.50

The boundaries for water hammer calculation are shown in Table 8.2

Table 8.2: *Boundaries and time step for opening and closing.*

Simulation - Opening			
Time Step [s]	0.005		
End Time [s]	1000		
Reservoir level			
H [m. a. s. l.]	1160		
Discharge left turbine			
Time [s]	0	100	1000
Discharge [m3/s]	0	9.9	9.9
Discharge right turbine			
Time [s]	0	100	1000
Discharge [m3/s]	0	9.9	9.9

Simulation - Closing				
Time Step [s]	0.005			
End Time [s]	1000			
Reservoir level				
H [m. a. s. l.]	1205			
Discharge left turbine				
Time [s]	0	60	150	1000
Discharge [m3/s]	9.9	7.7	0	0
Discharge right turbine				
Time [s]	0	60	150	1000
Discharge [m3/s]	9.9	7.7	0	0

8.2.2   Results for the water hammer of the bifurcation

The results for the head level in the pipe installation are shown in Figure 8.4. The maximum head level of 1242.2 [m. a. s. l.] occurs when the discharge is linearly reduced from 9.9 to 7.7 and finally to 0.0 m^3/s. The maximum allowable head level in the pipe installation is 10% of the maximum static head level in the nozzle corresponding to 1295.05 [m. a. s. l.] according to Andritz Hydro. The minimum head level of 1084.7 [m. a. s. l.] belongs to the linear opening of the turbines; no cavitation takes place. Note, that only two load cases are represented here whereas Andritz Hydro investigated several other flow conditions with non-linear closing and opening procedures.

The water hammer in the bifurcation is shown in Figure 8.5 and Figure 8.6: The geodetic height of the Y-bifurcator is 304.5 [m. a. s. l.]. With the maximum head level of 1241.5 [m. a. s. l.] a maximum pressure of 937 [MWC] is obtained. The numerical calculation is also compared with Wanda (Version: 3.72.851); both results for opening and closing are in good agreement with the numerical code. The slight differences between the curves are due to the slightly different pressure wave speed of the pipes (see also Section 8.1.1). With the results of the minimum and maximum pressure in the Y-bifurcator a structural design can be carried out (not shown here). The satisfying results of the water hammer code are encouraging for further implementations of boundaries, like differential effects in surge chambers or degassing processes.
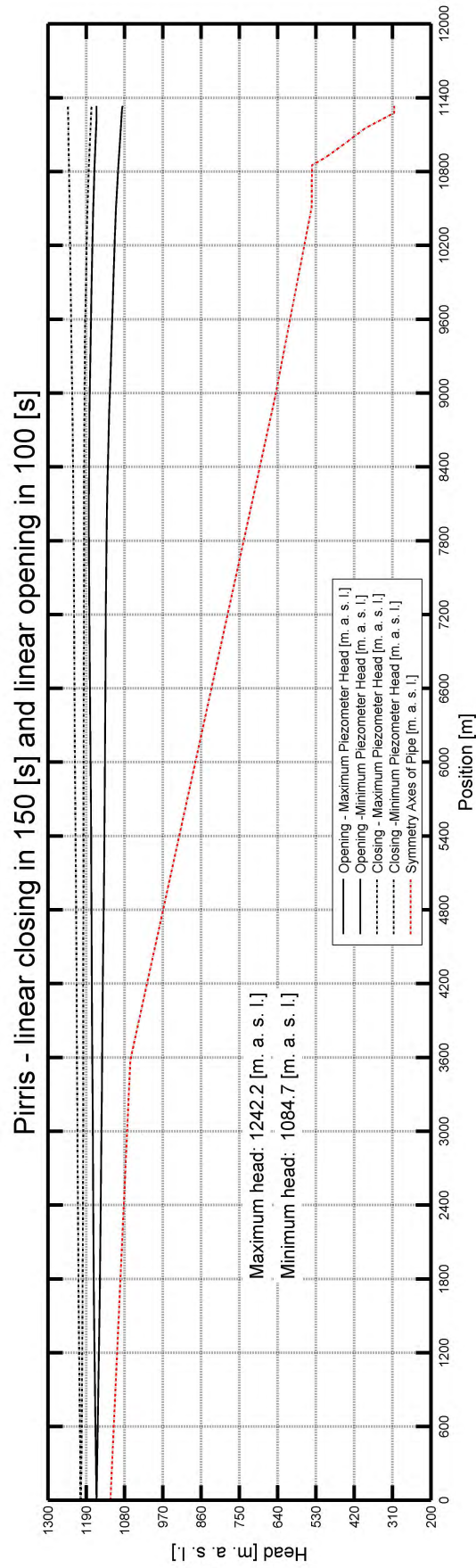
Figure 8.4: *Piezometric line of the pipe installation for opening and closing.*
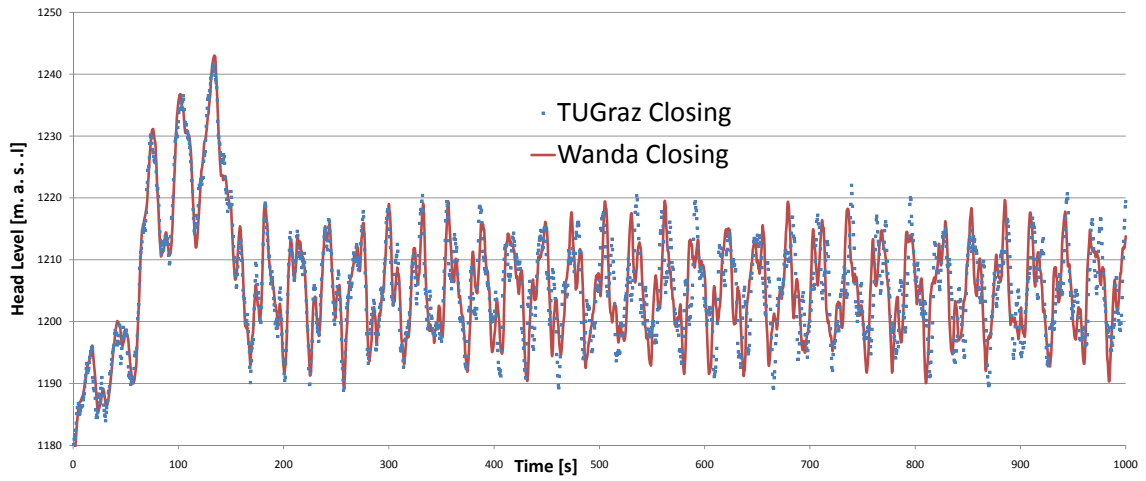
Figure 8.5: *Head level of the bifurcator for linear closing. The maximum Head level is 1241.5 [m. a. s. l.]*
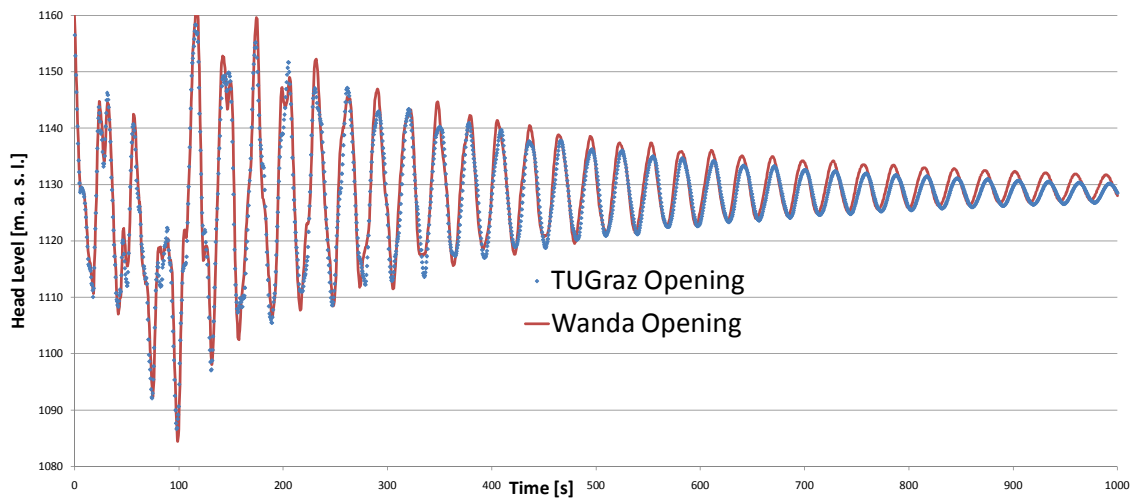
Figure 8.6: *Head level of the bifurcator for linear opening. The minimum Head level is 1086.7 [m. a. s. l.]*

Chapter 9

Summary and Outlook

9.1 Summary

In this thesis, the hydraulic investigation of a Y-bifurcator has been presented. The hydraulic model, which consists of plexiglass, was used to measure the energy loss along the pipe installation. This has been achieved with careful investigations of secondary flows via Particle Image Velocimetry and differential pressure measurements. With several numerical simulations further insight into the flow behavior could be gained. The main findings of this thesis are as follows:

Particle Image Velocimetry

The results of the hydraulic investigations of the flow behavior of a typical Y-Bifurcator have shown that the Particle Image Velocimetry (PIV), together with differential pressure measurements and Computational Fluid Dynamic simulations is a very effective tool to describe the performance of the Y-bifurcator. Due to the fact that a bend is located in the pipe installation upstream of the Y-bifurcator (15 times the pipe diameter) a secondary flow occurs. In order to be able to measure the head loss of the Y-bifurcator the velocity distribution needs to be known which is achieved by PIV. The results of the PIV-data, after having validated the velocity vectors, have shown that the reliability of the mean value of the velocity distribution and the standard deviation was considerably good, that is, the mean value of the flow deviated only around $7\,\%o$ in most cases. These velocity distributions have been measured with the natural seeding of the flow. In order to investigate the velocity lag of the seeding a microscope had been used to determine the diameter of the seeding. On account of the law of Stokes it could been shown that the seeding can follow the flow up to a turbulent frequency of 1.4 kHz. This is an encouraging result for further investigations with PIV when only natural seeding particles are available. The velocity correction factor α has been between 1.01 and 1.1 for the secondary flow. Care has been taken with the near wall velocities to calculate the α-value: due to the fact that the velocities close to the wall cannot be measured with PIV a linear function has been used to close that gap. The influence of this procedure has been checked with an analytical velocity profile, with which more and more of the profile has been replaced by a linear function. The result of this procedure showed that for small gaps (1-2% of the diameter) which have been closed with a linear function a deviation of only 2% occurred. Furthermore, due to the fact that four velocity planes have been available for one cross section the mean of the α-values has been calculated. To verify if the mean value of the four planes would be sufficient a 3D numerical simulation with Fluent has been carried out. In this simulation the α-value for the whole cross section as well as for the four planes has been calculated. The result of the comparison showed that the α-value for the four velocity profiles deviated only about 0.1 % from the full cross section of the CFD simulation.

Hydraulic losses - Loss coefficient ζ

After the secondary flow has been determined with the velocity correction factor α the Bernoulli equation has been used to calculate the head loss of the bifurcation. The loss coefficient ζ was defined as the head loss Δh divided by the kinetic velocity height, and by excluding any pipe friction. This has been done by defining substitute-cylinders between two control sections and by using the Colebrook and the Darcy-Weisbach equations in order to calculate the pipe friction and subtracting it from the measured head loss Δh. The equivalent sand roughness k_s, which is needed for the Colebrook equation to determine the pipe friction coefficient λ, has been measured by two different methods. The first method made use of the differential pressure loss between several control sections where in fact a linear friction gradient exists. With the known head loss Δh and with the Darcy-Weisbach equation and the Colebrook equations the equivalent sand roughness k_s has been evaluated. The other method of the k_s calculation made use of Particle Image Velocimetry (PIV) data. Close to the wall a universal law of velocity distribution comes into effect which is also known as the logarithmic law of the wall. With the measured axial velocity u and the corresponding distance y from the wall as well as the application of the equation of the law of the wall the equivalent sand roughness for rough pipes k_s could be calculated. The calculated k_s-value for both methods has been 0.015 mm.

The hydraulic model test is scaled after the Reynolds law which implies that the velocity in the model test equals the velocity of the prototype times the scale factor. This yields a velocity in the model test up to 43 m/s which is far too high for the pumps in the laboratory. In order to overcome this problem the head loss Δh as function of the discharge rate has been decomposed into a polynomial function with a quadratic, linear and constant term via the least square method. With the polynomial function the desired head loss has been calculated. Furthermore, a comparison has been carried out to determine whether it would be better to use the quadratic term of the polynomial function to calculate the head loss for higher discharge rates exclusively, or not. This assumption has been based on previous model tests in which the head loss as function of the discharge rate showed a purely quadratic behavior. The comparison showed better results if when exclusively the quadratic term of the least square method has been applied. This has been controlled also by the means of a numerical calculation, in which the desired discharge rate can be set according to the Reynold's model and the resultant head losses can be compared to the extrapolated head losses of the model test. The comparison of the CFD-calculation to the hydraulic model test with the extrapolated values displays good agreement.

To reduce the loss coefficient ζ a guide vane apparatus has been used (this concept had been tested in a previous model test (trifurcator), see also Mayr [2009]). The guide vane induced a swirling flow upstream of the Y-bifurcator. As a result, the loss coefficient could be reduced for one flow distribution.

Computational Fluid Dynamics

Several CFD simulations (Ansys and OpenFoam) have been conducted. The results of the CFD simulations have been compared to the PIV measurements. The quantities which had been compared to one another were: Kinetic energy of the mean flow, turbulent kinetic energy, Reynolds-stress tensor and the production of turbulent kinetic energy. The comparison between CFD and PIV showed acceptable agreement.

With the results of the numerical calculation a comparison of the head losses and the measured velocity distributions has been conducted for the hydraulic model test. The velocity distributions along the hydraulic model show good agreement between PIV and CFD as long as no strong secondary flow occurred. The influence of the secondary flows on the pressure distribution along the pipe has been low and thus - if only the loss coefficient ζ should be of interest - a numerical simulation without a model test will be sufficient in simple pipe flows.

Computational Fluid Dynamics with *OpenFoam*

The comparison of Fluent and *OpenFoam* for the symmetrical (80 ℓ/s per branch) and asymmetrical (only 80 ℓ/s for the left branch) discharge rate has been investigated. The results of the piezometric head as well as of the velocity along the center line of the pipe showed good agreement between Fluent and *OpenFoam*. The results of the symmetrical discharge rate have been also double-checked with the measurements of the hydraulic model test. On account of the promising outcome of *OpenFoam* which is a non- commercial, open source software, it is to be expected that this software will be more and more applied by the industry as well as by practitioners.

Programming of Water-Hammer with the method of characteristics

The water hammer calculation of the Pirris power plant showed a maximum head level of 937 [MWC]. The numerical simulation has been written as a Matlab/Octave script. The differential equations have been numerically solved with the method of characteristics. With the known maximum head level, a design of the Y-bifurcator is possible. The simulation has been double-checked with the software Wanda and shows satisfactory accordance.

9.2   Outlook

Based on Chapter 1 further questions arise concerning the results of the hydraulic investigation of the Y-bifurcator:

1. **Secondary flow**: PIV is a reliable and effective tool to quantify the roughness and the axial secondary flow in the hydraulic model tests. These measurements were obtained with a standard PIV set-up that is with one camera and one laser. With a second camera an even deeper insight into the flow would be possible with which the secondary flow within the cross section (swirl-flow) could even be rendered visible. With the knowledge about the in-plane velocity distribution a more accurate energy balance between two control sections could be achieved.

2. **Roughness**: The roughness measurement in the hydraulic model test with PIV was a very time-consuming procedure due to the reflecting laser-light from the pipe wall. Nevertheless, with a careful set-up a roughness measurement has been carried out successfully. It would be very interesting to compare these measurements - which had been conducted with natural seeding - to the fluorescenting particles with a wavelength other than that of the green laser light. With an optical filter which suppresses the green laser-light (and the reflecting light from the plexiglass wall) the fluorescenting particles could be made visible very well in the PIV-measurement.

3. **Swirling flow**: The guide vane device which has been used to induce the swirling flow - and thus, also to reduce the hydraulic losses - has been optimized to improve the approaching flow to the Kaplan-turbine and has a bulb in the middle of the device. The author expects that without this bulb more load distributions would show lower losses due to the swirling flow.

4. **Scaling effects**: The extrapolation method shown in this thesis to calculate the loss coefficient of the prototype has been double-checked with a numerical simulation. It would be helpful to repeat the numerical simulation with different scales, so that any scaling effects could be made visible. Further, another hydraulic model test based on different scales should be built to investigate the scaling effects.

5. **Computational Fluid Dynamics**: The numerical simulations with *OpenFoam* showed reliable results for a pressurized pipe flow. All further investigations concerning scaling effects should be performed with this free and open software. When the results are satisfactory an efficient tool for further research projects will be at hand.

6. **Water Hammer**: The code for the water hammer calculation has shown reliable results for the Pirris power plant when compared with the commercial Program Wanda. 6 boundaries have been implemented in the code (these are surge chamber, variable height and discharge at the end and starting point of the pipe, bifurcation, connection of two pipes and a resistance/throttle in the pipe). Further boundary elements like a surge chamber which would include differential effects or open channel flow would be worth implementing.

Bibliography

J. D. Anderson. *Computational Fluid Dynamics*. McGraw-Hill, Inc., New York, 1 edition, 1995. ISBN 0-07-11321ß-4.

ANSYS Fluent. Fluent 6.2 User's Guid, 2005. URL http://www.ansys.com.

H. J. Bartsch. *Taschenbuch Mathematischer Formeln*. Fachbuchverlag Leipzig, 18 edition, 1999. ISBN 3-446-21048-2.

B. Basara, H. Grogger, R. Klasinc, and D. Mayr. Experimental and numerical study of the flow through a trifurcation. In *28th IAHR World Congress*, pages 102–103, Graz, 1999.

W. Berner. Trifurkation, Druckverlust im Verteil- und Sammelbetrieb (Trifurcation, Pressure head losses for flow dividing and merging). *Report Nr. WT-70-401, Escher Wyss AG, unpublished*, 1970.

R. Bodo. Strömungsmessgrößen, 2010. URL http://www.gala-ev.org/messgroessen.htm.

K. Brabbée. Reibungs- und Einzelwiderstände in Warmwasserheizungen. *Gesundheits-Ingenieur.*, 36(48), 1913.

E. O. Brigham. *FFT-Anwendungen*. Oldenbourg Verlag, München, 1997. ISBN 3486215671.

C. F. Colebrook. Turbulent Flow in Pipes, with particular reference to the Transition Region between the Smooth and Rough Pipe Laws. *Journal of the Institution of Civil engineers*, 11: 133–156, 1938.

W. Dobler and G. Zenz. Particle Image Velocimetry of a Y-bifurcator. In *34th IAHR World Congress*, pages 2257–2265, Brisbane, 2011. Engineers Australia.

W. Dobler, H. Knoblauch, and G. Zenz. Hydraulic investigation of a Bifurcator. In *1st European IAHR Congress*, volume The First, Edinburgh, 2010a. International Association of Hydraulic Engineering and Research.

W. Dobler, H. Knoblauch, and G. Zenz. Hydraulische Untersuchung an einem Bifurkator. *Wasserbau in Bewegung ... von der Statik zur Dynamik - Beitrag zum 15. Gemeinschafts-Symposium der Wasserbau-Institute TU München, TU Graz und ETH Zürich vom 1. bis 3. Juli 2010 in Wallgau, Oberbayern*, 124:287–296., 2010b.

W. Dobler, M. Larcher, A. Arch, and G. Zenz. Numerische Untersuchung von Rohrströmungen am Beispiel eines Bifurkators. *Österreichische Wasser- und Abfallwirtschaft*, 2010c.

F. Durst. *Grundlagen der Strömungsmechanik*. Springer, Berlin, 1 edition, 2006. ISBN 103-540-313230.

K. Fahrmeir and T. Pigeot. *Statistik*. Springer, Berlin, 6 edition, 2007. ISBN 978-4-540-69713.

R. Gabl, S. Achleitner, J. Neuner, H. Goetsch, and M. Aufleger. 3D-numerical optimization of an asymmetric orifice in the surge tank of a high-head power plant. In *34th IAHR World Congress*, pages 2428–2435, 2011.

A. Gardel. Les pertes de charge dans les branchements en tedes conduites de section circulaire. Lausanne, 1970. Bulletin technique de la suisse romande.

J Giesecke and E Mosonyi. *Wasserkraftanlagen*. Springer-Verlag, Berlin, 1997. ISBN 3-540-60993-8.

G. Goch. Laborskript zur Vorlesung Messtechnik und Sensorik. Bremen, 2008. University of Bremen.

G. Heigerth. *Drossel- und Differential-Wasserschlösser von Regelkraftwerken mit freier Betriebsführung*. PhD thesis, Technische Hochschule Wien, 1970.

H. Herwig. *Strömungsmechanik*. Springer Verlag, Berlin, 2 edition, 2006. ISBN -10 3-540-32441-0.

I. E. Idelchik. *Handbook of Hydraulic Resistance*. CRC Press, Moscow, 3 edition, 1994.

P. Imitzer. Messungen von Geschwindigkeiten an einer Verteilrohrleitung (Trifurcator). *Diploma Thesis, TU-Graz, unpublished*, 2000.

T. Jahrbacher. Messungen der Geschwindigkeitsfelder in Trifurcationen bei drallbehafteter Zuströmung (Measurements of flow velocity on trifurcations with swirl superimposed the main flow). *Diploma Thesis, TU-Graz, unpublished*, 2001.

S. John and A. Gladwell. Hydraulic Studies of Large Penstock Trifurcation. *ASCE Hydraulic Engineering*, 91(1), 1965.

W. P. Jones and B. E: Launder. The prediction of laminarization with a two-equation model of turbulence. *International Journal of Heat and Mass Transfer*, 15:301–304, 1972.

D. L. King. Hydraulic Model Studies of Causey Dam Outlet Works, Weber Basin Project Utah. *United States Department of the Interior Bureau of Reclamation*, page 29, 1963.

L. Kinne. Beitrag zur Kenntnis der hydraulischen Verluste in Abzweigstücken. *Mitteilung des Hydr. Institutes der TH München*, 4, 1931.

R. Klasinc and H. Knoblauch. Head Losses in the Manifolds of Pumped Storage Systems. In *International Symposium on Pumped Storage Development '94*, Nanjing, 1994.

R. Klasinc, H. Knoblauch, and T. Dum. Power losses in distribution pipes. *Fluid flow modeling*, pages 280–291, 1992.

R. Klasinc, G. Heigerth, G. Zarfl, and D. Mayr. Musi II, Trifurcation. *Institut für Wasserbau und Wasserwirtschaft, TU-Graz, unpublished*, 1999.

H. Knoblauch. Dissipationsvorgänge in Rohrleitungssystemen (Energy dissipation in piping system). *Schriftenreihe zur Wasserwirtschaft*, 17, 1995.

H. Kobus. *Wasserbauliches Versuchswesen*. Deutscher Verband für Wasserwirtschaft und Kulturbau e. V. (DVWK), Bonn, 2 edition, 1984. ISBN 3-490-03997-1.

K. Kühlke. *Optik*. Harri Deutsch, Frankfurt, 2 edition, 2007. ISBN 978-8171-1741-3.

U. Lasminto and R. Klasinc. Numerical Modeling of a Y-Bifurcator using Realizable k-epsilon Turbulence Model. In *Fluid Power 2011*, pages 123–132, Maribor, 2011. University of Mariboru.

E. Laurien and H. Oertel. *Numerische Strömungsmechanik*. Vieweg+Teubner, Wiesbaden, 3 edition, 2009. ISBN 9783834805331.

B.K. Lee, H.W. Coleman, J.H. Kim, and H.I. Kwon. Hydraulic model studies of Y-branch. In *Hydraulic Engineering, ASCE*, pages 1689–1694, San Francisco, 1993. ASCE.

Matlab. Product Documentation, 2008. URL http://www.mathworks.de/help/techdoc/index.html.

D. Mayr. *Hydraulic Studies on Trifurcations*. Schriftenreihe zur Wasserwirtschaft, Graz, 58 edition, 2009.

J. S. McNown. Mechanics of manifold flow. *American society of civil engineers*, 119:1103, 1954.

D.S. Miller. *Internal Flow System*. BHRA (Information Services), Cranfield, Bedford MK43 0Aj, UK, 2 edition, 1990.

S F Moujaes and S Deshmukh. Three-Dimensional CFD Predications and Experimental Comparison of Pressure Drop of Some Common Pipe Fittings in Turbulent Flow. *Journal of Energy Engineering*, 132(2):61–66, 2007.

W. Müller and H. Stratmann. Druckverlust in Abzweigrohren und Verteilleitungen. *Technische Rundschau Sulzer*, 4, 1971.

J. Nikuradse. Gesetzmäßigkeiten der turbulenten Strömung in glatten Rohren. *VDI-Forschungsheft*, 3(356):1, 1932.

OpenFoam. OpenFoam, 2010. URL http://www.openfoam.com/features/.

S. V. Patankar and D. B: Spalding. A Calculation Procedure for Heat, Mass and Momentum Transfer in Three-dimensional Parabolic Flows. *Int. J. Heat Mass Transfer*, 15:1787, 1972.

F. Petermann. Der Verlust in schiefwinkligen Rohrverzweigungen. *Mitteilung des Hydr. Institutes der TH München*, 3, 1929.

S. B. Pope. *Turbulent Flows*. Cambridge University Press, Cambridge, 1 edition, 2006. ISBN 13 978-0-521-59125-6.

L. Prandtl. Bericht über Untersuchungen zur ausgebildeten Turbulenz. *ZAMM. Z. angew. Math. Meach.*, 5:136–139, 1925.

G. Preissler. Theoretische Erfassung des hydraulischen Verlustes an einer Rohrvereinigung. *Wissenschaftliche Zeitschrift der Technischen Universität Dresden*, 22, 1973.

G. Preissler and G. Bollrich. *Technische Hydromechanik*. VEB-Verlag für Bauwesen, Berlin, 2 edition, 1985.

M. Raffel, C. Willert, S. Wereley, and J. Kompenhans. *Particle Image Velocimetry*. Springer-Verlag, Berlin, 2 edition, 2007. ISBN 978-3-540-72307-3.

A. S. Ramamurthy, J. Qu, and C. Zhai. 3D Simulation of Combining Flows in 90 Degree Rectangular Closed Conduits. *Journal of Hydraulic Engineering*, 132(2):214–218, 2006. doi: 10.1061/(ASCE)0733-9429(2006)132:2(214).

A. Richter. Energy Head Losses due to a Spherical Pipe Junction for a Power Plant. In *IAHR-Symposion*, Trondheim, 1988.

W. Richter and W. Dobler. Hydraulische Untersuchung einer Düsendrossel mit CFD Simulationen und PIV-Messungen (Hydraulic Investigation of nozzles with CFD and PIV). In *Tagungsband des 13. Treffens junger WissenschaftlerInnen an Wasserbauinstituten*. Eigenverlag des Franzius-Instituts für Wasserbau und Küsteningenieurwesen (Leibniz Universität Hannover), 2011.

W. Richter, W. Dobler, and H. Knoblauch. Hydraulic and numerical modeling of an asymmetric orifice. In *4. IAHR International Symposium on Hydraulic Structures*, Porto, 2012.

A. Ruprecht, C. Bauer, E. Göde, B. Janetzky, P. Llosa, M. Maihofer, and B. Welzel. Strömungseffekte in einem Dreifach-Abzweiger (Flow effects in a trifurcation). In *10. Internationales Seminar Wasserkraftanlagen*, Vienna, 1998.

E. Ruus. Head losses in wyes and manifolds. *Journal of the Hydraulics Division*, 96(3):593–608, 1970.

E. Ruus, R. Syamals, and N. Laksmana. Hydraulic Studies of Large Penstock Trifurcation. *ASCE Journal of the Power Division*, 92(1), 1966.

W Sanz. *Computational Fluid Dynamics (Lecture notes)*. TU-Graz, Graz, 1st edition, 2008.

H. Schlichting and K. Gersten. *Grenzschicht-Theorie*. Springer-Verlag, Berlin, 9th edition, 1997. ISBN 3-540-55744-X.

R. Schröder and U. Zanke. *Technische Hydraulik*. Springer, Berlin, 2 edition, 2003. ISBN 3-540-00060-7.

H. Sigloch. *Technische Fluidmechanik*. Springer-Verlag, Berlin, 6th edition, 2005. ISBN 978-3-540-44633-0.

M. Tadjfar and F. T. Smith. Direct simulations and modelling of basic three-dimensional bifurcating tube flows. *Journal of Fluid Mechanics*, 519:1–32, 2004. ISSN 0022-1120. doi: 10.1017/S0022112004000606. URL http://www.journals.cambridge.org/abstract_S0022112004000606.

J. Ure. Besonderheit beim Bau der Verteilrohrleitung des Pumpspeicherwerks Erzhausen. *Techn. Mitt. Krupp Werksbericht*, 26(3/4):147–154, 1968.

K. H. Versteeg and W. Malalasekera. *Computational Fluid Dynamics*. Pearson Education Limited, Harlow, 2th edition, 2007. ISBN 978-0-13-127498-3.

G. Vogel. Untersuchung über den Verlust in rechtwinkligen Rohrverzweigungen. *Mitteilung des Hydr. Institutes der TH München*, 1:75–90, 1926.

Th. von Kármán. Mechanische Ähnlichkeit und Turbulenz. *Third Int. Congr. Applied Mechanics, Stockholm*, pages 85–105, 1930.

J. V. Williamson and T. J. Rhone. Dividing flow in branches and wyes. *Journal of the Hydraulics Division*, 99(5):747–769, 1973.

J. Woisetschläger. Laser in der Schwingungs- und Strömungsmeßtechnik (Lecture notes). Graz, 2008. TU-Graz.

List of Figures

List of Tables

Appendix

10.1 Input File - *OpenFoam*

10.1.1 File structure

The directories for the *OpenFoam* files are given in Table 10.1:

Table 10.1: *Directory and File structure for OpenFoam on a Linux computer*
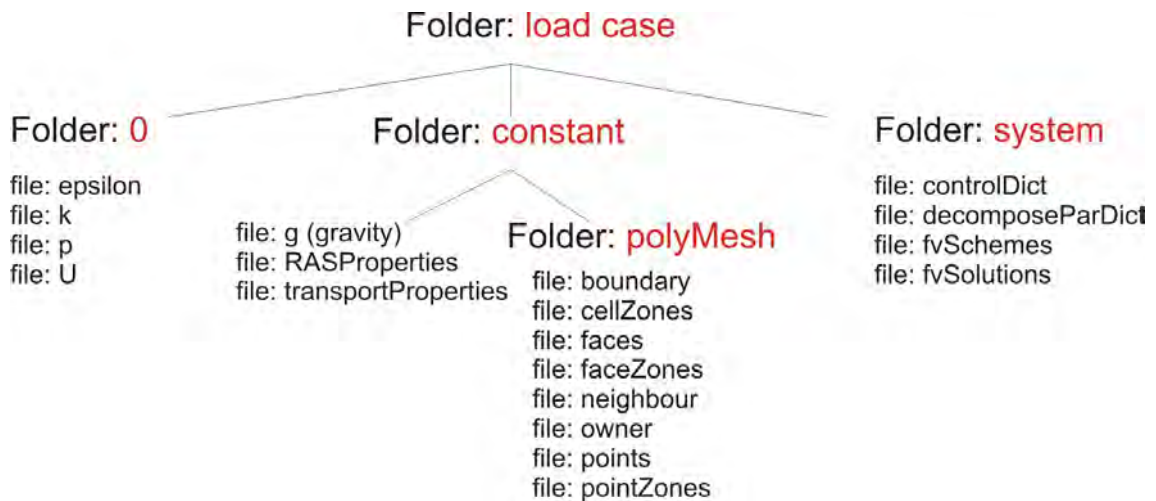
10.1.2 Folder 0

10.1.2.1 epsilon

```
/*--------------------------------*- C++ -*----------------------------------*\
| =========                 |                                                 |
| \\      / F ield          | OpenFOAM: The Open Source CFD Toolbox           |
|  \\    /  O peration       | Version:  1.7.1                                 |
|   \\  /   A nd            | Web:      www.OpenFOAM.com                      |
|    \\/    M anipulation   |                                                 |
\*---------------------------------------------------------------------------*/
FoamFile
{
    version     2.0;
    format      ascii;
    class       volScalarField;
```

```
    location    "0";
    object      epsilon;
}
// * * * * * * * * * * * * * * * * * * * * * * * * * * * * * * * * * * //

dimensions      [ 0 2 -3 0 0 0 0 ];

internalField   uniform 1;

boundaryField
{
    MAIN // This is the entrance of the main pipe
    {
        type                turbulentMixingLengthDissipationRateInlet;
        mixingLength    0.0175;    // mixingLenght=
                                    // 0.07 * Hydraulic Diameter =
                                    // 0.07*0.250=0.0175
        value           uniform 1;    // placeholder
    }

    LEFT // This is the the outlet of the left pipe
    {
        type                inletOutlet; //  Switches epsilon between
                                    // fixedValue and zeroGradient
                                    // depending on direction of U
        inletValue      uniform 0.00861  ;
    }

    REIGHT // This is the the outlet of the right pipe
    {
        type                inletOutlet;
        inletValue      uniform 0.00861;
    }

  plexi_wall
   {
        type                epsilonWallFunction; //standard wall function
        value           uniform 0;
    }
}


// ********************************************************************* //
```

10.1.2.2   Turbulent kinetic energy

```
/*--------------------------------*- C++ -*----------------------------------*\
| =========                 |                                                 |
| \\      / F ield          | OpenFOAM: The Open Source CFD Toolbox           |
```
- xvi -

```
|  \\    /   O peration    | Version:   1.7.1                                    |
|   \\  /    A nd          | Web:       www.OpenFOAM.com                         |
|    \\/     M anipulation  |                                                    |
\*-----------------------------------------------------------------------xvii---*/
FoamFile
{
    version     2.0;
    format      ascii;
    class       volScalarField;
    location    "0";
    object      k;
}
// * * * * * * * * * * * * * * * * * * * * * * * * * * * * * * * * * * * * * * //

dimensions      [ 0 2 -2 0 0 0 0 ];

internalField   uniform 1;

boundaryField
{
    MAIN
    {
        type            turbulentIntensityKineticEnergyInlet;
        intensity       0.05;        // 5% turbulent intensity
        value           uniform 1;
    }

    LEFT
    {
        type            inletOutlet;
        inletValue      uniform 1;
    }

    REIGHT
    {
        type            inletOutlet;
        inletValue      uniform 1;
    }

  plexi_wall
   {
        type            kqRWallFunction;
        value           uniform 0;
    }
}


// ******************************************************************* //
```

10.1.2.3 Turbulent eddy viscosity

```
/*--------------------------------*- C++ -*----------------------------------*\
| =========                 |                                                 |
| \\      /  F ield         | OpenFOAM: The Open Source CFD Toolbox           |
| \\    /   O peration      | Version:  1.7.1                                 |
|  \\  /    A nd            | Web:      www.OpenFOAM.com                       |
|   \\/     M anipulation   |                                                 |
\*---------------------------------------------------------------------------*/
FoamFile
{
    version     2.0;
    format      ascii;
    class       volScalarField;
    object      nuTilda;
}
// * * * * * * * * * * * * * * * * * * * * * * * * * * * * * * * * * * * * * //

dimensions      [0 2 -1 0 0 0 0];

internalField   uniform 0;

boundaryField
{
    MAIN
    {
        type            zeroGradient;
    }

    LEFT
    {
        type            zeroGradient;
    }

    REIGHT
    {
        type            zeroGradient;
    }

    plexi_wall
    {
        type            zeroGradient;
    }
}

// ************************************************************************* //
```

10.1.2.4 Pressure

```
/*--------------------------------*- C++ -*----------------------------------*\
```

```
| =========                 |                                                     |
| \\      /  F ield         | OpenFOAM: The Open Source CFD Toolbox               |
| \\    /   O peration      | Version:  1.7.1                                     |
|  \\ /     A nd            | Web:      www.OpenFOAM.com                          |
|   \\/     M anipulation   |                                                     |
\*---------------------------------------------------------------------------*/
FoamFile
{
    version     2.0;
    format      ascii;
    class       volScalarField;
    object      p;
}
// * * * * * * * * * * * * * * * * * * * * * * * * * * * * * * * * * * * * * //

dimensions      [0 2 -2 0 0 0 0];

internalField   uniform 0;

boundaryField
{
    MAIN
    {
        type            zeroGradient;
    }

    LEFT
    {
        type            fixedValue;
        value           uniform 0;
    }

  REIGHT
   {
        type            fixedValue;
        value           uniform 0;
    }

    plexi_wall
    {
        type            zeroGradient;
    }
}

// ************************************************************************* //
```

10.1.2.5 Velocity

```
/*--------------------------------*- C++ -*----------------------------------*\
| =========                 |                                                     |
| \\      /  F ield         | OpenFOAM: The Open Source CFD Toolbox               |
| \\    /   O peration      | Version:  1.7.1                                     |
```

```
|   \\  /    A nd          | Web:      www.OpenFOAM.com                    |
|    \\/     M anipulation |                                              |
\*---------------------------------------------------------------------*/
FoamFile
{
    version    2.0;
    format     ascii;
    class      volVectorField;
    object     U;
}
// * * * * * * * * * * * * * * * * * * * * * * * * * * * * * * * * * * * //

dimensions      [0 1 -1 0 0 0 0];

internalField   uniform (0 0 0);

boundaryField
{
   MAIN
    {
    type surfaceNormalFixedValue;
refValue uniform -3.26;
    }

    LEFT
    {
        type            inletOutlet;
        inletValue      uniform (0 0 0);
        value           uniform (0 0 0);
    }

    REIGHT
    {
        type            inletOutlet;
        inletValue      uniform (0 0 0);
        value           uniform (0 0 0);
    }

    plexi_wall
    {
        type            fixedValue;
        value           uniform (0 0 0);
    }
}

// ********************************************************************* //
```

10.2   Derivation of the water hammer equations

10.2.1   Water hammer based on the theory of the elastic water column

To calculate the water hammer in a pipe system the compressibility of the fluid and the elasticity of the pipe wall have to be taken into account. The change of density due to the pressure wave in the pipe propagates with the wave speed a [m/s]; these waves are longitudinal waves (Giesecke and Mosonyi [1997]). Due to the reflection of the pressure waves considerably higher magnitudes of waves can occur.

The mathematical derivation of the water hammer is based on Newton's second law:

$$\vec{F} = m \cdot \vec{a_{accel}} = m \cdot \frac{d\vec{V}}{dt} \tag{10.1}$$

Eq. 10.1 is also called **Momentum Equation** and states that the product of mass ($\rho \cdot dx \cdot A$) and the acceleration is equal to the resulting forces acting on the element dx.
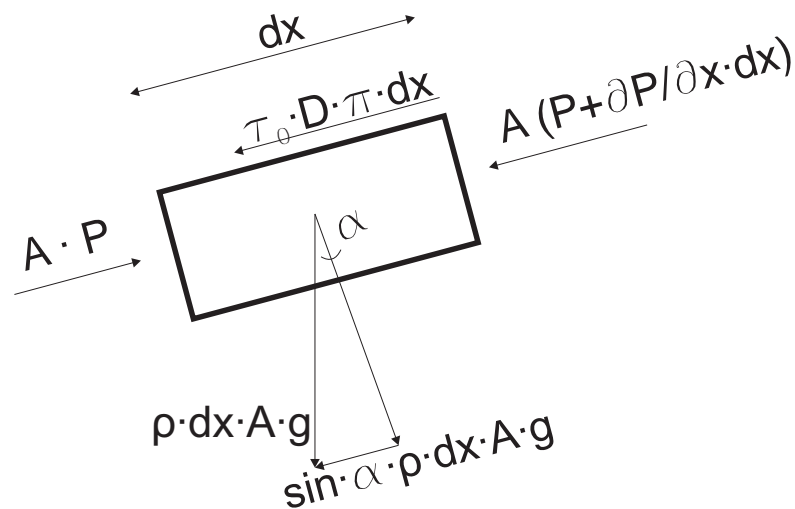
Figure 10.1: *Momentum equation of a pipe element*

Figure 10.1 shows the resulting forces acting on the pipe element of a finite length dx. With Eq. 10.1 and Figure 10.1 the momentum equation has the following shape:

$$-\frac{\partial P}{\partial x} - \rho_f \cdot \frac{dV}{dt} - \rho_f \cdot g \cdot sin\beta - \frac{4}{D} \cdot \tau_w = 0 \tag{10.2}$$

whereas P = pressure, ρ_f = density of water, g = gravity, β = angle, D = diameter and τ_w = wall shear stress.

With the quadratic relationship between wall shear stress (τ_w) and velocity (V) for turbulent flows:

$$\tau_w \propto V^2 \tag{10.3}$$

the empirical equation can be defined:

$$\tau_w = \frac{\lambda}{8} \cdot \rho_f \cdot V \cdot |V| \tag{10.4}$$

Replacing the wall shear stress in Eq. 10.2 yields:

$$-\frac{\partial P}{\partial x} - \rho_f \cdot \frac{dV}{dt} - \rho_f \cdot g \cdot sin\beta - \frac{\rho_f \cdot \lambda}{2 \cdot D} \cdot V \cdot |V| = 0 \tag{10.5}$$

The total differential of $V_{t,x}$ is (Bartsch [1999]):

$$dV = \frac{\partial V}{\partial x} \cdot dx + \frac{\partial V}{\partial t} \cdot dt \tag{10.6}$$

Rearranging with dx/dt=V yields forEq. 10.6:

$$\frac{dV}{dt} = V \cdot \frac{\partial V}{\partial x} + \frac{\partial V}{\partial t} \tag{10.7}$$

The final form of the **momentum equation** - including the fact that sin β=dz/dx, is: (Giesecke and Mosonyi [1997]):

$$\frac{1}{\rho_f} \cdot \frac{\partial P}{\partial x} + V \cdot \frac{\partial V}{\partial x} + \frac{\partial V}{\partial t} + g \cdot \frac{dz}{dx} + \frac{\lambda}{2 \cdot D} \cdot V \cdot |V| = 0 \tag{10.8}$$

The continuity equation is (cf. also with Eq. 6.6 and Eq. 6.7):

$$\frac{\partial \rho_f}{\partial t} + \nabla \cdot (\rho_f \cdot \vec{V}) = \frac{\partial \rho_f}{\partial t} + \rho_f \left(\nabla \cdot \vec{V} \right) + \vec{V} \cdot (\nabla \rho_f) = 0 \tag{10.9}$$

and if only one dimension is considered:

$$\frac{\partial \rho_f}{\partial t} + \rho_f \cdot \frac{\partial V}{\partial x} + V \frac{\partial \rho_f}{\partial x} = 0 \tag{10.10}$$

Taking into account the equation of state for the speed of sound $\rho_f = P/c^2$, Eq. 10.10 yields:

$$\frac{\partial P}{\partial t} + P \cdot \frac{\partial V}{\partial x} + V \cdot \frac{\partial P}{\partial x} = 0 \tag{10.11}$$

For the pressure the approximation $P \approx a^2 \cdot \rho_f$ is used instead of $\rho_f = P/c^2$. This condition is only valid for weakly compressible fluids like water. In order to consider the elasticity of the pipe the variable for the speed of sound will be replaced with the pressure wave velocity a. The **continuity equation** is then (Schröder and Zanke [2003]):

$$\frac{\partial V}{\partial x} + \frac{1}{a^2 \cdot \rho_f} \cdot \left(V \cdot \frac{\partial P}{\partial x} + \frac{\partial P}{\partial t} \right) = 0 \tag{10.12}$$

For the pressure wave velocity a one can write:

$$a = \sqrt{\frac{1}{\frac{1}{c^2} + \frac{\rho_f}{A} \cdot \frac{dA}{dP}}} \tag{10.13}$$

whereas $\frac{1}{A} \cdot \frac{dA}{dP}$ represents the widening of the pipe. According to Hooke's law for thin walled pipes with the wall thickness s one obtains:

$$\frac{\Delta r}{r} = \frac{r \cdot \Delta P}{E_s \cdot s} \tag{10.14}$$

where E_s is Young's modulus for steel pipe, r the radius and s the wall thickness. For the change of the cross sectional area one can write:

$$\Delta A = 2 \cdot \pi \cdot r \cdot \Delta r \tag{10.15}$$

Finally, for the widening of the pipe one can write:

$$\frac{1}{A} \cdot \frac{dA}{dP} = \frac{1}{E_s} \cdot \frac{D}{s} \tag{10.16}$$

and with the definition for the speed of sound $c = \sqrt{(E_f/\rho_f)}$, Eq. 10.13 can be rewritten according to Schröder and Zanke [2003]:

$$a = \sqrt{\frac{\frac{E_f}{\rho_f}}{1 + \frac{E_f}{E_s} \cdot \frac{D}{s}}} \quad < \quad c = \sqrt{\frac{E_f}{\rho_f}} \tag{10.17}$$

Generally, the Bulk modulus E_f in Eq. 10.17 is $E_f = 2 \cdot 10^9 \ N/m^2$ for water and Young's modulus $E_s = 2.1 \cdot 10^{11} \ N/m^2$ for steel.

10.2.2 Solution of the differential equation with the method of characteristics

The momentum equation (Eq. 10.8) and the continuity equation (Eq. 10.12) for unsteady pipe flows are partial, non-linear differential equations of hyperbolic type. Hyperbolic differential equations generally describe propagation problems; the transport of information occurs along a characteristic (Sanz [2008]). The gradient of the characteristic is equivalent to the propagation velocity of the pressure and the rate of change of velocity as long as the velocity of the fluid is smaller than the pressure wave velocity a.

The derivation for the method of characteristics is taken from Giesecke and Mosonyi [1997] and has the following form:

The continuity equation (Eq. 10.12) will be multiplied with the pressure wave velocity a:

$$a \cdot \frac{\partial V}{\partial x} + \frac{1}{a \cdot \rho_f} \cdot \left(V \cdot \frac{\partial P}{\partial x} + \frac{\partial P}{\partial t} \right) = 0 \qquad (10.18)$$

The momentum equation (Eq. 10.8) will be rearranged as follows:

$$\frac{\partial V}{\partial t} + V \cdot \frac{\partial V}{\partial x} + \frac{1}{\rho_f} \cdot \frac{\partial P}{\partial x} + g \cdot \frac{dz}{dx} + \frac{\lambda}{2 \cdot D} \cdot V \cdot |V| = 0 \qquad (10.19)$$

Subtraction and addition of Eq. 10.18 with Eq. 10.19 yields:

$$\frac{\partial V}{\partial t} + (V \pm a) \cdot \frac{\partial V}{\partial x} \pm \frac{1}{\rho_f \cdot a} \cdot \left((V \pm a) \cdot \frac{\partial P}{\partial x} + \frac{\partial P}{\partial x} \right) + g \cdot \frac{dz}{dx} + \frac{\lambda}{2 \cdot D} \cdot V \cdot |V| = 0 \qquad (10.20)$$

The terms $(V \pm a) = dx/dt$ are called characteristics, thus Eq. 10.20 can be recast into:

$$\frac{\partial V}{\partial t} + \frac{dx}{dt} \cdot \frac{\partial V}{\partial x} \pm \frac{1}{\rho_f \cdot a} \cdot \left(\frac{dx}{dt} \cdot \frac{\partial P}{\partial x} + \frac{\partial P}{\partial x} \right) + g \cdot \frac{dz}{dx} + \frac{\lambda}{2 \cdot D} \cdot V \cdot |V| = 0 \qquad (10.21)$$

With the total differential

$$\frac{dV}{dt} = \frac{\partial V}{\partial t} + \frac{\partial V}{\partial x} \cdot \frac{dx}{dt}$$
$$\frac{dP}{dt} = \frac{\partial P}{\partial t} + \frac{\partial P}{\partial x} \cdot \frac{dx}{dt} \qquad (10.22)$$

Eq. 10.21 can be rearranged into the form:

$$\frac{dV}{dt} \pm \frac{1}{\rho_f \cdot a} \cdot \frac{dP}{dt} + g \cdot \frac{dz}{dx} + \frac{\lambda}{2 \cdot D} \cdot V \cdot |V| = 0 \qquad (10.23)$$

The pressure gradient in Eq. 10.23 will be rewritten as a pressure height $P = \rho \cdot g \cdot (h - z)$:

$$\frac{1}{\rho_f \cdot a} \cdot \frac{dP}{dt} = \frac{g}{a} \cdot \left(\frac{dh}{dt} - \frac{dz}{dt} \right) \qquad (10.24)$$

Thus Eq. 10.23 yields:

$$\frac{dV}{dt} \pm \frac{g}{a} \cdot \left(\frac{dh}{dt} - \frac{dz}{dt} \right) + g \cdot \frac{dz}{dx} + \frac{\lambda}{2 \cdot D} \cdot V \cdot |V| = 0 \qquad (10.25)$$

The term dz/dx in Eq. 10.25 will be converted to

$$\frac{dz}{dt} = \frac{dz}{dx} \cdot \frac{dx}{dt} = (v \pm a) \cdot \frac{dz}{dx} \tag{10.26}$$

Replacing Eq. 10.26 in Eq. 10.25 yields:

$$\frac{dV}{dt} \pm \frac{g}{a} \cdot \left(\frac{dh}{dt} - (v \pm a) \cdot \frac{dz}{dx} \right) + g \cdot \frac{dz}{dx} + \frac{\lambda}{2 \cdot D} \cdot V \cdot |V| = 0 \tag{10.27}$$

When the velocity V fulfills the condition: $V < 0,05 \cdot a$ (Giesecke and Mosonyi [1997]), the convection term with dz/dx can be neglected. Thus Eq. 10.27 gives:

$$\frac{dV}{dt} \pm \frac{g}{a} \cdot \frac{dh}{dt} + \frac{\lambda}{2 \cdot D} \cdot V \cdot |V| = 0 \tag{10.28}$$

Integrating along the characteristic Eq. 10.28 can be solved (cf. also with Figure 10.2)

$$\left[V + \frac{g}{a} \cdot h \right]_U^P = \int_{t_U}^{t_P} \left(-\frac{\lambda}{2 \cdot D} \cdot V \cdot |V| \right) \cdot dt \quad + \text{ } Charakteristics \tag{10.29}$$

$$\left[V - \frac{g}{a} \cdot h \right]_R^P = \int_{t_R}^{t_P} \left(-\frac{\lambda}{2 \cdot D} \cdot V \cdot |V| \right) \cdot dt \quad - \text{ } Charakteristics \tag{10.30}$$
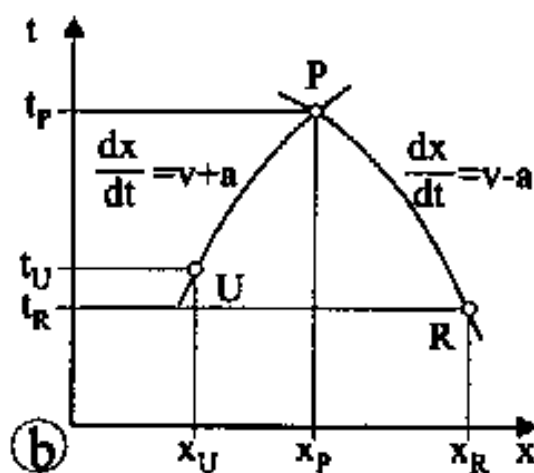
Figure 10.2: *Sketch of the characteristics (taken from Giesecke and Mosonyi [1997])*

Eq. 10.29 and Eq. 10.30 are solved by using the trapezoidal rule [A=$(x_P$-x_U)/2 · (f(x_P)+f(x_U))] for the integration. Additionally, with a nearly linear progression, dt = dx/($\pm$a) is set.

$$\left[V + \frac{g}{a} \cdot h\right]_P = \left[V + \frac{g}{a} \cdot h\right]_U + \frac{x_P - x_U}{2 \cdot a} \cdot \left(\left[-\frac{\lambda}{2 \cdot D} \cdot V \cdot |V|\right]_P + \left[-\frac{\lambda}{2 \cdot D} \cdot V \cdot |V|\right]_U\right)$$
$$(10.31)$$

and

$$H_P = h_U + \frac{a}{g} \cdot (V_U - V_P) - \frac{\Delta x \cdot \lambda}{4 \cdot g \cdot D} \cdot (V_P \cdot |V_P| + V_U \cdot |V_U|) \qquad (10.32)$$

Eq. 10.30 will be rearranged in the same form:

$$H_P = h_R - \frac{a}{g} \cdot (V_R - V_P) - \frac{\Delta x \cdot \lambda}{4 \cdot g \cdot D} \cdot (V_P \cdot |V_P| + V_R \cdot |V_R|) \qquad (10.33)$$

Due to the fact that the velocity for point P, U and R changes only marginally for one iteration step, one can write:

$$V_P \cdot |V_P| + V_U \cdot |V_U| = 2 \cdot V_P \cdot |V_U|$$
$$V_P \cdot |V_P| + V_R \cdot |V_R| = 2 \cdot V_P \cdot |V_R| \qquad (10.34)$$

Additionally, with Q=V · A Eq. 10.32 and Eq. 10.33 yields:

$$H_P = h_U + \frac{a}{g \cdot A} \cdot (Q_U - Q_P) - \frac{\Delta x \cdot \lambda}{2 \cdot g \cdot D \cdot A^2} \cdot (Q_P \cdot |Q_U|)$$
$$H_P = h_R - \frac{a}{g \cdot A} \cdot (Q_R - Q_P) + \frac{\Delta x \cdot \lambda}{2 \cdot g \cdot D \cdot A^2} \cdot (Q_P \cdot |Q_R|) \qquad (10.35)$$

With the abbreviations:

$$B = \frac{a}{g \cdot A}$$
$$R = \frac{\Delta x \cdot \lambda}{2 \cdot g \cdot D \cdot A^2} \qquad (10.36)$$

Eq. 10.35 can be rewritten as:

$$H_P = h_U + B \cdot (Q_U - Q_P) - R \cdot (Q_P \cdot |Q_U|)$$
$$H_P = h_R - B \cdot (Q_R - Q_P) + R \cdot (Q_P \cdot |Q_R|) \qquad (10.37)$$

With the following abbreviations for Eq. 10.37 :

$$B_U = B + R \cdot |Q_U|$$
$$C_U = h_U + B \cdot Q_U$$
$$B_R = B + R \cdot |Q_R|$$
$$C_R = h_R - B \cdot Q_R \tag{10.38}$$

the variables H_P und Q_P can be solved (Giesecke and Mosonyi [1997]):

$$H_P = \frac{C_U \cdot B_R + C_R \cdot BU}{B_U + B_R}$$
$$Q_P = \frac{C_U - C_R}{B_U + B_R} \tag{10.39}$$

10.3   Published Papers

Hydraulic investigation of a Y-bifurcator

W. Dobler[1], H. Knoblauch[1] and G. Zenz[1]

[1]*Department of Hydraulic Engineering and Water Resources Management,*
University of Graz, Austria, Stremayrgasse 10/II, 8010 Graz

Abstract

In this paper the model test of a Y-bifurcator of a power plant will be introduced. The model test consists of a $42°$ bend, a straight pipe from the bend to the Y-branch and two branching pipes with a branching angle of $40°$. The secondary flow caused by the bend will be made visible by a Particle Image Velocimetry (PIV) and quantified with the velocity correction factor α. The downscaling of the hydraulic model test is based on the Reynolds law. This causes too high discharge rates in the model test and an extrapolation with a linear polynomial, based on the least square method, is used to get the discharge rate in respect to the head loss. The head losses and the corresponding local loss coefficient ζ_{local} will be presented and compared by either a linear or polynomial extrapolation.

INTRODUCTION

Considerable efforts are undertaken to reduce hydraulic losses in pipe systems of a hydro-power plant. Beside the friction loss of a straight pipe the local losses due to built-in components like a junction or confuser are also of interest. The first important measurements for the local loss coefficient ζ_{local} in a bifurcator was done in Munich from 1928 to 1931 and are also known as the *Munich experiments* (Vogel [1928], Petermann [1929] and Kinne [1931]). Vogel [1928] represented results for right-angled bifurcators with diameters from Ø15 mm to Ø45 mm. The form of the intersection edges of the bifurcator were either sharp-edged or rounded. Vogel [1928] mentioned also the proportional relationship between the pressure losses and the quadratic discharge rate. Petermann [1929] and Kinne [1931] repeated the test series of Vogel [1928] with a branching angle of $40°$ and $60°$, respectively. McNown [1954] repeated the results of the *Munich experiments* with more accurate measurements at the hydraulic lab in Iowa. The branching angle of the test series in Iowa was $90°$ and the pipe diameters were form 12.7mm to 50.8mm.

Abundant data for loss coefficients of Y-bifurcators are presented in Miller [1990]. The parameter for the loss coefficients in Miller [1990] are the ratio of area for the main and branching pipe, discharge ratio, different branching angles and different forms of the intersection edge (rounded or edged). Kavianpour [2003] determined loss coefficients for two asymmetrical Y-bifurcators in a hydraulic model test made of plexiglass pipes. Kavianpour [2003] used for his investigation different stiffener inside the Y-bifurcator and also mentioned the important fact that no secondary flow should reach the turbine. Klasinc et al. [1992] reported the loss coefficient for an asymmetrical Y-bifurcator. For this model test the scaling law of Reynolds was used. This leads to too high discharge rates in the hydraulic model test and polynomial extrapolation methods are used. Based on the hydraulic model test of Klasinc et al. [1992] further investigations for a symmetrical Y-bifurcator are shown in this paper.

INSTALLATION OF THE HYDRAULIC MODEL TEST

The hydraulic model test is downscaled with a factor of 8.13, based on the Reynolds law, where the ratio of the inertia to the viscous force is the same in prototype and the model. In the hydraulic model test the Y-bifurcator consists of a main pipe with a inner diameter of 246mm and two branching pipes with a inner diameter of 172mm, respectively. The branching angle of the symmetrical Y-bifurcator is $40°$ and a stiffener is used for statical reason. 18 diameters (18-D) upstream of the Y-bifurcator is located a bend with an angle of $42°$ and after this bend exists a 12-D long pipe which ends in a flow conditioner (see Figure 1). Downstream of the Y-bifurcator is a 10-D long pipe with a inner diameter of 123mm and a confuser for each branch.

The flow conditioner consists of a pipe bundle to smooth the incoming flow and to get a fully developed turbulent flow before the flow enters the bend. The bend itself consists of 5 segments each of them rotated by $8.4°$. The Y-bifurcator consists of three cone-shaped volumes and a stiffener. After the confuser in the hydraulic model test two pelton turbines are located in the prototype. Instead of the pelton turbines a 10-D long pipe is installed in the hydraulic model test to get a fully redeveloped turbulent flow.

The water supply for the model test is done by a reservoir in the laboratory. The water level in the reservoir is 13m above the symmetry line in the Y-bifurcator. With this water head level a maximum discharge rate of 0.12 (m^3/s) is possible. Using pumps a discharge rate of 0.2 (m^3/s) is possible and the maximum allowable pressure of 1.3 (bar), due to the strength of the plexiglass-pipe, is achieved in the installation. The water, after passing the model test, enters another
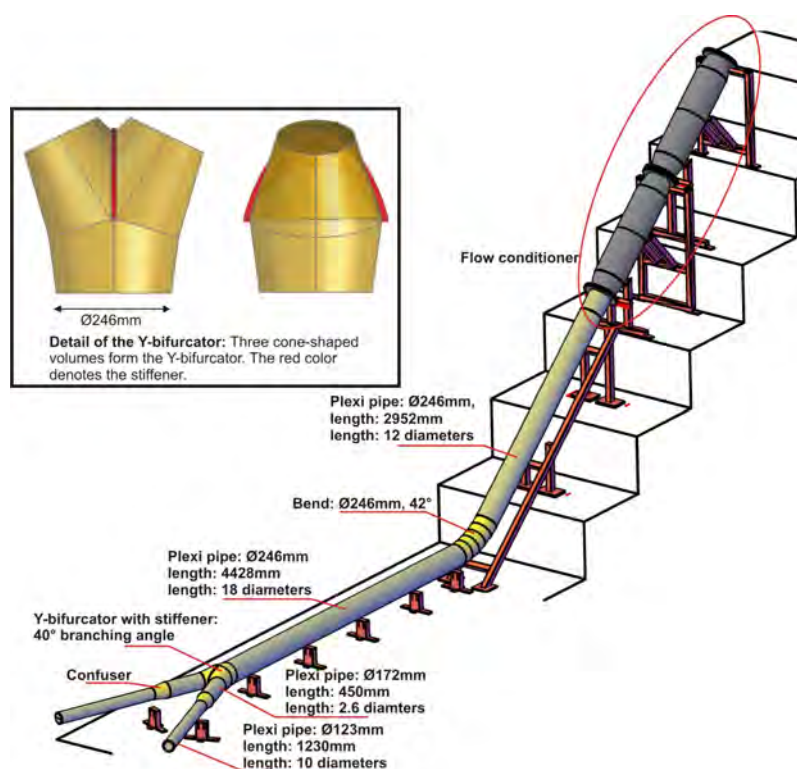
Figure 1: View of the whole plexiglass-pipe installation and a detail of the Y-bifurcator (top-left).

reservoir which is allocated below the model test.

Data acquisition

For the measurement of the loss coefficient ζ_{local} the pressure differences and the discharge rates are needed. The temperature needs not be recorded due to the constant temperature in the laboratory of $\pm 1 \, ^\circ C$.

The pressure difference is measured from the control section M1 in Figure 3 to every other control section, that is, from M2 to M6, L1 to L6 and R1 to R6 respectively. Each control section consists of 8 pressure-holes, regularly arranged around the plexiglass-pipe. The pressure-holes are burr-free and have a diameter of 1mm each. All eight bore holes are connected together to a single ring-line to get an average value of the head level in the control section. The pressure-sensor for the head level difference measurement has a maximum inaccuracy of $\pm 0.5\%$ of the full range. For each meassuring campaign the pressure-probe is calibrated against a constant water head level. The ring-line is

Figure 2: Howell-Bunger valve to vary continuously the discharge rate.

connected with the pressure-sensor by a air-free plastic tube. The signal (4-20mA) from the pressure-sensor is sent to a measurement amplifier and then recorded and stored by the software LabView.

The discharge rates are measured by three electromagnetic flow meters, one in the main pipe and one at each branching pipe. The measuring principle of the flow meter is based on the electromagnetic induction. The discharge rate can be continuously varied by two Howell-Bunger valves (see Figure 2) with an electric motor. The accuracy of the flow meters are $\pm 0.5\%$ of the discharge rate.
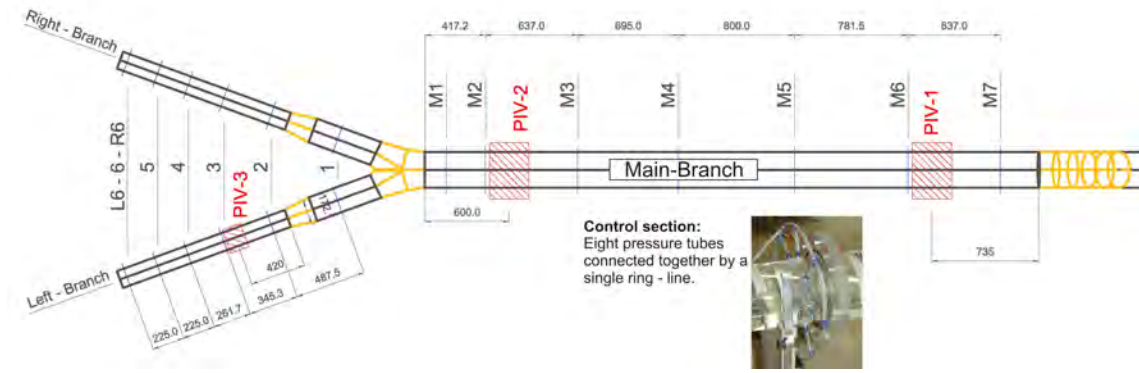
Figure 3: Plan view of the model test: Control section M1 to M7, L1 to L6 and R1 to R6. M, L and R stands for Main, Left and Right respectively. Position for PIV-measurements are the red hatched areas (two in the main pipe, one at the left-branch.)

Particle Image Velocimetry (PIV)

PIV is a non-intrusive device to measure velocities at a 2D-plane within the pipe installation. The basic parts of a PIV-measurement are a double pulsed laser which expands to a 2D laser light sheet, a high speed camera and a special PIV-box to avoid the astigmatism-effect due to the curved surface of the plexiglass-pipe. The natural particles in the flow (Ø0.1mm) are used as seedings. As can be seen in Figure 4, for each PIV-box 4 planes are used to measure the velocity vector fields. The physical recording time of the flow is 1 second and the sampling rate 1 kHz. With this set-up the axial secondary flow as well as the roughness of the plexiglass wall can be measured. The software to calculate the velocity is DynamicStudio 2.20.18 from DantecDynamics.
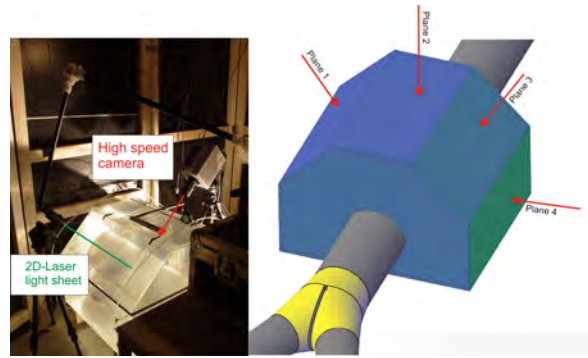
Figure 4: PIV - Set up: Figure left shows the laser, the PIV-box filled with water to avoid the astigmatism-effect and the High Speed Camera. Figure right shows the 4 investigation planes for the PIV-measurements.

HYDRAULIC EQUATIONS

The dimensionless coefficient ζ_{local} is defined as

$$\zeta_{local} = \frac{\Delta h_{local}}{V_{main\ pipe}^2/2g} \qquad (1)$$

whereas Δh_{local} is the local head loss in the Y-bifurcator without friction losses due to pipe friction, $V_{main\ pipe}$ the mean velocity in the main pipe and g the gravity. To calculate Δh_{local} the relationship

$$\Delta h_{tot} = \Delta h_{local} + h_f \qquad (2)$$

$$\Delta h + \alpha_1 \frac{V_1^2}{2g} = \alpha_2 \frac{V_2^2}{2g} + \Delta h_{tot} \qquad (3)$$
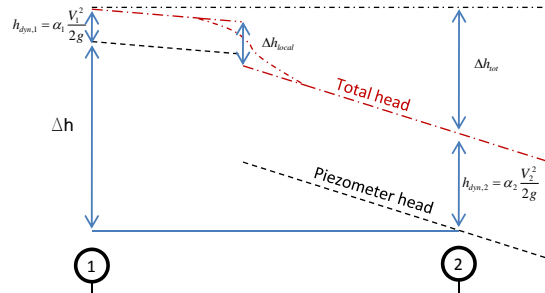
Figure 5: Definition of the local head loss Δh_{local}

is used. The introduced variables in Eq. 2 and Eq. 3 have following meaning (compare also with Figure 5): Δh_{tot} is the total head level difference which includes local (Δh_{local}) and pipe friction losses (h_f). Δh is the with the pressure-sensor measured piezometer head level difference in the hydraulic model test. α is the velocity correction factor for a non-uniform velocity distribution. V_1 and V_1 are the measured velocities due to the flow meters before and after the Y-bifurcator. h_f is the pipe friction due to the Darcy-Weisbach equation (see Eq. 4), whereas L is the length, D the diameter, V the velocity in the pipe and λ the friction coefficient. λ can be calculated with the Colebrook equation (see Eq. 5), whereas Re is the Reynolds number and k the equivalent sand roughness.

Finally, to calculate the friction loss h_f substitution cylinders need to be defined along the pipe installation. Depending on the control section in Figure 3 for the loss coefficient calculation, 5 substitution cylinders are defined to calculate the friction loss of the pipe installation between two control sections and subtract it from the total head level difference (Three cylinders for the Y-bifurcator and one for the main- and one for the branching pipe).

$$h_f = \lambda \, \frac{L}{D} \, \frac{V^2}{2g} \qquad (4)$$

$$\frac{1}{\sqrt{\lambda}} = -2.0 \, lg \left(\frac{2.51}{Re \, \sqrt{\lambda}} + \frac{k/D}{3.71} \right) \qquad (5)$$

$$u^+ = \frac{u}{u_\tau} = \frac{1}{\kappa} \, ln \left(\frac{y}{k} \right) + 8.5 \qquad (6)$$

$$y^+ = \frac{y \, u_\tau}{\nu} \qquad (7)$$

$$\frac{u_i}{\frac{1}{\kappa} \, ln \left(\frac{y_i}{k} \right) + 8.5} = \frac{u_{i+1}}{\frac{1}{\kappa} \, ln \left(\frac{y_{i+1}}{k} \right) + 8.5} \qquad (8)$$

An essential point in the loss coefficient calculation is the determination of the equivalent sand roughness in the plexiglass installation to determine the pipe friction losses h_f. A simple method to calculate the sand roughness is the application of the results of the measured piezometer head level difference where a linear loss gradient appears. This certain flow behaviour exist between the bend and the Y-bifurcator and downstream of th Y-bifurcator.

The other method to estimate the equivalent sand roughness is the use of the logarithmic law of the wall by von Kármán [1930]. The law of the wall is shown in Eq. 6, whereas u_τ is the friction velocity, κ the von Kármán constant, y the distance normal to the pipe wall, u the corresponding axial velocity for the distance y and k the equivalent sand roughness. Solving Eq. 6 in respect to u_τ a set of equations are defined and with PIV-results close to the wall (wall distance y_i and the corresponding axial velocity u_i, i denotes the step of the discrete points of the velocity vector field) the sand roughness can be calculated (see Eq. 8). With Eq. 6 and Eq. 7 the logarithmic law of the wall, which is valid between $30 \leq y^+ \leq 300$, can be plotted.

In Eq. 3 the α coefficients need to be defined. Due to the bend in the installation a slight secondary effect still exists shortly before the flow enters the Y-bifurcator. With PIV it is possible to calculate the α value before and after the Y-bifurcator (compare also with the label *PIV-2* and *PIV-3* in Figure 3). The analytical equation for the α coefficient (Preiß ler and Bollrich [1985]) is shown in Eq. 9, whereas A is the cross section area of the pipe and u the axial velocity due to PIV-measurement.

$$\alpha = \frac{1}{u_{mean}^3 \, A} \int^A u_A^3 \, dA \qquad (9)$$

EXTRAPOLATION OF THE PIEZOMETER HEAD LEVEL DIFFERENCE

The scaling ratio, based on the Reynolds law, between the prototype and the hydraulic model test is 8.13. This means that a 8.13-times higher velocity would be needed in the hydraulic model test which is not possible to achieve. Therefore, an extrapolation method is needed for the function of the discharge rate in respect to the piezometer head level difference Δh. In the work of Klasinc et al. [1992] a second order polynomial equation was used for the extrapolation due to the quadratic behaviour of the head loss in respect to the discharge rate. In this paper, the extrapolation is done by using a linear function of the **quadratic discharge rate** in respect to the head loss. With *Matlab(R2008a)* it is possible to find either for a linear- or a quadratic polynomial extrapolation the necessary function to approximate the measured head loss and extrapolate it beyond the possible discharge rate in the hydraulic model test. The subroutine in *Matlab* for the extrapolation method is called *polyfit* and is based on the least square method.

RESULTS AND DISCUSSION

Roughness

In Figure 6 the results for the determination of the roughness k due to the Δh_{local} - measurements are presented. The standard value for k of a plexiglass-pipe is 0.0015 (mm). Because of the built-in components (e.g. flanges) the roughness increases to a value for the main pipe of 0.01 and for the branching pipes of 0.019 (mm), respectively. The roughness k is also double checked by a PIV-measurement as can be seen in Figure 7. With Eq. 8 the k coefficient yields 0.0187 (mm) for the first point in the logarithmic layer. Therefore, the chosen roughness for the plexglass installation is 0.019 (mm) due to the PIV- and Δh_{local}- measurements.

In Figure 8 the velocity profiles four all four planes at the position PIV-2 (compare with Figure 4) are shown. The distorted velocity profile, which is caused by the secondary flow initialized by the bend is still visible. The calculated mean value of the alpha coefficient for all four planes is 1.08. This coefficient is calculated for a symmetrical flow distribution with 0.08 (m³/s) in the left and right branch. For a asymmetrical flow distribution (only left branch with 0.08 (m³/s)) the coefficient increase slightly to 1.10. It can be expected that the α coefficient of 1.08 is in good agreement with the α coefficient of other flow distributions. Therefore the α coefficient of 1.08 is chosen upstream of the Y-bifurcator. Downstream of the Y-bifurcator the measured α coefficient is 1.01 due to smoothing effect of the confuser.
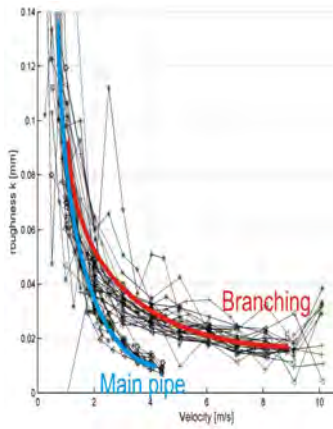
Figure 6: Sand roughness calculated from the Δh_{local} - measurements where a linear friction gradient exists.
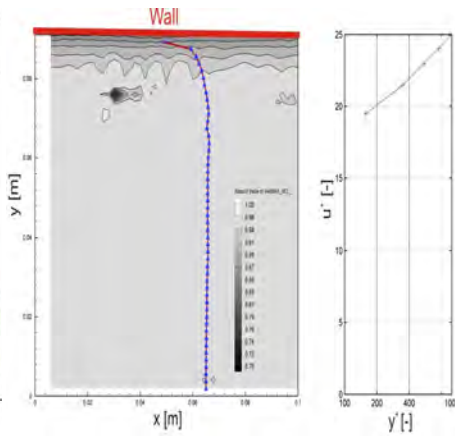
Figure 7: Left: Velocity profile (blue line) and contour plot close to the wall at Position PIV-2 in Figure 3. Right: Evaluation of Eq. 6 and Eq. 7.
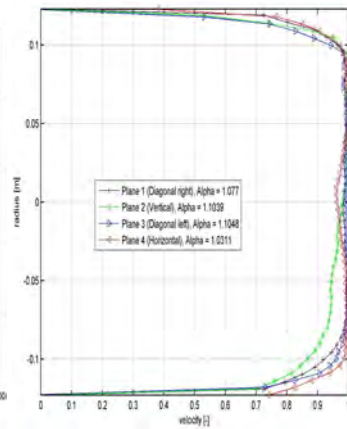
Figure 8: Velocity profiles made dimensionless with u_{max} extracted at the four planes in Figure 4 with their respective coefficient α.

Difference between the linear or quadratic polynomial extrapolation of the ζ_{local} coefficient

In Figure 9 an example of a linear ζ_{local} extrapolation is shown. The red line shows the measured and the blue line the extrapolated values. The flow distribution is symmetrically ($Q_{left} = Q_{right}$). As can be seen in Figure 9 the loss coefficient is nearly independent at a Reynolds number higher than 1×10^6.

In Figure 10 the extrapolated ζ_{local} values for a linear- and a quadratic polynomial extrapolation are shown. All loss coefficients in Figure 10 are in the hydraulic rough area, that is, they are independent of the Reynolds number. The loss coefficients are
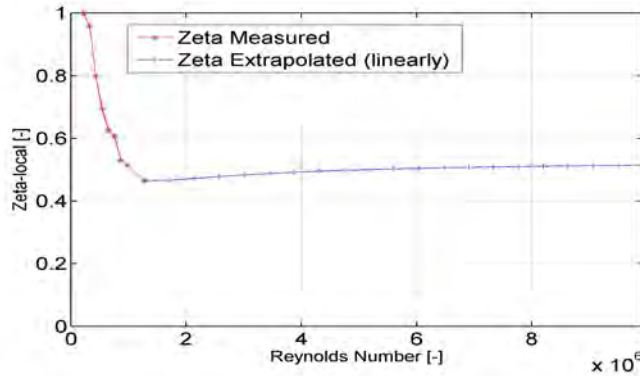
Figure 9: Example of ζ_{local} coefficient extrapolated with a linear polynomial, distribution: $Q_{left}/Q_{main} = 0.57$. Due to data protection the ζ_{local} coefficient is made dimensionless with the maximum ζ_{local} coefficient

calculated for four flow distributions (e.g. LC1 is Load case 1 with $Q_{left}/Q_{main} = 1$). The figure to the left in Figure 10 represents the result of the linear and the figure to the right of the quadratic polynomial extrapolation, respectively. Due to the numerous pressure difference measurements it is possible to calculate the loss coefficient for five pair of control sections, that is, control section M1-L3/R3, M3-L3/R3, M4-L4/R4, M5-L5/R5 and M6-L6/R6.
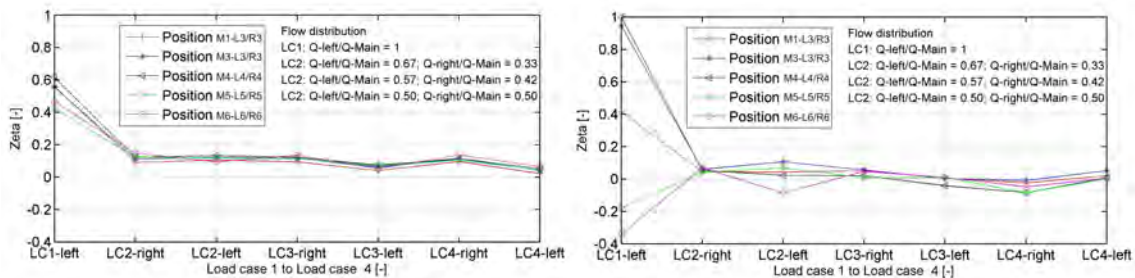
Figure 10: Comparison of the linear- (left figure) and quadratic polynomial extrapolation. ζ_{local} is plotted against the flow distribution (LC1 to LC4) and for fife different pairs of control sections (M1-L3/R3 to M6-L6/R6). Due to data protection the ζ_{local} coefficient is made dimensionless with the maximum ζ_{local} coefficient

If one checks the left figure in Figure 10 all 5 five curves (Position M1-L3/R3 to M6-L6/R6) are almost identical, which is reasonable because ζ_{local} does not include any friction loss h_f and thus is independent of the position of the control sections as long as no strong secondary flow occurs in the pipe. If the left picture is considered there can be clearly distinguished unreasonable loss coefficients for LC1-left, where the coefficients have a very high deviation and even negative quantities. Also, all five lines do not collapse to one single line as good as it can be seen in the left figure. In summary it can be said that the linear polynomial extrapolation causes less deviation as the quadratic polynomial extrapolation. The linear extrapolation is therefore more suitable for the determination of the loss coefficient ζ_{local}.

CONCLUSION

Due to the Reynolds law of similarity very high discharge rates would be necessary in the hydraulic model test. With a linear extrapolation of the quadratic discharge rate in respect to the piezometer head level difference the loss coefficient ζ_{local} can be calculated. It can be shown that the linear extrapolation yields more reasonable results than does the polynomial extrapolation of Klasinc et al. [1992]. The roughness calculation either with PIV or with the measured head level differences in the hydraulic model test shows almost the same result. The secondary flow cased by the bend is quantified with the velocity correction factor α and thus it is possible to calculate the loss coefficient ζ_{local}.

ACKNOWLEDGMENTS

NOMENCLATURE

α	Velocity correction factor (-)
Δh	Piezometer head level difference (m)
Δh_{local}	Local head loss (m)
Δh_{tot}	Total head level difference (m)
κ	von Kármán constant (-)
λ	Friction coefficient (-)
ν	Kinematic viscosity (m^2/s)
ζ_{local}	Local loss coefficient (-)
A	Area (m^2)
D	Inner diameter (m)
g	Gravity (m/s^2)
h_f	Friction loss (m)
k	Equivalent sand roughness (m)
L	Length of a substitution cylinder (m)
Q	Discharge rate (m^3/s)
Re	Reynolds - Number (-)
u	Axial velocity (m/s)
u^+, y^+	Dimensionless distance and velocity (-)
u_τ	Friction velocity (m/s)
V	Mean velocity (m/s)
y	Distance from the center line of the pipe (m)

REFERENCES

M R Kavianpour. Hydraulic behavior of Y-Branches. *Waterpower XIII*, 2003.

L Kinne. Beitrag zur Kenntnis der hydraulischen Verluste in Abzweigstücken. *Mitteilung des Hydr. Institutes der TH München*, 4, 1931.

R Klasinc, H Knoblauch, and T Dum. Power losses in distribution pipes. *Fluid flow modelling*, 1992.

J S McNown. Meachanics of manifold flow. *American society of civil engineers*, 119:1103, 1954.

D.S. Miller. *Internal Flow System*. BHRA (Information Services), Cranfield, Bedford MK43 0Aj, UK, 2 edition, 1990.

F Petermann. Der Verlust in schiefwinkligen Rohrverzweigungen. *Mitteilung des Hydr. Institutes der TH München*, 3, 1929.

G Preiß ler and G Bollrich. *Technische Hydromechanik*. VEB-Verlag für Bauwesen, Berlin, 2 edition, 1985.

G Vogel. Untersuchungen über den Verlust in rechtwinkligen Rohrverzweigungen. *Mitteilung des Hydr. Institutes der TH München*, 2:61–64, 1928.

Th von Kármán. Mechanische Ähnlichkeit und Turbulenz. *Third Int. Congr. Applied Mechanics, Stockholm*, pages 85–105, 1930.

Particle Image Velocimetry of a Y-bifurcator

W. Dobler[1] and G. Zenz[1]
[1]Institute of Hydraulic Engineering and Water Resources Management
Graz University of Technology
Graz, 8010
AUSTRIA
E-mail: w.dobler@tugraz.at

Abstract: *In this paper PIV-Measurements are presented for a Y-bifurcator of a power plant. The Plexiglas model test consists of a 42 degree bend, a straight pipe from the bend to the Y-branch and two branching pipes with a branching angle of 40 degrees. At several locations PIV-Measurements upstream and downstream of the Y-bifurcator are carried out by using natural seeding particles. The quality of the seeding particles will be presented by means of the velocity lag and the size of the particles. A confidence interval for a typical PIV-Measurement is calculated to demonstrate the reliability of the mean velocity. The result of the PIV-Measurement shows the velocity profile and the secondary flow within the Plexiglas installation. The secondary flow will also be quantified by the velocity correction factor α. Due to the reflection at the Plexiglas surface, the velocity profile will be closed with a linear function. The accuracy of this procedure will be checked with a CFD calculation.*

Keywords: *Hydraulic model test, Particle Image Velocimetry (PIV), secondary flow, velocity correction factor, numerical simulation*

1. INTRODUCTION

As is well-known a pipeline between a reservoir and a power plant is necessary to transport the water in the shortest way to the power plant, with low energy losses and with economical low prized pipe installation. The penstock consists therefore mostly of a single pipe which distributes the water - shortly before the power plant - to several turbines. The distribution is in many cases done by a Y-bifurcator which is investigated by numerous authors, like (King, 1963), (Lee *et a*l, 1993), (Ruus, 1970) and (Williamson & Rhone, 1973). In the Hermann Grengg Laboratory a 8.13 times smaller hydraulic model test of a Y-bifurcator is set up to investigate the hydraulic behavior of a dividing flow. As a further challenge, a bend is located 18 times the diameter upstream of the Y-bifurcator which causes a slight secondary flow in the pipe installation (see Figure 1). This makes it necessary to get more information of the velocity and pressure distribution along the pipe installation of the hydraulic model test. With the Bernoulli-Equation it is possible to calculate the head loss between two control sections up- and downstream of the bifurcator. With

$$z_1 + \beta_1 \frac{P_1}{g\,\varrho} + \alpha_1 \frac{V_1^2}{2\,g} = z_2 + \beta_2 \frac{P_2}{g\,\varrho} + \alpha_2 \frac{V_2^2}{2\,g} + h_l \tag{1}$$

one can calculate the head loss h_l, whereas z is the geodetic height, β the pressure correction factor, P the static pressure, α the velocity correction factor, g the gravity and final V the mean velocity in the pipe. The index 1 and 2 denotes a control section before and after the Y-bifurcator where the mean velocity V and the pressure P can be measured with flow meters and pressure probes, respectively (see also the previous paper (Dobler *et a*l, 2010) for this hydraulic model test). The pressure correction factor β is zero because no strong curved streamline occur in the control sections (apart from the bend). The velocity correction factor α, which quantifies the axial secondary flow, will be closer investigated by means of PIV. The discharge rate for the bifurcation is either 160 l/s (each branch 80 l/s) or 80 l/s (the flow streams only through the left branch).
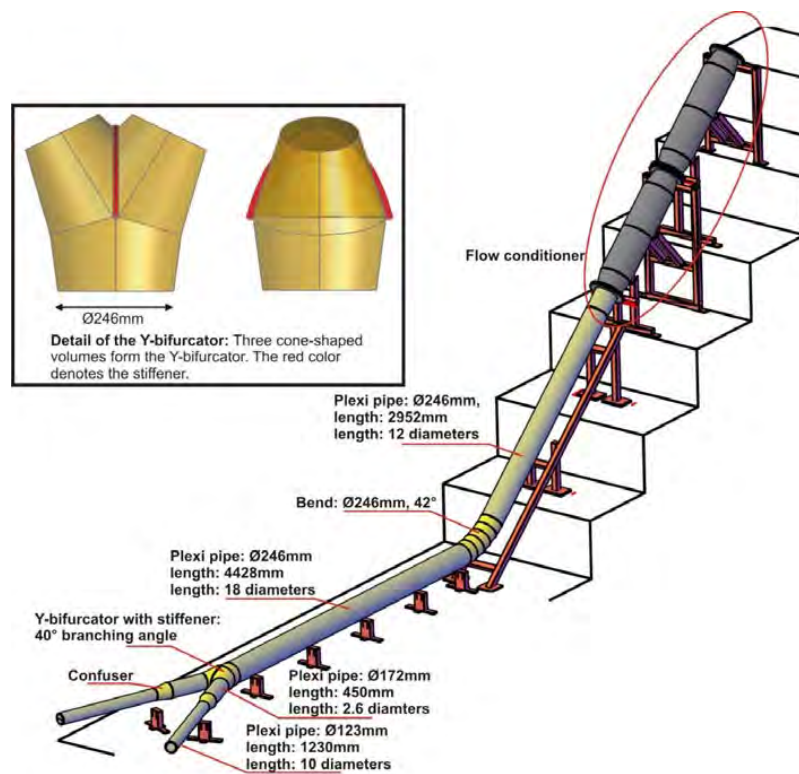
Detail of the Y-bifurcator: Three cone-shaped volumes form the Y-bifurcator. The red color denotes the stiffener.

Ø246mm

Flow conditioner

Plexi pipe: Ø246mm,
length: 2952mm
length: 12 diameters

Bend: Ø246mm, 42°

Plexi pipe: Ø246mm
length: 4428mm
length: 18 diameters

Y-bifurcator with stiffener:
40° branching angle

Confuser

Plexi pipe: Ø172mm
length: 450mm
length: 2.6 diamters

Plexi pipe: Ø123mm
length: 1230mm
length: 10 diameters

Figure 1 Set up of the hydraulic model test

2. SET UP FOR PIV-MEASUREMENTS

Particle Image Velocimetry (PIV) is an optical method to obtain instantaneous velocity vector fields of a 2D-Plane within a fluid. The positions for the measurements are shown in Figure 2. For each PIV-Box four planes are available to investigate the axial velocity.
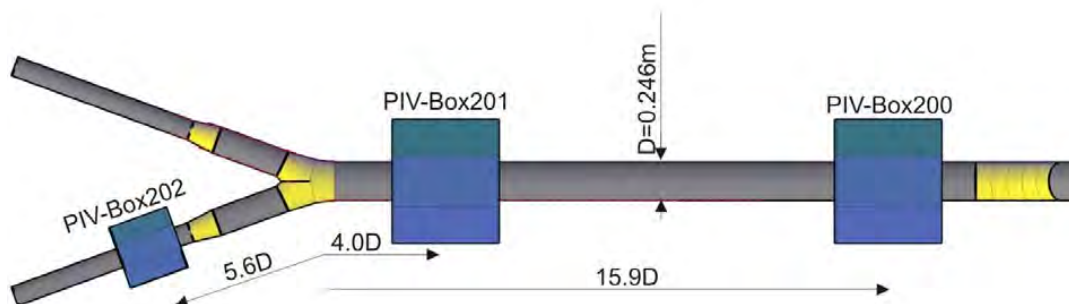
Figure 2 Position for PIV-Box to measure the axial velocities

The laser for the PIV-measurement is a Litron Laser – Model (LDY303-PIV) with a repetition rate of 0.2 – 10 kHz with 21.5 – 1.85 mJ. The wave length is 527 nm (green light). The camera is a Photron FASTCAM SA-1 with a frame rate of 5.4 kHz and resolution of 1024 times 1024 pixel. The working memory has a storage capacity of 16 GB. For a measurement the camera is normally oriented to the 2D-Laser light sheet (see Figure 3, left) and all the illuminated particles (seeding) are recorded. With the images from the camera a cross correlation is done to get the velocity vector field.

Figure 3: PIV-Box (filled up with water) to avoid the astigmatism effect of the curved pipe surface. Four planes are available to measure the axial velocity
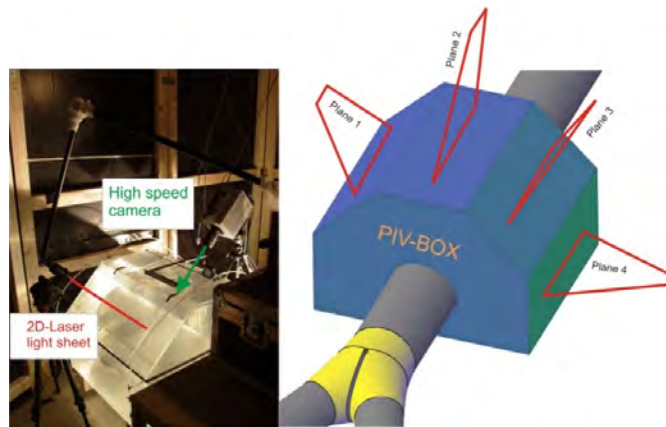
2.1. Natural seeding

Du to the size of the hydraulic model test and the reservoir for the water supply it is not possible to add seeding with a certain property (density, diameter...) to the flow. Therefore, natural seeding are used to measure the velocity within the pipe. To estimate the quality of the natural seeding the average size and the density of the seeding is necessary.
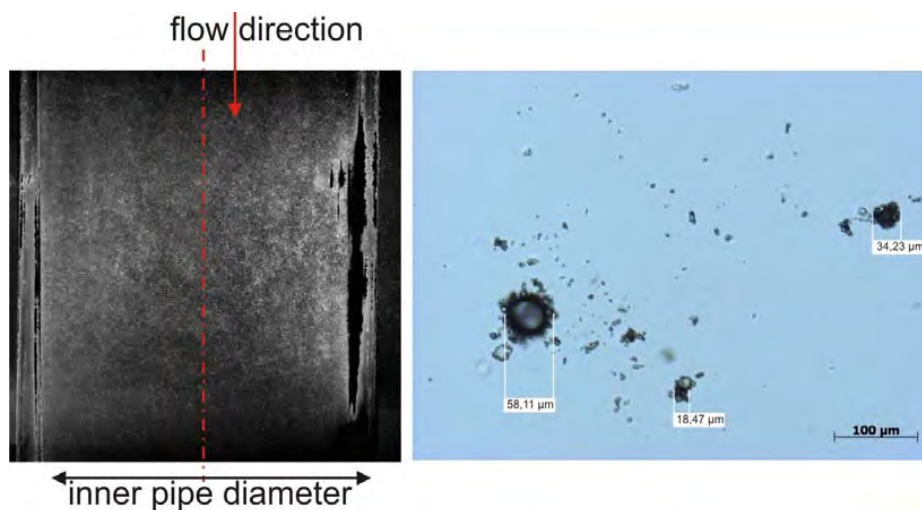
Figure 4 The picture on the left shows the raw data of an instantaneous PIV-measurement where the mean value of the gray levels is subtracted. The picture on the right shows the natural seeding with an optical microscope.

Figure 4 shows a representative example image of a PIV-measurement right after the bend (PIV-BOX 200, Plane 4), where the natural seeding can clearly be distinguished. The diameter of the natural seeding is determined by using a microscope (see Figure 4, right). Several probes had been taken from the water reservoir to check the particle diameter. In the majority of cases the particle size was between 20 and 50 micrometer.

2.2. Velocity Lag of the natural seeding

PIV measures the velocity of the natural seeding and not of the actual flow velocity, carrying the

natural seeding. Every particle, depending on the size and density of the particle, has a velocity lag. One of the methods to estimate the velocity lag in a laminar flow for a spherical particle within a constant acceleration can be made by using the law of Stokes where the forces for gravity, buoyancy, resistance and inertia are in equilibrium (see also (Raffel *et a*l, 2007)). With

$$u_p = u_{end} \left(1 - e^{-\frac{t}{\psi}} \right) \qquad (2)$$

and

$$\psi = \frac{2 \ \rho_p \ r^2}{9 \ \rho_f \ \upsilon} \qquad (3)$$

gives the particle velocity u_p depending on the time t. The other variables are u_{end} which is the end velocity, ψ the relaxation time, ρ_p the density of the seeding, ρ_f the density of the fluid, υ the kinematic viscosity, r the seeding diameter and finale g the gravity. The density for the particle was estimated by using a lower and upper limit of 800 and 1200 kg/m^3. This definition is based on the consideration that only floating particles (density close to water) can be drawn in by the pumps in the reservoir. The diameter of the seeding particle is 50 micrometer which represents the upper limit from the investigation with the optical microscope. The result for the end velocity u_p is shown Figure 5. The particle reaches the end velocity, for example 1 m/s, depending on the density, in approximately 7 10^{-4} seconds (for other end velocity u_p the same time is needed). This result can also be interpreted as having a low pass filter where every turbulent frequency which is higher than 1.4 kHz is blocked due to the inability of the particles (velocity lag) to follow the higher frequency of the flow.
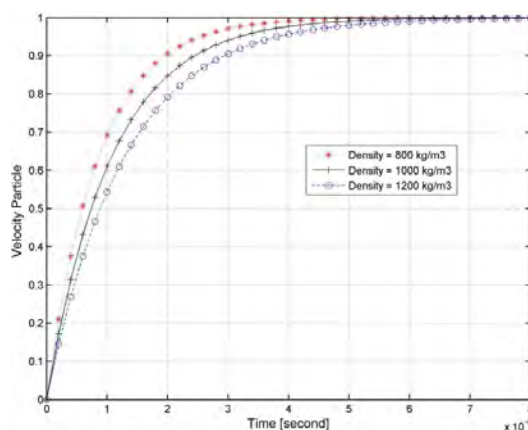

Figure 5 Time response of the natural seeding in accelerating flow

2.3. Confidence interval

With the software of Dantec Dynamics 2.20.18 the raw date with a recording time of at least 1 second and a frame rate between 1000 and 3000 will be evaluated to eliminate any outlier (these are peak, range and moving average validation, the recording time in the pretests was longer to check convergence). After that, the statistical accuracy of the steady state flow of the measurement is checked by a confidence interval with a t-distribution. This implies that the data are nearly normal distributed which will be demonstrated with the red marked example point in Figure 6.
With a confidence level of (1-α)=95% the reliability of the mean value, based on a t-distribution, is

$$\left[u - t_{1-\alpha/2}(n-1) \frac{S}{\sqrt{n}}, \ u + t_{1-\alpha/2}(n-1) \frac{S}{\sqrt{n}} \right] \qquad (4)$$

whereas u is the mean velocity, n the sample size and S the standard deviation.
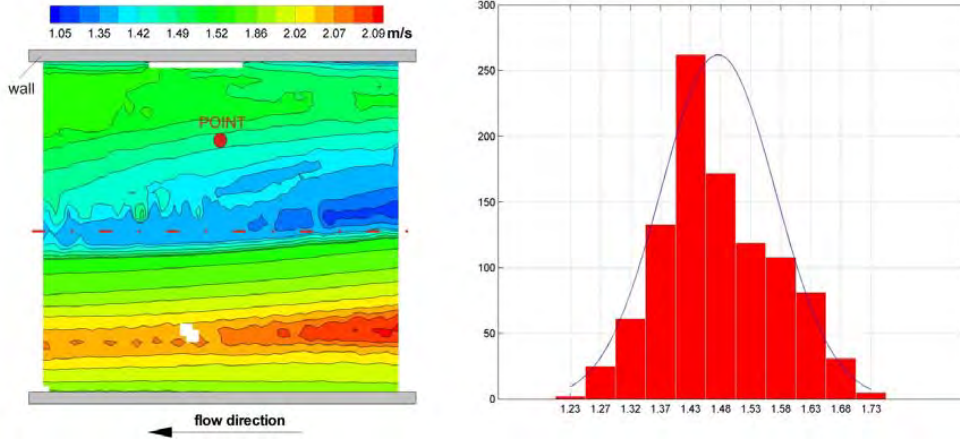
Figure 6 The right figure shows the histogram of the nearly normal distributed longitudinal velocities [m/s] taken from the location marked with the red point in the left figure, where the mean velocities are shown. Location: Piv-Box 200, Plane 2, 80 l/s.
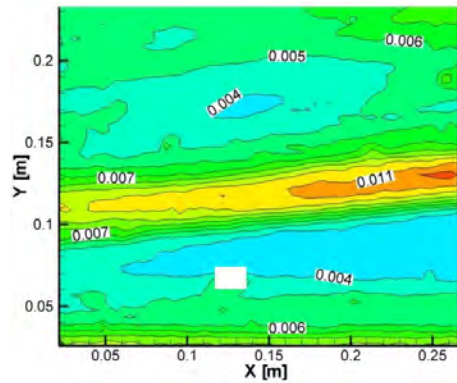

Figure 7 Confidence interval of the mean velocity in longitudinal direction [m/s]

Figure 7 shows the result of the reliability of the mean value of Figure 6. The highest confidence interval is ±0.011 m/s with a longitudinal mean velocity of approximately 2 m/s which indicates a good measurement. For other locations of PIV-measurements (PIV-Box 201 and PIV-Box 202, for all four planes in Figure 2 and Figure 3) equivalent results for the reliability of the mean value (in longitudinal and lateral direction) are achieved. The reliability of the standard deviation is also checked with a χ^2-distribution and shows similar good results as for the mean value (not shown in this paper).

3. VELOCITY CORRECTION FACTOR

Due to the bend upstream of the Y-bifurcator and the short pipe between the bend and the Y-bifurcator (18 times the diameter D) a weak secondary flow is still presented. The simply 1D-consideration of the Bernoulli equation is not valid anymore and a velocity correction factor α is introduced to quantify the axial velocity. Generally, α is defined as (taken from (Preißler & Bollrich, 1980))

$$\alpha = \frac{E_{k,real}}{E_{k,theoretical}} = \frac{1}{u^3 A} \int^A u_A^3 \, dA \tag{5}$$

whereas $E_{k,real}$ is the kinetic energy of the real flow with velocity u_A, $E_{k,theoretical}$ is the kinetic energy of

the mean velocity u, A is the cross section area and dA the differential cross section area.
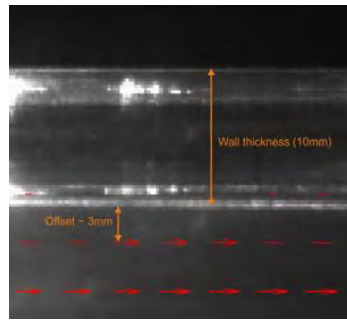

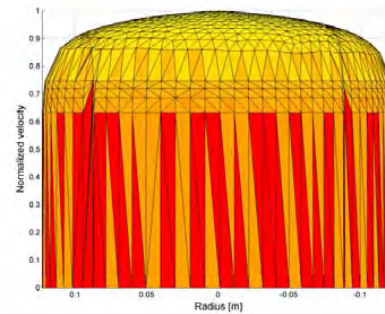**Figure 8 Close up view of the near wall region. The last 3 mm to the wall cannot be measured**

Figure 9 Logarithmic Velocity profile (see Equation 7)

For each PIV-Box four planes (see Figure 3) are used to calculate the velocity correction factor α. To evaluate a single velocity profile Equation 5 needs to be rewritten as

$$\alpha = \frac{1}{u^3 A} \int_{-R}^{+R} u_y^3 \, \pi \, y \, dy \qquad (6)$$

whereas π y is the half circumference, y is the integration variable between the range of –R and +R, u_y is a velocity profile extracted from the four planes in Figure 3 and R is the radius of the pipe. Before Equation 6 will be evaluated one further comment is necessary: In Figure 8 is shown a close-up view of the boundary layer and the first row of evaluated velocity vectors which are 3 mm away from the wall. Due to the reflecting light it is not possible to resolve the last 3 mm and the velocity profile will be closed with a linear function. To estimate the accuracy of this method a 3 dimensional logarithmic velocity profile of a fully turbulent flow with the same Reynolds number is used which is (taken form (Sigloch, 2005), see also Figure 9):

$$\frac{u_{max} - u_{(r)}}{u_\tau} = -\frac{1}{\kappa}\left[ln\left(1 - \sqrt{\frac{r}{R}}\right) + \sqrt{\frac{r}{R}} \right] \qquad (7)$$

whereas u_{max} is the maximum velocity, u_τ is the friction velocity, κ is the von Karman-Constant, R is the pipe radius and u is the velocity at radius r.
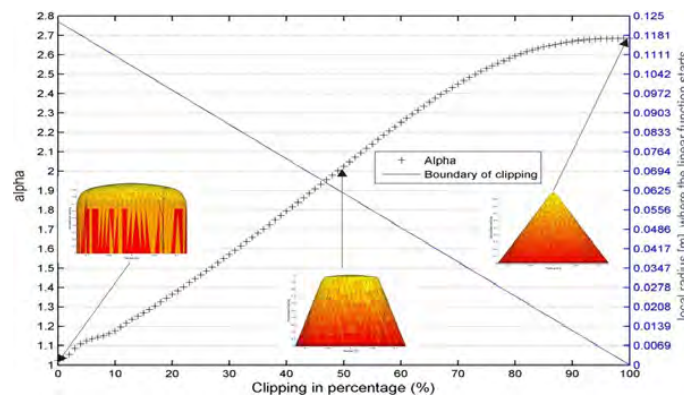

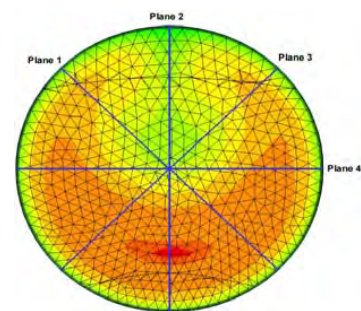**Figure 10 Replacement of the logarithmic velocity profile with a linear function**

Figure 11 Axial velocities from CFD: 4 lines labelled as Plane 1 to Plane 4 (same position as in Figure 3) are chosen to calculate the α-values

The friction velocity is estimated by using

$$u_\tau \approx 0.2 \, Re^{-0.125} \, u_{mean} \qquad\qquad (8)$$

whereas Re is the Reynolds number and u_{mean} the mean velocity.

With this generic velocity profile more and more of the logarithmic part will be replaced with a linear function as can be seen in Figure 10. The influence on the calculated α-value with the linear/logarithmic velocity profile is also plotted in Figure 10: At 0% replacement (no linear function) α yields a value of 1.024 (turbulent flow, Re = 10^6), when 100% is substituted with a linear function then the theoretical α value of 2.7 is calculated. For the case where the last 3 mm are replaced with a linear function which correspond to a clipping of 2.4 % (3/R = 3/124=2.4%), a α-value of 1.044 is obtained. Thus, the calculated α-value is only about 2% larger than the "true" value with 1.024. Therefore, it can be expected that the velocity profiles of the secondary flow of the PIV-Measurements plus the linear functions, show similar results as with the logarithmic profile of Equation 7 and the added linear function.

As already mentioned four flow profiles for each PIV-box are used to calculate one single α value of the three dimensional, axial velocity profile. It is therefore necessary to check if the mean value of all four planes is close enough to the exact α value of the whole control section. For that purpose a CFD calculation is done to simulate the secondary flow induced by the bend. The numerical calculation is carried out with Fluent 12.1 with a hybrid mesh of 1.6 million tetrahedron and hexahedron elements. The turbulence model is k-ε with the standard wall function for the near wall treatment. A velocity profile at location "PIV-Box 200" (see Figure 2) will be extracted, to calculate the α value for the whole 3D profile and also for the four lines (see Figure 11). Equation 5 is evaluated to calculate the alpha value for the 3D-Velocity profile and Equation 6 is used to calculate the four α values for the extracted velocities at the blue lines in Figure 11. The results are shown in Table 1: For the 3D-Velocity profile a α-value of 1.043 [-] is obtained and for the mean value 1.042 [-] which is only about 0.1 [%] lower than for the 3D profile. Therefore, it can be expected that the mean of the α-values from the four planes of the PIV-measurement represent the axial secondary flow of the whole 3D profile.

Table 1 Comparison of the velocity correction factor of the entire 3D flow profile and of the mean of the four velocity flow profiles (numerical simulation, location: PIV-Box 200)

3D-Velocity Profile	Plane 1 - diagonal left	Plane 2 - vertical	Plane 3 - diagonal right	Plane 4 - horizontal	Mean of Plane 1 to 4
-	-	-	-	-	-
1.043	1.026	1.098	1.026	1.018	1.042

The results (discharge 80 l/s) of the PIV-measurement with the linear modification of the near wall region are shown in Figure 12 and Figure 13. Shortly before the flow enters the Y-bifurcator (PIV-Box 201) a weak secondary flow is still visible and the mean value of the four planes for the velocity correction factor α yields 1.037; the velocity factor after the Y-bifurcator (PIV-Box 202) yields a slightly lower value of 1.030. With these α-values the Bernoulli equation (see Equation 1) can be used to calculate the hydraulic loss of the Y-bifurcator including the induced secondary flow of the bend as shown in Figure 14.

4. CONCLUSION

With the use of natural seeding it is possible to carry out PIV-Measurements to investigate the secondary flow up- and downstream of a Y-bifurcator. The quality of this measurement is checked with the velocity lag of the particles which shows that the particles can follow the flow up to a frequency of 1.4 kHz. Additionally, the confidence interval of the mean value of the steady state flow is calculated and confirms the good quality of the results. The secondary flow of the pipe installation is quantified with the velocity correction factor α, based on the velocity profile of several PIV-measurements. Due to the reflection at the inner pipe surface parts of the velocity profile are replaced with a linear function. The calculated α-values, including the linear function, show only a ≈2% deviation in comparison to a complete logarithmic profile without any linear function. The mean value of the calculated α-values for the 2D-Velocity profiles represents accurately enough the 3D-Velocity profile of a control section. This

is double-checked with numerical simulation where the difference between the 2D and 3D-velocity profile is only about ≈0.1%.

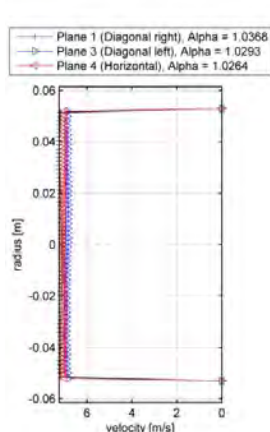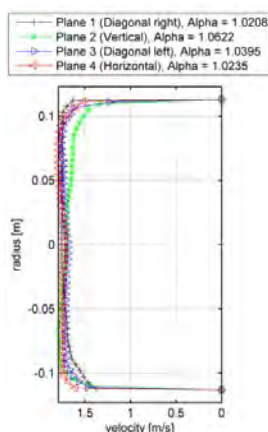**Figure 12 Velocity profile PIV-Box 202**
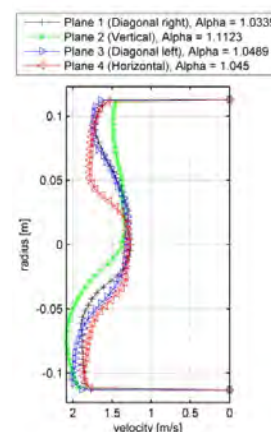

Figure 13 Velocity profile PIV-Box 201

Figure 14 Velocity profile PIV-Box 200

5. ACKNOWLEDGMENTS

6. REFERENCES

Dobler, W., Knoblauch, H., & Zenz, G. (2010). *Hydraulic investigation of a Bifurcator. The First European IAHR Congress* (Vol. The First). Edinburgh.

King, D. L. (1963). *Hydraulic Model Studies of Causey Dam Outlet Works, Weber Basin Project Utah. Laboratory Report, Hyd.* (p. 29). Denver.

Lee, B. K., Coleman, H. W., Kim, J. H., & Kwon, H. I. (1993). *Hydraulic model studies of Y-branch.* PROC NATL CONF HYDRAUL ENG, ASCE, NEW YORK, NY(USA)*, 1993,* (p. 1689:1694).

Preißler, G., & Bollrich, G. (1980). *Technische Hydromechanik* (1st ed.). Berlin: VEB Verlag für Bauwesen.

Raffel, M., Willert, C., Wereley, S., & Kompenhans, J. (2007). *Particle Image Velocimetry* (2nd ed.). Springer.

Ruus, E. (1970). *Head losses in wyes and manifolds.* Journal of the Hydraulics Division, 96(3), 593-608.
Sigloch, H. (2005). Technische Fluidmechanik. New York (6th ed., pp. 1-569). Springer-Verlag Berlin Heidelberg.

Williamson, J. V., & Rhone, T. J. (1973). *Dividing flow in branches and wyes.* Journal of the Hydraulics Division, 99(5), 747:769.

10.4   Curriculum Vitae

Wolfgang Dobler

CONTACT INFORMATION	Institute of Hydraulic Engineering and Water Resources Management Faculty of Civil Engineering Graz University of Technology	office: +43 316 873 8361 mobile: +43 650 85 199 50 e-mail: hydro@tugraz.at

<small>RESEARCH INTERESTS</small>   Hydraulic model test, Computational Fluid Dynamics, water hammer, ADCP/ADV field measurements, Particle Image Velocimetry, Matlab and TCL programming.

<small>EDUCATION</small>   *Graz University of Technology*, Graz, Styria, Austria

- *Doctor of Philosophy*   **November 2007 – present**
- *Diploma Study*   **October 1999 – October 2006**

Iowa, Institute of Hydraulic Research, Iowa City, Iowa, USA   **January 2006 – June 2006**

Tampere, University of Technology, Tampere, Finland   **September 2002 – May 2003**

<small>SELECTED PUBLICATIONS</small>

1. **Dobler W**, Larcher M, Arch A, Zenz G, *Numerische Untersuchung von Rohrströmungen am Beispiel eines Bifurkators*, Fachzeitschrift: Österreichische Wasser- und Abfallwirtschaft, Heft 3-4, Seite: 54-57, 2010

2. Schneider J, **Dobler W**, Arch A, Badura H, *Durchschleusen von Trübeströmungen durch einen alpinen Speicher*, Fachzeitschrift: Österreichische Wasser- und Abfallwirtschaft, Heft 11-12, Seite: 183-191, 2010

3. **Dobler W**, Zenz G, *Particle Image Velocimetry of a Y-bifurcator*, IAHR 34th World Congress, Proceedings of the 34th IAHR World Congress (CD-ROM), Page: 2257-2265, 2011, Brisbane, Australia, reviewed

4. **Dobler W**, Knoblauch H, Zenz G, *Hydraulic investigation of a Y-bifurcator*, First IAHR European Division Congress, Proceedings of 1st, IAHR European Division Congress (USB-Stick), 6 Pages, 2010, Edinburgh, United Kingdom , reviewed

5. **Dobler W**, Knoblauch H, Zenz G, *Hydraulische Modellierung eines Bifurkators*, Gemeinschafts-Symposium der Wasserbau-Institute TU München, TU Graz und ETH Zürich: Wasserbau in Bewegung, Berichte des Lehrstuhls für Wasserbau Nr.124, Seite: 287-296, 2010, Wallgau, Deutschland, reviewed

6. Zenz G, Dorfmann C, **Dobler W**, *Entsanderanlage Högmoos*, Forschungsbericht, Institut für Wasserbau und Wasserwirtschaft TU-Graz, 63 Seiten, 2011

7. Zenz G, Knoblauch H, Richter W, **Dobler W**, Lazar Friedrich, *Hydraulischer Modellversuch - Wasserschloss Burgstall* Forschungsbericht, Institut für Wasserbau und Wasserwirtschaft TU-Graz, 232 Seiten, 2011

8. Zenz G, Schneider J, **Dobler W**, Richter W, Lazar Friedrich, *Wasserschloss Atdorf - Hydraulischer Modellversuch*, Forschungsbericht, Institut für Wasserbau und Wasserwirtschaft TU-Graz, 102 Seiten, 2011

9. **Dobler W**, *Hydraulische Untersuchungen an einem Bifurkator*, 12. Treffen junger WissenschaftlerInnen (Juwi), Tagungsband ISBN 978-3-933761-97-2, Seite: 34-45, Universität Stuttgart, Deutschland, 2010

10. Richter W, **Dobler W**, and Knoblauch H, *Hydraulic and numerical modeling of an asymmetric orifice*, 4. IAHR International Symposium on Hydraulic Structures, Porto, 2012.